

**INELASTIC LIGHT SCATTERING STUDIES ON STRONG
NETWORK GLASSES**

By

SOUMEE CHAKRABORTY

Enrolment No. PHYS 02 2010 04 016

Indira Gandhi Centre for Atomic Research, Kalpakkam

A thesis submitted to the

Board of Studies in Physical Sciences

In partial fulfillment of requirements

for the Degree of

DOCTOR OF PHILOSOPHY

of

HOMI BHABHA NATIONAL INSTITUTE



April, 2017

Homi Bhabha National Institute¹

Recommendations of the Viva Voce Committee

As members of the Viva Voce Committee, we certify that we have read the dissertation prepared by **Soumee Chakraborty** entitled **Inelastic Light Scattering Studies on Strong Network Glasses** and recommend that it may be accepted as fulfilling the thesis requirement for the award of Degree of Doctor of Philosophy.

Chairman – **Dr. M. Kamruddin**



Date: 13/8/17

Guide / Convener – **Dr. V. Sivasubramanian**



Date: 13/09/17

Examiner – **Prof. Chandrabhas Narayana**



Date: 13/09/17

Member 1– **Dr. N. V. Chandra Shekar**



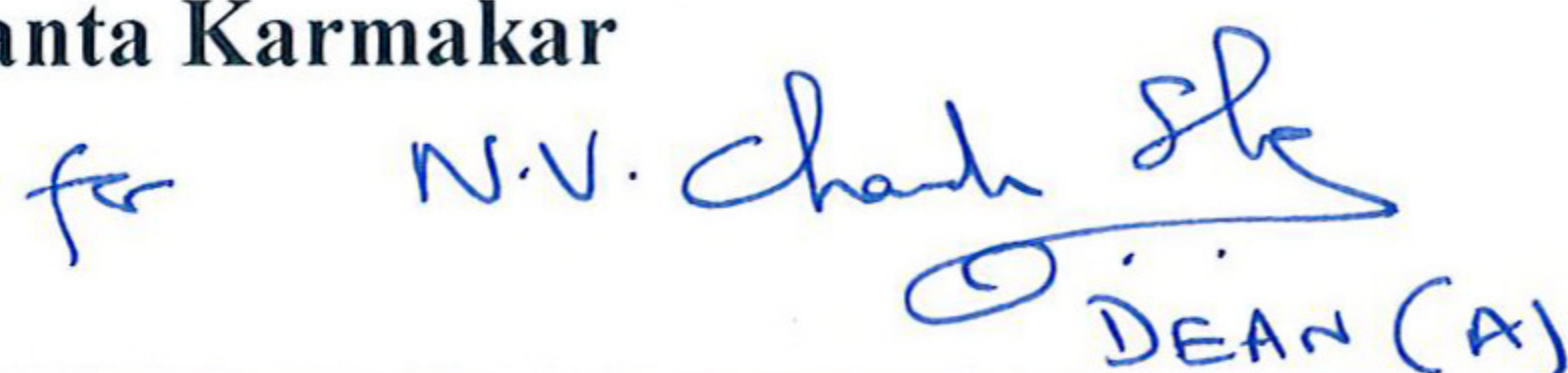
Date: 13/9/17

Member 2– **Dr. T. N. Sairam**



Date: 13/09/17

Member 3– **Dr. Sukanta Karmakar**


for N.V. Chandra Shekar
DEAN (A)

Date: 13/9/17

Final approval and acceptance of this thesis is contingent upon the candidate's submission of the final copies of the thesis to HBNI.

I/We hereby certify that I/we have read this thesis prepared under my/our direction and recommend that it may be accepted as fulfilling the thesis requirement.

Date: 13/09/17

Place: Kalpakkam

<Signature>

Co-guide (if applicable)



<Signature>

Guide

¹ This page is to be included only for final submission after successful completion of viva voce.

STATEMENT BY AUTHOR

This dissertation has been submitted in partial fulfillment of requirements for an advanced degree at Homi Bhabha National Institute (HBNI) and is deposited in the Library to be made available to borrowers under rules of the HBNI.

Brief quotations from this dissertation are allowable without special permission, provided that accurate acknowledgement of source is made. Requests for permission for extended quotation from or reproduction of this manuscript in whole or in part may be granted by the Competent Authority of HBNI when in his or her judgment the proposed use of the material is in the interests of scholarship. In all other instances, however, permission must be obtained from the author.

Soumee Chakraborty

(Soumee Chakraborty)

DECLARATION

I, hereby declare that the investigation presented in the thesis has been carried out by me. The work is original and has not been submitted earlier as a whole or in part for a degree/ diploma at this or any other Institution/ University.

Soumee Chakraborty

(Soumee Chakraborty)

List of Publications arising from the thesis

A. Journals/ Preprints

1. “Temperature evolution of Raman spectrum of iron phosphate glass”, **S. Chakraborty** and A. K. Arora, *Vibrational Spectroscopy*, **2012**, *61*, 99-104.
2. “Composition and temperature-induced structural changes in lead-tellurite glasses on different length scales”, **S. Chakraborty**, A. K. Arora, V. Sivasubramanian, P. S. R. Krishna and R. Venkata Krishnan, *J. Phys.: Condens. Matter*, **2012**, *24*, 505401-505411.
3. “Glass transition, kinetics of crystallization and anomalous phase transformations in tellurite melts”, **Soumee Chakraborty**, R. Venkata Krishnan, V. Sivasubramanian and S. Kalavathi, *Materials Research Express*, **2014**, *1*, 045203-045223.
4. “Anomalous variation of Boson peak and fragility and their correlations with intermediate-range structure in PbO-B₂O₃ glasses”, **Soumee Chakraborty**, V. Sivasubramanian, L. Herojit Singh, R. Venkata Krishnan and A. K. Sinha, *J. Alloys and Comp.*, **2017**, *713*, 95-107.
5. “Temperature dependence of elastic properties in lead borate glasses across the glass transition”, **Soumee Chakraborty** and V. Sivasubramanian (under preparation).

B. Published Conference Proceedings

1. “Raman study of glass transition in iron phosphate glasses”, **S. Chakraborty** and A. K. Arora, *AIP Conf. Proc.*, **2012**, *1447*, 563-564.
2. “Anomalous Brillouin shift in lead-tellurite glass above glass transition”, **S. Chakraborty**, A. K. Arora, V. Sivasubramanian and P. S. R. Krishna, *AIP Conf. Proc.*, **2013**, *1512*, 574-575.

C. Conference Papers- Unpublished (Abstract only)

1. “Raman study of glass transition in lead-tellurite glass”, **S. Chakraborty**, A. K. Arora and P. S. R. Krishna, *XXIII International Conference on Raman Spectroscopy*, Bangalore, India [12-17 August 2012].
2. “Low frequency Raman scattering in lead borate binary glasses”, **Soumee Chakraborty**, L. Herojit Singh and V. Sivasubramanian, *XXIV International Conference on Raman Spectroscopy*, Jena, Germany [10-15 August 2014].

Soumee Chakraborty

(Soumee Chakraborty)

To
my beloved family

ACKNOWLEDGEMENTS

First and foremost, I take this opportunity to thank my thesis advisor Dr. V. Sivasubramanian for giving me opportunity to work in the field of structural glasses. He introduced me to the technique of Brillouin spectroscopy and guided me into its operation and data analysis. His valuable and expert advice, constant enthusiasm and encouragement, has made it possible for me to complete my work.

I sincerely thank and express my heartfelt gratitude to Dr. A. K. Arora who has been my mentor in research. I thank him for introducing me to the physics of amorphous solids and Raman spectroscopy, for useful discussions and suggestions to conduct experiments, understand experimental data, find out proper explanations and a critical assessment of my articles. He has been my light through the dark tunnel whenever I felt lost.

I thank Dr. T. R. Ravindran for his immense help and support in carrying out Raman spectroscopic measurements throughout the course of my research work and providing valuable suggestions for the thesis.

I sincerely thank Dr. Kitheri Joseph for teaching me the technique of melt-quenching for synthesizing glasses and providing me my first glass sample for study.

I extend my sincere thanks to my collaborators, Dr. P. S. R. Krishna (BARC, Mumbai) for synthesis of lead-tellurite glasses, Dr. R. Venkat Krishnan and Shri Abhiram Senapati for DSC measurements, and Dr. S. Kalavathi, Dr. A. K. Sinha (RRCAT, Indore) and Shri Manavendra Singh (RRCAT, Indore) for XRD measurements,

Dr. S. Tripura Sundari for ellipsometry and Dr. Govind K. Sharma for ultrasonic sound echo measurements.

I am grateful to my doctoral committee members, Dr. M. Kamruddin, Dr. N. V. Chandra Shekar, Dr. T. N. Sairam and Dr. S. Karmakar for sharing their valuable time and for their suggestions during my Ph.D. tenure. I extend my sincere thank to Dr. B. V. R. Tata (ex-Chairman of my DC) for providing me with helpful feedback and evaluating my work at each stage. I especially thank Dr. N. V. Chandra Shekar (Dean, Physical Sciences) for encouraging and advising me to compile my work into my Ph. D. thesis. I sincerely thank former Group Directors and present Group Director for all their support and encouragement.

I am indebted to all my teachers who have taught me various lessons at different stages of life. I owe a special thank to Dr. K. S. Vishwanathan and Shri M. C. Valsakumar for making classes so interesting that students relish getting deep into those subjects.

My work would never have been completed without an active cooperation and support from a lot of colleagues and friends. I thank my lab-mates Dr. R. G. Joshi, Dr. Karuna Kara Mishra, Dr. K. Kamali for their cooperation and timely help during my thesis tenure. A special thank to my batchmates; Deepak, Gurpreet, Herojit, Maneesha, Vinita and Manan who have always been with me through jolly and tough times. I express my sincere thanks to my seniors, Dr. P. Rajini, who had introduced me to curve-fitting programs, and Dr. A. T. Satya, Dr. K. Gururaj, Dr. K. Prabakar and Dr. P. K. Sahoo for their encouragement and support. I acknowledge the affection and support from my juniors; Karthickeyan, Madhusmita, Anees, Shraddhanjali, Rajitha and Radhakrishna.

I convey my heartfelt thanks to my husband, Dr. Anirban Pal, who has been a constant source of motivation and encouragement throughout my Ph.D. The technical deliberations with him have helped me a lot in comprehending the results of my thesis work.

I take this opportunity to thank my adorable son, Ayinteeek, who has shown unlimited patience throughout my thesis writing period, tolerated and forgave me for my late absence from home every day and, for never being a demanding child.

I thank my brother for his immense support and guidance throughout my academic life.

Above all, I express my deepest gratitude to my parents whose unconditional love and support has given me the freedom to pursue my career. They have been the lodestar of my life. Their kind blessings and constant encouragement have enabled me to bring this work to completion.

CONTENTS

	Page No.
SYNOPSIS	xv
LIST OF FIGURES	xxv
LIST OF TABLES	xxxi
LIST OF SYMBOLS	xxxii
CHAPTER 1 INTRODUCTION	1
1.1 Definition of Glass	1
1.2 Glass formation: Supercooled liquid and the glass transition	4
1.2.1 Thermodynamics as T_g is approached: Entropy crisis and the Kauzmann temperature	7
1.2.2 Dynamics as T_g is approached: Relaxation processes	9
1.2.2.1 Different behaviour in dynamics: strong and fragile glass-formers	11
1.3 Theories of glass formation	15
1.3.1 Structural theories of glass formation	15
1.3.1.1 Zachariasen's Continuous Random Network (CRN) theory	16
1.3.1.2 Phillips-Thorpe's topological constraints theory	17
1.3.2 Kinetic theory of glass formation	18
1.4 Crystallization/ Devitrification: Kinetics of phase transitions	20
1.5 Classification of structural order in glass: order within disorder	23
1.5.1 Medium-range order and the first sharp diffraction peak	24
1.6 Vibrational properties of glasses	26
1.6.1 The vibrational density of states (VDOS)	27
1.6.2 The Debye model of specific heat	27

2.2.1.5 Theory of Brillouin scattering	79
2.2.1.6 Brillouin scattering instrumentation	82
2.2.1.6.1 Principle of Fabry-Pérot Interferometer	83
2.2.1.6.2 Working of Tandem Interferometer	84
2.2.1.6.3 Concept of 3+3 pass Fabry-Pérot Interferometer	87
2.2.1.6.4 Brillouin spectrometer set-up	88
2.2.2 X-ray diffraction	91
2.2.2.1 X-ray diffraction in glass	91
2.2.2.2 Synchrotron x-ray diffraction	93
2.2.3 Density measurement	94
2.2.4 Differential scanning calorimetry	95
2.2.5 Ultrasonic pulse echo technique	97
2.2.6 Ellipsometry and refractive index	98
CHAPTER 3 COMPOSITION AND TEMPERATURE-INDUCED STRUCTURAL AND DYNAMICAL CHANGES IN LEAD- BORATE GLASSES AT DIFFERENT LENGTH-SCALES	99
3.1 Introduction	99
3.2 Experimental	102
3.3 Results and discussion	104
3.3.1 Composition dependence of density, T_g and sound velocities	104
3.3.2 Composition dependence of high-frequency Raman modes	108
3.3.3 Composition dependence of low-frequency Raman spectrum	112
3.3.4 Composition dependence of FSDP	122
3.3.5 Composition dependence of fragility	126
3.3.6 Composition dependence of longitudinal acoustic	

mode	135
3.3.7 Temperature dependence of elastic properties	136
3.3.8 Scaling of elastic properties	137
3. 4. Conclusions	139
CHAPTER 4 COMPOSITION AND TEMPERATURE-INDUCED STRUCTURAL CHANGES IN LEAD-TELLURITE GLASSES AND MELTS AT DIFFERENT LENGTH- SCALES	141
4.1 Introduction	141
4.2 Experimental	144
4.3 Results and discussion	146
4.3.1. X-ray diffraction	146
4.3.2. Brillouin scattering	146
4.3.3. High-frequency Raman scattering	155
4.3.4. Thermal analysis: Glass transition and the Kauzmann temperature	167
4.3.5. Crystallization kinetics: Non-isothermal studies	170
4.3.5.1. Isokinetic method: JMA Analysis	172
4.3.6. Structural studies: Phase formation during heating and cooling crystallization	175
4.4. Conclusions	179
CHAPTER 5 TEMPERATURE-INDUCED STRUCTURAL CHANGES IN IRON-PHOSPHATE GLASS AT SHORT-RANGE LENGTH- SCALE	181
5.1 Introduction	181
5.2 Experimental	184
5.3 Results and discussion	184
5.4 Conclusions	194

CHAPTER 6	SUMMARY AND CONCLUSIONS	195
6.1	Summary	195
6.2	Conclusions	199
6.3	Future scope	201
	REFERENCES	202

SYNOPSIS

Glass is an amorphous solid lacking long-range order and exhibits glass transition behaviour. Despite the lack of long-range order, glasses do possess a high degree of short-range order. A glass is formed by quenching of a melt fast enough which takes it to the supercooled liquid state where the dynamics drastically slows down as the liquid approaches the glass transition temperature, T_g . Below T_g , the glass thus formed, possesses a disordered configuration close to that of the supercooled liquid but displays mechanical properties of a solid. Therefore, any material, inorganic, organic or metallic, forms glass upon melt-quenching. Glasses of atomic systems have thus been classified based on the chemical bonding characteristics. Organic glasses are polymeric solids composed of intermeshed long-chain organic molecules. Glasses formed by fast quenching of metals and their alloys results in the formation of metallic glasses. Inorganic glasses with covalent bonding and strongly bound network structures formed by local atomic polyhedra are called as network glasses. This thesis addresses structural aspects of network glasses as probed by Raman and Brillouin spectroscopy.

The components of network glasses are network formers, modifiers and intermediates. The network formers (oxides of silicon, boron, germanium, etc.) form a highly cross-linked network of chemical bonds. Structure of network glasses is tunable using modifiers as well as intermediates. The randomness in bond lengths and polyhedral orientations, the openness in structure and the varying degree of coordination allows the glass structure to accommodate large variation in composition, which is achieved using modifiers. These are usually oxides of monovalent/divalent cations (lithium, sodium, potassium, calcium, lead, etc.) that change the bonding in the parent glass network and hence help to improve or tailor glass properties. Intermediates (oxides of titanium, aluminium, zirconium, zinc, magnesium, etc.) are species that behave either as glass former or modifier depending on their concentration in the glass. Since the properties of a glass are controlled by the microscopic structure, which in turn depends on the composition of the glass, investigating the inter-relationship between composition and network structure constitutes an important study and such study enables one to prepare

glass compositions [1] with desired properties. Glasses are known to have wide-ranging applications in optics, electronics, fiber-optic cables, radiation protection, solar energy, nuclear waste-loading etc. and hence studies mentioned above have technological [2] importance.

Understanding the interplay of dynamics and structure has evoked great interest in condensed matter physics owing to the variety of universal phenomena linked to glass and the supercooled liquid [3] states. Two length-scales generally characterize the structure of a glass: a short-range structure defining the nearest neighbour atomic polyhedra and an intermediate-range order defining regions of structural inhomogeneities associated with density fluctuations. Such density fluctuations strongly scatter phonons and localize the low-energy vibrational excitations, which leads to enhancement of the vibrational density of states (VDOS) [4]. This increase of VDOS in the low-frequency range emerges in the form of a Boson peak (BP), whose frequency provides estimates of the intermediate-range order. Raman spectroscopy is an ideal technique to measure VDOS in glasses. Thus, the BP in glasses can be studied using low-frequency Raman spectroscopy [5]. BP has been found to be a universal characteristic of glassy systems and does not have a crystalline counterpart [4]. However, a decisive conclusion about the microscopic origin of the BP has not appeared, even though there are theories attributing it to transverse modes [6], or coupled rotation of tetrahedra [7], or propagating acoustic modes [8]. Although the appearance of BP is a signature of the lack of long-range order, its peak frequency and intensity depends strongly on the structure of the investigated system. Another evidence for the presence of intermediate-range order [4] in glasses is the universal appearance of the first sharp diffraction peak (FSDP) observed in diffraction experiments. The BP and FSDP reflect the dynamic and static characteristics of glasses, respectively. There are many reports which have correlated [9] the BP and the FSDP, while some others [10] have contested such correlations. Moreover, understanding the dynamics of the various relaxation processes and their relation to the glass transition has aroused great interest in recent years [3]. Especially, it is not clear why some glass formers show an Arrhenius temperature dependence of viscosity (or relaxation time τ_α) close to T_g , while others exhibit a super-Arrhenius behaviour. The activation energy of the viscous flow at T_g provides a quantitative assessment for the strong or fragile

character of a glass former and is related to the degree of structural reorganization with temperature near T_g . The change of viscosity near T_g is governed by the flow unit size, and hence fragility characteristics of glass formers is also related to the intermediate-range structure [11]. Apart from viscosity measurements, calorimetric and spectroscopic techniques have been reliably utilized to quantify fragility in glasses [12]. It is thus thought that the fragility of a liquid may be embedded in the properties of the glassy state. Strong glass forming liquids like SiO_2 , GeO_2 , B_2O_3 , etc. have a highly-connected, covalently-bonded network. In such network glasses the transformation to liquid state occurs through temperature-activated bond breaking which explains their temperature dependence of viscosity and relaxation time. Subtle structural changes are captured clearly using vibrational spectroscopy, where the breaking of bonds in a continuous network is expected to lead to significant changes in the vibrational spectrum in the form of intensity and softening of the phonon modes involved [13]. Vibrational spectroscopy thus becomes an indispensable tool to probe the phonon modes and can provide information on structure of glasses.

The aim of the present thesis is to investigate the above-mentioned aspects by inelastic light scattering techniques of Raman and Brillouin spectroscopy of strong network glasses as a function of composition and temperature to monitor structural changes at short-, intermediate-range and bulk scale. Raman spectroscopy is a sensitive probe of local order, structure and coordination through an analysis of mode-frequencies, line-widths and relative intensities of the spectral features. Acoustic modes are captured using Brillouin spectroscopy which gauges elastic deformations that are sensitive to the connectivity of structural elements. A combined use of these two techniques allows one to capture vibrations that span different frequency regimes and probe different length-scales for understanding the structure and dynamics in glasses across and around T_g . This thesis explores the implications of glass modification on the network structure by varying the concentration of modifier and focuses on its consequences on glass structure and properties. Three systems of network glasses have been chosen based on the constituent structural units: borate, tellurite and phosphate glasses. Oxides of divalent cations have been used as modifiers. The corresponding unmodified glass systems have coordination number of three, mixture of three and four, and four, respectively for the borate, tellurite

and phosphate glasses. The basis for the choice of these systems is the unique response of these glasses to structural modification.

In borate systems, the initial three-coordinated (BO_3) network structure favours up-conversion of some fraction of units to four-coordinated (BO_4) borons with modifier addition up to a certain concentration. Borate and modified-borate glasses exhibit substantial intermediate-range order ($\sim 20 \text{ \AA}$) arising from superstructural units. Network modifiers play an important role in defining the length-scale of the intermediate-range order. In this thesis, the effect of glass modifiers on intermediate-range order in lead-borate glasses is captured from a detailed composition-dependent study of the BP. A comparison of the length-scales of intermediate-range order obtained from the BP and FSDP helps understand the origin of these features. Effect of glass modification on fragility has also been studied. These results are discussed in Chapter 3 of the thesis. Thereafter, tellurite glass systems are investigated. Tellurite glasses have a mixture of four- (TeO_4) and three- (TeO_3) coordinated polyhedral units and the fraction of TeO_3 increases with increasing modifier concentration. The effect of modification with simultaneous increase of temperature on the short-range and bulk elastic properties forms an interesting study. Chapter 4 explores the effect of structural modification at different length-scales in lead-tellurite glasses using Raman and Brillouin scattering. Temperature dependence of elastic response above T_g has been monitored to infer tuning of fragility appearing as a consequence of glass modification. This thesis also reports crystallization kinetics on a modified-tellurite glass where microstructural evolution was studied. These results are discussed in detail in Chapter 4 of the thesis. Finally, phosphate glass system was investigated. Phosphate glasses have four-coordinated (PO_4) polyhedral units that do not change coordination state with modification. Iron-phosphate glass having the composition $[40\text{Fe}_2\text{O}_3:60\text{P}_2\text{O}_5]$ was studied using Raman spectroscopy for the changes induced in the local structure when it is taken from glass to supercooled liquid and across T_g . This glass composition possesses the best chemical durability and is being investigated widely for applications in nuclear waste-immobilization. The effect of temperature on VDOS was studied to understand structural relaxation in glass and supercooled liquid states. Details of these results are presented in Chapter 5 of the thesis.

This thesis is organized into six chapters and contents of each chapter are summarized below.

Chapter 1: Introduction

This chapter introduces glass formation from the definitions of the supercooled liquid and the glass transition. The associated dynamics and the strong-fragile classification are also elaborately described. The glass structure and its modification, ordering at different length-scales and characterization of the amorphous structure have been discussed. This chapter highlights the different vibrational modes in glasses, the relation of VDOS to Raman spectrum and BP. Structure of borate, tellurite and phosphate glasses is also discussed in detail. The chapter ends with a presentation of scope of the work and investigations carried out for the present thesis.

Chapter 2: Synthesis of glasses and characterization techniques

This chapter presents the details of glass synthesis procedures and experimental techniques used for investigation of their structure and dynamics. Inelastic light scattering theory of Raman and Brillouin spectroscopy are described. The different analysis procedures used for glasses are discussed. Detailed technical aspects of the light scattering set-ups are also discussed. A brief discussion on differential scanning calorimetry (DSC), x-ray diffraction and ellipsometry is provided.

Chapter 3: Composition and temperature-induced structural and dynamical changes in lead-borate glasses at different length-scales

Borate glasses are extensively studied for their non-monotonic variation of properties upon introduction of a modifier (the borate anomaly) [14]. This unique behaviour of borates is attributed to the presence of superstructural units at low-modifier concentration and the conversion of some of the boron atoms from BO_3 to BO_4 . This chapter presents the changes in dynamic and structural behaviour in lead-borate $[\text{xPbO}:(1-\text{x})\text{B}_2\text{O}_3]$ glasses in a wide variation of x (0.2-0.8). PbO forms borate glasses over a large range of modifier concentration. We study in detail the short-range borate structure using density, T_g , sound velocity, elastic constants and Raman spectroscopy. Low-frequency Raman spectroscopy and x-ray diffraction were used to study the composition-dependence of the BP and the FSDP. Fragility was determined from rate-

dependent DSC. Properties such as, T_g and elastic moduli exhibit broad maxima around $x = 0.3$, in congruence with the average coordination number $\langle r \rangle$ of boron atoms, and attributed to the gradual conversion of BO_3 to BO_4 units, using Raman spectroscopy. However, dynamic properties like the BP and fragility behave similar to the above structural properties except for an anomalous dip at $x = 0.3$. PbO was found to act as a glass former for higher concentrations. Static correlation lengths estimated from the FSDP did not follow a linear trend with dynamic correlation lengths (from BP), indicating a different spatial origin. However, the BP position and fragility were found to vary linearly. This correlation was found to emerge from the evolution of network packing and connectivity with the addition of modifier. An anomalous variation in dynamical properties reflects the critical role of Pb^{2+} in tuning the intermediate-range structure of the vitreous network. Moreover, using high-temperature Brillouin scattering on lead-borate glasses from 300-1150 K, a drastic decrease of network rigidity above T_g was observed, which was attributed to network disruption and structural relaxation in the supercooled liquid.

Chapter 4: Composition and temperature-induced structural changes in lead-tellurite glasses and melts at different length-scales

Tellurium oxide glasses are being increasingly studied for their remarkable non-linear optical properties [15]. For enhancing their optical behaviour, other heavy metal-oxides such as PbO and ZnO have been incorporated [16]. The introduction of a network modifier elongates one of the Te-O bonds in TeO_4 and results in a gradual formation of TeO_3 units with addition of more metal oxide [17]. The elastic properties of glassy materials exhibit significant changes across T_g , even though the local atomic structure do not exhibit dramatic changes. To study the structural evolution of the system at different length-scales and across T_g , $x\text{PbO}:(1-x)\text{TeO}_2$ ($x = 0.1-0.3$) glasses were investigated using high-temperature Brillouin and Raman spectroscopy in the temperature range 300-723 K. Samples prepared above this composition exhibited partial crystallization and hence were not studied. For all the samples investigated, the temperature-dependence of longitudinal acoustic (LA) mode was found to exhibit a scaling below T_g and a rapid softening above T_g . From an analysis of Raman spectra, several modes were found to exhibit hardening suggesting stiffening of the force constants with temperature, the effect

being more pronounced in glasses with higher x . The stiffening of force constants of molecular units with temperature at a microscopic length-scale and decrease of elastic constant attributed to loss of network rigidity on a macroscopic length-scale appear to be inconsistent with each other. These different behaviours at two length-scales are understood on the basis of a microscopic model involving TeO_n and PbO units in the structure, which connects the two processes.

Metastable phases formed during crystallization of TeO_2 -rich glasses exhibit efficient second-harmonic generation [18]. Unusual crystallization behaviour was observed for $\text{Li}_2\text{O}:\text{TeO}_2$ glasses, where crystallization occurred easily on heating the glass but hardly occurred when the corresponding liquid was cooled [13]. Such interesting thermal behaviour stimulates further investigations on crystallization of TeO_2 glasses. In this chapter, the structural evolution during temperature-induced crystallization processes in $0.3\text{PbO}:0.7\text{TeO}_2$ glass is described using DSC, Raman spectroscopy and x-ray diffraction. The kinetics of crystallization is investigated using both isokinetic and isoconversional methods to determine the kinetic parameters during crystallization of the glass. Crystallization was found to agree well with the Johnson-Mehl-Avrami model, suggesting the microstructural evolution as two-dimensional growth. The structural evolution of the devitrified phases depicted coexistence of phases (PbTeO_3 and $\alpha\text{-TeO}_2$). Anomalous crystallization into $\text{Pb}_2\text{Te}_3\text{O}_8$ phase was observed when the devitrified melt was cooled, which is explained using amorphous phase separation inherent to tellurites.

Chapter 5: Temperature-induced structural changes in iron-phosphate glass at short-range length-scale

Iron-phosphate glasses have been extensively investigated for their possible applications in vitrification of environmentally hazardous nuclear wastes [19]. This glass is a network of PO_4 tetrahedral units, where iron enters the network as Fe^{2+} or Fe^{3+} cations. Glasses with oxygen-to-phosphorous (O/P) ratio $\sim 4, 3.5$ and 3 are, respectively, classified as ortho-, pyro- and meta-phosphates having corresponding PO_4 units with $0, 1$ and 2 bridging oxygens (Q^0, Q^1 and Q^2 tetrahedra) as the dominating structures. We have studied a $40\text{Fe}_2\text{O}_3:60\text{P}_2\text{O}_5$ (mol%) glass with a ferric-pyrophosphate structure, which has

been shown to possess the best chemical durability [19]. No change of structure was reported from Raman and IR spectra of these glasses, obtained by varying the melting temperature [20]. The aim in this study was to observe if at all any structural signature of glass transition is manifested in the VDOS. Towards this, detailed Raman spectroscopic studies were carried out in the temperature range 81-873 K. The temperature-dependences of mode wave-numbers of nearly all the modes were found to exhibit anomalies near T_g . Below T_g , the asymmetric stretching of Q^0 , Q^1 and Q^2 tetrahedra exhibit conventional anharmonic behaviour, whereas the network vibration, iron-polyhedral and PO_4 network bending modes show hardening. The asymmetric vibrations of Q^1 and Q^2 along with the network vibration mode became anomalously narrower at high temperatures. The decrease in intensities of Q^0 and Q^1 species demonstrates a redistribution of VDOS as the network relaxes in the glassy state itself. Thus the occurrence of mode hardening/ softening and redistribution of VDOS provide evidence of structural relaxations in the iron-phosphate glass.

Chapter 6: Summary

This chapter presents a summary and conclusions of investigations carried out in strong network glasses using Raman and Brillouin spectroscopy, DSC and x-ray diffraction. The chapter ends with directions for future work. The significant findings from these studies are as follows:

1. Formation of various superstructural units and their subsequent destruction with increasing PbO was evidenced from high-frequency Raman scattering in a set of lead-borate glasses. PbO was found to act as a glass former for $x > 0.5$.

2. Dynamic properties such as BP and fragility in $xPbO:(1-x)B_2O_3$ behave similar to short-range structural properties except an anomalous dip at $x = 0.3$. The corresponding dynamic correlation length exhibits a decrease except a peak at $x = 0.3$ with increasing x . Analysis of the BP and FSDP revealed that while BP arises from intermediate-range ordering within the network units, the FSDP arises due to ordering of voids between such units.

3. The anomalous behaviour of the BP and fragility are found to be connected to their common origin in the intermediate-range ordered structures and reflects the critical role of Pb^{2+} in tuning the intermediate-range structure of the vitreous network.

4. LA mode frequency in lead-tellurite glasses shows a scaling behaviour in the glassy state. PbO was found to affect the tellurite network by stiffening the molecular units at a microscopic scale, while reducing the network rigidity on a macroscopic length-scale, upon increasing the temperature.

5. Microstructural evolution during devitrification in $0.3\text{PbO}:0.7\text{TeO}_2$ confirms a two-dimensional growth mechanism. This glass is found to crystallize into PbTeO_3 phase while heating, while anomalous crystallization into $\text{Pb}_2\text{Te}_3\text{O}_8$ phase is observed when the devitrified melt was cooled. This interesting observation is explained using amorphous phase separation inherent to the tellurite glass system owing to the presence of unique asymmetric structural units in the melts.

6. Raman mode frequencies and line-widths of iron-phosphate glass were found to exhibit anomalous behaviour and discontinuous changes were observed across T_g . These anomalies are attributed to structural relaxations in the glass.

References:

- [1] M.M. Smedskjaer, J.C. Mauro, S. Sen, Y. Yue, *Chemistry of Materials* 22 (2010) 5358.
- [2] I.W. Donald, P.M. Mallinson, B.L. Metcalfe, L.A. Gerrard, J.A. Fernie, *Journal of Materials Science* 46 (2011) 1975.
- [3] C.A. Angell, *Science* 267 (1995) 1924.
- [4] S.R. Elliott, *EPL (Europhysics Letters)* 19 (1992) 201.
- [5] R. Shuker, R.W. Gammon, *Physical Review Letters* 25 (1970) 222.
- [6] S.N. Taraskin, S.R. Elliott, *EPL (Europhysics Letters)* 39 (1997) 37.
- [7] U. Buchenau, H.M. Zhou, N. Nucker, K.S. Gilroy, W.A. Phillips, *Physical Review Letters* 60 (1988) 1318.
- [8] P. Benassi, M. Krisch, C. Masciovecchio, V. Mazzacurati, G. Monaco, G. Ruocco, F. Sette, R. Verbeni, *Physical Review Letters* 77 (1996) 3835.

- [9] A.P. Sokolov, A. Kisluk, M. Soltwisch, D. Quitmann, *Physical Review Letters* 69 (1992) 1540.
- [10] C. Levelut, N. Gaimes, F. Terki, G. Cohen-Solal, J. Pelous, R. Vacher, *Physical Review B* 51 (1995) 8606.
- [11] A.P. Sokolov, R. Calemczuk, B. Salce, A. Kisluk, D. Quitmann, E. Duval, *Physical Review Letters* 78 (1997) 2405.
- [12] E. Stavrou, S. Kriptou, C. Raptis, S. Turrell, K. Syassen, *physica status solidi (c)* 8 (2011) 3039.
- [13] M. Tatsumisago, S.-i. Kato, T. Minami, Y. Kowada, *Journal of Non-Crystalline Solids* 192–193 (1995) 478.
- [14] A.C. Wright, N.M. Vedishcheva, B.A. Shakhmatkin, *MRS Online Proceedings Library Archive* 455 (1996) 381 (16 pages).
- [15] Y. Yoshinori, T. Katsuhisa, S. Jinhai, H. Kazuyuki, *Journal of Physics: Condensed Matter* 14 (2002) 13493.
- [16] K. Kumar, S.B. Rai, D.K. Rai, *Spectrochimica Acta Part A: Molecular and Biomolecular Spectroscopy* 66 (2007) 1052.
- [17] T. Sekiya, N. Mochida, A. Ohtsuka, M. Tonokawa, *Journal of Non-Crystalline Solids* 144 (1992) 128.
- [18] G. Vrillet, C. Lasbruggas, P. Thomas, O. Masson, V. Couderc, A. Barthélémy, J.-C. Champarnaud-Mesjard, *Journal of Materials Science* 41 (2006) 305.
- [19] D.E. Day, Z. Wu, C.S. Ray, P. Hrma, *Journal of Non-Crystalline Solids* 241 (1998) 1.
- [20] X. Fang, C.S. Ray, A. Moguš-Milanković, D.E. Day, *Journal of Non-Crystalline Solids* 283 (2001) 162.

LIST OF FIGURES

Figure No.	Figure caption	Page No.
1.1	Schematic of atomic arrangement in (a) crystal and (b) glass.	2
1.2	Schematic of interesting problems in glass physics.	3
1.3	Change of volume/ enthalpy with decreasing temperature at constant pressure during crystallization and glass formation. (Figure from Ref. [2]).	5
1.4	A schematic diagram of the temperature dependence of (a) the specific heat, C_P , and (b) the entropy, S , of a crystal, liquid, supercooled liquid and glass. (Figure from Ref. [9]).	8
1.5	α -relaxation time (full squares) and β -relaxation time (open squares) in an organic glass former, sorbitol, as a function of the inverse temperature. The dashed red line indicates the glass transition temperature. (Adapted from Ref. [15,16]).	10
1.6	(a) Behaviour of viscosity η as a function of temperature for different glass formers in supercooled liquid state. The dashed black line indicates the viscosity $\eta(T_g)=10^{12}$ Pa.s. (b) Angell plot of (a) plotted with scaled temperature T_g/T . (Figure from Ref. [5]).	13
1.7	Behaviour of heat capacity C_P as a function of the reduced temperature T/T_g for different glass-forming liquids. The glass transition corresponds to a discontinuity in the temperature dependence of C_P . (Figure from Ref. [21]).	14
1.8	Various theories of glass formation.	15
1.9	Schematic of atomic arrangement in B_2O_3 glass which satisfies Zachariasen's rules of glass formation.	16
1.10	Temperature variation of (a) the heat capacity C_P and (b) reduced heat capacity C_P/T^3 for crystalline quartz (orange triangles) and glassy silica (blue circles). (Figure from Ref. [16,41]).	30
1.11	Experimental VDOS (blue circles) of glassy sorbitol measured using inelastic neutron scattering. The red curve depicts the Debye ω^2 -prediction and the inset shows an enlarged image of the low-energy data. (b) Reduced density of states $g(\omega)/\omega^2$ depicting a Boson peak for the glass and a constant Debye level in red dashed line. (Figure from Ref. [16,41]).	32
1.12	Typical network-forming glasses: (a) two-dimensional representation of a single-component SiO_2 glass, whose network connectivity can be depolymerized (b) by the addition of a network modifier (Na_2O). (Figure adapted from Ref. [5]).	38
1.13	Typical modified borate glass showing directly bonded neighbours in	39

	network formers and network sites containing modifier cations, which denote the short-range order in such a network glass.	
1.14	MRO in a typical network glass can be depicted by connectivity of the network former (green lines), correlations between cations of network former and modifier (blue lines), and spatial distribution of modifiers (red line).	39
1.15	Typical two-dimensional representation of (a) BO_3 triangular and (b) BO_4^- tetrahedral structural units depicting all bridging oxygen atoms (red circles) found in modified borate glasses.	42
1.16	A two-dimensional schematic representation of vitreous B_2O_3 depicting the formation of the network structure from a combination of BO_3 units and boroxol (B_3O_6) rings. Boron atoms are depicted by the cyan circles and oxygen atoms by red circles. (Figure from Ref. [57]).	42
1.17	Bray & O'Keefe's NMR data [57] depicting B_4 for alkali-borate glass systems: $\text{Li}_2\text{O}-\text{B}_2\text{O}_3$ (blue filled circles), $\text{Na}_2\text{O}-\text{B}_2\text{O}_3$ (red filled squares), $\text{K}_2\text{O}-\text{B}_2\text{O}_3$ (green filled triangles), $\text{Rb}_2\text{O}-\text{B}_2\text{O}_3$ (magenta inverted filled triangles) and $\text{Cs}_2\text{O}-\text{B}_2\text{O}_3$ (cyan asterisks). The black curve (Eq. 1.20) denotes the value of B_4 if the entire added network modifier leads to the formation of BO_4^- tetrahedra with no NBO atoms.	43
1.18	Commonly occurring borate superstructural units: (a) boroxol group, (b) pentaborate group, (c) triborate group, (d) di-pentaborate group, (e) diborate group and (f) di-triborate group.	45
1.19	Ball and stick representation of the structural units present in tellurite glass. Left: Trigonal bipyramidal TeO_4 . Center: Distorted trigonal bipyramidal TeO_{3+1} . Right: Trigonal pyramidal TeO_3 . Dots represent lone pair electrons. Bond lengths (in nm) are taken from [66]. (Fig. from Ref. [67]).	47
1.20	Network structure of a modified tellurite glass. The entry of a modifier cation (grey circles) induces distortion in the tbp units and creates NBOs in the structure.	47
1.21	Phosphate tetrahedral units: oxygen atoms (pink) connected to phosphorus atoms (blue); ultra-phosphate Q^3 (cross-linking) units; meta-phosphate Q^2 (middle) units; pyro-phosphate Q^1 (terminal or end) units; ortho-phosphate Q^0 (isolated) units. (Fig. from Ref. [68]).	49
2.1	Energy level diagram of Rayleigh and Raman (or, Brillouin) scattering.	58
2.2	Feynman diagram of the Raman process.	66
2.3	A comparison of the various reduction schemes by Eq. 2.20, 2.22, 2.23 applied to the depolarized low-frequency Raman spectrum of vitreous silica. The arrow denotes the energy of the Boson peak. The figure has been reproduced from Ref. [42].	71
2.4	A schematic of the Renishaw micro-Raman spectrometer.	76
2.5	A schematic of the Horiba U1000 Raman spectrometer.	78

2.6	The transmission spectra of individual interferometers FP1 and FP2, and a tandem system (adapted from Ref. [83]).	85
2.7	A mechanically scanning tandem Fabry-Pérot.	86
2.8	Schematic of the Tandem Fabry-Pérot interferometer (manufactured by JRS Instruments) showing the light path. The figure has been adapted from Ref. [84]).	88
3.1	The density and glass transition temperature (T_g) in lead-borate glasses of various composition x . Dashed lines are guides to the eye. Values for pure B_2O_3 (shown in open symbols) are from Ref. [107].	105
3.2	The longitudinal (squares), transverse (circles) and Debye (triangles) velocities of the lead-borate glasses. Values for pure B_2O_3 (shown in open symbols) are from Ref. [107]. Inset shows the variation of the longitudinal (L), shear (G), bulk (K) and Young's (E) modulus. Dashed curves are guides to the eye.	106
3.3	Average coordination number calculated by considering (a) purely ionic bonds (black squares) and (b) purely covalent bonds (red circles).	108
3.4	High-frequency Raman spectra of lead-borate glasses corrected for the Bose factor.	109
3.5	Low-frequency Raman (reduced) spectra for the lead-borate glasses (a) depicting the background-corrected Boson peak with the high-frequency tail reaching the same value in all samples, which aids for a reasonable comparison of intensities from (b) the log-normal fits shown by the red curves. The blue arrow is a guide to the eye for the growing peak assigned to lead oxide polyhedra.	115
3.6	Boson peak frequency of lead-borate glasses. Value for pure B_2O_3 are from Ref. [107]. Inset shows the Boson peak frequency and the Debye frequency normalized to 1 for $x = 0$.	116
3.7	Dynamic correlation lengths in lead-borate glasses. Insets show the variation of (a) the average inter-particle distance, a and (b) the ratio of the dynamic correlation length L to a with increasing x .	120
3.8	X-ray diffraction of the lead-borate glasses depicting the first sharp diffraction peak (FSDP) in glasses with low x in the shaded region.	123
3.9	FSDP (a) position, (b) width and (c) intensity for various x .	124
3.10	Dynamic and static correlation lengths. Inset shows that these correlation lengths are not related linearly.	126
3.11	Fragility (m) of lead-borate glasses. Value at $x = 0$ is taken from Ref. [145]. Inset shows the $\log \beta$ vs. $1000/T_g$ plots for the calculation of the activation energy E_a/R . Lines are linear fits to the data for various x .	129
3.12	Schematic representation of the lead-borate glass network for low x compositions ($x = 0.0, 0.2, 0.3$) depicting the dynamic correlation length L	130

in pink shaded regions and static correlation length D in blue encircled regions. The top panel of the plot shows the dynamic properties (ω_{BP} and m) scaled at their respective highest values while the bottom panel shows similar scaling for the short-range structural properties ($\langle r \rangle$, T_g and V_1). The gray shaded region in the plot indicates the anomalous dip in dynamic properties at the composition ($x = 0.3$) where the structural properties exhibit a maxima.

- 3.13 The dependence of $\Delta C_p/C_{pg}$ for various x . Inset shows the rise in heat capacity across the glass transition. 133
- 3.14 Correlation of I_0^{BP} and average coordination number. Insets show (a) correlation of fragility and average coordination number and (b) dependence of I_0^{BP} on x . 133
- 3.15 Correlation between Boson peak frequency and fragility. 134
- 3.16 (a) Brillouin spectra of $x\text{PbO}:(1-x)\text{B}_2\text{O}_3$ ($x = 0.2, 0.3, 0.4, 0.5$) glasses at ambient. (b) The longitudinal acoustic (LA) mode frequency (ν_B) of lead-borate glasses for increasing x . 135
- 3.17 Temperature dependence of Brillouin spectra of $x\text{PbO}:(1-x)\text{B}_2\text{O}_3$ glass for $x = 0.3$ at several temperatures depicting the longitudinal acoustic (LA) mode. 136
- 3.18 Temperature (T) dependence of the Brillouin shift (ν_B) of the LA mode of $x\text{PbO}:(1-x)\text{B}_2\text{O}_3$ ($x = 0.2, 0.3, 0.4, 0.5$) glasses. 137
- 3.19 Scaled temperature dependence of the LA mode frequency of $x\text{PbO}:(1-x)\text{B}_2\text{O}_3$ ($x = 0.2, 0.3, 0.4, 0.5$) glasses. $\nu_B(T)$ is scaled with respect to ν_B at T_g and T is scaled with respect to T_g . 138
- 4.1 X-ray diffraction of $x\text{PbO}:(1-x)\text{TeO}_2$ ($x = 0.1-0.3$) glasses. 146
- 4.2 Brillouin spectra of $x\text{PbO}:(1-x)\text{TeO}_2$ ($x = 0.1-0.3$) glasses at ambient. The inset represents the spectra for $x = 0.2$ at various temperatures. 147
- 4.3 Temperature dependence of the Brillouin shift and line-width of the LA mode for $x =$ (a) 0.1, (b) 0.2 and (c) 0.3. The dashed vertical line marks the glass transition in the respective glass composition. 149
- 4.4 Scaled temperature dependence of the LA mode frequency of $x\text{PbO}:(1-x)\text{TeO}_2$ ($x = 0.1-0.3$) glasses. $\nu_B(T)$ is scaled with respect to ν_B at ambient and T is scaled with respect to T_g . 153
- 4.5 Raman spectra of $x\text{PbO}:(1-x)\text{TeO}_2$ glasses for (a) $x = 0.1-0.3$ at ambient and (b) $x = 0.2$ at selected elevated temperatures. The insets show the corresponding reduced Raman spectra obtained after correcting for the thermal population factor. 156
- 4.6 The reduced Raman spectrum for the lead-tellurite glass with $x = 0.1$ at 323 K, along with the Gaussian fits and a linear background. The dashed curves represent the fitted Gaussians. The total fitted spectrum is shown as a continuous curve. 158

4.7	Temperature dependence of the mode frequencies of the (a) 674 cm ⁻¹ mode and (b) 751 cm ⁻¹ mode for the glasses with $x = 0.1, 0.2$ and 0.3 . The lines through the data are guides to the eye. The dashed vertical lines mark the glass transition in the respective glass composition.	160
4.8	Temperature dependence of Γ of the (a) 674 cm ⁻¹ mode and (b) 751 cm ⁻¹ mode for the glasses with $x = 0.1, 0.2$ and 0.3 . The lines through the data are guides to the eye. The dashed vertical lines mark the glass transition in the respective glass composition.	161
4.9	Temperature dependence of the intensity ratio of the 674 cm ⁻¹ mode with respect to the 751 cm ⁻¹ mode (I^{674}/I^{751}) for the glasses with $x = 0.1, 0.2$ and 0.3 . The lines through the data are guides to the eye. The dashed vertical lines mark the glass transition in the respective glass composition.	164
4.10	Schematic diagram of the lead-tellurite network glass showing building blocks such as TeO _n and PbO units. Addition of PbO to the glass breaks the inter-molecular network bonds between the units and weakens the network. Consequent conversion of some of the TeO ₄ -tbp units into TeO ₃ -tp units ($\langle m \rangle < \langle n \rangle$) makes the intra-molecular Te-O stretching vibration force constant stiffer.	166
4.11	DSC thermograms of 0.3PbO:0.7TeO ₂ glass at different heating rates. The glass transition temperature (T_g) and the peak crystallization temperatures (T_{cry}) are indicated in the figure (subscripts 1 and 2 refer to first and second crystallization peaks).	168
4.12	Dependence of T_g and T_{cry1} on $(\log \beta)$.	168
4.13	Baseline-corrected exothermal curves of the two-stage crystallization of 0.3PbO:0.7TeO ₂ glass at various heating rates.	171
4.14	Kissinger plots of $\ln(T_{cry}^2/\beta)$ versus $1000/T_{cry}$ for the (a) first and (b) second crystallization peaks. Inset: Plot of $\ln(T_g^2/\beta)$ versus $1000/T_g$ to evaluate the glass transition activation energy.	171
4.15	Fractional crystallization (α) as a function of temperature for the first peak obtained from the DSC thermograms at various heating rates. The solid red lines show the curve fitting according to Eq. 4.13 using the method of least squares.	174
4.16	X-ray diffraction patterns for the glass samples annealed at (a) 648 K and (b) 693 K while heating, and (c) the melt-cooled sample at ambient. The symbols at the top of the peaks indicate the respective phases they correspond to.	176
4.17	Raman spectra of 0.3PbO:0.7TeO ₂ glass at various temperatures while heating. Inset shows the spectra at various temperatures while cooling the sample.	178
5.1	Raman spectra of iron-phosphate glass at various temperatures.	185
5.2	The reduced Raman spectra obtained after correction for the thermal	186

population factor. The low wavenumber part of the 300 K spectrum is also shown after an ordinate expansion by a factor of 6.

- 5.3 The reduced spectra at 300 and 773 K for (a) the low-wavenumber region (below 850 cm^{-1}) and (b) the high-wavenumber region (above 850 cm^{-1}), along with the Gaussian fits and a linear background. The continuous curves represent the fitted Gaussians. The total fitted spectra are also shown as continuous curves. 188
- 5.4 Temperature dependence of mode wavenumbers for all the eight modes. The lines through the data are guides to the eye. 190
- 5.5 Temperature dependence of Γ of (a) the 170 and 634 cm^{-1} modes and of (b) the 946 , 1090 and 1247 cm^{-1} modes. The lines through the data are guides to the eye. The dashed vertical line marks the glass transition. 191

LIST OF TABLES

Table No.	Table caption	Page No.
3.1	Mode wavenumber and assignment of the high-frequency Raman bands in lead-borate glasses.	110
3.2	Summary of the various models for the Boson peak.	119
4.1	T_g values, slope of mode frequency above T_g , density, refractive index, ultrasonic sound velocities and those estimated from Brillouin measurements, and longitudinal elastic modulus at ambient for lead-tellurite glasses.	148
4.2	Observed Raman mode wavenumbers in lead-tellurite glasses and their assignments.	157
4.3	Effect of PbO network modifier on micro- and macroscopic length-scales.	165
4.4	Values of the activation energy (E), Avrami (growth) exponent (b) and the frequency factor (K_0) obtained by fitting the experimental fractional crystallization data for the first exothermic peak at different heating rates using Eq. 4.13.	175
5.1	Observed Raman bands of 40Fe ₂ O ₃ :60P ₂ O ₅ glass at ambient temperature and their assignments.	189

LIST OF SYMBOLS

Melting temperature	:	T_m
Glass transition temperature	:	T_g
Volume	:	V
Enthalpy	:	H
Thermal expansion coefficient	:	α_T
Specific heat capacity at constant pressure	:	C_P
Entropy	:	S
Kauzmann temperature	:	T_K
Shear viscosity	:	η
High-temperature limit of the shear modulus	:	G_∞
High-temperature limit of the viscosity	:	η_∞
Boltzmann's constant	:	k_B
Activation energy	:	E
Fragility index	:	m
Rate of nucleation per unit volume	:	I_v
Devitrification/ crystallization temperature	:	T_{cry}
Crystallized volume fraction	:	α
Crystal growth rate	:	u
Avrami (growth) exponent	:	b
Growth rate constant	:	K
Universal gas constant	:	R
Scattering vector	:	Q
Structure factor	:	$S(Q)$
Phonon wave vector	:	q
Longitudinal sound velocity	:	V_l
Transverse sound velocity	:	V_t
Phonon frequency	:	ω
Vibrational density of states	:	$g(\omega)$
Debye velocity	:	V_D
Debye frequency	:	ω_D

Density	:	ρ
Specific heat at constant volume	:	C_V
Debye temperature	:	θ_D
Thermal conductivity	:	κ
Susceptibility tensor	:	$\bar{\chi}$
Polarization vector	:	\vec{P}
Electric field vector	:	\vec{E}
Dielectric/ elastic susceptibility	:	χ
Nuclear displacement or normal coordinate	:	r
Wavelength	:	λ
Scattering cross-section	:	σ
Solid angle	:	Ω
Refractive index	:	n
Velocity of light in vacuum	:	c
Elastic constant	:	C
Longitudinal modulus	:	L
Shear modulus	:	G
Bulk modulus	:	K
Young's modulus	:	E
Transmittance	:	T
Finesse	:	F
Reflectance	:	R
Free spectral range	:	$\Delta\lambda$
Resolution	:	$\delta\lambda$
Dynamic correlation length	:	L
Static correlation length	:	D
Brillouin shift	:	ν_B
Line-width	:	Γ

Glasses are known for their significant properties to mankind since early civilizations. Many of the uses of glass in modern world continue to exploit their optical transparency, structural rigidity, compositional flexibility, property tailoring suitability, luster and durability [1]. Containers, windows, lighting, insulation, fiber and other hand-crafted art objects are typical of its traditional uses. Through the application of basic sciences to the study of glass, newer properties of glasses have been developed and hence, new opportunities for the application of glasses have been conceived. The glassy state is ubiquitous in nature and technology [2]. The properties of glasses have been exploited for technological applications, from optical components to optical fibers, solid-state memories and lasers, and also for pharmaceutical and biological applications [3]. Despite this widespread technological interest, a deep microscopic understanding of the glassy state remains a challenge for condensed matter physicists [4].

1.1 Definition of Glass

What is a glass? This important question is poorly understood and remains unanswered today beyond the level of general statements, although substantial progress in understanding has been made in recent years [5]. Glasses used traditionally are silica-based glasses. Then, is silica an essential component of glass? The answer is ‘no’ since a limitless number of inorganic glasses can be formed which does not contain silica [6]. Glass is formed traditionally by cooling of a melt. However, there are various routes to the glassy state [4] and one can form glasses by vapour deposition, sol-gel processing of solutions, heavy-ion irradiation or pressure-induced amorphization of crystals. Traditional glasses are inorganic and non-metallic. Still, metallic glasses have become

common in present-age technology. Therefore, the chemical nature of the material can also not be used to define a glass. However, every glass shares two common characteristics: (a) no glass has long-range periodic order of atoms (as shown in Fig. 1.1) and, (b) every glass exhibits glass transition behaviour. This transition occurs over a temperature range known as the glass transition region. Therefore, a glass can be defined as “an amorphous solid, completely lacking in long-range, periodic atomic structure and exhibiting a region of glass transition behaviour” [6]. Hence, any material, whether inorganic, organic or metallic, formed by any technique, if exhibits glass transition behaviour, is to be called a glass. Fig. 1.1 compares the arrangement of atoms in a crystal and a glass. It can be seen that unlike a crystal, a glass exhibits a disordered arrangement of atoms and hence, lacks periodicity.

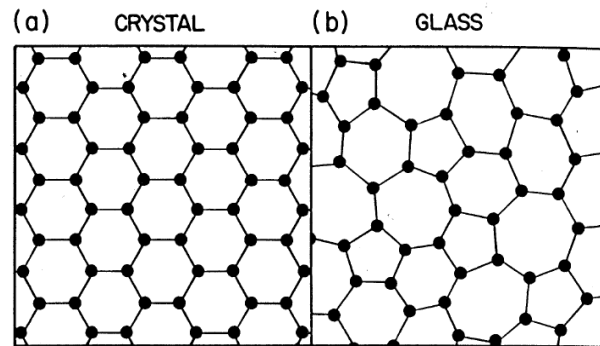


Fig. 1.1 Schematic of atomic arrangement in (a) crystal and (b) glass.

The type of disorder mentioned above is known as topological disorder and glasses exhibiting such disorder are called structural glasses. In general, the concept of glass relates to systems, in which a degree of freedom (a) fluctuates at a rate that depends strongly on temperature or pressure and which (b) becomes so slow at low temperature or high pressure that the fluctuations become frozen. At this point, properties determined by the slow degree of freedom, change value more or less abruptly giving the glass transition. Apart from ‘structural glasses’, such features are also exhibited [7] by spin glasses and orientational (dipolar) glasses. In spin glasses, the underlying crystalline

lattice is preserved, but each atomic site possesses a spin or magnetic moment, and these spins are aligned randomly. The term ‘glass’ is analogous to the magnetic disorder of a spin glass and positional or topological disorder of a structural glass. Quite similarly, a dipole glass is one in which the lattice points in a periodic lattice are occupied by molecules containing a dipole moment and these moments orient randomly. Furthermore, the magnetic susceptibility in spin glasses decreases suddenly as the fluctuations in magnetization freeze in, while in structural glass-forming liquids, it is the heat capacity, compressibility and dielectric susceptibility. Thus, in the most general terms, a glass can be defined [8] as, “a condensed state of matter which has become non-ergodic by virtue of the continuous slow-down of one or more of its degrees of freedom”.

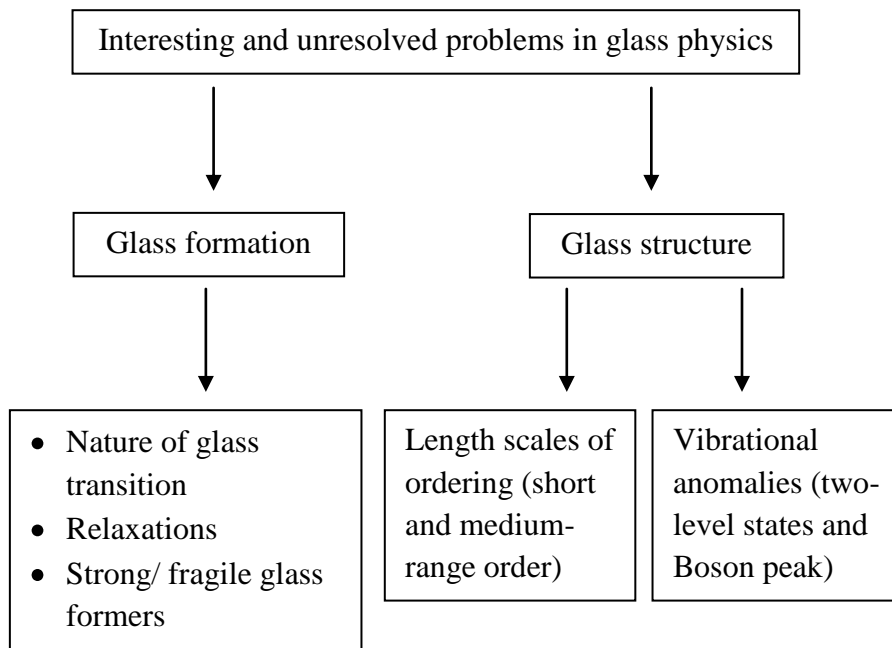


Fig. 1.2 Schematic of interesting problems in glass physics.

Structural glasses are distinguished from most others by the large change in heat capacity which accompanies the freezing-in of a particular structural state. Considering the significance of the heat capacity jump and the kinetic stability of the equilibrated state such that it can be studied and characterized, Angell [7] defines structural glass as, “an

amorphous state which is capable of passing continuously into the viscous liquid state, usually, but not necessarily, accompanied by an abrupt increase in heat capacity”. While this definition puts metallic glasses in the category of amorphous solids because although formed from a liquid, they crystallize before ever achieving the supercooled liquid state while heating, it still accepts many substances as glasses which were produced initially by routes that never involved a liquid state [8]. In this thesis, we focus specifically on structural glasses which have been formed from liquids.

Fig. 1.2 presents an overview of the interesting and controversial problems in glass physics which are yet to be understood thoroughly. In this thesis, we have tried to look into some of these aspects in structural glasses. In the sections to follow, we discuss these phenomenologies of structural glasses in greater detail, which will form the basis of understanding the outcomes of this thesis.

1.2 Glass formation: Supercooled liquid and the glass transition

While cooling a liquid below its melting temperature T_m , generally two phenomena takes place: crystallization or glass formation. On slow-cooling, the liquid may crystallize by nucleation and growth mechanisms at T_m and the atoms organize among themselves to form a long-range periodic structure. However, if the cooling rate is fast enough, the crystallization can be avoided; the liquid can be supercooled below T_m and eventually a glass is formed [6]. Liquids at temperatures below their melting points are called supercooled liquids [9].

The occurrence of these solid phases (crystal and glass) can be checked by looking at the temperature dependence of the extensive thermodynamic variables such as volume, entropy or enthalpy at constant pressure. Fig. 1.3 shows a schematic of a liquid’s volume or enthalpy change during cooling. The crystallization process corresponds to an

abrupt jump in volume or enthalpy at T_m which marks a first-order phase transition, while the glass formation is characterized by a smooth decreasing behaviour. In this case, as the liquid is cooled below T_m rapidly enough so that detectable nucleation and growth cannot occur, it falls out of equilibrium and becomes supercooled. Conventionally, the crystal is regarded as the equilibrium state below T_m and the supercooled liquid, a metastable state. However, as long as no crystal nuclei are present, the supercooled liquid state can be regarded as the equilibrium state [9].

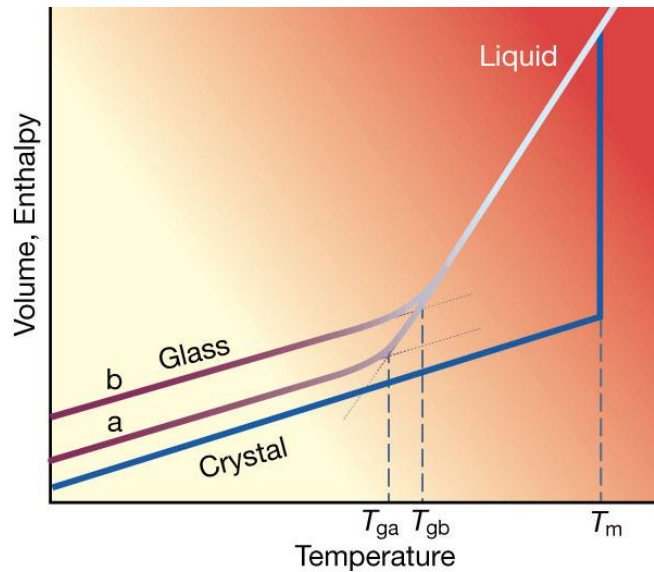


Fig. 1.3 Change of volume/ enthalpy with decreasing temperature at constant pressure during crystallization and glass formation. (Figure from Ref. [2]).

Upon further cooling, the liquid viscosity increases. This increase in viscosity eventually becomes so great that the atoms can no longer completely rearrange to the equilibrium structure (supercooled liquid line) during the time allowed by the experiment. Since these rearrangements are necessary for the liquid to find its equilibrium value at that temperature, the experimentally obtained value begins to lag behind the equilibrium structure (see Fig. 1.3) which it would reach if sufficient time were allowed [3]. The enthalpy and volume begin to deviate from the equilibrium line, following a curve of

gradually decreasing slope until the viscosity becomes so great that the structure remains frozen and a glass is formed. In contrast to a supercooled liquid, a glass is continually relaxing, possibly too slowly to measure, toward a more stable state. Generally, experimental observations are made on time scales fast compared to the molecular motions which allow the glass to relax, and then the glass is mechanically stable for practical purposes, even though it is thermodynamically unstable. Thus, the glass is considered as a metastable state of matter.

The temperature region lying between the limits where the volume is in between the equilibrium liquid and the frozen solid is called the glass transformation/ transition region and the temperature at which the slope change occurs in the curve is known as the glass transition temperature T_g . In molecular liquids, near T_g it may take minutes or hours for a molecule less than $\sim 10 \text{ \AA}$ in diameter to reorient [9].

The temperature at which the enthalpy departs from the supercooled liquid (equilibrium) curve is controlled by the viscosity of the liquid, *i.e.*, by kinetic factors. Therefore, the possibility to obtain a glass does not strictly depend on the material itself, but rather depends on the available time allowed to a system to solidify into a disordered structure. Moreover, use of a slower cooling rate (curve 'a' with T_{ga} as shown in Fig. 1.3) will allow the enthalpy to follow the equilibrium curve to a lower temperature [6]. Thus, T_g will shift to a lower temperature and the glass obtained will have a lower enthalpy and volume than that obtained using a faster cooling rate (curve 'b' with T_{gb} as shown in Fig. 1.3). The atomic arrangements in each case will be different. Thus, T_g is a function of the cooling rate, and so are the thermodynamic and dynamic properties of a glass. However, practically, the dependence of T_g upon cooling rate is relatively weak: an order of magnitude change in cooling rate may change T_g by only 3-5 K [9,10]. Cooling at very high rates is called quenching; glasses formed by quenching have larger specific volume

because their properties are frozen-in at a higher temperature and a corresponding higher volume.

It is of much importance to comprehend that glass transition is not a first-order phase transition. In fact, glass transition is not a thermodynamic phase transition at all. It is a kinetic event which depends upon crossing of an experimental time scale and the time scales for molecular rearrangements, *i.e.*, they are liquids which are frozen on time scales of experimental observation. Thus, as depicted in Fig. 1.3, there is no unique glassy state for a material: the thermodynamic and dynamic properties of a glass depend upon how it was formed [9].

1.2.1 Thermodynamics as T_g is approached: Entropy crisis and the Kauzmann temperature

The change in slope of the thermodynamic variables (volume V and enthalpy H) at T_g implies a discontinuity in the corresponding derivative variables, such as thermal expansion coefficient $\alpha_T = -[d(\ln V)/dT]_P$ or specific heat capacity $C_P = [dH/dT]_P$. Fig. 1.4 (a) shows a schematic of a typical specific heat curve for the crystal, liquid, supercooled liquid and glass [9]. The specific heat is largest in the supercooled liquid and on crossing T_g from the liquid side, C_P drops abruptly in a narrow temperature range, close to the value found in the crystal. The temperature at which C_P drops rapidly depends on the rate of cooling of the liquid. The two separate curves in the figure indicate cooling at two different rates. The thermodynamic relation,

$$S(T_2) - S(T_1) = \int_{T_1}^{T_2} \frac{C_P(T)}{T} dT \quad (1.1)$$

allows one to determine entropy S from specific heat data. The slope of S versus T must be largest in the liquid and supercooled liquid phases since C_P is largest in these phases. This is seen in Fig. 1.4 (b).

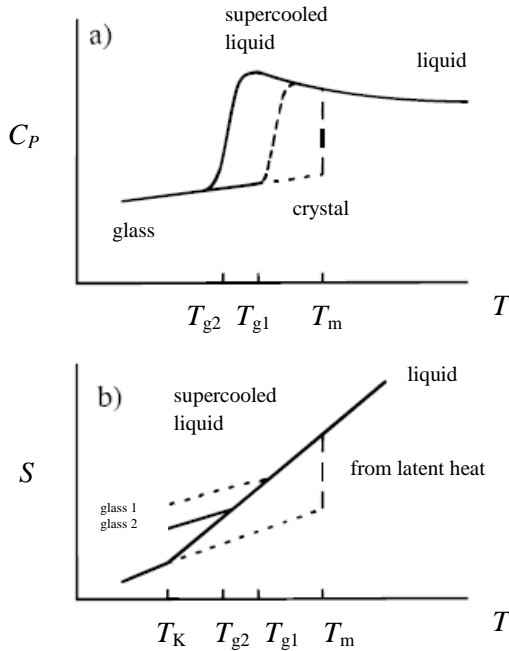


Fig. 1.4 A schematic diagram of the temperature dependence of (a) the specific heat, C_P , and (b) the entropy, S , of a crystal, liquid, supercooled liquid and glass. (Figure from Ref.[9]).

However, Kauzmann [11] pointed out a paradox that if the specific heat did not drop at T_g , and the rapid decrease of the liquid entropy were to continue to arbitrarily low temperature, then the liquid would eventually have the same entropy as the crystal. This point, obtained by extrapolation to the crystal entropy line, is known as the Kauzmann temperature, T_K . Below this temperature the crystal would have larger entropy than the supercooled liquid. Although it seems unrealistic to have a liquid with entropy smaller than that of the ordered crystal, it does not violate any law of thermodynamics. However, the third law of thermodynamics would be violated if the liquid entropy continued to decrease much below T_K without any change in slope because then S becomes negative well above $T = 0$ K [12]. This is known as the entropy crisis [13] due to Kauzmann and effectively puts a limiting value on T_g since the glass transition must intervene at a temperature above T_K in order for the entropy of the glass to remain positive. Thus, in order that $T_g \leq T_K$, no matter how slowly a liquid is cooled, one should always expect a drop in C_P at a temperature above the Kauzmann temperature [9].

1.2.2 Dynamics as T_g is approached: Relaxation processes

As depicted in Fig. 1.3, the volume (and enthalpy) of a given liquid decreases with decreasing temperature. This implies that whenever the temperature is decreased by some amount, the volume will decrease by some amount given by the thermal expansion coefficient. However, the volume does not reach its new equilibrium value instantaneously, rather the liquid equilibrates in some way over time. This process is called structural relaxation and refers to the typical timescales on which the density fluctuations relax. The associated characteristic time is called as the structural relaxation time or the alpha relaxation time τ_α .

Most interestingly, around T_m , the typical timescales of alpha relaxations is \sim a few picoseconds while at T_g , the typical timescales is ~ 1000 s, *i.e.*, 15 orders of magnitude larger [14]. This increase of relaxation time is even more remarkable because the corresponding decrease of temperature is $\sim T_m/3$ only. This increasing relaxation time is accompanied by a concomitant increase of shear viscosity η of the liquid. The viscosity of a liquid is a macroscopic measure of its resistance to flow. Typical high-temperature value of η near T_m is $\sim 10^{-4}$ Pa.s. The relation with relaxation times can be understood by a simple Maxwell model which gives $\eta = G_\infty \tau_\alpha$, where G_∞ is the instantaneous (elastic) shear modulus which does not vary considerably in the supercooled state [14].

If the glass is kept below T_g it tries to approach equilibrium, though it happens slowly, and the volume and other properties are therefore time-dependent. This means the glass ages. Since the relaxation time increases very rapidly in the vicinity of T_g , this means that the aging processes are very slow already a few degrees below T_g . When considered at times shorter than the relaxation time the glass behaves like a solid in all senses. It is therefore possible to measure and assign meaningful values to the properties of the glass, including the thermodynamical derivatives. The freezing-in of the liquid at

T_g has the consequence that the structure of the glass is that of the liquid when it fell out of equilibrium at T_g . The glass is hence a disordered solid, and it cannot be distinguished from a liquid from a structural point of view. It displays all the salient microscopic features of a liquid, but has the macroscopic characteristics of a solid.

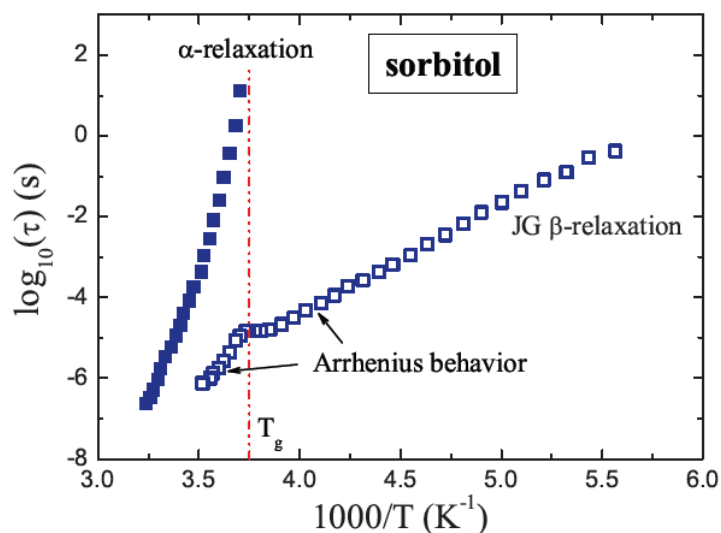


Fig. 1.5 α -relaxation time (full squares) and β -relaxation time (open squares) in an organic glass former, sorbitol, as a function of the inverse temperature. The dashed red line indicates the glass transition temperature. (Adapted from Ref. [15,16]).

Usually supercooled liquids exhibit more than one relaxation process at temperatures near T_g . Alpha relaxation processes are slow processes and corresponds to molecular motions. Secondary relaxation processes occur on shorter time scales and have higher frequencies. Various systems exhibit different types of secondary relaxations governed by different molecular mechanisms [9]. Some are trivial rotational motion of a small isolated group of the entire molecule and others are non-trivial as in rigid molecular glass formers. Among the different secondary relaxations, the most famous is the Johari-Goldstein (JG) β -relaxation, due to its inter-molecular character and its presence in all types of glass formers [17,18]. The origin of this process is a matter of dispute and many theoretical and experimental works have been performed on this topic [9]. The

mechanism of the interplay between α and β -relaxations in the liquid-glass transformation is sometimes considered as the key to understand how and why a glass forms from equilibrium melt. According to Johari [18], glass-formers are generally considered to be composed of small groups of particles trapped in cages formed by their neighbours, in which the particles are entangled for a time that increases on decreasing the temperature due to increasing η . The β -relaxation is related to the particle vibrations within their local cages called as cage-rattling motion, while the structural (α) relaxation time corresponds to the time necessary for a particle to escape the cage. Fig. 1.5 shows the relation between the α and β (JG) relaxation in the case of sorbitol [15]. While the α -process diverges at T_g , β persists in the glassy state below T_g . The JG process can be described, both in the glassy and in the supercooled liquid state by an Arrhenius law, whereas, the α -process exhibits different behaviour in various systems which is elaborated in the following section.

1.2.2.1 Different behaviour in dynamics: strong and fragile glass-formers

One of the most challenging aspects of the glass transition phenomena is to understand the behaviour of the structural relaxation time or viscosity on approaching T_g . In Nobel laureate, P. W. Anderson's words, "The deepest and most interesting problems in solid-state theory is probably the theory of the nature of glass and the glass transition...Whether it will help make better glass is questionable" [9,19]. Fig. 1.6(a) represents the temperature-variation of the viscosity for different network glass-forming liquids (selenium, silica, germania, GeSe_4 , etc.). Another way in which glass transition is defined traditionally is the temperature T_g at which the viscosity reaches $\sim 10^{12}$ Pa.s. It is interesting to see that for organic glass formers such as o-terphenyl (OTP) or toluene, the temperature decrease can lead to a change in η by several orders of magnitude under only

tens of degrees temperature change. Therefore, the way in which the change in η with temperature takes place strictly depends on the nature of the system.

Based upon these experimental observations, Angell [20] plotted the viscosity on a logarithmic scale against the inverse temperature, rescaled to the corresponding T_g of each glass former. This plot is known as the “Angell” plot (Fig. 1.6 (b)). An immediate inspection of this figure leads to the conclusion that various supercooled liquids behave very differently. Some liquids exhibit weak temperature dependence of viscosity that can be described by an Arrhenius law,

$$\eta = \eta_{\infty} \exp[E/k_B T] \quad (1.2)$$

where η_{∞} is the high-temperature limit of the viscosity, k_B is the Boltzmann’s constant and E is a nearly constant activation energy, suggesting a simple mechanism for relaxation by locally breaking a chemical bond. The typical relaxation time is then dominated by the energy barrier to activate this process. Typical examples are SiO_2 and GeO_2 . However, as one moves down the figure, other liquids (e.g. B_2O_3 , $2\text{SiO}_2\text{-Na}_2\text{O}$, As_2Se_3 or Se) exhibit a viscosity behavior that shows an important bending at intermediate values of T_g/T , whereas organic glass formers (OTP and toluene) display the most pronounced curvature and can be described by a super-Arrhenius behaviour,

$$\eta = \eta_{\infty} \exp[E(T)/k_B T] \quad (1.3)$$

where the activation energy explicitly depends on temperature [5]. This suggests that glass formation is a collective phenomena for such glass-formers. With these observations, Angell proposed a classification of supercooled liquids depending on the temperature dependence of the viscosity (or τ_{α}), and consequently on the sensitivity of the rearrangements in the liquid structure to temperature changes. He distinguished ‘strong’ and ‘fragile’ glass-forming liquids into systems, where the underlying relaxation and activation energy is independent of temperature or has an explicit dependence,

respectively. The terminology ‘strong-fragile’ is not related to the mechanical properties of the glass.

Looking at their structure, strong glass-formers present covalent (directionally-oriented bonds) and can form networking arrangements that strongly decrease the ability of the system to rearrange its structure by varying temperature. On the other hand, fragile liquids are mainly dominated by simple, non-directional Coulomb attractions or by van der Waal’s interaction forces. Their microscopic structure can be easily altered close to T_g and with small thermal excitations, it can be rearranged in a variety of different particle orientations.

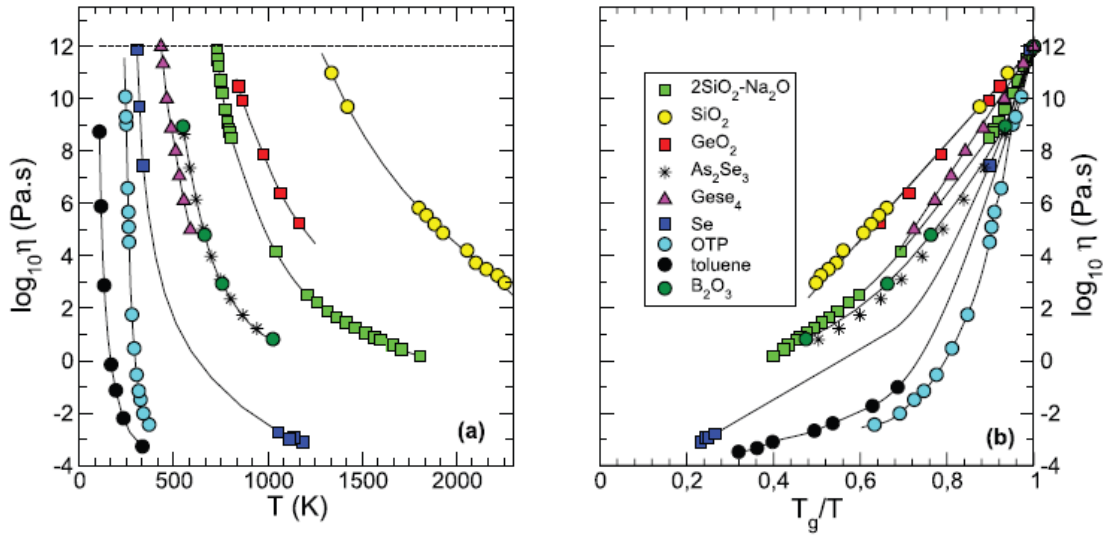


Fig. 1.6 (a) Behaviour of viscosity η as a function of temperature for different glass formers in supercooled liquid state. The dashed black line indicates the viscosity $\eta(T_g)=10^{12}$ Pa.s. (b) Angell plot of (a) plotted with scaled temperature T_g/T . (Figure from Ref. [5]).

To quantify the fragility behaviour, Angell [20] introduced the fragility index m defined as the slope of $\log(\eta(T))$ versus T_g/T close to T_g ,

$$m = \left[\frac{d \log_{10} \eta}{d(T_g/T)} \right]_{T=T_g} \quad (1.4)$$

As seen in Fig. 1.6(b), large slopes correspond to fragile glass-formers displaying a variable $E(T)$ and a rapid evolution of η as one approaches T_g , while small slopes correspond to strong glass-formers. The fragility ranges from $m = 14.8$ for network glasses ($m = 20$ for silica) up to ~ 214 for polymers [5].

The strong-fragile character of supercooled liquids was also found to be reflected in the configurational heat capacity [21]. As shown in Fig. 1.7, strong liquids display a small jump in C_p on crossing T_g , while fragile ones present a marked discontinuity. The heat capacity just manifests the structural changes described by the activation energies related to the shape of the viscosity curve on approaching T_g . For this reason, the jump in C_p is bigger in systems in which the activation energy increases between the melting point and the glass transition.

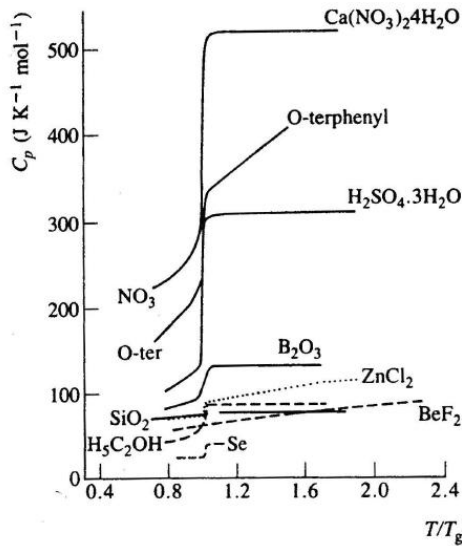


Fig. 1.7 Behaviour of heat capacity C_p as a function of the reduced temperature T/T_g for different glass-forming liquids. The glass transition corresponds to a discontinuity in the temperature dependence of C_p . (Figure from Ref. [21]).

Apart from these interesting dynamics of glass-forming liquids close to T_g , an equally intriguing question is ‘Why do certain materials have a greater glass-forming ability than others?’ and this remains one of the unsolved mysteries of glass science. This question is addressed in the following section.

1.3 Theories of glass formation

Although many empirical theories have been developed which are reasonably successful in accounting for the glass-forming tendencies in certain specific cases, there is no general rule which may be used universally to predict glass-forming ability of a given material. Glass formation theories are broadly classified as: structural and kinetic. In Fig. 1.8, we depict a schematic of some of the most relevant theories of glass formation used in this thesis work, and discuss about them briefly in the following paragraphs.

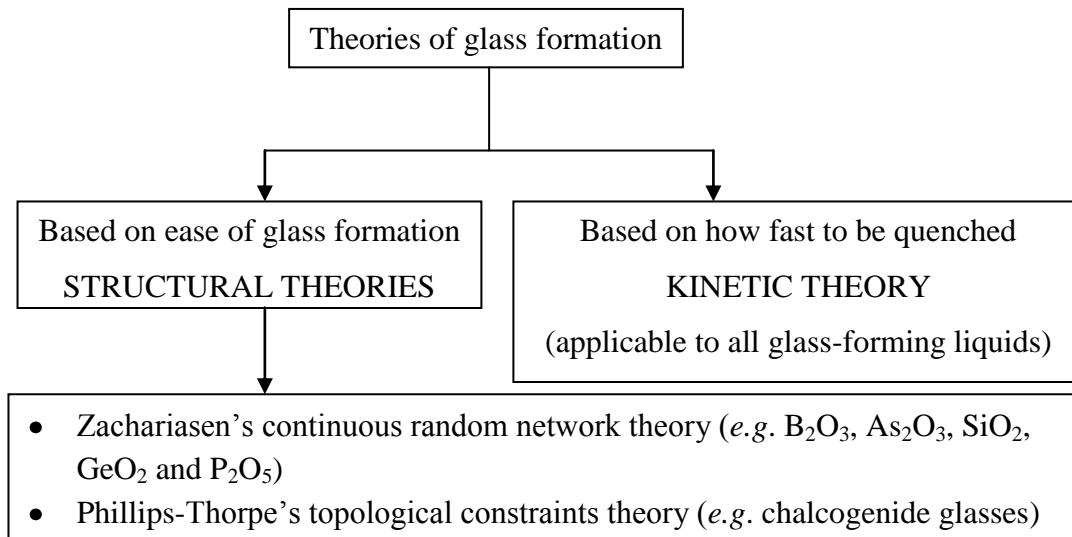


Fig. 1.8 Various theories of glass formation.

1.3.1 Structural theories of glass formation

The very first glasses known and synthesized by mankind were silicates. As a result, the first theories that advanced to explain why some materials form glasses while others do not, were based on the existing knowledge of the behaviour of silicate melts and the structure of silicate crystals [6]. These theories assume that some unique features of certain melts lead to glass-formation in them, while absence of those features prevents

glass-formation in other substances. These theories came to be known as structural theories of glass formation.

1.3.1.1 Zachariasen's Continuous Random Network (CRN) theory

Zachariasen observed that the mechanical strengths of glasses are comparable to those of crystals. This gave him the idea that the atoms in glass are linked together by the same forces as in crystals and the atoms oscillate about the same equilibrium positions. From the x-ray diffraction studies of silicate glasses, he noted that they have a network as opposed to close-packed structures. These networks consist of tetrahedra connected at all four corners just as in the corresponding crystals but the networks are not periodic and symmetrical as in crystals. These networks extend in all three dimensions such that the average behavior in all directions is the same, *i.e.*, the properties of glasses are isotropic. Consequently, he defined [3] glass as “a continuous three-dimensional network with energy content comparable to that of the corresponding crystal but without periodicity and symmetry”.

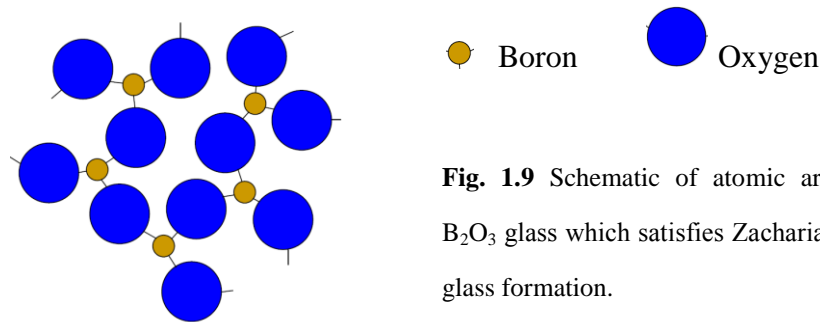


Fig. 1.9 Schematic of atomic arrangement in B_2O_3 glass which satisfies Zachariasen's rules of glass formation.

Zachariasen, thus, concluded that the ability to form such networks provides the condition for glass-formation. Thereafter, he formulated [22] the following rules for the structural arrangement in oxide (A_2O_x) glasses (see Fig. 1.9 for B_2O_3 glass as an example), which could produce such a network:

- (a) The co-ordination number (CN) of the cation (A) must be small (*e.g.* B has coordination number 3 in B_2O_3).

- (b) An oxygen atom (O) is not linked to more than two cations (A) (*e.g.* an O in B_2O_3 glass is linked to two B atoms).
- (c) The oxygen polyhedrons may share only corners, not edges or faces (*e.g.* the BO_3 planar triangular units constituting the B_2O_3 glass are connected by corner-shared O atoms).
- (d) At least three corners of every oxygen polyhedron must be shared by other polyhedra (*e.g.* three O atoms of each BO_3 triangular units are shared by three other units to form a continuous network).

Essentially, (a) and (b) states that sufficient network cations must be present to allow a continuous structure to form, (c) states that the network is an open structure and (d) states that sufficient bonds linking the network polyhedra exist for the formation of a continuous network structure [6]. These conditions are fulfilled by the oxides of B_2O_3 , As_2O_3 , SiO_2 , GeO_2 , P_2O_5 , etc.

1.3.1.2 Phillips-Thorpe's topological constraints theory

According to Phillips-Thorpe's theory [23,24], glass-forming ability is determined by comparing the number of atomic degrees of freedom with the number of inter-atomic force field constraints. If the number of constraints is less than the available degrees of freedom, then the network is considered flexible or floppy, and if the number of constraints is greater than the degrees of freedom, the network becomes over-constrained or stressed rigid. The optimum glass compositions are those in which the number of constraints exactly equals the degrees of freedom, in which case the glass network is isostatic. In the floppy regime, the atoms may easily arrange themselves into the minimum energy configuration of the crystalline state, whereas, in the over-constrained regime, rigid structures easily percolate throughout the system, also resulting in crystallization [25].

Phillips and Thorpe obtained the condition for an optimum glass network in three-dimensional space as a system where the average coordination number of atoms is 2.4. This critical value of $\langle r \rangle = 2.4$ is called the rigidity percolation threshold, because, at this composition, rigid structures percolate throughout the glass, leading to an isostatic network. Phillips-Thorpe's constraint theory has met with much success in predicting critical behavior of chalcogenide systems (As_2S_3 , Se, etc.) about the rigidity percolation threshold. It also has been extended to oxide glasses, glassy metals and proteins [25].

1.3.2 Kinetic theory of glass formation

The knowledge of a large number of non-silicate, polymeric and metallic glasses in recent years have made it clear that virtually any material can be formed a glass. Therefore, the question is not whether a material will form a glass, but rather how fast must it be cooled to avoid detectable crystallization. This is called as the critical cooling rate. Good glass formers are those which form glasses at slow cooling rates ($\ll 1\text{K/min}$). Materials which form glasses at very high quenching rates ($\gg 100\text{ K/min}$) are known as 'marginal' glass formers. Hence, the emphasis in glasses have shifted from control of glass formation by selection of materials, to control of glass formation by changes in processing [6]. This has given rise to a new approach known as kinetic theory of glass formation.

Crystallization requires a nucleus (nucleation) on which the crystal can grow (crystal growth). The nucleation may be either homogeneous (forming spontaneously within the melt) or heterogeneous (forming at a pre-existing surface, such as, due to an impurity, crucible wall, etc.). Therefore, the nucleus is precursor to the crystal. If there is no nucleation, there will be no crystal formation and the material will form a glass.

Nucleation occurs due to constant vibrations and diffusion of the atoms of the system because of their thermal energy at elevated temperatures. Two barriers have to be overcome to form a nucleus: the thermodynamic barrier (W^*) is the ‘free-energy change’ that occurred in the system after the formation of the nucleus and the kinetic barrier (ΔG_D) is the ‘activation energy’ required for an atom to pass over the liquid-nucleus interface to rearrange in space to form an ordered crystal from a disordered liquid. The rate of nucleation, I_v then becomes,

$$I_v = A \exp \left[\frac{-(W^* + \Delta G_D)}{k_B T} \right] \quad (1.5)$$

where A is a constant, k_B is the Boltzmann constant and T is the absolute temperature. W^* is the actual work required to form a nucleus of critical size, *i.e.*, one which will grow instead of re-dissolving into the melt [3,6].

The kinetic barrier to crystallization is known to be a function of the viscosity of the liquid. It is very large if the viscosity is large at the nucleation temperature. Melts which exhibit a large barrier to nucleation also exhibit good glass-forming behaviour. Inhibition of crystal growth is also achieved using complex melt structures which inhibit rearrangement of the melt into the ordered crystalline structure by using many different elements into the composition, so that the redistribution of atoms to the appropriate sites on the growing crystals is more difficult. This approach is routinely used in commercial glass technology. Furthermore, elimination of heterogeneous nuclei prevents crystal growth in melts which crystallize from heterogeneous nucleation process. Elimination of heterogeneous nuclei is enhanced by the addition of strong fluxes to a batch, which explains the strong effect of lead oxide in enhancing the ease of glass formation [6].

Just like the possibility of crystallization to occur when a melt is cooled, a glass once formed by avoiding this crystallization may be susceptible to devitrify or crystallize

again when the glass is heated through the supercooled liquid regime. This devitrification, is desirable for some applications, or when undesirable, is termed ageing.

1.4 Crystallization/ Devitrification: Kinetics of phase transitions

Thermal crystallization occurs in many disordered solids when heated. Elemental glasses such as S and Se are likely to crystallize, since the material has only topological structural disorders. In contrast, crystallization can be appreciably suppressed in multi-component glasses, because of the compositional disorder [12]. Stable glasses such as SiO_2 and As_2S_3 do not crystallize but continuously transform to a liquid through the supercooled states. Crystallization may bring undesired changes in macroscopic properties. When a transparent oxide glass is crystallized, it tends to become frosty. However, crystallization (and amorphization) in Te-alloy films, accompanying optical and electrical changes, is a central subject of research in the recent phase-change memory devices [12].

Similar to glass transition, devitrification is not a phase transition but a relaxational phase change. The devitrification/ crystallization temperature T_{cry} also becomes higher with the heating rate $\partial T/\partial t$. Then the obvious question is, what is the difference between glass transition and crystallization? A clear difference as revealed by calorimetric measurements is that glass transition appears endothermic but crystallization is exothermic. In addition, the change between a glass and the supercooled liquid may be reversible, while a crystal cannot directly transform to the glass.

The theoretical basis for interpreting the kinetics of phase transformations is provided by the formal theory of transformation kinetics as developed by Johnson and Mehl [26], and Avrami [27-29], essentially based on calorimetric experiments carried out under isothermal conditions. These models describe the evolution with time, t , of the

volume fraction crystallized, α , in terms of the nucleation frequency per unit volume, I_v and the crystal growth rate, u as [30]:

$$\alpha = 1 - \exp \left[-G \int_0^t I_v \left(\int_{t'}^t u d\tau \right)^a dt' \right] \quad (1.6)$$

Here G is a geometric factor which depends on the shape of the growing crystal and a is an integer or half-integer related to the dimensionality of crystal growth. When u is independent of time for the special case of interface-controlled or diffusion-controlled growth, a assumes the respective values of 1, 2 or 3 for one-, two- or three-dimensional growth. I_v and u are independent of time under conditions of isothermal crystallization when Eq. (1.7) is integrated as

$$\alpha = 1 - \exp(-G' I_v u^a t^b) \quad (1.7)$$

where $b = a + 1$, for $I_v \neq 0$ and G' is the corresponding geometric factor. Eq. (1.8) is taken as a specific case of the Johnson-Mehl-Avrami (JMA) transformation relation describing the time-dependence of the fractional crystallization as

$$\alpha = 1 - \exp[-(Kt)^b] \quad (1.8)$$

where b is called the Avrami (growth) exponent and represents the growth morphology, while the rate constant K is a function of temperature and generally depends on both the nucleation rate and the growth rate, and is assumed to exhibit an Arrhenian temperature dependence as

$$K = K_0 \exp(-E/RT) \quad (1.9)$$

Here K_0 is the pre-exponential factor, E is the effective activation energy describing the overall crystallization process and R is the universal gas constant. K_0 is considered as a typical vibrational frequency ($\sim 10^{13}$ Hz) and E is the barrier height between a disordered state and the corresponding crystal. It is intuitive that when a glass is transformed into a crystal, disordered bonds must be cut and reconnected to the ordered structure.

Accordingly, it may be plausible that E correlates with the bond strength and heating induces thermal segmental motion, leading to crystallization.

The JMA rate equation is obtained by differentiating Eq. (1.9) with respect to time,

$$\frac{d\alpha}{dt} = bK (1 - \alpha) [-\ln (1 - \alpha)]^{(b-1)/b} \quad (1.10)$$

The JMA rate equation is strictly applicable only to isothermal crystallization conditions and deviations are observed if the assumptions on which the equation are based are not satisfied [31]. Henderson [32] pointed out that JMA analysis can be extended to non-isothermal conditions, when the conversion rate depends only on temperature and not on previous thermal history, and the entire nucleation process takes place during the early stages of transformation.

Once, a material is synthesized, the determination of its atomic arrangement in space is a key pre-requisite for any subsequent study devoted to understand any of its physical or chemical properties. In crystals, the determination of the structure is simplified by the periodicity, where the whole lattice can be considered as a periodic repetition of a fundamental building block, the unit cell, which is often formed by only few atoms.

In glasses, the situation is completely different. The structure of glass is characteristic of the instantaneous structure of a liquid; isotropic and lacking long-range order. However, atoms are constrained to vibrate around their disordered equilibrium positions, so that their dynamics is characteristic of a solid. The following section discusses how the disorder in a glass, such as lack of long-range order, can be characterized.

1.5 Classification of structural order in glass: order within disorder

The glassy state is characterized by what it is not. It is not a form of matter with long-range order; it does not have large regions in which the atoms are arranged in a periodic array; there are no crystallites of a size large enough to give sharp Bragg diffraction spots. The key to the definition of the structure of glass is the distinction between long- and short-range ordering. The controversy in understanding glass structure remains as to ‘How disordered is the atomic structure of a glass?’ Despite the lack of long-range translational and orientational order, glasses do possess a high degree of short-range order. Therefore, while discussing the structure of a glass, it is useful to consider the types of structural order that can exist in such materials at various length-scales. Such categorization is convenient in two ways: the classification is hierarchial (a particular type of order at one length-scale can be dictated by order at a smaller scale) and the various experimental probes are generally sensitive to structural correlations at different length-scales. The possible types of structural order in glass are [33]:

- (a) short-range order (SRO) in the range 2-5 Å;
- (b) medium-range order (MRO) in the range 5-20 Å and
- (c) long-range structures (LRS) for length-scales > 20 Å.

Short-range order involves one atom and its nearest neighbors. In the case of covalently-bonded glasses, where directional bonding is dominant, SRO can be characterized in terms of well-defined coordination polyhedra. The SRO is often very similar to the local ordering in crystals: the number of nearest neighbors, the bond distances and the bond angles are rather well-defined.

MRO is defined as the next highest level of structural organization beyond SRO. It is difficult to measure experimentally and to interpret unambiguously, but a variety of techniques have allowed several types of structural ordering corresponding to MRO to be

identified. It arises from orientational correlation beyond the nearest neighbor distances. On a length-scale just beyond SRO, 5-10 Å, larger structural units (superstructural units) can be formed by aggregating basic coordination polyhedra connected together in well-defined relative orientations to form regular rings or three-dimensional clusters [33]. In a larger length-scale, between 10-20 Å, a further level of MRO can be associated with the connection between these structural units to form layer-like or chain-like or isolated clusters.

By definition, no long-range periodic structures are present in glass and hence, the LRS is characterized by inhomogeneities in the structure and phase separation.

1.5.1 Medium-range order and the first sharp diffraction peak

As understood from the previous section, in general, glassy materials are characterized by two length-scales: short-range structure defining the nearest neighbour coordination polyhedra and a medium-range order defining regions of ordering beyond the first nearest neighbor distance. The evidence of SRO is obtained from diffraction experiments. The existence of medium-range correlations in the glass structure has been admitted from various experimental results (vibrational spectroscopy and x-ray diffraction).

A feature of diffraction data from glasses which has long been considered as the characteristic signature of the existence of MRO is the first peak in the total structure factor, known as the first sharp diffraction peak (FSDP), occurring at values of scattering vector $Q = 1-2 \text{ \AA}^{-1}$, depending on the material [33]. This peak is anomalous in a number of ways. Firstly, it is considerably narrower than other peaks in the structure factor, $S(Q)$, and hence its name. The structure factor is a mathematical function that describes the amplitude and phase of a wave diffracted from atomic planes in a material. The intensity

of a diffracted beam is directly related to the amplitude of the structure factor. Furthermore, the behaviour of the FSDP [33] as a function of temperature and pressure differs from that of the other peaks in $S(Q)$: the FSDP in chalcogenides increases (reversibly) in intensity with increasing temperature [34], whereas other peaks in the structure factor decrease in intensity with increasing temperature in accordance with Debye-Waller behaviour. Also with increasing pressure [35], it rapidly decreases in intensity and shifts to higher Q , unlike other peaks. Even though, detailed microscopic understanding of the structural origin of FSDP has remained elusive [36], proposals made in literature for the MRO structural origin of FSDP can be categorized as: quasi-crystalline structures, clusters or chemical-order pre-peak [33].

In the quasi-crystalline model, it was assumed that pseudo-crystalline layer-like structural arrangements which spatially repeat at intervals D are present in glass [34]; the FSDP position is given as $Q \approx 2\pi/D$. This was thought natural since the crystal structures of many glass-forming chalcogenides (such as, As_2S_3 or GeSe_2) are layer-like. However, this model was found inconsistent with many experimental observations, such as, observation of FSDP even in the liquid state of chalcogenide glasses and occurrence of FSDP in glasses such as SiO_2 where the crystalline polymorphs are not layer-like. On the other hand, the cluster model explains FSDP as structural correlations between ill-defined clusters [37]. However, the structural identity of such clusters in glasses remains obscure. The chemical-order pre-peak model [38] proposes that the FSDP arises from the clustering of interstitial voids around cation-centered clusters. This model explains the anomalous pressure dependence of the FSDP: increase of pressure densifies the glass structure by reducing the interstitial volume, thereby leading to a decrease in the FSDP intensity. The anomalous temperature dependence is understood as resulting from the decrease of density with increasing temperature which increases the interstitial volume.

This increase in voids with increasing temperature also explains the survival of FSDP into the molten state in some glasses.

Even though, microscopic description of the FSDP is under debate, it is evident of the presence of medium-range order in glasses. As distinct as the structural ordering at different length-scales, glasses also display some universal anomalous behaviour in vibrational properties as discussed in the following section, which makes the study of glasses extremely challenging.

1.6 Vibrational properties of glasses

Atoms in solids oscillate around their equilibrium positions at all temperatures, both at 0 K (zero-point motion) and at finite temperatures (thermal fluctuations). Below T_g , the glass dynamics is restricted to these microscopic vibrations which are responsible for sound propagation, heat transfer and other thermodynamic quantities in solids. It is natural that glasses support sound waves within the macroscopic limit as do the corresponding crystalline materials. As the phonon wave vector, $q \rightarrow 0$, the vibrational excitations have the characteristics of linearly propagating acoustic waves, with speeds of sound, V_l and V_t (the two transverse branches are degenerate because of isotropy). Increasing the frequency, the lack of periodicity does not allow a plane wave-description. However, in the long-wavelength limit, the system would be expected to appear as a continuum and, as a consequence, the thermal properties should behave in the same way for a glass or a crystal. However, experimentally, strong differences were observed in the low-temperature thermal properties of glasses and crystals. These aspects of glasses are described below.

1.6.1 The vibrational density of states (VDOS)

To describe the vibrational properties in crystals as well as in glassy systems, the vibrational density of states (VDOS), is generally employed. The VDOS, $g(\omega)$ is defined as,

$$g(\omega) = \sum_k \delta(\omega - \omega_k) \quad (1.11)$$

where $g(\omega)d\omega$ is the number of vibrational states lying in between ω and $\omega + d\omega$. The summation over k in Eq. 1.12 is over all the phonon dispersion curves in the case of crystals and covers the first Brillouin zone. The peaks present in the crystal VDOS represent the van Hove singularities. These singularities are associated with ω where ever the dispersion curve flattens near a Brillouin zone boundary. On the other hand, the lack of periodicity in glasses does not let a Brillouin zone to be defined rigorously and the summation index k of Eq. 1.12 is only a label for the vibrational eigenstates. Moreover, the typical sharpness of the crystalline VDOS disappears, as the van Hove singularities are smeared out as a consequence of the finite width of the energy distribution of vibrational excitation about a given q value. In spite of this, the VDOS represents the natural link between a microscopic description of a solid medium and its macroscopic properties and knowledge of $g(\omega)$ permits one to derive the thermodynamic properties of the system. Such a link is provided for the low-frequency limit of the VDOS by the Debye model.

1.6.2 The Debye model of specific heat

The Debye model [39] provides the quantum mechanical description of the low-temperature specific heat behaviour of solids. In the low-temperature limit, thermally excited vibrational modes are the acoustic excitations having wavelengths greater than the inter-particle distances. The solid can thus be treated as an elastic continuum in which

acoustic waves can propagate. The vibrational excitations of the solid are described by the three acoustic branches exhibiting linear dispersion relation between frequency ω and wave vector q of phonon as, $\omega = V_D q$. The Debye velocity V_D is obtained by averaging the longitudinal (V_l) and transverse (V_t) sound velocities as,

$$\frac{3}{V_D^3} = \left(\frac{1}{V_l^3} + \frac{2}{V_t^3} \right) \quad (1.12)$$

The total number of vibrational modes in the Debye model is $3N$, where N denotes the number of atoms in the system. This constraint on the VDOS defines a limiting frequency ω_D , known as the Debye frequency [39], which represents the highest frequency for the acoustic modes,

$$\omega_D = V_D (6\pi^2 \rho)^{1/3} \quad (1.13)$$

where ρ is the number density. The VDOS predicted by Debye model is given as,

$$g(\omega) = \frac{3}{\omega_D^3} \omega^2 \quad (1.14)$$

This description of the VDOS allows a correct evaluation of the low-temperature specific heat,

$$C_V = \frac{12\pi^4}{5} N k_B \left(\frac{T}{\theta_D} \right)^3 \quad (1.15)$$

where $\theta_D = \hbar\omega_D/k_B$ and is known as the Debye temperature. This is the temperature specific to a system, above which all the phonon modes are excited. Therefore, at low-temperatures, the specific heat of crystals is dominated by the contribution from the acoustic excitations and is well-described by the Debye or continuum model, that predicts a T^3 -dependence for the specific heat at low-temperature (Eq. 1.16) and a ω^2 -dependence (Eq. 1.15) for the vibrational density of states $g(\omega)$ at low-frequencies [39]. These predictions have indeed been confirmed experimentally for dielectric crystals [39]. However, since the local atomic arrangement is not considered in this model, crystals and glasses can both be described within the same approximation and glasses can be expected

to display similar thermal properties at low-temperatures as that of crystals. However, the low-frequency dynamics and concurrently, the low-temperature thermal properties of glasses, exhibit unusual behavior that strongly differs from that of their crystalline counterparts and hence are considered anomalous. Glasses display a universal low-temperature dependence of the specific heat, and a broad excess over the Debye T^3 -prediction at temperatures of ~ 10 K and below, a region where the Debye approximation works well for the corresponding crystals [40]. These aspects of glasses are discussed below.

1.6.3 Anomalous thermal properties of glass

Experimental studies in glasses have established a roughly linear temperature dependence of the specific heat (C_P proportional to T) and approximately quadratic temperature variation of the thermal conductivity (κ proportional to T^2) at temperature $T < 1$ K which are in contrast to the T^3 -behaviour of these quantities in crystals [41]. Fig 1.10 (a) shows the temperature behavior of the heat capacity C_P for crystalline and glassy silica. It can be easily identified that C_P in the low-temperature range decreases much slowly with temperature for glassy silica. This behavior has been found in all glasses [40]. Therefore, heat capacity in glasses can be described by adding a linear term to the Debye predictions:

$$C_P \sim aT + bT^3 \quad (1.16)$$

Hence, below 1 K, the heat capacity is essentially linear in temperature. These features have found explanation in terms of two-level systems (TLS) identified with tunneling states in atomic-double-well potentials [40]. This model assumes the existence of local structural instabilities of the glass, capable of tunneling among different configurations of the system. This means that the anomalous behavior below 1 K is not due to the sound

waves themselves, but rather to additional excitations, the tunneling states, which scatter the sound waves.

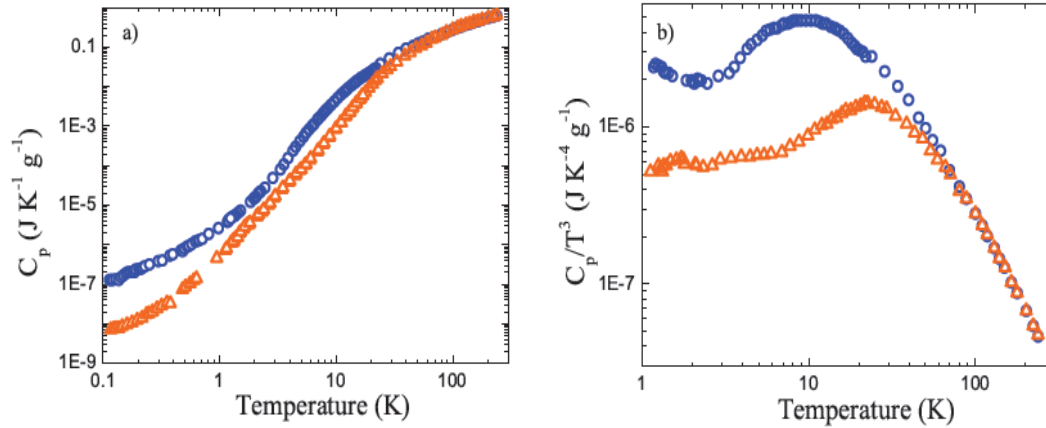


Fig. 1.10 Temperature variation of (a) the heat capacity C_p and (b) reduced heat capacity C_p/T^3 for crystalline quartz (orange triangles) and glassy silica (blue circles). (Figure from Ref. [16,41]).

Above 1 K, C_p starts to deviate from this quasi-linear temperature behavior and at about 10 K, exhibits a broad hump, as detected in the Debye-predicted cubic temperature dependence plot (see Fig. 1.10 (b)). The thermal conductivity exhibits a plateau at this temperature range [41]. The anomalies below 1 K appear to be universal in the sense that they are shared by a large variety of glass systems, and the TLS model is generally accepted in literature. However, the excess of heat capacity between ~ 1 -20 K, has been subjected to much controversy [42]. As shown in Fig. 1.10 (b), the excess in C_p/T^3 is present also in crystalline quartz, however, this excess appears at higher temperatures and is related to the effect of transverse acoustic vibrational excitations near the boundary of the first Brillouin zone [41]. The increase in the heat capacity with respect to the Debye prediction at ~ 10 K has been widely investigated but its origin is still poorly understood [43].

The failure of the Debye model to describe the specific heat of glasses at ~ 10 K temperature range should correspond to an anomalous feature in the low-frequency part

of the VDOS in glasses in accordance with Eq. 1.15 and Eq. 1.16. As will be discussed in the following section, the excess C_P as depicted in Fig. 1.10(b), is indeed a manifestation of an excess found at ~ 1 THz in the VDOS over that of the Debye ω^2 -prediction (Eq. 1.15) and is indeed detected as a broad hump in $g(\omega)$ of glasses [44].

1.6.4 The excess-VDOS in glasses: the Boson peak

The excess-VDOS observed ~ 1 THz (~ 10 meV) is a universal feature of glasses, appearing as a characteristic broad asymmetric peak when plotted in the reduced density of states $g(\omega)/\omega^2$ as a function of the excitation energy [42]. This broad band is referred in literature as the ‘Boson peak’ since its intensity scales with temperature approximately according to the Bose-Einstein statistics [44]. Since the VDOS is directly accessible using inelastic neutron [45] and light scattering spectroscopies [44], the Boson peak is widely studied in variety of glassy systems using these techniques. Fig. 1.11 (a) shows the VDOS measured in glassy sorbitol by means of inelastic neutron scattering [16]. Comparing the experimental data (blue filled circles) to the Debye prediction (red curve), an excess of low-energy modes in the glass is visible. This excess becomes more evident when we consider the reduced VDOS, $g(\omega)/\omega^2$ (Fig. 1.11 (b)).

The Boson peak seems to be correlated to several properties of glass-formers as well. For example, it was proposed that there exists a correlation between the Boson peak intensity and the fragility of the corresponding supercooled liquid [43]. It was observed that the less fragile the melt, the higher is the intensity of the Boson peak which means strong liquids have a larger degree of disorder than the fragile ones when the system is frozen-in and the glass is formed. Furthermore, in some strong systems, such as B_2O_3 , the Boson peak is still well-evident in the supercooled liquid [46]. However, despite of large number of theoretical and experimental reports, the microscopic origin of the excess

modes giving rise to the Boson peak is still controversial [47,48]. In the next section, an overview of the most widely used models for the origin of the Boson peak is presented.

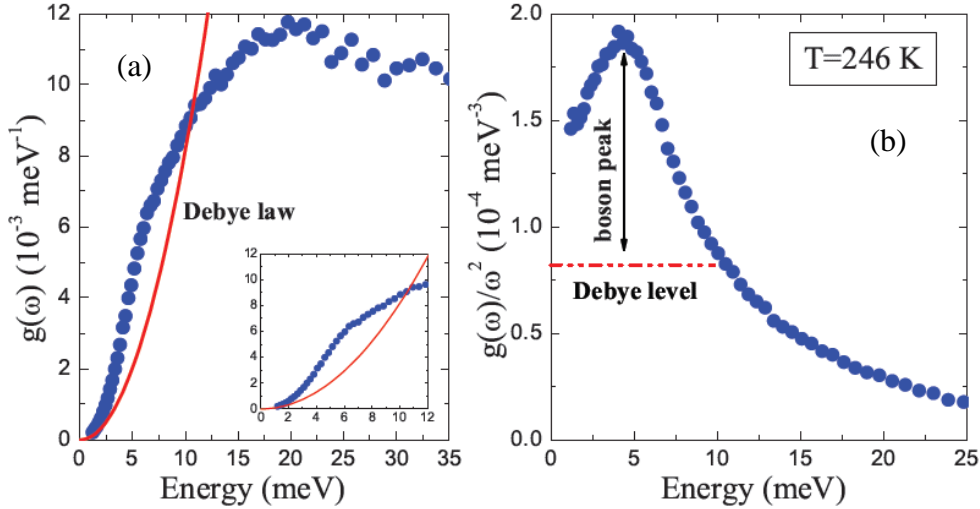


Fig. 1.11 (a) Experimental VDOS (blue circles) of glassy sorbitol measured using inelastic neutron scattering. The red curve depicts the Debye ω^2 -prediction and the inset shows an enlarged image of the low-energy data. (b) Reduced density of states $g(\omega)/\omega^2$ depicting a Boson peak for the glass and a constant Debye level in red dashed line. (Figure from Ref. [16,41]).

1.6.5 Theoretical models for the Boson peak

There is a general agreement that the Boson peak is a manifestation of structural disorder in glass. What is still not agreed upon in literature is whether this peak arises from some peculiar behaviour of the acoustic modes present in the corresponding energy range or from some additional modes specific to the glassy state. Basically, three distinct viewpoints have been proposed to explore its origin: existence of defect modes or soft modes, strong scattering of sound waves from disorder, and vibrational heterogeneities on the nanometric scale. In the following, we briefly discuss these different approaches used to explain the Boson peak. It is noteworthy, that even starting from distinctly different assumptions, the predictions of these models are qualitatively similar on

experimental results and is therefore, extremely difficult to distinguish between the different models from the experimental point of view.

1.6.5.1 Soft-potential model

The soft-potential model (SPM) [49,50] assumes the existence of additional quasi-local modes, which coexist and hybridize with the sound waves, giving rise to the Boson peak. This model is an extension of the two-level system (TLS) model which very well-describes the thermal anomalies of glasses below 1 K, as mentioned earlier. SPM predicts that in addition to TLS, there are soft mode excitations in glasses which are responsible for their universal behavior especially at higher temperatures. These low-frequency vibrations originate from localized vibrations of small groups of atoms in local defects of the amorphous structure or from low-lying optical modes in parent crystals. These excitations are described by unique anharmonic soft atomic potential. The model describes the quasi-local excitations as low-frequency harmonic oscillators which weakly couple to the sound waves of the elastic continuum medium. This coupling leads to a dipole-dipole interaction between different harmonic oscillators, which destabilizes the quasi-localized harmonic modes. The vibrational instability is controlled, under a certain frequency (lower than the Debye frequency) by the anharmonicity and creates a new stable spectrum of harmonic vibrations with a Boson peak feature and an asymmetric double-well potential typical of the TLS tunneling modes. In this model, the Boson peak energy depends on the interaction strength among the different harmonic oscillators: the stronger the interactions, the higher in energy will the Boson peak maximum appear.

1.6.5.2 Model of fluctuating elastic constants

This viewpoint ascribes the excess modes in the Boson peak to arise because of strong scattering of sound waves [51] from disorder in the glass [52,53]. The model by

Taraskin *et. al.* [52] proposes that the atoms occupy ideal crystalline positions and the system is described as composed of coupled harmonic oscillators interacting through random, independent elastic force constants K_{ij} , between atoms i and j . The strength of these force constants are controlled by a probability distribution $P(K_{ij})$. On increasing the width of the distribution, the system becomes unstable with negative force constants K_{ij} , and this instability gives rise to the Boson peak. This model describes the Boson peak from purely harmonic modes and denies the necessity of the existence of localized states or strongly anharmonic modes (as in SPM). More precisely, the enhancement in the VDOS is associated with the lowest van Hove singularity in the spectrum of the reference crystalline system, pushed down in frequency by disorder-induced level-repelling and hybridization effects [52].

On the other hand, under the frame work of harmonic approach, Grigera *et. al.* [53] proposed a different microscopic model based on topological disorder of the atoms. This model forwarded the idea that the Boson peak marks the transition between acoustic-like excitations and a disorder-dominated regime for the vibrational spectrum. Schirmacher *et. al.* [51] proposed a macroscopic elastic and lattice-independent model which considers the system as an elastic continuum in which the transverse elastic constant is assumed to vary randomly in space. The model predicts a correlation between the excess VDOS and the damping of the acoustic waves present in the corresponding energy range.

1.6.5.3 Model based on vibrational heterogeneities on nanometric scale

This approach attributes the Boson peak to vibrational heterogeneities/inhomogeneities of the elastic response in glasses on the nanometric length-scale [48,54]. It assumes the system to be inhomogeneous, consisting of aggregate of regions with different elastic constants. The glass is thus, characterized by more cohesive domains

separated by softer inter-domain zones on the nanometric spatial range and the Boson peak arises from vibrational modes spatially localized in such regions. A correlation between the size of these elastic heterogeneities and the fragility of the different materials has been proposed as well [43]. The idea is that stronger glasses would display a more inhomogeneous elastic response with respect to fragile systems. This model explains why the amplitude of the Boson peak is higher in strong glasses. In the case of fragile systems, instead, the excess of modes would become broader and less intense due to the disappearance of the elastic heterogeneities.

The Boson peak has also been suggested to reflect a crossover from long wavelength vibrations propagating in the continuous media to localized vibrations on a characteristic length-scale. The long wavelength vibrations scatter strongly from elastic inhomogeneities in the structure due to the topological disorder in glass. The scattering leads to a drastic decrease in the phonon mean-free path and can increase the VDOS in certain energy range. These excess vibrations thus become localized by the strong scattering. Phonon localization may be viewed in terms of the Ioffe-Regel criterion, $k_{IR}L_{IR} \sim 1$, where k_{IR} and L_{IR} are the magnitude of phonon wave vector and mean-free path at Ioffe-Regel frequency, respectively [36]. Thus, the phonon mean-free path is assumed to be $\sim 1/k_{IR}$. This length has been interpreted as the correlation length for the disordered structure of the system [33] and can be calculated using the Boson peak energy. The energy of the peak is inversely proportional to the size of these spatially correlated regions. This correlation length has also been connected to MRO as obtained from FSDP [38].

1.7 Network glass and its modification: glass formers and modifiers

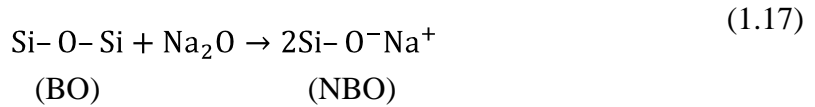
As described in the previous sections, understanding the interplay of dynamics and structure has evoked great interest in condensed matter physics owing to the variety

of universal phenomena linked to glass and the supercooled liquid states. In fact, glassy dynamics depend strongly on the network topology, *i.e.*, the way bonds and bond angles are arranged to form the network connectivity. Among other glasses, the field of network glasses is of special interest probably because they are most familiar and are historically, those which have attracted early interest [1]. This is partly due to the effect of the x-ray determined structure at the local, intermediate or long-range which appears to be central to the understanding of many chemical and physical properties including those revealing the slowing down of the dynamics [5]. The classification of network glasses is discussed below.

Zachariasen's random network model gives the formation of single-component oxide glasses, such as, B_2O_3 , As_2O_3 , SiO_2 , GeO_2 , P_2O_5 , etc. Such glasses are called as network glasses owing to the presence of inter-connected polyhedral units resulting from directional covalent bonding. The disordered arrangement of such polyhedral units on longer scales is then representative of glasses which form a highly cross-linked network of chemical bonds in three-dimensions. In fact, stoichiometric mixtures of Group III-Group IV elements (e.g. silicon, boron, germanium, etc.) with Group VI oxides and chalcogenides (oxygen, sulphur, selenium) indeed lead to a network structure that is composed at the very local level by geometrical building blocks typical of a short-range order, *e.g.* the SiO_4 tetrahedron in silicates [5].

Addition of alkali and alkaline-earth oxides alter the network structure of such single-component glasses and thus, create multi-component glasses, such as, M_2O-SiO_2 , $M_2O-MO-SiO_2$, etc. (where M can be a monovalent or divalent alkali or alkaline-earth metal cation). While such elements (M) are usually present as ions, they compensate by attracting nearby non-bridging Group VI atoms which induce a disruption of the network

structure. Such a modification for the $\text{Na}_2\text{O-SiO}_2$ system which converts some bridging oxygen (BO) into non-bridging oxygen (NBO) is shown below (see Fig. 1.12):



Stanworth [6] attempted to quantify such mixed-bond concept by the use of the partial ionic character model of Pauling. He classified oxides into three groups on the basis of electronegativity of the cation [6]. Cations which form bonds with oxygen with a fractional ionic character near 50% have small difference in electronegativity between cation and oxygen, thus having greater strength of covalent bond, should act as network formers and produce good glasses. Network formers generally have coordination numbers between 3 or 4, and electronegativity between 1.8 to 2.1, such as, B, Si, Ge, P, As, Sb, V, etc. Cations with slightly lower electronegativity (1.5 to 1.7) which form slightly more ionic bonds with oxygen, cannot form glasses by themselves, but can partially replace cations from the first group and are known as intermediates. Intermediates generally have coordination number between 4–6, such as, Al, Ti, etc. Cations with very low electronegativity (0.7 to 1.3) form highly ionic bonds with oxygen and never act as network formers. Since these ions only serve to modify the network structure created by the network forming oxides, they are termed as modifiers. Network modifiers generally have coordination number ≥ 6 , such as, Li, Na, K, Ca, Sr, Ba, etc.

The presence of NBOs in the network glasses lowers the relative number of strong bonds in the glass and this leads to an important modification of the melt viscosity, relaxation time and various dynamic quantities in the liquid state. Of course, an appropriate alloying of such components permits one to tune dynamic quantities of glass-forming liquids in an almost systematic fashion, allowing for the detection of anomalies which provide a greater insight into the glass transition phenomenon [5].

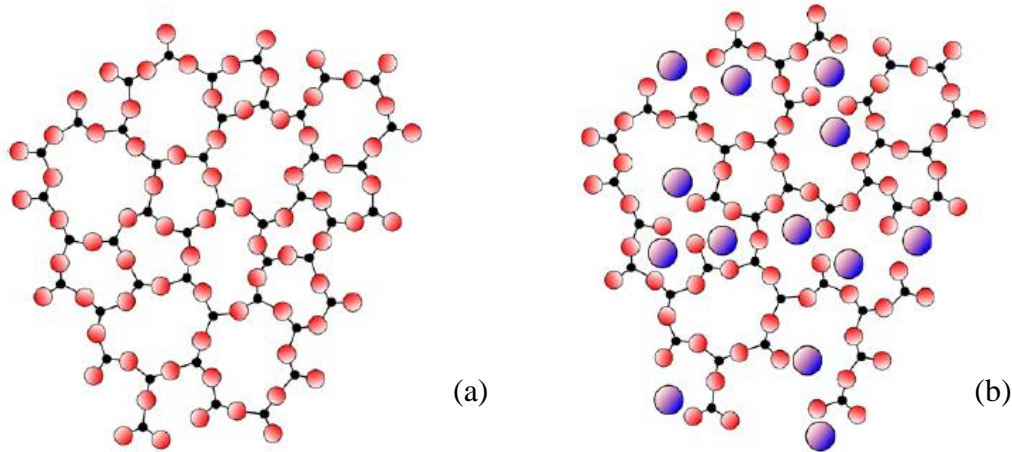


Fig. 1.12 Typical network-forming glasses: (a) two-dimensional representation of a single-component SiO_2 glass, whose network connectivity can be depolymerized (b) by the addition of a network modifier (Na_2O). (Figure adapted from Ref. [5].)

1.7.1 The composition-structure-property relationship in modified glasses

Just as any other material, the physical and mechanical properties of network glasses are determined by the atomic-level structures: the atomic configuration and chemical bonding. To understand the intriguing properties of glasses both in the supercooled and glassy states, the underlying structural origins need to be unraveled. Furthermore, the evolution of these properties as a function of chemical composition or temperature relies on a correct understanding of the structure of the single component glass and the changes induced in the structure upon the addition of a modifier.

The structural models of multi-component glasses rely on the combination of experimental data, such as, diffraction of x-rays and neutrons, along with various spectroscopic methods and numerical modeling. Glass structures are modeled for determination of cation coordination, inter-atomic distances and bond angles at various length-scales of ordering. The short-range order, which concerns the cation-oxygen polyhedral units, is accessible by spectroscopic methods. As for example, the short-range order in a typical alkali-modified borate glass involves quantification of coordination

numbers and symmetries of the network former (B_2O_3) structural units, and site quantification of the modifier (see Fig. 1.13).

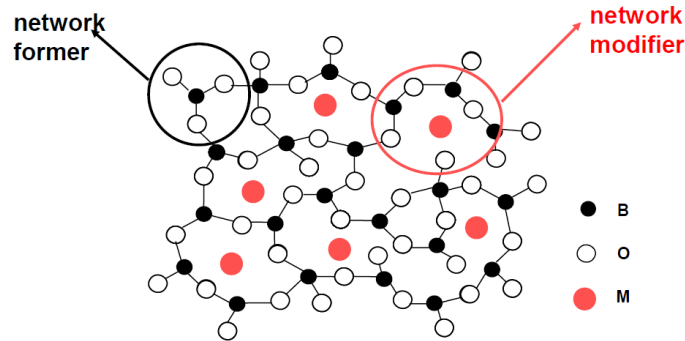


Fig. 1.13 Typical modified borate glass showing directly bonded neighbours in network formers and network sites containing modifier cations, which denote the short-range order in such a network glass.

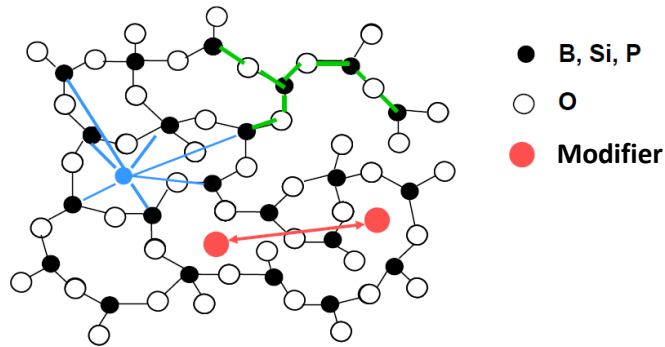


Fig. 1.14 MRO in a typical network glass can be depicted by connectivity of the network former (green lines), correlations between cations of network former and modifier (blue lines), and spatial distribution of modifiers (red line).

Medium-range order involves the ordering of polyhedral and cationic modifier sites. As depicted in Fig. 1.14, for an oxide glass containing B, Si or P atoms as network former, the correlations in connectivity of network former, correlations between cations of network former and modifier, and spatial distribution of modifiers, can all depict medium-range order. Insight on such ordering is again obtained using diffraction studies and inelastic scattering techniques. It is natural to assume that the short-range structure

governs the structural properties which are possibly modified by the medium-range structures. Examples of structure-related properties are density, bulk modulus, specific heat, thermal conductivity, linear thermal expansion coefficient, glass transition temperature, Debye temperature, etc.

Some properties of glasses derive their origin from the general glass structure itself. Whether the bonding is ionic, covalent, van der Waals, metallic or a mixture of these, the inherent disorder in the glass gives rise to slightly more open packing than found in the corresponding crystal. Owing to the absence of dislocation mechanism for deformation, glasses mostly display a brittle failure mechanism. The randomness is clearly responsible for the liquid-like isotropic nature of glass properties. Unlike crystals, glasses do not have a sharp melting point and rather exhibit glass transition in a range of temperature. This is because they lack unique bond lengths and dissociation energies unlike crystals. Moreover, properties like viscosity may be expected to increase with the degree of connectivity. Also, the creation of NBOs leads to increased fluidity in glass-formers. This is the reason for lowering of viscosity at a given temperature on increased addition of a modifier like Na_2O to silica glass [6]. On one hand, the increased cross-linking (increase of average coordination number) in network glasses such as chalcogenides is responsible for increasing the rigidity properties, glass transition temperatures and hardness; on the other hand, an increase of NBOs in the glass structure generally leads to an increase in the thermal expansion coefficient [1]. This is because the average atomic separation between the NBO and the ionically bonded interstitial cation can increase with temperature more rapidly. Owing to much open volume, the interstices in glass structure act as sieves through which mass can move and hence conduction of charge predominantly occurs by ionic movement through such interstices. Network-modifying ions (alkali ions, in particular), carry the bulk of the charge conduction in glasses.

Since there are no stoichiometric requirements for glass compositions, one can produce a continuum of multi-component glass compositions and expect the physical properties to vary continuously with composition. For many glasses, such as silicates, the addition or substitution of a component results in smooth monotonic transition of properties from one composition to the other [1]. While in many other glass systems, such as borates or borosilicates, properties do not change monotonically with modification. These are governed by the changes induced in the microscopic network structure upon addition of the modifier and the dependence of the physical property on the specific aspect of the structure. In the following sections, the network structure of three systems of glasses is described: borates, tellurites and phosphates. Changes in the SRO upon glass modification are also discussed. These glasses are considered strong according to Angell's classification. The interplay of structure and dynamics at different length-scales, and the structure-property relationship in these glasses upon modification, forms the primary theme of this thesis.

1.7.2 The structure of modified-borate glasses

Borates are very important glass-forming materials. A number of physical and chemical properties make borates one of the outstanding components in the commercial glass industry: borate (B_2O_3) glass can be considered to possess the highest glass-forming tendency because molten B_2O_3 does not crystallize by itself even when cooled at the slowest rate (it crystallizes only under pressure [55]); boron is highly soluble in silicate melts and it lowers the T_g , T_m , viscosity and thermal expansivity of borosilicate melts and provides them with high chemical durability.

Boron (B) has only three electrons in its valence shell, leading to a planar (sp^2 hybridized) BO_3 triangular structural unit (Fig. 1.15 (a)) for glassy B_2O_3 and a vacant p_z orbital perpendicular to the plane of the triangle. The size of B^{3+} ion is very small and it

can fit into the trigonal void created by three oxide ions in mutual contact to form a BO_3 unit. These units are the primary building blocks in all borate glasses. Several structural studies have been performed on B_2O_3 [56] and it is considered that boroxol (B_3O_6) rings, which consist of three BO_3 units in hexagonal planar arrangement of six B–O bonds is a major constituent of the glass structure (see Fig. 1.16). Boroxol is very much stable because of the possible delocalization of the electrons among the π -bonded p -orbitals of B and O perpendicular to the B–O–B plane. The B_2O_3 glass structure is considered to be made up of $\sim 70\%$ of boroxol units which are connected through simple BO_3 units.

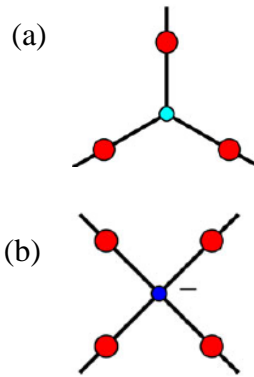


Fig. 1.15 Typical two-dimensional representation of (a) BO_3 triangular and (b) BO_4^- tetrahedral structural units depicting all bridging oxygen atoms (red circles) found in modified borate glasses.

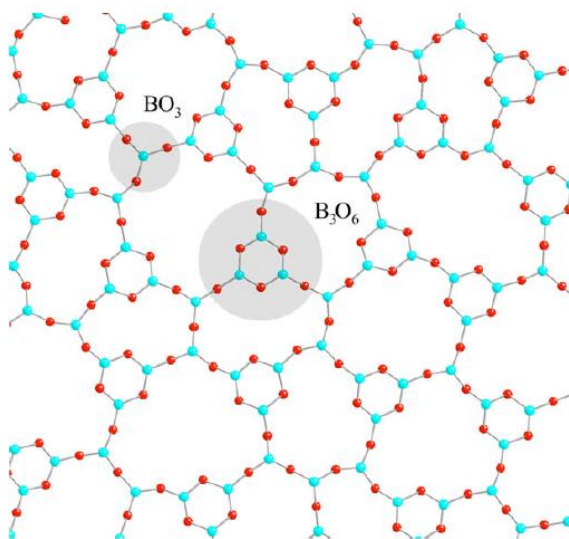


Fig. 1.16 A two-dimensional schematic representation of vitreous B_2O_3 depicting the formation of the network structure from a combination of BO_3 units and boroxol (B_3O_6) rings. Boron atoms are depicted by the cyan circles and oxygen atoms by red circles. (Figure from Ref. [57]).

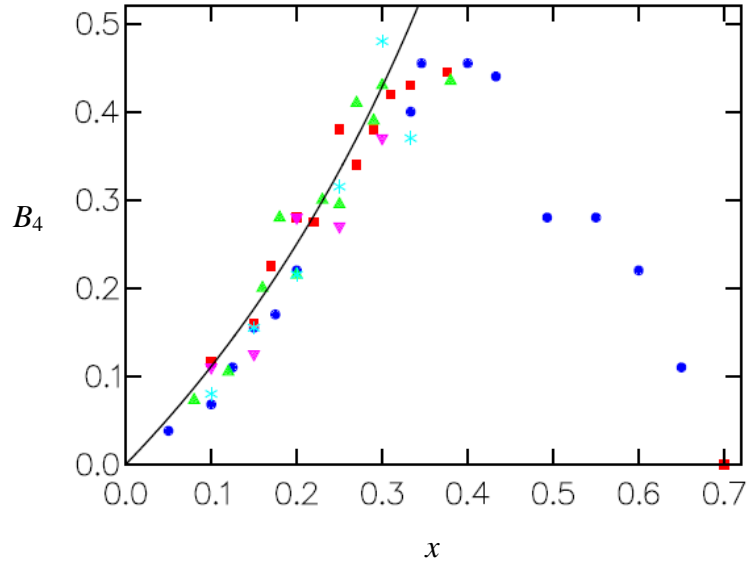


Fig. 1.17 Bray & O’Keefe’s NMR data [57] depicting B_4 for alkali-borate glass systems: $\text{Li}_2\text{O-B}_2\text{O}_3$ (blue filled circles), $\text{Na}_2\text{O-B}_2\text{O}_3$ (red filled squares), $\text{K}_2\text{O-B}_2\text{O}_3$ (green filled triangles), $\text{Rb}_2\text{O-B}_2\text{O}_3$ (magenta inverted filled triangles) and $\text{Cs}_2\text{O-B}_2\text{O}_3$ (cyan asterisks). The black curve (Eq. 1.20) denotes the value of B_4 if the entire added network modifier leads to the formation of BO_4^- tetrahedra with no NBO atoms.

The vacant p_z orbital in B can accept a donor (dative) bond from an oxygen lone-pair (*e.g.* on a NBO atom), so that both B and O achieve the stable octet configuration [57]. This happens when an oxide ion is available as the B_2O_3 glass is modified (by the addition of alkali or alkaline-earth or transition metal-oxides) for such additional bonding. In the simplest binary-borate glasses, the modifier oxide initially converts the trigonal borons (BO_3 units) to tetrahedral borons (BO_4^- units) by the coordination of O^{2-} to two trigonal borons,



BO_4^- tetrahedral units, as shown in Fig. 1.15 (b), are thus readily formed in borate glasses upon addition of modifier oxide. The negative charge on the BO_4^- basic structural unit is delocalized over the whole unit and hence there is an energy penalty if they are immediate neighbours. It was observed [58] from numerous ^{11}B NMR (nuclear magnetic resonance) experiments on various modified-borate glasses that as the mole fraction, x , of

the network-modifying oxide increases, B_4 (mole fraction of BO_4^- units) first increases, then passes through a maximum and finally decreases, the variation with x being similar for all glass systems. These results are shown for alkali-borate glasses in Fig. 1.17. The solid black line in the figure denotes the value of B_4 if whole of the added modifier results in the formation of BO_4^- tetrahedra,

$$B_4 = \frac{x}{1 - x} \quad (1.19)$$

that is, there are no NBO atoms. In the crystalline state, the formation of NBO atoms first occurs at the diborate composition ($x = 0.33$), in α - $Na_2O \cdot 2B_2O_3$ [57]. When the modifier concentration increases further, the concentration of BO_4^- units decreases rapidly. Beyond the composition corresponding to the maximum in Fig. 1.17, the reconversion of BO_4^- units to BO_3 units starts and B_4 drops rapidly. This has consequences on various observed properties of borate glasses as they exhibit extrema at specific values of x . Since such behaviour is not observed in alkali-silicate glasses (properties vary monotonically with the fraction of modifier oxide), which has been the subject of numerous earlier studies, this behaviour was considered anomalous for borate glasses and the effect has been described as the ‘borate anomaly’ [55].

Another special characteristic of borate glasses is the presence of superstructural units in them. Superstructural units (Fig. 1.18) are rigid combinations of the basic borate structural units (BO_3 and BO_4^- units) with no internal degrees of freedom in the form of variable bond or bond torsion angles and are based on three-membered rings of the basic structural units (six-atom rings), which with the exception of the diborate group are rigidly planar, as revealed by crystallography, and by the sharp Raman lines arising from their breathing modes, as observed for the boroxol group (Fig. 1.18 (a)) in the Raman spectrum for vitreous B_2O_3 at 808 cm^{-1} [58]. Krogh-Moe proposed a model which explains the structure of borate glasses by the formation of such superstructural units and

this could aid to resolve the structures of borates in accordance with the borate anomaly [1,58]. The relative concentrations of these superstructures are strong function of the glass composition and network modifying cation [59]. Thus, two special features that characterize borate structures and set them apart from those of other glasses are: (a) the addition of a network modifier to B_2O_3 initially results in the conversion of BO_3 triangular into BO_4^- tetrahedral structural units, rather than in the formation of NBOs, which only occur at higher network-modifier fractions, x and (b) up to the diborate composition ($x = 0.33$), the structures of borates are dominated by superstructural units. It is these two aspects of the structures of borates that are primarily responsible for their unusual behavior in physical properties.

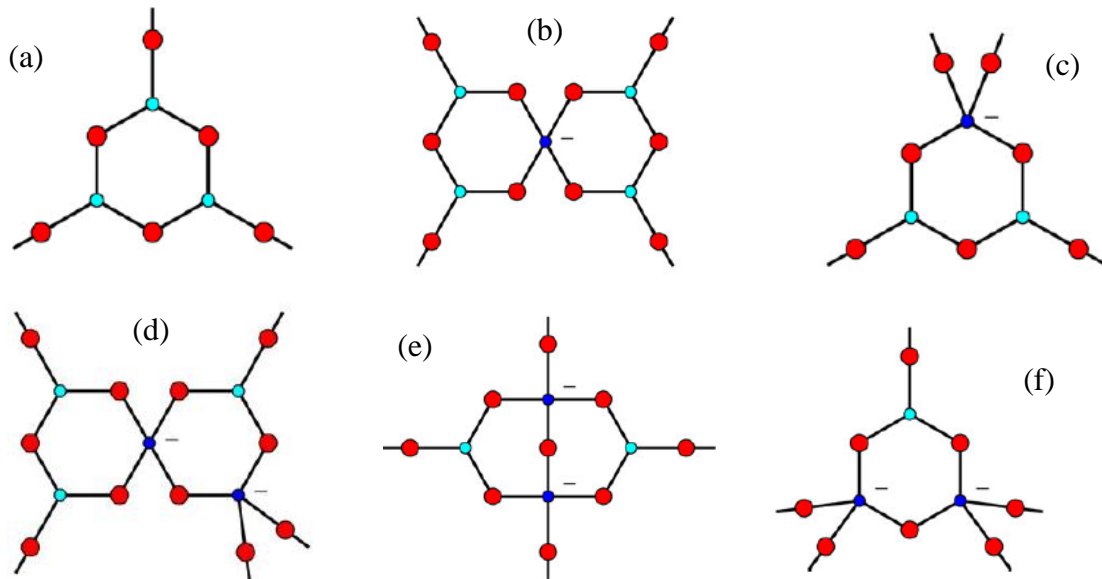


Fig. 1.18 Commonly occurring borate superstructural units: (a) boroxol group, (b) pentaborate group, (c) triborate group, (d) di-pentaborate group, (e) diborate group and (f) di-triborate group.

1.7.3 The structure of modified-tellurite glasses

Unlike good glass-formers such as, SiO_2 and B_2O_3 , pure tellurium oxide (TeO_2) does not get completely vitrified, but binary tellurite glasses formed by combining metal-oxide modifiers such as, monovalent alkali cations M_2O ($M = Li, Na, K, Rb, Cs$) or

divalent metal cations MO ($M = \text{Mg, Sr, Ba, Zn, Pb}$), yield stable network glasses possessing interesting properties [60]. The most intensively studied among these, is their excellent infra-red transmittance and large refractive indices [61]. In addition, these glasses have been shown as having very high third-order non-linear optical susceptibilities in comparison to other industrially used silicate, borate or phosphate glasses [62]. Owing to these properties, tellurite glasses are being considered as promising materials for optical amplifiers and non-linear optical devices. In order to gain insights to the origin of these properties in TeO_2 -based glasses, much attention has been focused to understand their structure [63]. The short-range structure [64,65] of these glasses has been widely studied using x-ray absorption, Raman and NMR spectroscopies.

The structure of tellurite glasses is generally suggested as a network of TeO_4 , TeO_{3+1} and TeO_3 polyhedra sharing corners. Numerous reports describe the structure of tellurite glasses as being similar to the crystalline phase of paratellurite ($\alpha\text{-TeO}_2$), which is a three-dimensional network of TeO_4 trigonal bipyramids (tbp) [63]. Since the short-range atomic order of both crystalline and glassy phases obey the same principles of atomic bonding, the crystalline lattice is regarded as the parent compound of the glass [64]. Each TeO_4 unit has two types of Te-O bonds: two shorter equatorial Te-O_{eq} bonds and two longer axial Te-O_{ax} bonds oriented at larger angle in a plane perpendicular to the $\text{O}_{\text{eq}}\text{-Te-O}_{\text{eq}}$ plane, with the lone electron pair at the tellurium atom located in the equatorial plane (see Fig. 1.19). The TeO_4 tbp connect with each other forming $\text{Te}_{\text{eq}}\text{O}_{\text{ax}}\text{-Te}$ linkages. Using Raman spectroscopic investigations [63], it has been shown that the introduction of a network modifier (M) elongates one of the Te-O_{ax} bonds and results in the gradual formation of the deformed TeO_{3+1} units and subsequently with the addition of more metal-oxide, the weakly bonded oxygen in TeO_{3+1} gets disconnected to form TeO_3 trigonal pyramids (tp) with terminal Te=O bond [63], as depicted in Figs. 1.19 and 1.20.

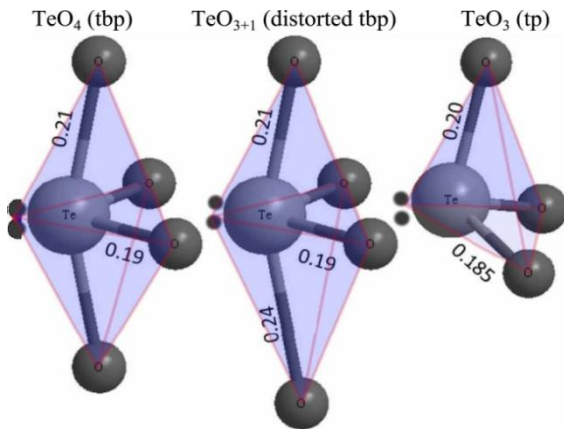


Fig. 1.19 Ball and stick representation of the structural units present in tellurite glass. Left: Trigonal bipyramidal TeO_4 . Center: Distorted trigonal bipyramidal TeO_{3+1} . Right: Trigonal pyramidal TeO_3 . Dots represent lone pair electrons. Bond lengths (in nm) are taken from [66]. (Fig. from Ref. [67]).

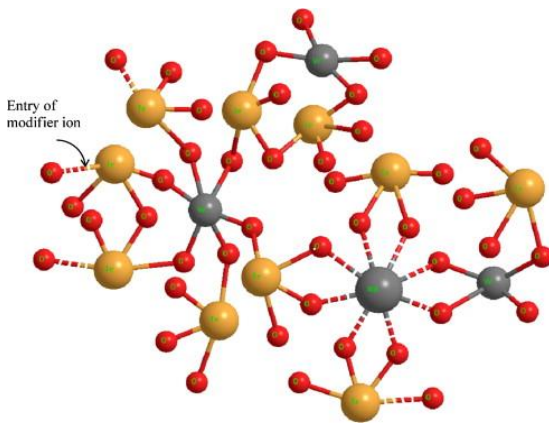


Fig. 1.20 Network structure of a modified tellurite glass. The entry of a modifier cation (grey circles) induces distortion in the tbp units and creates NBOs in the structure.

In both the tbp and tp structures, Te bonds to oxygen through its sp^3d hybridized orbitals. In tbp, it involves hybridisation of $5s$, $5p$ and d_{z^2} orbitals. As shown in Fig. 1.19, the lone pair on Te is accommodated in an equatorial orbital in tbp and the other four orbitals are used in bonding to the bridging oxygens. On the other hand, in the formation of tp, there is first the formation of sp^3 hybridised orbitals, of which, one is used to accommodate the lone pair, two for bonding to bridging oxygens, and the other one is bonded to an oxygen whose p -orbital overlaps with one of the d -orbitals of Te, forming a π -bond. This oxygen is therefore double bonded to Te (terminal oxygen). It has been reported that modification of TeO_2 glass induces a preference for tp units, although both tbp and tp units are present in the structure [63]. While tp units can only form chains, tbp units can give rise to 3-dimensional network structures. Thus, the fraction of tp and tbp units can make a big difference for the final glass structure.

The lone electron pair in Te complicates the short-range atomic arrangement in TeO_2 , making the first coordination sphere around Te highly asymmetric and variable. The excellent optical properties of tellurite glasses have their origin in the polarizability of the tellurite units that can be controlled by glass modification. The primary role of a network modifier is to cause negatively charged NBOs to be formed at the expense of bridging oxygen. Therefore, the three-dimensional network of the glass former, TeO_2 , is depolymerized by modifier addition [61] and creation of variable coordinated units determine the special properties of tellurite glasses.

1.7.4 The structure of modified-phosphate glasses

Phosphate (P_2O_5) forms both single and multi-component glasses. The basic building block in phosphate glass is a 3-connected and 4-coordinated PO_4 tetrahedral unit. One of the coordination arises from $\text{P}=\text{O}$, which has distinctly shorter bond distance compared to the other three bonds. Thus, the structure of phosphate glasses can be described as a network of phosphate tetrahedra that are linked through covalent bonding of corner shared oxygen atoms, referred to as bridging oxygen (BO) atoms. Oxygen atoms that do not link two phosphate tetrahedra are called non-bridging; the ratio of bridging to non-bridging oxygens (NBO) depends on the glass composition. Phosphate glasses typically consist of long polymer-like phosphate chains. The linked phosphate tetrahedra have one, two, three, or four non-bridging oxygens. These units can be classified using the Q^n terminology, where the superscript n represents the number of bridging oxygen atoms per tetrahedron (Fig. 1.21). For example, a Q^2 tetrahedron links to two others through bridging oxygens in a phosphate chain anion, with Q^1 tetrahedra terminating the ends of the chains. The role of network modifying oxides in the glass is to break up or depolymerize the phosphate chains as the $[\text{O}]/[\text{P}]$ ratio increases [68]. The phosphate chain and ring anions are linked by bonds between various modifying metal

cations and the non-bridging oxygen; these bonds are more ionic in nature. Therefore, with increasing ratio of modifier oxide to P_2O_5 glass, the structural species gradually change from Q^3 to Q^0 (ultra-phosphate \rightarrow meta-phosphate \rightarrow pyro-phosphate \rightarrow ortho-phosphate) in the modified-phosphate glasses as shown in Fig. 1.21.

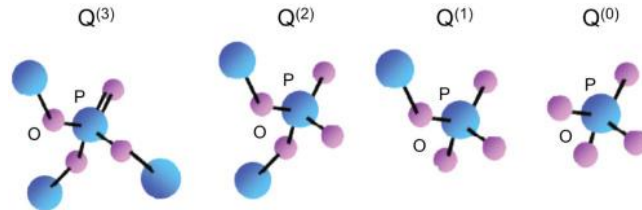


Fig. 1.21 Phosphate tetrahedral units: oxygen atoms (pink) connected to phosphorus atoms (blue); ultra-phosphate Q^3 (cross-linking) units; meta-phosphate Q^2 (middle) units; pyro-phosphate Q^1 (terminal or end) units; ortho-phosphate Q^0 (isolated) units. (Fig. from Ref. [68]).

In the three above glass systems (borate, tellurite and phosphate), the modification of the primary network in the glass results in the formation of chemically different types of oxygens in the network. For example, in phosphates, it can be a bridging oxygen (BO) or a non-bridging oxygen (NBO) or an oxygen double bonded to P, often called the terminal oxygen. In borates, it could be a BO attached to trigonal boron or a BO attached to tetrahedral B or an NBO associated only to trigonal borons. These structurally and chemically different oxygens can be identified and quantified by using x-ray photoelectron spectroscopy [55].

1.7.5 PbO as a modifier

The behaviour of lead (Pb^{2+}) as a modifier cation is also unique in oxide glasses. It plays a dual role. In some concentration regions it enters into the network structure when it is referred as a network former. In other concentration regions it stays as Pb^{2+} allowing the O^{2-} ion of PbO to break the oxygen bridges, when it is described as a modifier. The composition at which the role of lead changes from that of a network

former to a network modifier is associated with the changes in the trends of elastic properties [55]. The composition-dependent role of lead is dependent on the availability of oxygen coordination that it can get from the host.

1.8 The scope of the present thesis

The performance of every glass product is governed by the underlying properties of the glass at the atomic scale. Many aspects of the microscopic behavior of glass-forming systems, both in the supercooled and in the glassy state, remain poorly understood despite the efforts done in the last decades [9]. The properties of a glass are controlled by the microscopic structure and dynamics, which in turn depends on the composition of the glass. Thus, investigating the inter-relationship between composition, network structure and dynamics is important as it enables one to prepare glass compositions with desired properties.

The aim of the present thesis is to investigate the dynamics and structure of strong network glasses and to monitor structural changes at short-range, medium-range and bulk scale by using inelastic light scattering techniques of Raman and Brillouin spectroscopy. By ‘strong network glasses’ we mean ‘strong glasses’ as a counterpart of ‘fragile glasses’. As discussed above, covalently bonded oxide glass systems, such as SiO_2 , B_2O_3 , P_2O_5 , form network glasses which exhibits ‘strong’ characteristics according to Angell’s classification. In general, modification with alkali or alkaline earth oxides enhances the fragility. In this thesis, three systems of network glasses have been chosen based on the constituent structural units: borate, tellurite and phosphate glasses. The basis for the choice of these systems is the unique response of these glasses to structural modification. The corresponding unmodified glass systems have coordination number of three, mixture of three and four, and four, respectively for the borate, tellurite and phosphate glasses, as discussed in the previous sections. In this thesis, iron and lead have been used as modifier

cations which replace some of the parent network cation and form new linkages that alter the glass properties. Borate glasses exhibit a unique structure where some fraction of the initial three-coordinated units convert to four-coordinated borons with increasing modifier amount up to a certain concentration of doping. Tellurite glasses are formed of four-coordinated units which gradually reduce to higher fraction of three-coordinated units with increased modification. Phosphates form four-coordinated polyhedral networks which do not change coordination but exhibit changes in connectivity with modification. This thesis explores the implications of glass modification on the network structure by varying the concentration of modifier and focuses on its consequences on glass structure and properties. Using temperature as a thermodynamic parameter, the dynamics of the glass-forming systems are also studied across the glass transition.

Raman spectroscopy is a sensitive probe of local order, structure and coordination through an analysis of mode-wavenumbers, line-widths and relative intensities of the spectral features [69]. Acoustic modes are captured using Brillouin spectroscopy which gauges elastic deformations that are sensitive to the connectivity of structural elements. A combined use of these two techniques have allowed us to capture vibrations that span different frequency regimes and probe different length-scales for understanding the structure and dynamics in these glasses across and around T_g .

This thesis is organized into six chapters. **Chapter 1** provides a brief introduction to the phenomenology of glasses and introduces most of the physical concepts used in the thesis. It highlights the different vibrational modes in glasses, the significance of the medium-range order and the Boson peak. It also provides a detailed description of network glasses with focus on borate, tellurite and phosphate glasses. **Chapter 2** presents the details of glass synthesis procedures and experimental techniques used for investigation of their structure and dynamics. **Chapter 3** presents the effect of

modification by lead oxide on the medium-range order in lead-borate [$x\text{PbO}:(1-x)\text{B}_2\text{O}_3$] glasses from a detailed composition-dependent study of the Boson peak using low-frequency Raman scattering. A comparison of the length-scales of medium-range order obtained from the Boson peak and FSDP (measured using synchrotron x-ray source) helped to understand the origin of these features. Effect of glass modification on fragility, determined from heating rate-dependent differential scanning calorimetry, has also been studied in this chapter. Moreover, using high-temperature Brillouin scattering on the lead-borate glasses from 300-1150 K, a drastic decrease of network rigidity above T_g was observed. **Chapter 4** explores the effect of structural modification at different length-scales in lead-tellurite [$x\text{PbO}:(1-x)\text{TeO}_2$] glasses using Raman and Brillouin scattering. Temperature dependence of elastic response above T_g has been monitored to infer relative change of fragility appearing as a consequence of glass modification. Temperature-dependent Raman scattering has been carried out to monitor the short-range structural changes both in the glass and supercooled states. This chapter also reports crystallization kinetics on a modified-tellurite glass where microstructural evolution was studied. **Chapter 5** presents Raman spectroscopic studies on iron-phosphate glass [$40\text{Fe}_2\text{O}_3:60\text{P}_2\text{O}_5$] where changes induced in the local structure was studied when it is taken from glass to supercooled liquid and across T_g . The effect of temperature on VDOS was studied to understand structural relaxation in glass and supercooled liquid states. **Chapter 6** provides a summary of the results obtained, highlights of the inferences drawn and the conclusions from the various studies. It also discusses possible directions for the future studies. The important findings from these studies are as follows:

- Dynamic properties such as Boson peak and fragility in $x\text{PbO}:(1-x)\text{B}_2\text{O}_3$ glasses behave similar to short-range structural properties except an anomalous dip at $x = 0.3$. This anomalous behaviour is found to be connected to the common origin of these

properties in the intermediate-range ordered structures and reflects the critical role of Pb^{2+} in tuning the intermediate-range structure of the vitreous network [70].

- Longitudinal acoustic mode frequency in lead-tellurite glasses shows a scaling behaviour in the glassy state. PbO was found to affect the tellurite network by stiffening the molecular units at a microscopic scale, while reducing the network rigidity on a macroscopic length-scale, upon increasing the temperature [71].
- 0.3PbO:0.7TeO₂ glass is found to crystallize into PbTeO₃ phase while heating, while anomalous crystallization into Pb₂Te₃O₈ phase is observed when the devitrified melt was cooled. This interesting observation is explained using amorphous phase separation inherent to the tellurite glass system owing to the presence of unique asymmetric structural units in the melts [72].
- Raman mode-wavenumbers and line-widths of iron-phosphate glass were found to exhibit anomalous behaviour and discontinuous changes were observed across T_g . These anomalies are attributed to structural relaxations in the glass [73].

This chapter discusses the various experimental techniques employed in this thesis for the synthesis of glass samples and study of their structure, dynamics and thermal properties. Bulk glass preparation by mixing and melting the powder oxides is discussed. A detailed theoretical background and instrumentation describing the characterization technique, the measurement schemes and methods of analysis for the chosen techniques are presented. Vibrational spectroscopy was carried out using inelastic light scattering techniques (Raman and Brillouin scattering). Vibrational dynamics of the synthesized network glasses was investigated and the structural units that form the vitreous network were identified using Raman spectroscopy. Elastic properties of the glasses were determined using Brillouin spectroscopy. X-ray diffraction (XRD) was used to establish the amorphous phase of the samples. Glass transition and heat capacity were measured using differential scanning calorimetry (DSC). Refractive indices of some of the glasses were determined using ellipsometry.

2.1 Glass Synthesis

It was once thought that relatively few materials could be prepared as amorphous solids, and such materials (mostly, oxide glasses and organic polymers) were called glass-formers. It is now known that the amorphous solid state is a universal property of condensed matter [10]. Glass formation is understood as a matter of bypassing crystallization. Therefore, nearly all materials can be prepared as glass, if cooled fast enough [10]. Besides the conventional method of melt-quenching, glasses and amorphous solids are also prepared using melt-spinning, splat-quenching or by vapour condensation techniques [1]. In this thesis work, synthesis of three different glass systems, (a) lead-

borate, (b) lead-tellurite and (c) iron-phosphate glasses were prepared using melt-quenching and splat-quenching techniques. The detailed synthesis procedures are described in the following sections.

2.1.1 Melt-quenching technique

The melt-quench method is the earliest discovered technique for the preparation of glasses. In this process, the inorganic raw materials are accurately weighed according to composition, mixed and homogenized thoroughly before being put into high-grade alumina or platinum crucible. Then the mixture is melted at a temperature depending upon the melting points of its constituents. Thereafter, the melt is rapidly cooled by pouring on copper or stainless steel plates/ moulds. This is known as melt-quenching.

The rate of cooling required for the formation of glassy phase is different for different materials. Good glass formers like silica (SiO_2) and borate (B_2O_3) glass form glassy phase even under very slow cooling rates ($\ll 1$ K/s), whereas, preparation of metallic glasses require cooling rates $\sim 10^5$ K/s [74]. Typical cooling rates attainable using the melt-quench method are $10\text{-}10^3$ K/s. This method is industrially used for obtaining large-sized materials compared to single crystals or polycrystalline ceramics. Various phosphates, borates and silicates are prepared by the melt-quench method where the sample is taken to its melting point (T_m) and quenched, and this is sufficient to obtain a glass. For the present thesis, lead-borate and iron-phosphate glasses were prepared by melt-quenching.

Lead-borate [$x\text{PbO}:(1-x)\text{B}_2\text{O}_3$] glasses were prepared for $x = 0.2, 0.3, 0.4, 0.5, 0.6, 0.7, 0.8$ using lead oxide (PbO) and boric acid (H_3BO_3) as starting materials. A 10 g batch of well-mixed and homogenized materials were heated in alumina crucibles at 523 K for 24 h and further heated at 723 K for another 24 h. Finally, the mixture was melted at

1223 K for 1 h in a furnace. The melts were then poured on a stainless steel quenching plate kept at 300 K. The glasses thus obtained, were transparent colourless to pale-yellow (on increasing PbO). The glass samples were powdered for XRD measurements, and pellets were polished to optical quality for light scattering measurements.

Synthesis of iron-phosphate [40Fe₂O₃:60P₂O₅] glass was carried out using iron oxide (Fe₂O₃) and ammonium dihydrogen phosphate (NH₄H₂PO₄) [75]. The mixture was homogenized by grinding thoroughly using mortar and pestle. This batch mixture was calcined in a platinum crucible at 873 K for 1¹/₂ h in an electric furnace for facilitating decomposition of NH₄H₂PO₄. The temperature was then increased to 1423 K where the melt was maintained in air for homogenization. The melt was then air-quenched on a stainless steel plate and glass was formed from rapid solidification of the melt. The glass pellets were polished for Raman scattering measurements.

2.1.2 Splat-quenching technique

Splat-quenching is very much similar to melt-quenching. The principle remains the same as the melt is brought into contact with a cold metallic substrate and the heat is extracted by conduction. However, in order to achieve a sufficient cooling rate, the thickness of the sample has to be minimized. Splat-quenching typically involves pouring the melt between two cooled stainless steel/ copper rollers that are circulated with water to transfer the heat away from the melt, causing it to solidify instantaneously [76]. This technique enables achieving quenching rates $\sim 10^3$ - 10^5 K/s. In this thesis, splat-quenching was employed to synthesize lead-tellurite glasses, since tellurites have low glass-forming tendency and require higher quenching rates compared to phosphates and borates, in order to form homogeneous glasses. The rapid quenching was achieved here by pouring the melt in between two stainless steel plates.

Lead-tellurite [$x\text{PbO}:(1-x)\text{TeO}_2$] glasses were prepared for $x = 0.1, 0.2, 0.3$ using lead oxide (PbO) and tellurium oxide (TeO_2) as starting materials. A 5 g batch of well-homogenized powders were ground and melted in alumina crucibles at 1008 K for 1 h and at 1073 K for 10 min in an electric furnace. The melts were then poured on to a stainless steel plate at ambient temperature, and immediately pressed on by another plate. The glasses obtained were homogeneous and pale yellow in color.

The lead-borate, lead-tellurite and iron-phosphate glasses synthesized using the above methods were characterized for their structural, dynamical and thermal properties using the following characterization techniques. In the sections to follow, we describe in detail, the theory and instrumentation of inelastic light scattering and its relevance to the study of glass structure at different length-scales. We also describe XRD, DSC and ellipsometry techniques which have been used to study these glasses.

2.2 Characterization techniques

2.2.1 Inelastic light scattering in solids

When electromagnetic waves propagate through a medium, most of the radiation is either transmitted or absorbed. A very small fraction of light is scattered by inhomogeneities in the medium. These inhomogeneities may be static or dynamic. Defects in crystals act as static scatterers and scatter light elastically (Rayleigh scattering). However, a small fraction of the photons (approximately, 1 in 10^7) scatter at optical frequencies different from that of the incident light. This is inelastic light scattering, produced by time-dependent fluctuations associated with acoustic waves, optical phonons or other elementary excitations in the solid. Optical processes such as reflection and absorption, are usually much stronger than scattering since they involve the lowest order of interactions between radiation and excitations in the medium. The light

scattering processes are weak since they involve either higher-order optical interactions or other processes such as electron-phonon interactions.

Inelastic light scattering by sound waves (acoustic waves) of long wavelength in a medium was proposed theoretically by Brillouin (1922) and independently by Mandelstam (1926) [77]. These theories were refined quantum mechanically by Smekal (1923) who developed the theory of light scattering by two discrete levels, and subsequently by Kramers and Heisenberg (1925) [78]. The breakthrough in light scattering was made by Raman (1928), who along with Krishnan, reported the first experimental evidence of inelastic light scattering by molecular vibrations in solids and liquids [79]. Landsberg and Mandelstam independently observed the effect in quartz in the same year [78].

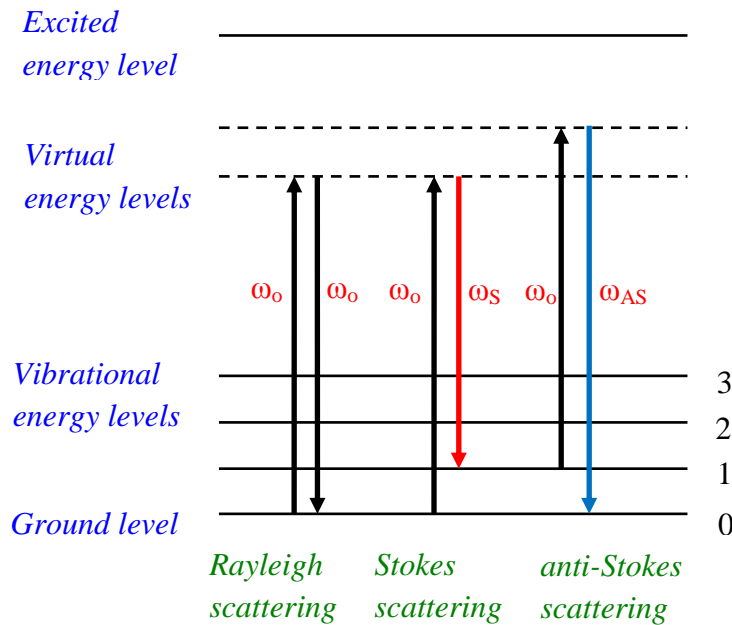


Fig. 2.1 Energy level diagram of Rayleigh and Raman (or, Brillouin) scattering.

The shift in frequency of the inelastically scattered radiation provides information on the interaction process of the incident light with the material and infers the structure of the material. The inelastic scattered light has two components: (a) Brillouin scattering:

due to long wavelength acoustic phonons and (b) Raman scattering: due to internal vibrations of molecules or optical phonons (short wavelength vibrations) in crystals. Basically, Raman and Brillouin scattering are governed by the same effect: the scattering of light by phonons; either acoustic or optical. But the equipment required to detect acoustic phonons using Brillouin spectroscopy is different, since one has to approach a few GHz to the incident light in order to detect the very long wavelength (low frequency shift) acoustic phonons.

The inelastic light scattering process can be understood in a simplified manner from an energy level diagram (see Fig. 2.1). A laser beam with frequency (ω_o), typically in the visible region is incident on the sample. The light excites the atoms/ molecules in the sample to a virtual state and then decays back to a lower energy state. When the decay is to the initial state, it is called as Rayleigh scattering, and the emitted photons are of the same frequency ω_o . When the decay is to a different state, it is either called Stokes scattering (when the final energy state is higher than the initial state) with emitted photon of energy ω_s , or anti-Stokes scattering (when the final energy state is lower than the initial state) with emitted photon of energy ω_{AS} . The light emitted in the de-excitation is collected and studied. The shift in frequency ($\omega_o - \omega_s$ or $\omega_{AS} - \omega_o$) is measured and is equal to the vibrational frequency (ω_v) of the corresponding phonons. Thus, both Brillouin and Raman spectroscopy are extended to the generation (Stokes) or annihilation (anti-Stokes) of any elementary excitation (phonons, magnons etc.) in the solid state. The ground state population is much higher compared to that of the excited states, owing to the Maxwell-Boltzmann distribution. This makes the Stokes lines stronger than the anti-Stokes lines. Hence, measuring the Stokes side of the Raman spectrum is more popular since both the lines provide same information of exactly same difference in frequency ω_v .

The light scattering process is governed by the energy conservation equations,

$$\hbar\omega_V = \hbar\omega_0 - \hbar\omega_S \text{ (Stokes process)} \quad (2.20)$$

or, $\hbar\omega_V = \hbar\omega_{AS} - \hbar\omega_0$ (Anti – Stokes process)
and momentum conservation laws,

$$\vec{q} = \vec{k}_0 - \vec{k}_S \text{ (Stokes process)} \quad (2.21)$$

$$\text{or, } \vec{q} = \vec{k}_S - \vec{k}_0 \text{ (Anti – Stokes process)}$$

where, k_0 and k_S are the wave vectors of the incident and scattered photon and q is the phonon wave vector. q has a dependence on the scattering angle θ as,

$$q = 2k_0 \sin \frac{\theta}{2}. \quad (2.22)$$

The inelastic scattering of light by matter can be described by the classical and quantum mechanical theory. From the classical theory point of view, an incoming photon is scattered by the lattice. This process induces a phonon in the solid and reduces the energy of the photon by the energy lost in the scattering event. On the other hand, the approach carried in the quantum theory involves the photon-phonon interaction mediated by an electron.

2.2.1.1 Classical theory

Electromagnetic radiation E can induce dipole moment, $\mu = \alpha E$, in a material, where α is the polarizability. Selection rule of the Raman effect is a change of this polarizability of a bond in the lattice upon interaction with light. The classical method involves individual atomic dipole moments which combine to form a macroscopic polarization vector (\vec{P}). The material's response to an electromagnetic field is expressed through the dielectric susceptibility χ . Therefore, the classical theory describes inelastic light scattering in terms of the macroscopic polarization induced in a polarizable solid by the electric field \vec{E} of the electromagnetic radiation,

$$\vec{P} = \bar{\chi}\vec{E} \quad (2.23)$$

where, $\bar{\chi}$ is the dielectric susceptibility, which is a second rank tensor. For any one normal coordinate of the solid (*i. e.*, for one dimension), it can be written as,

$$P = \chi E = \chi E_0 \cos \omega_0 t \quad (2.24)$$

where, E_0 is the vibrational amplitude and ω_0 is the frequency of the incident laser. It can be observed from Eq. (2.5) that the induced polarization oscillates with the frequency of the incident field. If the vibration is simple harmonic with frequency ω_V , the nuclear displacement r is written as,

$$r = r_0 \cos \omega_V t \quad (2.25)$$

where r is called the normal coordinate of the vibration and r_0 is the vibrational amplitude. The atomic vibrations will modify the susceptibility, and therefore, expanding χ as a Taylor series in terms of normal coordinates and assuming small displacement (since the amplitudes of atomic vibrations are small compared to the lattice constants), χ becomes a linear function of r and is expressed as,

$$\chi = \chi_0 + \left(\frac{\partial\chi}{\partial r}\right)_0 r \quad (2.26)$$

where χ_0 is the susceptibility at equilibrium position and $\left(\frac{\partial\chi}{\partial r}\right)_0$ is the rate of change of χ with respect to the change in r , evaluated at the equilibrium position, represents an oscillating susceptibility. Combining Eq. (2.5), (2.6) and (2.7), the polarization is obtained as,

$$P = \chi_0 E_0 \cos \omega_0 t + \left(\frac{\partial\chi}{\partial r}\right)_0 E_0 r_0 \cos \omega_0 t \cos \omega_V t$$

or,
$$P = \chi_0 E_0 \cos \omega_0 t + \frac{1}{2} \left(\frac{\partial\chi}{\partial r}\right)_0 E_0 r_0 [\cos(\omega_0 + \omega_V)t + \cos(\omega_0 - \omega_V)t] \quad (2.27)$$

According to the classical theory, the first term represents a static polarization, oscillating with the incident field and radiating light of frequency ω_0 (Rayleigh scattering), while the

second term represents the polarization induced by the lattice displacement (phonon), which contains both positively shifted (anti-Stokes) and negatively shifted (Stokes) components with respect to the incident light frequency. Furthermore, for the vibration to be Raman-active, $\left(\frac{\partial\chi}{\partial r}\right)_0$ should be non-zero, *i.e.*, the rate of change of susceptibility with the vibration should be non-zero.

The above derivation is a simplified way to understand the Raman effect in a polarizable bond. The important converging point of light scattering experiments and theory is the scattering cross-section. The classical theory [80], as described above, states that the scattered light is produced by a polarization determined by a second order susceptibility χ , an excitation amplitude X and the incident field E ,

$$P^i = \epsilon_0 \chi^{ij}(\omega_0, -\omega) X^*(\vec{q}, \omega) E_0^j \quad (2.28)$$

In a solid, light penetrates only a certain amount from the surface depending on the wavelength and the properties of the material, so that it makes no sense to work with the scattering cross section since not all volume is emitting a Raman signal. Instead, a spectral differential cross section, which has dimensions of area divided by frequency, is defined as the rate at which energy is removed from the incident radiation because of its scattering in volume v into a solid angle $d\Omega$ with a scattered frequency ω_S and $\omega_S + d\omega_S$. The spectral differential cross-section for scattering by an excitation is related to the power spectrum of quasiparticle excitations in the medium by,

$$\frac{d^2\sigma}{d\Omega d\omega_S} = \frac{\omega_0 \omega_S^3}{(4\pi\epsilon_0)^2} \frac{vV}{c^4} \frac{\eta_S}{\eta_0} |\epsilon_0 \hat{n}_S^i \hat{n}_0^j \chi^{ij}(\omega_0, -\omega)|^2 \langle X(\vec{q}) X^*(\vec{q}) \rangle_\omega \quad (2.29)$$

Here v is the fractional volume of that part of the sample which contributes to the scattered light, V is the total volume of the sample, $\omega_0 \omega_S^3$ is the frequency factor, η_S/η_0 is the refractive index ratio that arises to treat the intensities of the light beams inside the

scattering medium, $\hat{n}_S^i(\hat{n}_0^j)$ is the unit vector parallel to the scattered (incident) field direction. $\chi^{ij}(\omega_0, -\omega)$ is the second order susceptibility derivative, $\left(\frac{\partial\chi}{\partial r}\right)_0$, which is related to an appropriate macroscopic property of the scattering medium and is a function of the incident frequency and the frequency of the quasiparticle excitation. The excitation of the medium responsible for inelastic light scattering gives rise to a power spectrum of fluctuations $\langle X(\vec{q})X^*(\vec{q}) \rangle_\omega$, which depends on the relevant fluctuations of the scattering excitations. Assuming the medium is at a finite temperature, there are thermally excited fluctuations present. This $X(\vec{q})$ is the Fourier amplitude of $X(\vec{r})$ which can be density fluctuation caused by atomic vibrational displacement or normal mode coordinate. If there are free carriers present, there can be fluctuations in their charge density or spin density. The power spectrum plays a central role in the classical theory of light scattering. It can be calculated by the fluctuation-dissipation theorem [80]. This theorem relates the power spectrum of amplitude fluctuations to the imaginary (dissipative) part of the linear response function,

$$\langle X(\vec{q})X^*(\vec{q}) \rangle_\omega = \frac{\hbar}{\pi} [n(\omega) + 1] \text{Im} T(\vec{q}, \omega) \quad (2.30)$$

where $n(\omega)$ is the Bose-Einstein factor and $T(\vec{q}, \omega)$ is the linear response function. A classical calculation of linear response function is demonstrated by considering X to be a molecular vibrational coordinate, represented by a damped harmonic oscillator equation,

$$\ddot{r}_\sigma + \Gamma_\sigma \dot{r}_\sigma + \omega_\sigma^2 r_\sigma = -Nf \exp(-i\omega t) \quad (2.31)$$

where for the σ mode of vibration, r_σ measures the vibrational displacement, ω_σ is its natural frequency, Γ_σ is the damping constant and f is the amplitude of force. The interactions between N identical molecules of the medium are assumed weak and the linear response function for such an equation is,

$$T(\vec{q}, \omega) = \frac{1}{N(\omega_\sigma^2 - \omega^2 - i\omega\Gamma_\sigma)} \quad (2.32)$$

and,

$$Im T(\vec{q}, \omega) = \frac{\omega \Gamma_\sigma}{N((\omega_\sigma^2 - \omega^2)^2 + \omega^2 \Gamma_\sigma^2)} = \frac{\pi g_\sigma(\omega)}{2N\omega_\sigma} \quad (2.33)$$

where,

$$g_\sigma(\omega) = \frac{\Gamma_\sigma/2\pi}{(\omega_\sigma - \omega)^2 + (\Gamma_\sigma/2)^2} \quad (2.34)$$

which has a Lorentzian frequency dependence and a full width Γ_σ at half its peak maximum. Thus, the power spectrum for the Stokes line is given by,

$$\langle X(\vec{q})X^*(\vec{q}) \rangle_\omega = \langle r_\sigma(\vec{q})r_\sigma^*(\vec{q}) \rangle_\omega = \frac{\hbar}{2N\omega_\sigma} [n(\omega_\sigma) + 1]g_\sigma(\omega) \quad (2.35)$$

The symmetry properties of the second order susceptibility for the particular excitation determine the symmetry properties of the scattering cross section. The symmetry of the vibrational modes are obtained from site symmetries of atoms in the unit cell. Group theory ascertains that a particular vibrational mode is Raman active, only if its symmetry is same as that of χ^{ij} . Using these selection rules, the symmetry of the susceptibility tensor and hence the symmetry of the underlying phonon can be identified by Raman experiments with different scattering geometries.

The classical theory provides correct frequency dependence for Rayleigh and vibrational Raman scattering. It depicts how Stokes and anti-Stokes lines arise, but, it does not throw light as to why anti-Stokes lines are weaker than Stokes, or what govern the Raman line intensities. A quantum mechanical treatment is required for this.

2.2.1.2 Quantum theory

The quantum theory of light scattering involves the excitation of an electron by the incoming photon and the scattering event includes photon-electron and electron-lattice interaction. This method treats the atom quantum mechanically. The classical harmonic oscillator variables are replaced by the atomic energy levels and wave functions, and the interaction Hamiltonian of the molecule or solid with light, which

enters in the expression for the scattering cross-section, is expressed in terms of the matrix elements of the susceptibility operator.

In accordance with the above assumption, in solids, a virtual electron-hole pair is created which can interact with the lattice. The quantum mechanical treatment of inelastic light scattering process is based on time-dependent perturbation theory. For light scattering from phonons, we need to consider two types of perturbation terms in the Hamiltonian in order to calculate the transition electric susceptibility. The contribution of electrons to the transition electric susceptibility involves a two-photon process in which the scattering medium, through the electron-radiation interactions, annihilates the incident photon and creates a scattered photon. This occurs with creation (Stokes process) or annihilation (anti-Stokes process) of a crystal excitation. The scattering process can be viewed as the mixing of three waves, which occurs in three steps of photon or phonon induced electronic transitions as described with the aid of a Feynman diagram (Fig. 2.2) in the following sequence:

1. The first electronic transition to an intermediate electron-hole pair state takes place with the annihilation of the incident photon ω_0 . This state is referred to as the intermediate state $|a\rangle$. The process is mediated by the Hamiltonian which describes the coupling of electron to the radiation, H_{e-r} .
2. The second electronic transition to another electron-hole pair state occurs with the creation of a phonon. Therefore, the electronic intermediate state $|a\rangle$ is scattered by the lattice. A phonon is created and the intermediate state is converted into another intermediate state $|b\rangle$. This is an electron-lattice interaction, hence related to the H_{e-ion} .

3. The third transition to the electronic ground state takes place with the creation of the scattered photon. Thus, the electron-hole pair of state $|b\rangle$ decays radiatively as a photon ω_S is emitted via H_{e-r} .

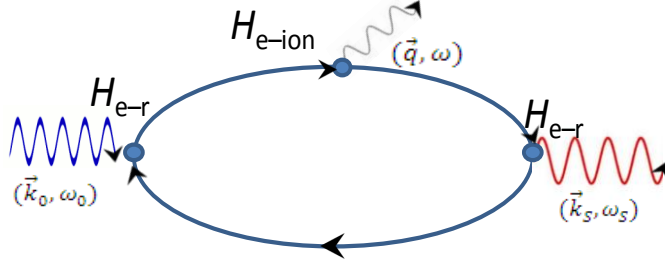


Fig. 2.2 Feynman diagram of the Raman process.

This sequence of the light scattering process depicts the Stokes scattering (Fig. 2.2). Energy is conserved only in the total process, where as wave vector is conserved in each step. Owing to the time reversal invariance, the Feynman diagram can also be read from the right to the left. This order of time represents the anti-Stokes process. A phonon is annihilated and its energy is added to the energy of the incoming photon.

Each vertex in the Feynman diagram represents an interaction. The first-order Raman process is described by a third-order time-dependent perturbation theory. Using Fermi's golden rule we can derive the transition probability,

$$P \approx \frac{2\pi}{\hbar} \left| \sum_{a,b} \frac{\langle s | H_{e-r} | b \rangle \langle b | H_{e-ion} | a \rangle \langle a | H_{e-r} | 0 \rangle}{(\hbar\omega_0 - E_a + i\Gamma_a)(\hbar\omega_S - E_b + i\Gamma_b)} \right|^2 \quad (2.36)$$

Here, E_a and E_b are the intermediate electronic energy levels in the process, Γ_a and Γ_b are their corresponding widths. The states $|a\rangle$ and $|b\rangle$ can be real or virtual states. The functional form of H_{e-ion} contains the Raman selection rules. These rules are given by group theory and contain the tensor properties of H_{e-ion} , which follows the symmetry of the crystal lattice. Selection rules for inelastic light scattering in glasses is discussed below.

2.2.1.3 Selection rules and Raman scattering in glass: Reduction schemes

In a bulk crystal, the phonon eigen state is a plane wave and the wave vector selection rule for first-order Raman scattering requires $q \approx 0$, where q is the phonon wave vector. This is known as the Raman selection rule for crystals. From Eq. 2.3, the maximum wave vector q transferred to a phonon takes place for the back-scattering geometry ($\theta = 180^\circ$) where $q = 2k_0$. This is the maximum value of q that can be accessed in a light scattering experiment. An important consequence of this momentum conservation rule is that using visible electromagnetic radiation, $q \sim 10^5 \text{ cm}^{-1}$ can be excited. This is very small compared to the Brillouin zone boundary in a typical crystal ($\sim 10^8 \text{ cm}^{-1}$). Therefore, inelastic light scattering using visible radiation can probe phonons with $q \approx 0$, *i.e.*, only near the centre of the Brillouin zone. This argument is valid for first-order Raman scattering.

Depending on its intrinsic structure, every crystal has different number of normal modes of vibration (phonons). Their number, type and symmetry depend on the number of atoms in the primitive cell of the crystal and the symmetry of the lattice. As discussed in Sec. 2.2.1.1, the selection rules for Raman scattering requires that components of the susceptibility tensor χ^{ij} transform by the same symmetry operations as the normal modes. The number of Raman active modes determines the number of bands that can be observed in the spectrum of a specific material. The limitation to $q \approx 0$ phonons means that phonons excited in Raman or Brillouin spectroscopy are of very long wavelength ($q = 2\pi/\lambda$) and their wavelength is comparable to the order of magnitude of the crystal size (large number of unit cells). This means neighbouring unit cells oscillate in phase and the determination of the normal mode symmetry for the crystal is same as treating the unit cell as a molecule.

In the case of disordered crystals, however, the $q = 0$ selection rule is relaxed because of the lack of translational symmetry, and activation of phonons is possible within π/d of the centre of the Brillouin zone, where d is the spatial length of periodicity. Thus, scattering also takes place from phonons with $q \neq 0$. Therefore, phonons other than zone centre can also take part in the Raman process. This is known as selection rule breaking and also permits a different number of modes than that predicted by group theory.

Much of the study of Raman scattering in crystalline materials focuses on the few allowed single-phonon processes. The corresponding interest in glassy materials is on the breakdown of selection rules and the broad range of allowed scattering processes. In glass, Brillouin zone is not defined and momentum conservation can be achieved even when the wave vector of the incident photon interacts with any part of the defective Brillouin zone. Because of the absence of a well-defined crystal momentum, a larger wealth of information about vibrational spectra can be extracted from Raman scattering in glasses. The results on the structure of glasses obtained from the Raman spectra are both supplementary and complementary to information obtainable by the traditional structural analysis techniques of x-ray, electron and neutron diffraction. Thus, Raman spectroscopy is a powerful tool for the determination of the structure, environment and dynamics of glasses. The chemical composition and structure of molecules forming the glass network influence the Raman scattering and no two spectra are exactly the same. Thus, the Raman-shifted signal is very useful in distinguishing the structures of different compositions of glasses.

Shuker and Gammon [81] have demonstrated how to go from the concept of a disorder-induced breakdown of selection rules to a quantitative representation of the vibrational density of states (VDOS) as measured by Raman scattering. They assumed

that: (a) the vibrations are harmonic, so that they can be analyzed into normal modes; (b) the vibrations couple to light through the displacement dependence of the electronic polarizability of the material; and (c) the coherence length L , which characterizes the spatial extent of a normal mode vibrational state, is short compared with optical wavelengths [81]. Naturally, any density of states, so derived, is only a Raman-effective VDOS, which is a convolution of the true vibrational spectrum with mode-dependent matrix elements. It is obvious that in a perfect harmonic crystal $L \rightarrow \infty$ and a vibrational normal mode is a true phonon with a plane wave envelope to its wave function and hence a well-defined wave vector. In glasses, vibrational modes can be viewed as being nearly localized; then in terms of the correlation length, the eigen vector envelope may be represented by a plane wave factor $\exp(i\mathbf{q}\cdot\mathbf{r})$ times a spatial damping factor $\exp(-r/L)$. This means that the vibrational eigen vector envelope for a mode with a given energy will include many q 's. Thus q is not a good quantum number in these systems and there is a disorder-induced breakdown in the selection rules for scattering. The exponential damping mixes the formerly distinct q states. The eigen vector envelope can then be represented as $e^{iq_j r} e^{-r/L}$ for the j th mode. Its Fourier transform is proportional to the scattered Raman intensity of the j th mode. Summing over all modes and allowing all q_j 's to contribute to the sum, the Stokes scattered light can be expressed as [77]:

$$I_{\alpha\beta\gamma\delta}(\omega) \propto \sum_b C_b^{\alpha\beta\gamma\delta}(\omega) g_b(\omega) \left[\frac{1}{\omega} \right] [1 + n(\omega, T)] \quad (2.37)$$

where,

$$n(\omega, T) = \left[\exp\left(\frac{\hbar\omega}{k_B T}\right) - 1 \right]^{-1} \quad (2.38)$$

is the Bose-Einstein distribution function, with \hbar and k_B being the Planck and Boltzmann constants, respectively. Each band of vibrational states b is assumed to have a photon-phonon coupling constant $C_b^{\alpha\beta\gamma\delta}(\omega)$ with the superscripts $\alpha\beta$ and $\gamma\delta$ describing the polarizations of the incident and scattered photons. This is also called as the Raman

coupling coefficient that is proportional to the scattering cross section of a vibrational mode at frequency ω . There is an extra multiplication factor of $(\omega_0 - \omega)^4$, where ω_0 is the incident photon frequency. The expression in Eq. 2.18 is the principal result of the calculation of Shuker and Gammon and depicts how the Raman spectrum of an amorphous solid is composed of the Bose-Einstein factor, the harmonic propagator $1/\omega$, the transition probabilities which are contained in the coupling constant, and the VDOS. If $I^{\text{expt}}(\omega)$ is the measured Stokes Raman intensity for a particular polarization geometry, then the reduced Raman spectrum is given as,

$$I^{\text{red}}(\omega) = \frac{\omega I^{\text{expt}}(\omega)}{1 + n(\omega, T)} \propto C(\omega)g(\omega) \quad (2.39)$$

Thus, the reduced Raman spectrum simply involves the density of states $g(\omega)$ and frequency dependent matrix element factors $C(\omega)$, which are assumed to be smoothly and slowly varying. Thus, the reduced Raman spectrum reflects the basic features of the VDOS, indicating that Raman scattering is useful to study the VDOS in glasses.

In an inelastic neutron scattering experiment, one measures the dynamic structure factor $S(q, \omega)$, where q is the momentum transfer and ω is the energy transfer to the medium. Three main scattering mechanisms contribute to $S(q, \omega)$: the elastic part, the one-phonon scattering mechanism, and the multiphonon background. In the incoherent approximation, the one-phonon term is related to the VDOS through,

$$S_{\text{inc}}(q, \omega) \propto q^2 e^{-2W} g(\omega) \frac{1 + n(\omega, T)}{\omega} \quad (2.40)$$

where $2W$ is the exponent of the Debye-Waller factor. It can be easily observed that Eq. 2.18 and Eq. 2.21 are similar with respect to the frequency dependence of the measured quantities, *i.e.*, first-order vibrational Raman intensity (Raman scattering) and dynamic structure factor (neutron scattering); the significant difference is that the Raman data are weighted by the coupling coefficient $C_b^{\alpha\beta\gamma\delta}(\omega)$.

Eq. 2.18 is the basic equation for the introduction of various reduction approaches to the experimental Raman spectral intensity $I^{expt}(\omega)$. The reduction scheme depicted in Eq. 2.20 is called as the reduced Raman spectrum. This approach isolates the VDOS weighted by the coupling coefficient. It filters out the trivial effects of the thermal population factor in the low-frequency part of the spectrum [42]. Another useful reduced form is,

$$\chi''(\omega) = \frac{I^{expt}(\omega)}{1 + n(\omega, T)} \propto \frac{C(\omega)g(\omega)}{\omega} \quad (2.41)$$

This form is known as the susceptibility representation. It is used for analyzing relaxational effects in depolarized light scattering spectra dealt with in the mode coupling theory [42].

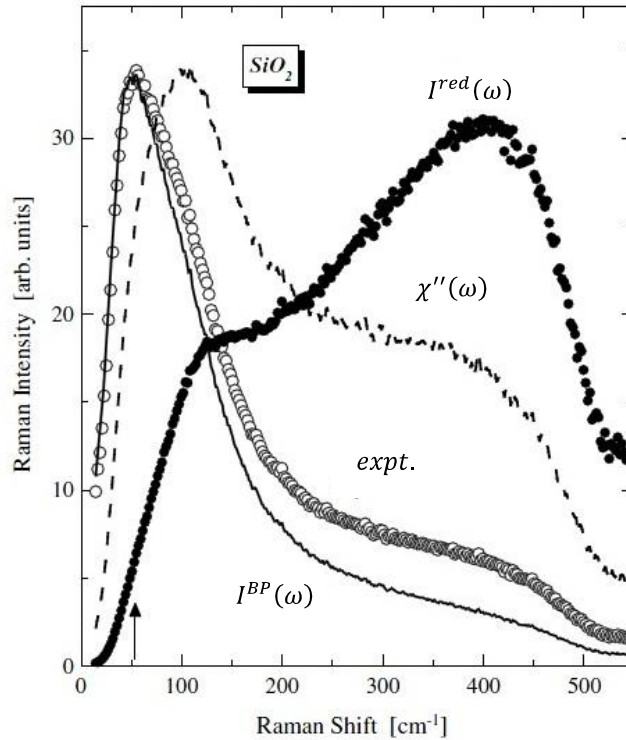


Fig. 2.3 A comparison of the various reduction schemes by Eq. 2.20, 2.22, 2.23 applied to the depolarized low-frequency Raman spectrum of vitreous silica. The arrow denotes the energy of the Boson peak. The figure has been reproduced from Ref. [42].

The Debye theory predictions of the low-frequency VDOS in crystalline solids gives $g(\omega) \propto \omega^2$. The Boson peak, as discussed in Chapter 1, appears exclusively for glassy materials in the low-frequency part of VDOS and appears as an excess over the Debye prediction. The Boson peak reduction scheme considers this excess as $g(\omega)/\omega^2$ and restores the experimentally measured well-resolved Boson peak in Raman scattering as,

$$I^{BP}(\omega) = \frac{I^{expt}(\omega)}{\omega[1 + n(\omega, T)]} \propto \frac{C(\omega)g(\omega)}{\omega^2} \quad (2.42)$$

An illustrative example of the various reduction schemes depicted through Eqs. 2.20, 2.22 and 2.23 is shown in Fig. 2.3 applied to the room temperature depolarized Raman spectrum of vitreous silica [42]. This comparison reveals that the $C(\omega)$ -modulated VDOS obtained by the reduced representation of Eq. 2.20 is featureless in the region (indicated by arrow) where the experimental data shows the Boson peak. The transformation by Eq. 2.23 leaves the frequency dependence of the experimentally measured spectrum almost intact. Thus, to retain the Boson peak, the reduced representation of Eq. 2.23 is usually employed in the analysis of Raman data. The schemes presented in Eq. 2.20 and Eq. 2.23 have been used in the present thesis for eliminating temperature effects and frequency reduction of the Boson peak, respectively. The experimental details of Raman spectrometer are discussed below.

2.2.1.4 Raman scattering instrumentation

A typical Raman spectrometer has four major components as discussed below:

(a) Excitation source: Prior to the development of lasers in the 1960s, mercury lamps were used as excitation sources for Raman spectroscopy. Continuous wave (CW) lasers emitting in the visible range are now commonly used. Lasers are ideal excitation sources for Raman spectroscopy as they are (a) highly monochromatic and extraneous lines are much weaker, (b) highly collimated making it ideal for measurement on micron-sized

samples, (c) possess high output power and (d) are highly polarized, making it ideal to study symmetry properties. Typical commercially available gas lasers are Ar⁺ (351.1–514.5 nm), Kr⁺ (337.4–676.4 nm) and He-Ne (632.8 nm). More recently, solid state lasers such as Nd:YAG and diode lasers are also being used for Raman spectroscopy. In this work, we have used the 514.5 nm line from an Ar⁺ laser and a diode pumped solid state laser (DPSS) of 532 nm (second harmonic of the 1064 nm line) for all Raman studies.

(b) Sample illumination and light collection system: Raman scattering being a very weak process, the laser light has to be focused well on to the sample and the scattered light has to be collected efficiently. The small diameter of the laser beam (~ 1mm) aids in proper focusing of the laser on the sample. Appropriate scattering geometries and optics are essential to collect the scattered light efficiently. Commonly used scattering configurations are 180° and 90° geometries. As can be seen from Eq. 2.3, the maximum wave vector transfer to the phonon takes place in the case of 180° geometry. We have used the 180° backscattering geometry in all the Raman scattering measurements. The collection optics consists of a system of lenses and mirrors. The light gathering power of a lens is expressed by its *F*-number,

$$F = \frac{f}{D} \quad (2.43)$$

where *f* is the focal length of the lens and *D* is its diameter. The smaller the *F*-number, the larger is the light gathering power. It is important to match the *F*-number of the collection optics to that of the monochromator. This is to ensure that there is no under-filling or over-filling of gratings and mirrors and hence to maximize the total light throughput.

(c) Light dispersive and wavelength selector unit: Both prism and grating monochromators and spectrographs have been used extensively to measure Raman spectra. In a single monochromator, extraneous or stray light that bounces around the spectrometer overlaps the weak Raman scattered signal. This stray light is caused mainly

by undiffracted light being scattered from the face of the grating. Such stray light can be reduced considerably [78] by arranging two spectrometers in tandem so that the Raman output of one is filtered by the second. With this idea, the construction of double monochromators began. In this thesis, we have used a single monochromator with high throughput (Renishaw (InVia) micro-Raman spectrometer) for recording Raman spectra at high wavenumber. We have also used a double monochromator with high stray light rejection and high resolution (Horiba U1000 Raman spectrometer) for recording Raman spectra in the low-wavenumber region.

(d) Detection and data processing system: Earliest detection methods employed prolonged exposure on photographic plates to record Raman spectra. Presently sensitive detection is possible using photon counting (photomultiplier tubes) and photodiode array (charge coupled device) detectors. The photomultiplier tube (PMT) consists of a photocathode that emits electrons when photons strike it; it has a series of dynodes, each of which emit secondary electrons when an electron strikes it; and an anode which collects these electrons as an output signal. Background noise is the primary limiting factor in the performance of a PMT. This is known as dark current which is caused by the spurious emission of electrons from the photocathode and dynodes. A large fraction of dark current is of thermionic origin and can be reduced if the tube is cooled by water, liquid nitrogen or thermoelectrically (Peltier-cooled). The Raman signal is processed by photon counting method, where electron pulses generated by individual photons reaching the photocathode are measured.

In recent years, detection of Raman signal using charge coupled devices (CCDs) has increased. A CCD is a silicon-based semiconductor array of photosensitive elements, each one of which generates photoelectrons and stores them as charge. Each element is called a pixel. Typically pixel size is $25 \mu\text{m}^2$. On command, the charges on pixels in a

row are shifted from one end to the other and read by a single analogue-to-digital converter, where they are recorded.

We have used two Raman spectrometers for measurements reported in this thesis: a Renishaw micro-Raman and a Horiba Jobin-Yvon U1000 high-resolution Raman spectrometer.

2.2.1.4.1 Renishaw micro-Raman spectrometer

The Renishaw micro-Raman spectrometer (model InVia) is a high-throughput single monochromator-based system. It comprises of one or more lasers as excitation source, a microscope unit coupled to a monochromator and a CCD camera detector. The working of this spectrometer is briefly discussed below with the help of Fig. 2.4.

(a) Excitation source: For all Raman measurements using this spectrometer, the 514.5 nm line from an Ar⁺ laser has been used as excitation source. The laser unit is mounted on an optical table along with the system unit. The laser unit contains several neutral density filters in a filter wheel, which are used to attenuate the laser power and select appropriate power for a specific measurement.

(b) Sample illumination and light collection system: The laser light entering the system unit passes through a rejection filter F_1 , whose purpose is to reject all but the desired lasing line from the laser for excitation of the sample. Then a plasma filter for eliminating the plasma lines corresponding to the desired wavelength is used. For our measurements, we have selected the 514.5 nm line from an Ar⁺ laser which emits a range of wavelengths from 351.1–514.5 nm. Thereafter, the laser beam passes through a spatial filter which comprises of a set of objective O_1 and pinhole P_1 to converge the beam to a 10 μm spot. The purpose of this optical arrangement is to spatially filter the beam and shape it into a Gaussian shape. A second objective lens O_2 is used to make a well-collimated parallel

beam. Two mirrors M_1 and M_2 are used to reflect the laser beam on to the edge filter F_2 . The angle of the edge filter is adjusted in such a way that the laser beam falls on mirror M_3 and is directed into the optical path of the microscope. The light falls on the microscope objective lens O_3 which focuses it on the sample to illuminate it. The sample is placed on a piezoelectric transducer-controlled mechanical stage which helps in positioning and focusing the beam on the sample. The light scattered from the sample is collected back in the back-scattering geometry by the same microscope unit which incidents it on the edge filter F_2 . This filter blocks the Rayleigh component of the scattered light and passes the Raman signal into the monochromator unit through slit P_2 .

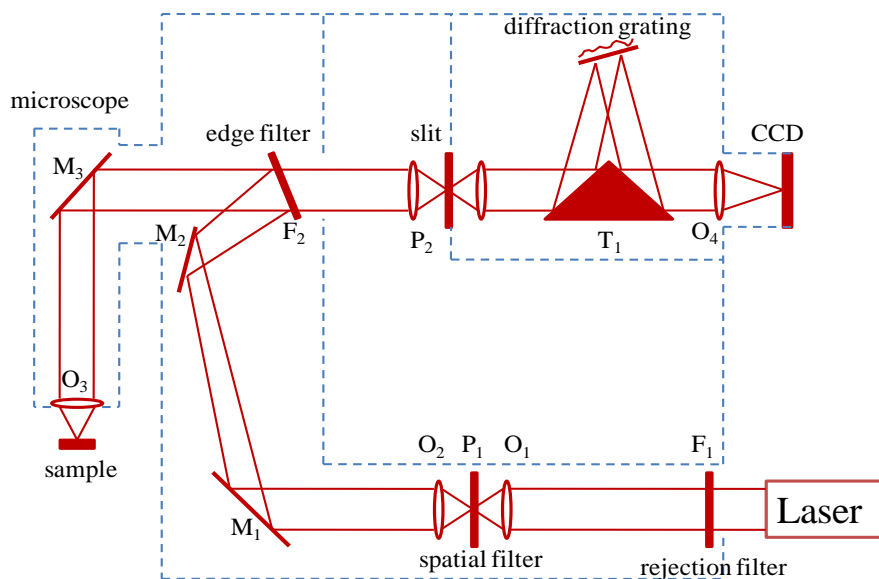


Fig. 2.4 A schematic of the Renishaw micro-Raman spectrometer.

(c) Light dispersive and wavelength selector unit: Inside the monochromator unit, the scattered light strikes the prism mirror T_1 which directs it to the grating. The grating disperses the light and sends it back to T_1 which directs it to the detector through lens O_4 . For the present studies, 1800 grooves/mm grating was used that results in an instrument resolution of $\sim 1.5 \text{ cm}^{-1}$ per pixel. The lower wavenumber limit of detecting Raman signal using this spectrometer is 65 cm^{-1} . Below this range, the edge filter eliminates Raman

intensities also along with Rayleigh background. All measurements in this thesis involving Raman modes $> 65 \text{ cm}^{-1}$ were carried out using this spectrometer.

(d) Detection and data processing system: The detector is a Peltier-cooled (upto 197 K) CCD camera where the dispersed light is focused. The CCD converts light into charges which is read by the readout electronics. Data acquisition is carried out using the WiRE 3.2 software (data analysis software of Renishaw) which allows the user to set the spectral range, accumulation time and laser power.

2.2.1.4.2 Horiba U1000 Raman spectrometer

To study the vibrational spectra of glasses below 100 cm^{-1} and specifically to study the Boson peak, we have used the Horiba U1000 Raman spectrometer, which is a high-resolution, double monochromator-based system. It comprises of a laser as the light source, two monochromators in tandem and a PMT detector. The working of this spectrometer is briefly discussed below with the help of Fig. 2.5.

(a) Excitation source: For all Raman measurements using this spectrometer, a frequency-doubled 532 nm line from a Nd:YAG laser was used as excitation source. The laser unit is mounted on an optical table along with the system unit. Using suitable delivery optics, the laser beam is sent into a macro chamber.

(b) Sample illumination and light collection system: The macro chamber contains the sample. The laser light that enters the macro chamber is incident on the sample. The backscattered light from the sample is directed into the spectrometer through entrance slit S_1 .

(c) Light dispersive and wavelength selector unit: Inside the spectrometer chamber, the scattered light enters the first monochromator *mono 1*, strikes the spherical mirror M_1 and is directed to grating G_1 . Gratings determine the resolution of a spectrometer to a large

extent. The more the number of grooves per mm in the grating, the more is the dispersion and the higher is the resolution. The signal loss caused by improved resolution can be compensated by widening the slit width. The grating disperses the light and sends it to spherical mirror M_2 which sends it to the second monochromator *mono 2* through the intermediate slit S_2 . Only a portion of the spatially dispersed and ordered spectrum is communicated to *mono 2* by G_1 and M_2 of *mono 1*. Using a similar arrangement, the second monochromator disperses the light again using grating G_2 and finally the dispersed light exits the spectrometer through the exit slit S_3 . The spectrometer has a long 2×1000 mm focal length with a high precision drive mechanism. The double monochromator technology is ideally suited for very high spectral resolution (using PMT detection) and to very high stray light rejection. The monochromators work in the double additive mode and renders an instrument resolution of $\sim 0.15 \text{ cm}^{-1}$ with PMT using very small exit slit before PMT. The lower limit of detecting Raman signal using this spectrometer is typically 5 cm^{-1} with PMT.

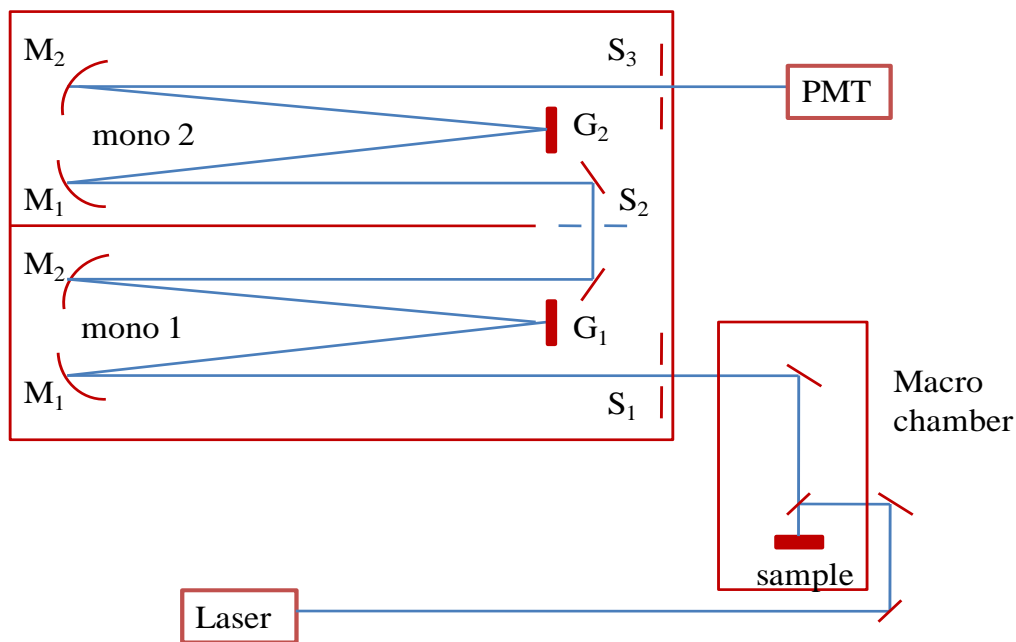


Fig. 2.5 A schematic of the Horiba U1000 Raman spectrometer.

(d) Detection and data processing system: The dispersed light obtained at exit slit S3 is focused on to the PMT detector. The movement of the gratings is motorized and software controlled which aligns the dispersed light at specific angles to the corresponding wave number. The PMT records the spectra by mono-channel detection. Data acquisition is carried out using the LabSPEC software (data analysis software of Horiba).

2.2.1.5 Theory of Brillouin scattering

Brillouin scattering, which is similar to Raman scattering, is inelastic scattering of light by acoustic phonons in a solid. Brillouin spectroscopy is thus, a valuable probe to measure acoustic phonons near the centre of the Brillouin zone. Very small volumes of sample may be probed and it is a non-contact measurement technique. Acoustic phonons are vibrations in the lattice associated with translations of the centre of mass in the unit cell. These phonons propagate through the lattice at the speed of sound. Thus, Brillouin scattering results from sound waves caused by thermal fluctuations in the lattice [80]. The velocity of sound can be determined directly from the Brillouin shift and hence elastic constants, relaxation processes and phase transitions can be accurately studied. A high-resolution measurement of the spectral width of the scattered light enables one to obtain information on acoustic attenuation arising from anharmonicity, structural relaxations or other possible mechanisms [77]. Brillouin spectroscopy of glasses directly gauges the complex elastic modulus which can be estimated from monitoring the acoustic mode frequency and its line-width. It gives information on the integration of the structural units on a mesoscopic length scale.

Some of the concepts developed in the study of fluids are relevant to solids and since sound waves studied by visible light scattering are of long wavelength, the microscopic structure of fluids can be ignored to a first approximation. Therefore, a

hydrodynamic medium can be regarded as a continuous isotropic medium. A thermodynamic treatment of its fluctuations leads to a spectrum consisting of two types of scattered light components [80]: (a) a quasi-elastic Rayleigh component centered at ω_0 due to non-propagating entropy fluctuations and (b) a Brillouin doublet symmetrically located about the unshifted Rayleigh line and separated from it by a frequency as that of a sound wave propagating through the solid. This Rayleigh-Brillouin scattering arises from fluctuations in susceptibility which is due to variations in the thermodynamic quantities, such as density and temperature. The state of a fluid in thermodynamic equilibrium consisting of a single constituent can be described by two variables, such as the pressure $P(\mathbf{r}, t)$ and the entropy $S(\mathbf{r}, t)$ so that the effect of fluctuations in these variables on the susceptibility can be expressed as [80],

$$\delta\chi(\mathbf{r}, t) = \left(\frac{\partial\chi}{\partial P}\right)_S \delta P(\mathbf{r}, t) + \left(\frac{\partial\chi}{\partial S}\right)_P \delta S(\mathbf{r}, t) \quad (2.44)$$

In this thesis, χ is used both for dielectric and elastic susceptibility at appropriate places. Using Eq. 2.10, the differential cross section for light scattering by a fluid can be written as,

$$\frac{d^2\sigma}{d\Omega d\omega_S} = \frac{\omega_0\omega_S^3 vV}{16\pi^2 c^4} \langle |\delta\chi|^2 \rangle_\omega \cos^2\theta \quad (2.45)$$

where θ is the scattering angle. Evaluation of $\langle |\delta\chi|^2 \rangle_\omega$ gives an expression of the form,

$$\frac{d\sigma}{d\Omega} = \frac{\omega_0\omega_S^3 v k_B T}{16\pi^2 c^4} \left[\beta_S \rho^2 \left(\frac{\partial\chi}{\partial\rho}\right)_S^2 + \frac{T}{\rho C_P} \left(\frac{\partial\chi}{\partial T}\right)_P^2 \right] \cos^2\theta \quad (2.46)$$

where β_S is the adiabatic compressibility, ρ is the density and C_P is the specific heat. Sound waves can be treated as pressure (density) fluctuations at constant entropy to a good approximation. The first term in the square brackets in Eq. 2.27 is associated with the excitation of the Brillouin doublet corresponding to two sound waves travelling in opposite directions but having same frequency. The second term is associated with the

Rayleigh component and corresponds to non-propagating temperature (entropy) fluctuations. Therefore, a hydrodynamic treatment of fluids predicts the existence of Brillouin lines with frequency of the sound wave, placed symmetrically about the Rayleigh line.

The kinematics of the scattering process follows directly from the conservation of frequency (energy) and wave vector (momentum) as depicted in Eqs. 2.1 and 2.2, respectively. Using visible light as an excitation source, the maximum wave vector transferred to the phonon is $q \sim 10^5 \text{ cm}^{-1}$. For this q , the acoustic phonon frequency is very small ($\sim 1\text{-}2 \text{ cm}^{-1}$). In this limiting value of q , the wavelengths of the phonons are of the order of hundreds of unit cells. This allows the lattice to be modeled as an elastic continuum and the acoustic phonon frequency depends linearly on q , i.e., $\omega_B = Vq$, where V is the sound velocity. Using Eq. 2.3, the dependence of the Brillouin mode frequency on the scattering angle can be written as,

$$\omega_B = 2Vk_0 \sin \frac{\theta}{2} \quad (2.47)$$

where $k_0 = n\omega_0/c$, where n is the refractive index and c is the velocity of light in vacuum. Classically, this relation is identical to Bragg reflection from a grating of spacing $2\pi/q$ moving with velocity V . If the density variation caused by the sound waves is assumed to produce a well-defined diffraction grating for the incident light, the Brillouin components are regarded as a Doppler shift of the incident light caused in the process of Bragg reflection by the moving sound waves.

The sound velocities obtained from the above relation can be used to determine the elastic constants of the medium. From the longitudinal and transverse sound velocities in an isotropic medium the corresponding elastic constants can be estimated using the relation $C = \rho V^2$ when the density ρ is known. For an isotropic solid, its elastic behavior is fully described by the longitudinal modulus ($L = C_{11}$) and shear modulus ($G =$

C_{44}). Between the components of the related elastic stiffness tensor, the isotropic relation $C_{11} = C_{12} + 2C_{44}$ holds [82]. Hence, two independent elastic constants exist in an isotropic solid such as, glass which corresponds to two Brillouin (longitudinal and transverse acoustic) modes in a Brillouin spectrum.

Moreover, the spectral line-shape of the Brillouin spectrum contains information on the bulk structure of the material. It contains contribution from instrumental function and phonon life-time. The line-shape of the scattered light is in general a combination of Gaussian (instrumental) and Lorentzian (phonon) functions. Study of these line-widths provides information on the life-times of phonons and various damping mechanisms in the material. The phonon life-time refers to the time taken by a phonon to scatter or be attenuated. In conjunction with its group velocity, the phonon life-times define how far a phonon can carry its energy, *i.e.*, the phonon mean free path. The reason for attenuation may be either collision with impurities or defects within the sample or the boundaries of the sample, or the intrinsic anharmonicity of the lattice even in perfect crystals. Using Eq. 2.25, $\omega_B = 2vk_0 = 1-2 \text{ cm}^{-1}$ for the back-scattering geometry, the relative shift ω_B/ω_0 is very small. To obtain an accurate measurement of the acoustic phonon, the resolving power of the spectrometer should be $\sim 10^7$. This cannot be achieved in a dispersive instrument like conventional Raman scattering based up on gratings. Hence, a Fabry-Pérot interferometer, which can achieve such resolution, is used. This is discussed in detail below.

2.2.1.6 Brillouin scattering instrumentation

The inelastically scattered light from acoustic phonons undergo an extremely small change in frequency from the unshifted Rayleigh line and a high-resolution spectrometer is required to detect these phonons. We have performed the Brillouin

measurements using a high-contrast 3+3 pass tandem Fabry-Pérot interferometer (JRS Scientific Instruments) which consists of two Fabry-Pérot interferometers in series.

2.2.1.6.1 Principle of Fabry-Pérot Interferometer

A Fabry-Pérot Interferometer (FPI) is an ideal choice for high-resolution spectroscopy where a resolution of MHz to GHz, and a high throughput, is required. A Fabry-Pérot interferometer is made of two plane mirrors mounted exactly parallel to one another, with a spacing L_1 between them, where multiple reflections between the two surfaces result in light wave interference. When two waves with the same frequency combine, the resulting pattern is determined by the phase difference between the two waves. Depending on the wavelength of light, the angle of incidence, the thickness of the mirrors and the refractive index of the material, waves that are in phase will experience constructive interference (transmission maxima), while waves that are out of phase will experience destructive interference (transmission minima). In an interferometer a single incident beam of coherent light is split into two beams by a partially-reflecting mirror. The two beams will travel different paths until they are recombined before arriving at a detector. The difference in the distance traveled by each beam creates a phase difference between them, which creates an interference pattern. For a given spacing L_1 , the FPI will transmit only certain wavelengths λ as given by the transmittance [83],

$$T = \frac{\tau_0}{1 + \left(\frac{4F^2}{\pi^2}\right) \sin^2\left(\frac{2\pi L_1}{\lambda}\right)} \quad (2.48)$$

where τ_0 is the maximum possible transmission determined by losses in the system, λ is the wavelength of transmitted light and F is the finesse, a quality factor depending primarily on the mirror reflectivity R and flatness,

$$F = \frac{4R}{(1-R)^2} = \frac{\Delta\lambda}{\delta\lambda} \quad (2.49)$$

F is, thus, also related to the spacing between successive transmitted wavelengths $\Delta\lambda$ known as the free spectral range (FSR) and determines the width $\delta\lambda$ (resolution) of a given transmission peak. Eq. 2.29 shows that only those wavelengths satisfying,

$$2L_1 = n\lambda \quad (2.50)$$

for integral values of n will be transmitted. The FSR is given as,

$$FSR = \frac{c}{2L_1} \quad (2.51)$$

where c is the velocity of light. The FPI is used as a spectrometer by varying the spacing L_1 so as to scan the light intensity at different wavelengths. However, it is apparent that the measured light intensity at a given spacing is the sum of the intensities at all wavelengths satisfying Eq. 2.31. Therefore, an unambiguous interpretation of the spectrum requires *a-priori* knowledge that the spectrum of light lies within the boundaries of a wavelength spread $< \Delta\lambda$. However, the outstanding difficulty is that when the mirror plates are separated far enough to give high resolution, the successive orders are so close together that the patterns overlap. The FSR of the FPI can be increased by decreasing L_1 (Eq. 2.32). However, $\delta\lambda$ also increases with increase of FSR and the resolution decreases. Eq. 2.30 connects these two quantities with F . But in practice, due to limitations on the quality of mirror and reflectivity, F cannot be made greater than ~ 150 . Therefore, the limiting value of FSR and resolution is fixed by the limits of achievable values of F . In order to increase FSR without compromising resolution, a tandem combination of two interferometers came into use.

2.2.1.6.2 Working of Tandem Interferometer

To increase the FSR at a fixed $\delta\lambda$, two FPI's are used in series. The wavelengths transmitted by the combination must individually and simultaneously satisfy the interference conditions,

$$2L_1 = n\lambda \text{ and } 2L_2 = m\lambda \quad (2.52)$$

for integral values of n and m . When the spacing of L_1 and L_2 are set so as to individually transmit wavelength λ (see Fig. 2.6 for FP1 and FP2), the light passing through the combination of FP's will have a transmission spectrum as shown in Fig. 2.6 for the tandem arrangement. The neighbouring peaks do not coincide, and they coincide only after several times the FSR of FP1. Small ghost peaks remain because of the intervening transmission peaks of each interferometer. The FSR of the tandem arrangement is thus increased considerably over that of a single FPI, while the resolution remains same.

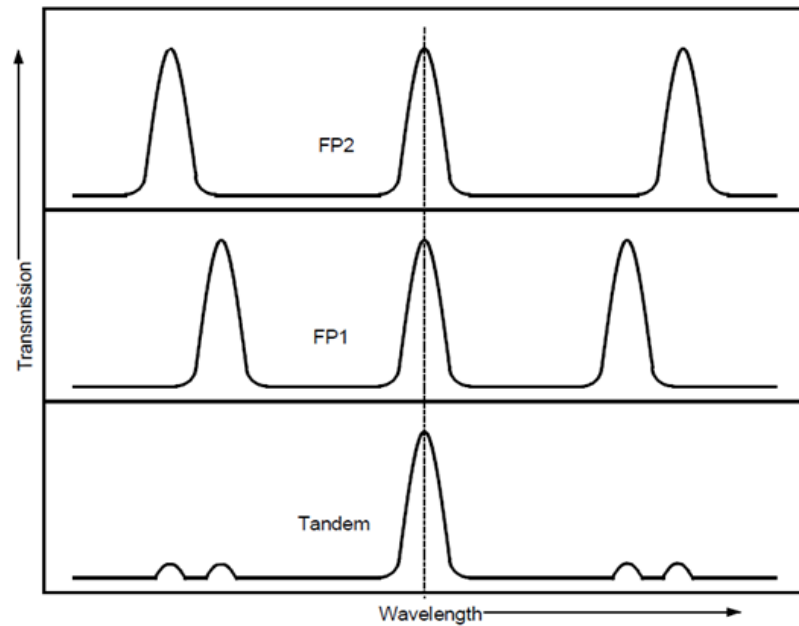


Fig. 2.6 The transmission spectra of individual interferometers FP1 and FP2, and a tandem system (adapted from Ref. [83]).

In order to use the tandem interferometer system as a spectrometer, the two FPI's have to be scanned synchronously with simultaneous change of spacing L_1 and L_2 , and the system should satisfy,

$$\frac{\delta L_1}{\delta L_2} = \frac{L_1}{L_2} \quad (2.53)$$

where δL_1 and δL_2 are the incremental changes in mirror spacing in FP1 and FP2 simultaneously, for their respective spacing of L_1 and L_2 . A typical spacing of the mirrors is such that $L_2 \sim 0.95L_1$ and typical values of δL_1 and δL_2 is ~ 1 to a few μm . However, practical operation of a tandem FP requires (a) the establishment and (b) the maintenance of strict parallelism of the mirror plates throughout the course of the experiment. To combine the two interferometers and obtain synchronization in scanning, the concept of mechanical scanning on a single scanning stage is used.

The principle of tandem scan is shown in Fig. 2.7. FP1 is located in the direction of the translation stage movement. One of its mirrors sits on the translation stage while the other on a separate angular orientation device. FP2 lies with its axis at an angle ϕ to the translation stage direction. Again one mirror is mounted on the translation stage and the second mirror of the pair lies on an angular orientation device which can also allow a small translation of the mirror for adjustment purposes. In this arrangement, when the translation stage is moved to the right, the mirror spacing in FP1 and FP2 are set to L_1 and $L_1 \cos\phi$, respectively. Hence, Eq. 2.34 is satisfied and the two interferometers scan synchronously.

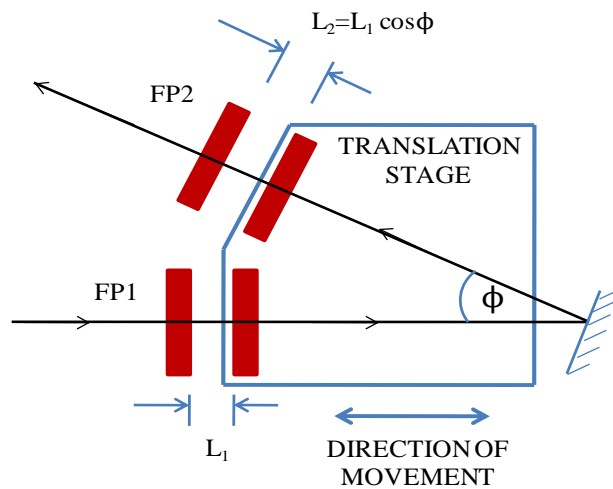


Fig. 2.7 A mechanically scanning tandem Fabry-Pérot.

The movement of the translation stage is achieved by attachment of the plate to the moving platform of a deformable parallelogram that is driven by a single piezoelectric transducer. Such mechanical scanning enables fast and repetitive scanning. The important features of this system are: (a) complete dynamic synchronization [correct relative spacing] over a large scanning range of several μm and (b) good static synchronization [relative spacing of the FP's do not deviate from the correct relative value by $\sim 20\text{\AA}$] due to compact design which enables both FP's to share the same environment.

2.2.1.6.3 Concept of 3+3 pass Fabry-Pérot Interferometer

Since finesse is restricted to limitation of ~ 150 owing to the limitations in the reflectivity achieved, there is an upper limit on the maximum possible contrast. Contrast C is defined as the maximum to minimum in transmittance T and is given as,

$$C = \left(\frac{1 + R}{1 - R} \right)^2 \quad (2.54)$$

The required contrast depends on the nature of the sample and the elastic scattering strength. In opaque materials, the elastic scattering increases by a factor of $\sim 10^5$ compared to the Brillouin component. For single pass of transmitted light through the FP, contrast $C \sim 10^3$. This contrast is not sufficient for unambiguous detection of Brillouin signal. For transparent and strongly scattering samples, a contrast $\sim 10^7-10^9$ is required, whereas for opaque and strong surface scattering sample, $C \sim 10^{10}-10^{12}$ is essential. Multi-pass operation is a way to increase the spectral contrast. For n -passes the contrast increases as $C_n \sim (C)^n$. Thus, for the present 3+3 pass system, a theoretical contrast $C_6 \sim 10^{18}$ is achievable. For practical purposes, maximum contrast $\sim 10^{14}$ is achievable using this instrument. This is sufficient for Brillouin scattering experiments on opaque samples.

2.2.1.6.4 Brillouin spectrometer set-up

The Brillouin spectrometer consists of a laser as an excitation source, a 3+3 pass tandem Fabry-Pérot interferometer, an avalanche photodiode detector and control electronics.

(a) Excitation source: The excitation source is a diode-pumped solid state laser (InnoLight Diabolo 500), with a free space wavelength of 532 nm. It is a narrow line-width, extremely long coherence length (1 km) laser operating in true single frequency. The laser light is split into two beams with the help of a glass plate. One of the beams is used as reference beam to align the spectrometer. The other beam is used to excite the sample and the scattered light is collected from a backscattering geometry and focused on to a camera lens, which collimates the light. Another lens is used to focus the collimated light into the entrance pinhole of the spectrometer. For aligning the spectrometer, a typical power of ~ 1 mW is sufficient. Remaining power is incident on the sample.

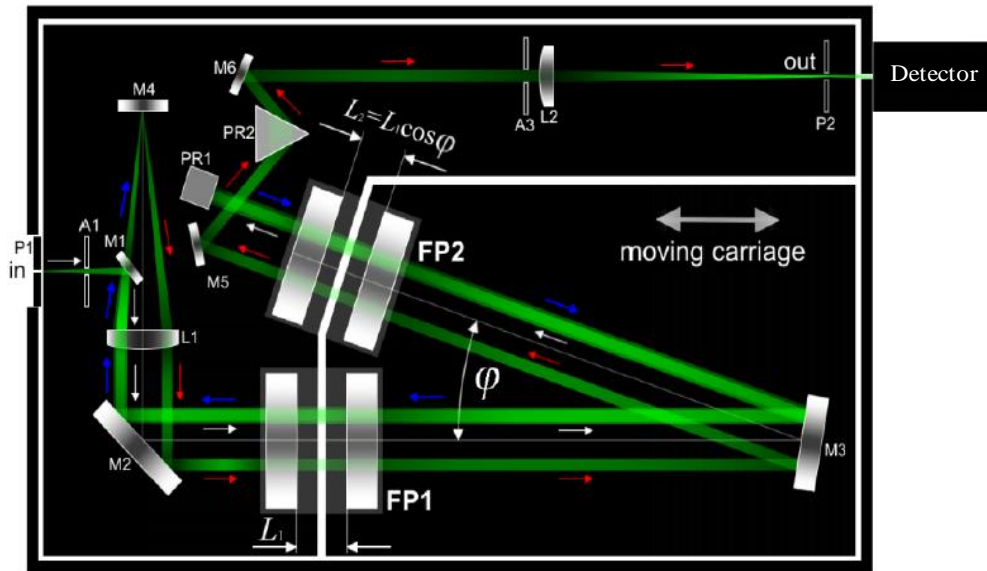


Fig. 2.8 Schematic of the Tandem Fabry-Pérot interferometer (manufactured by JRS Instruments) showing the light path. The figure has been adapted from Ref. [84].

(b) 3+3 pass tandem Fabry-Pérot interferometer: The spectrometer box contains the two FP's in series. It consists of two sets of optical arrangements: (a) alignment optics and (b) tandem optics. The interferometer is normally used in a multi-pass tandem mode if both FP's have been pre-aligned parallel and with correct relative spacing. The alignment mode is based on the idea that when the FP is transmitting, the reflected intensity should approach zero. Therefore, a correct alignment will give a minimum value of reflected intensities, whenever either FP1 or FP2 transmits.

After this pre-alignment procedure, the optical system is switched to multi-pass measurement configuration, which is called the tandem mode. In this mode, transmission will be observed with only minor adjustments to optimize the transmission. Fig. 2.8 depicts the optical arrangement in this mode to facilitate the 3+3 pass of the transmitted light. Scattered light from the sample is focussed into the input pinhole of the spectrometer using external optics. The aperture A1 directs light to mirror M1, which after collimation using lens L1, sends it to mirror M2. M2 reflects the light, which passes through FP1 and reaches mirror M3, which reflects it to prism PR1. On this path, it passes through FP2. This path is shown by white arrows in the figure, which makes 1+1 pass. PR1 reflects the light which retraces the path and reaches M1. This path of light is indicated by the blue arrows, which again makes 1+1 pass. M1 transmits the light to mirror M4, which reflects it. The light falls on L1 again and passes through FP1 and FP2, thereby completing the 3+3 passes. This path is indicated by the red arrows. The light then strikes mirror M5 and passes through a set of optics and through the output pinhole, reaches the detector.

(c) Avalanche photodiode detector: Given the low intensity of Brillouin signals, single-photon counting is necessary for detection. An avalanche photodiode (APD) is a highly sensitive semiconductor electronic device that exploits photoelectric effect to convert

light to electric voltage pulses. APDs can be thought of as photo-detectors that provide a built-in first stage of gain through avalanche multiplication. They have low-background noise, single-photon detection capability with quantum efficiency higher than a typical PMT. The single-photon signals are then passed to an amplifier, a pulse shaper, and then counted and stored by a multichannel analyzer.

(d) Control electronics: A scanning stage consisting of a deformable parallelogram rides on top of a roller translation stage for the tandem action of the interferometers. The scanning stage is actuated by a piezoelectric transducer and the roller translation stage enables the mirror spacing to be set to a desired value. A parallel-plate capacitor is then used to measure the scan displacement and this information is used in a feedback loop to make the scan displacement linear with respect to the applied scan voltage. This ensures that the same frequency band is always added to the same store channel of the APD with successive repetitive scans over the spectrum. For Brillouin spectroscopy, a particular store channel has to correspond to a particular frequency shift rather than the absolute frequency. A trigger derived from the elastically scattered light (laser frequency) starts the APD. This trigger pulse at the peak of the laser line, from the zero-crossing discriminator, starts the repetitive-scanning operation.

In order to avoid the noise caused by building vibrations (typically having maximum amplitudes at ~ 10 - 20 Hz), the optical table is rigidly mounted on the floor and the spectrometer is isolated from the optical table by means of a dynamic isolation system, using feedback control.

For easy operation of the interferometer, a simple procedure for obtaining mirror alignment is needed. This is achieved in the JRS-interferometer by a motorized variation of the position of the optical components, which permits operation in reflection mode

from the two FPs, instead of in the transmission mode. Switching between the two modes is also motorized.

2.2.2 X-ray diffraction

X-ray diffraction is a primary technique for the identification and characterization of compounds based on their diffraction pattern. When a monochromatic beam of x-rays interact with a target material, the atoms in the target scatter the x-rays. When the material possesses a regular structure (crystalline), the layers of atoms act like a diffraction grating for the x-rays, and the scattered x-rays undergo constructive and destructive interference. The condition for constructive interference relates the wavelength (λ) of x-ray to the diffraction angle, θ , and the lattice spacing of each set of planes (d_{hkl}) in the crystal, and is given by the Bragg's law,

$$n\lambda = 2d_{hkl} \sin \theta \quad (2.55)$$

Here, (hkl) represents the corresponding Miller index of the particular plane. Thus, the diffracted beam carries information about the inter-planar spacing and the underlying symmetry of a crystalline solid. The characteristic x-ray diffraction pattern is a fingerprint of a crystalline material. For unknown structure, a detailed analysis using Rietveld refinement method is done. The angles of possible diffractions depend on the size, shape and orientation of the unit cell of the solid. The intensities of the diffracted waves depend on the kind and arrangement of atoms in the crystal structure. If the detection angle is systematically changed, all possible diffraction peaks from the powdered sample will be detected.

2.2.2.1 X-ray diffraction in glass

Due to the disordered arrangements of atoms, x-ray diffraction pattern of glass consists of one or more broad diffuse patterns [85]. It is distinctly different from the

powder pattern of a crystalline material, which shows a large number of fairly sharp peaks. This tells us that glass does not have a unit of structure that repeats itself periodically in three dimensions [39]. Although there is no long-range order, the diffracted intensity shows broad humps at low angles indicating short-range order. It was realized that x-ray scattering pattern of glass showing maxima and minima can be produced solely by the existence of a few fairly definite inter-atomic distances in the material. The x-ray scattered intensity from a glass is given by the Debye equation [85],

$$I(Q) = \sum_m \sum_n \frac{f_m f_n \sin Q r_{mn}}{Q r_{mn}} \quad (2.56)$$

where f is the form factor, $Q = \frac{4\pi}{\lambda} \sin \theta$ is the scattering vector and r_{mn} is the distance from any atom m to n . This scattered intensity is used to determine the structure factor $S(Q)$ which gives the structural correlations of the atoms in the glass,

$$S(Q) = \frac{I(Q)}{N \langle f(Q) \rangle^2} \quad (2.57)$$

where N = number of atoms. The quantity $S(Q)$ is very important for glass since it is related to the real-space pair distribution function $\rho(r)$ by a Fourier transform,

$$\rho(r) - \rho_0 = \frac{1}{(2\pi)^3} \int_0^\infty 4\pi Q^2 [S(Q) - 1] \frac{\sin Qr}{Qr} dQ \quad (2.58)$$

where ρ_0 is the atomic density. Thus, from a Fourier analysis of the x-ray scattering profile, one can directly obtain the radial distribution function ($4\pi r^2 \rho(r)$), which provides the inter-atomic distances in the glass and the number of neighbouring atoms about each kind of atom.

For this thesis work, both lab source and synchrotron radiation x-ray sources were used. Room temperature powder x-ray diffraction patterns of samples were recorded using a computer-controlled x-ray diffractometer (STOE, Germany). The diffractometer consists of a flat pyrolytic graphite secondary monochromator that selects the Cu K_α

(1.5418 Å) radiation from a copper target source and a NaI:Tl scintillation counter detector. The diffraction patterns were recorded in a θ - 2θ geometry, where the sample plane is fixed and the source and detector move simultaneously.

2.2.2.2 Synchrotron x-ray diffraction

A synchrotron light source is a source of electromagnetic radiation, usually produced in a storage ring, for scientific purposes. Synchrotron light is produced by accelerating high energy electrons or other charged particles. Once the high energy electron beam has been generated, it is directed into auxiliary components such as bending magnets and insertion devices in storage rings. These supply strong magnetic fields perpendicular to the beam and in the process the circulating electrons generate photons. These photons comprise the synchrotron radiation. The radiation is projected at a tangent to the electron storage ring and captured by beamlines. These beamlines may originate at the positions of bending magnets, which mark the corners of the storage ring; or insertion devices, which are located in the straight sections of the storage ring. The beamline includes x-ray optical devices which control the band-width, photon flux, beam dimensions, focus and collimation of the rays. The optical devices include slits, attenuators, crystal monochromators and mirrors. A high photon flux in a small area is the most common requirement of a beamline. The design of the beamline will vary with the application. At the end of the beamline is the experimental end station, where samples are placed in the line of the radiation, and detectors are positioned to measure the resulting diffraction, scattering or secondary radiation. Several experimental methods take advantage of the high intensity, tunable wavelength, collimation and polarization of synchrotron radiation at beamlines which are designed for specific kinds of experiments.

X-ray diffraction measurements at ambient on lead-borate glasses [$x\text{PbO}:(1-x)\text{B}_2\text{O}_3$] were performed using a synchrotron radiation source at the beam line (BL-12) of

INDUS II at the Raja Ramanna Centre for Advanced Technology (RRCAT), Indore, India with 17 keV x-ray photons. Energy selection was done using a Si(111) single crystal. The Debye-Scherrer rings were detected using a high-purity Germanium (HPGe) image plate detector with 3450×3450 pixels. The diffraction image from the detector was integrated into two-dimensional patterns using FIT2d software for further analysis.

2.2.3 Density measurement

The density ρ of an object is defined as the ratio of its mass to its volume; $\rho = m/V$. Mass and volume are extensive (extrinsic) properties of matter. This means they depend on the amount of matter. Density is an intensive (intrinsic) property and reflects how much mass is packed into a given three-dimensional space. Experimentally, mass and volume measurements are required to calculate density. Masses are measured on electronic balances. An analytical balance (accuracy ± 0.0001 g) has been used for precise measurement of mass of the glasses.

Density determination is performed by Archimedes' principle (buoyancy method), which states that a body immersed in a fluid apparently loses weight by an amount equal to the weight of the fluid it displaces. This method allows determination of the density of solids, as well as liquids. However, precise determination of volume of the sample is not always straight forward. Simple and precise methods of mass determination can eliminate the need to measure volume. The buoyancy method involves weighing of a solid sample in both air ($M_{solid\ air}$) and a liquid ($M_{solid\ liq}$) of known density (ρ_{liq}) at constant temperature, to measure the density of the solid,

$$\rho_{solid} = \rho_{liq} \frac{M_{solid\ air}}{M_{solid\ air} - M_{solid\ liq}} \quad (2.59)$$

Densities of the glasses were measured with randomly chosen glass pieces using glycerine as the liquid medium. The error in density measurements is ± 0.005 g/cc.

2.2.4 Differential scanning calorimetry

Differential scanning calorimetry (DSC) is a thermal analysis technique to study thermal transitions in a substance. A material is heated and the changes taking place are recorded. Glass transition, crystallization, melting, etc. are examples of thermal transitions. DSC measures the difference in heat absorbed or released by a sample as compared to an inert reference, as both are heated, cooled or kept at constant temperature. The temperature program for a DSC is designed such that the sample holder temperature increases linearly as a function of time and the reference sample should have a well defined heat capacity over the entire temperature range to be scanned.

The instrument can be of two types: (a) power-compensated DSC, which keeps the power supply constant and, (b) heat-flux DSC, which keeps the heat-flux constant. In power-compensating DSC, the sample and reference are provided with different heating units with a temperature sensor and controller. The temperature difference between the sample and reference is maintained zero with the aid of a control loop mechanism. Whenever the sample or reference lags behind the expected programmed heating due to thermal transitions in the sample, excess heating power is given either to sample (during endothermic transition) or to reference (during exothermic transition) to maintain the temperature difference as zero.

In heat-flux DSC, the temperature difference between the sample and reference is recorded as a direct measure of the difference in heat flow to the sample and reference. Using calorimetric calibration, this signal is correlated to the difference in heat flow. In the present work, experiments were carried out using a heat-flux DSC.

The result of a DSC experiment is a curve of heat flux versus temperature or versus time. It is generally used to measure glass transition temperature (T_g),

crystallization temperature (T_c) and melting temperature (T_m). Glass transition occurs as the temperature of a glass is increased. This will appear as a step in the baseline of the recorded DSC signal. No thermodynamic phase transition occurs during a glass transition and the step is only due a change in heat capacity. As the temperature increases, the glass structure relaxes and becomes less viscous. At some point, the molecules may obtain enough freedom of motion to spontaneously arrange themselves into a crystalline form. This is known as devitrification and the temperature at which it occurs is called the crystallization temperature (T_c). This transition from glass to crystalline solid is an exothermic process and results in a peak in the DSC signal. As the temperature increases the sample eventually reaches its melting temperature (T_m). The melting process results in an endothermic peak in the DSC curve. Thus, the ability to determine transition temperatures and enthalpies of reactions makes DSC a valuable tool.

Glass transition temperatures of the lead-borate and lead-tellurite glass samples were determined by a heat flux DSC (M/s. Mettler Toledo model 821e/700, United States) with a heating rate of 10 K/min. For all measurements, nearly 30 mg of sample was taken in a Pt crucible. Empty Pt crucibles were used as reference and accuracy of measurement was ± 1 K. Kinetics of the glass transition was studied in lead-borate glasses $[x\text{PbO}:(1-x)\text{B}_2\text{O}_3]$ at 2, 5, 10 and 15 K/min to estimate the activation energy of glass transition.

Furthermore, since DSC allows performing a thermal analysis of the system by monitoring the enthalpy variations on varying the temperature across T_g , it was possible to collect information on the heat capacity, $C_p = (\partial H/\partial T)_p$. T_g is generally measured as the temperature corresponding to the change of curvature in the rise of C_p . The heat capacity for the glassy and supercooled phase of the lead-borate glasses were obtained by heating at a constant rate of 10 K/min, from the amorphous solid state. The jump in heat capacity

across T_g was measured as the difference between the C_p of the two states ΔC_p . Kinetics of crystallization was studied in a lead-tellurite glass [30PbO: 70TeO₂] at 2, 4, 6 and 10 K/min heating rates. The variation of the weight of samples used for crystallization studies was $\sim \pm 1 \mu\text{g}$.

2.2.5 Ultrasonic pulse echo technique

Ultrasonic pulse echo method is a nondestructive technique to study elastic properties of materials by determining the velocities of sound propagation. In this method, a very short ultrasonic pulse is created at the surface. When the wave reaches a boundary between two media, one part of energy is transmitted through the boundary and another part is reflected. This reflection/ backscatter from the internal structure or edge of the sample is analyzed. A transmitter generates an ultrasonic pulse wave which is reflected by the back wall of the specimen and obtained by the receiver.

The ultrasonic method uses two types of waves: longitudinal and transverse. In a longitudinal wave, the particle motion is in the same direction as the propagation of the wave, while in a transverse wave, the particle motion is perpendicular to the direction of the wave propagation. The delay time between the incident and reflected wave is measured. With a prior knowledge of the thickness of the sample, i.e., the path of traverse of the wave, the sound velocity can be estimated. The accuracy of estimation of sound velocities depends on the accuracy of thickness measured. In the present work, glass samples were polished by standard procedures and made optically flat. The thickness was measured using a screw gauge. The longitudinal and transverse sound velocity measurements were performed at room temperature using the ultrasonic pulse echo from a 15 MHz delay line contact transducer (Accu-Tron, United States). The accuracy of the measurement was $\pm 15 \text{ m/s}$.

2.2.6 Ellipsometry and refractive index

Ellipsometry is an optical technique for determining the dielectric properties of a material by measuring the change of polarization of light upon reflection/transmission and comparison to a model. It is important to ensure the polarization of incoming light is known, in order to successfully characterize the sample by measuring the polarization of the reflected light. For the present measurements, the ellipsometer uses a rotating compensator technique, which means that the incoming light is first linearly polarized and then there is varying phase difference added to the polarized light with a rotating angle. There is another polarizer on the detector side, which measures the actual polarization of the reflected light beam. Using white light sources and monochromators, spectral information can be obtained about the sample.

Ellipsometry measures the ratio of the complex Fresnel reflection coefficients. As this is a complex number, it can be divided into an amplitude term and a phase shift term, which correspond to the ellipsometric angles, amplitude ratio Ψ and phase difference Δ . These parameters contain the physical properties of the layer structure, such as the layer thickness and refractive index. The polarization state of light obtained by these parameters forms a highly nonlinear equation which needs to be solved by numerical methods, on a model-based approach. These models assume that the sample is composed of a number of homogeneous layers, with certain approximate thickness and optical functions. The relative phase shift, thus calculated, is compared with the measured quantities in a numerical regression procedure. The refractive indices of lead-tellurite glasses $[x\text{PbO}:(1-x)\text{TeO}_2]$ at 532 nm were obtained using a rotating polarizer-type ellipsometer (SOPRA, France).

3

COMPOSITION AND TEMPERATURE-INDUCED STRUCTURAL AND DYNAMICAL CHANGES IN LEAD-BORATE GLASSES AT DIFFERENT LENGTH-SCALES

3. 1. Introduction

Borate (B_2O_3) glass is a very good glass-former with an intriguing structure that has posed enormous fundamental challenges owing to its being completely different from the conventional silicate glasses [56]. B_2O_3 glass has a layered structure of boroxol (B_3O_6) rings, where each boron atom is three-coordinated (B_3) [86]. Borate glasses are extensively studied for their non-monotonic variation of properties upon the introduction of a modifier (the borate anomaly) [87]. This unique behaviour of borates is attributed to the presence of superstructural units at low modifier concentration and the conversion of some of the boron atoms from three- to four-coordinated species, when a modifier cation is added to the glass structure [86]. The negative charge on the created BO_4^- tetrahedron gets delocalized over the entire structural unit, which makes it energetically unfavourable for these tetrahedra to be immediate neighbours [88]. A large number of alkali, alkaline-earth and transition metal oxides have been used as modifier and the fraction of four-coordinated boron species (B_4) have been studied [87] across a large range of compositions using nuclear magnetic resonance (NMR) and optical spectroscopies, and several structural models have been proposed to corroborate these results [88]. It has been shown that small, divalent cations are not compatible with borate glass formation. Moreover, larger divalent cations also do not form single phase glasses at low modifier concentrations owing to the fact that two BO_4^- tetrahedra in close proximity are required to balance the charge on a divalent cation. Among other divalent cations, large and more

easily polarized cations (Ba^{2+} and Pb^{2+}) form single phase glasses even at very slow quenching rates as the large coordination shells of these cations help separate two BO_4^- tetrahedra by at least one BO_3 unit [88].

The differences in properties between the various modified borate glasses with the modifier oxide concentration, x , is due to the influence of the modifier cation on the borate network [56]. The critical role of the modifier cations in tuning the local network packing while they occupy cages within the network, has not been given enough attention in published literatures [86]. This occupancy of modifier cations further influences the distribution of superstructural units in the network. Therefore, it is important to consider the glass structure as a whole, which includes the superstructural units and the modifier cations, and the interplay between these constituents determines the variation of a particular property with x . Among the divalent modifiers, Pb^{2+} forms glasses over a broad glass-forming region [87]. The local structure of lead-borate glasses has been extensively investigated using various techniques such as neutron [89] and x-ray diffraction [90], Raman spectroscopy [91] and NMR [92] to understand the structural unit groups and their distribution, the coordination number of boron and lead, and the Pb–O bonding character.

Though these aspects reveal their short-range structure and influence properties like density, glass transition and sound velocities, the dynamical properties of glasses are often ascribed to structural correlations over an intermediate-range scale [93]. The manifestation of these correlations is found in two peculiar characteristics inherent to glassy systems: the first sharp diffraction peak (FSDP) [94] in the x-ray or neutron diffraction and the Boson peak [95] in the low-frequency vibrational spectra, which are based on static and dynamic properties, respectively. There are many reports which have correlated [96] the Boson peak and the FSDP, while others have contested [97] such

correlations. Although the appearance of the Boson peak [95] is a signature of the lack of long-range order, its frequency position and intensity depends strongly on the structure of the investigated system. Borate and modified-borate glasses exhibit substantial intermediate-range order [98] ($\sim 20 \text{ \AA}$) arising from the superstructural units. Network modifiers [99] play an important role in defining the length-scale of the intermediate-range order. Furthermore, the change of viscosity near T_g is governed by the flow unit size, and hence fragility characteristics of glass formers is also related to the intermediate-range structure [100]. B_2O_3 is a strong glass former and addition of modifier significantly changes its fragility [101]. The fragility of alkali-modified [102] and Sn-modified [103] borate glasses also exhibits the borate anomaly. Apart from viscosity measurements, calorimetric and spectroscopic techniques have been reliably utilized to quantify fragility in glasses [104].

Existing literature on borate glass modification using alkali or divalent metal oxides largely focus on the coordination change of boron and the ionic linkages formed in the network. PbO acts differently as it plays the dual role of modifier at low x and glass former at higher x [92]. Hence, lead-borate glasses can be expected to behave distinctly different from alkali-modified glasses. Most studies [105] on PbO-modified glasses have investigated the short-range structure [92] and found it to be similar to alkali modification. The valency of the cation will also affect the local packing of borate groups to satisfy the charge balance around it. This is expected to have an impact on the intermediate-range order, even though the local order may remain similar. Moreover, the study of the elastic properties over a wide temperature range is important to understand the nature of the supercooled liquid as it approaches the glass transition. Thus, the objective of this study is to present the nature of dynamic and structural behaviour in lead-borate [$x\text{PbO}:(1-x)\text{B}_2\text{O}_3$] glasses in a wide variation of x (20-80 mol% PbO) and their elastic properties above T_g . A detailed study of the borate structure using density, T_g ,

sound velocity, elastic constants and high-frequency Raman scattering have been reported. While these properties are governed by the local atomic structure, the dynamic properties are sensitive to the intermediate-range order. Low-frequency Raman spectroscopy was carried out to study the composition dependence of the Boson peak and to determine the dynamic correlation lengths. X-ray diffraction was carried out to detect the FSDP and to study its correlation with the Boson peak. Fragility was determined from the rate-dependent differential scanning calorimetry (DSC). The results are discussed in the context of anomalies in the behaviour of dynamic properties like Boson peak and fragility. The average coordination number $\langle r \rangle$ has been estimated for the various glasses and has been compared with fragility. Thus, the changes induced by the lead oxide modifier and the evolution of the structure with composition have been understood at different length-scales by combining calorimetric, spectroscopic and diffraction techniques. We have further discussed correlations among the various properties to elucidate the effect of Pb^{2+} on the borate glass network in the short- and intermediate-range length-scales. We have also investigated the elastic properties at high temperature up to 1150 K using Brillouin spectroscopy to study the evolution of the structure as a function of temperature and to elucidate the structural differences between the glassy and supercooled lead-borates.

3. 2. Experimental

Lead-borate glasses with compositions $x\text{PbO}:(1-x)\text{B}_2\text{O}_3$ ($x = 0.2, 0.3, 0.4, 0.5, 0.6, 0.7, 0.8$) were prepared by melt-quenching technique. Details of the synthesis procedure are discussed in Chapter 2. The values of T_g and heat capacity change at T_g (ΔC_p) were measured by a heat flux DSC at a heating rate of 10 K/min. Heating rate-dependent DSC was carried out at 2, 5, 10 and 15 K/min to determine the fragility values. The longitudinal and transverse sound velocity measurements were performed at room

temperature using ultrasonic pulse echo technique from a 15 MHz delay line contact-transducer (Accu-Tron).

All the samples used for the Raman scattering measurements were optically polished under same conditions and obtained with the same thickness. The high-frequency Raman spectra were collected using Renishaw (model Invia) micro-Raman spectrometer using 514.5 nm line from an Argon ion laser. In order to eliminate the trivial temperature effects, the raw spectra were corrected for the thermal population factor using, $I^{\text{red}}(\omega) = \omega I^{\text{expt}}(\omega) / [1 + n(\omega, T)]$, as described in Eq. 2.20, where $I^{\text{expt}}(\omega)$ is the measured Raman intensity, ω is the Raman shift in cm^{-1} and $n(\omega, T) = [\exp(\hbar\omega/kT) - 1]^{-1}$ is the Bose-Einstein occupation number. The low-frequency Raman spectra were excited with a diode-pumped solid state (Elforlight) laser ($\lambda = 532 \text{ nm}$) and were recorded in the spectral range $5\text{-}325 \text{ cm}^{-1}$ in the backscattering geometry using a Jobin-Yvon U1000 double monochromator and detected using a cooled photomultiplier tube (PMT). The focal point of the sample in these Raman measurements was first fixed by measuring real-time acquisition of the 521 cm^{-1} peak of a standard silicon crystal placed in a sample holder and adjusted for maximum counts. Silicon was used since the lead-borate glass samples do not have any sharp and intense Raman mode which could be used to adjust the maximum counts. The holder was fixed in that position of maximum counts such that every time a new glass sample was placed in it, the sample came automatically in focus. This made the focussing and optical alignment exactly same for each sample. All the measurements were made with same slit size of the spectrometer and for exactly same acquisition time per channel of PMT. The slit widths were so adjusted that the resulting spectral resolution was 0.25 cm^{-1} . The raw Raman intensity $I^{\text{expt}}(\omega)$ was corrected for the reduced Raman intensity $I(\omega)$ to determine the frequency of the Boson peak using the first-order approximation for disordered solids, $I(\omega) = I^{\text{expt}}(\omega) / \omega [1 + n(\omega, T)]$, as described in Eq. 2.23. The line shape of the Boson peak is well-fitted using a log-normal function

[106] to estimate the peak position. X-ray diffraction was measured using synchrotron source at INDUS II with 17 keV photons and detected using image plate detector. The data was recovered using FIT2d. To analyze the intensity of the FSDP, the asymptotic of intensity was fixed at large q . Treating this as $I(q) = 1$, the diffraction patterns were normalized with this intensity, so that asymptotically the pattern intensity goes to 1. This scaled intensity is used to fit a Lorentzian at the FSDP to evaluate its intensity, position and width.

Brillouin scattering experiments were performed in a 180° back-scattering geometry with a Sandercock (3+3)-pass tandem Fabry-Perot interferometer using a wavelength of 532 nm from a single-mode DPSS laser. The spectra were recorded between 300 and 1150 K using a commercially available heating stage with a stability of ± 0.1 K. The sample temperature was measured using a thermocouple placed adjacent to the sample inside the heating stage, while measurements were performed with increasing temperature. The Brillouin spectra were analyzed for mode frequencies and line widths through curve fitting.

3. 3. Results and discussion

3.3.1 Composition dependence of density, T_g and sound velocities

Fig. 3.1 shows the dependence of glass density and T_g on PbO in the lead-borate glasses. The values for B_2O_3 are taken from Kojima *et al.* [107]. It can be observed that the increase in the mole fraction of PbO in lead-borate glasses leads to a significant increase in density, while the T_g exhibits a broad maxima $\sim x = 0.3$. This is in good agreement with T_g data reported for alkali-borate glasses [108] and tin-borate glasses [109] and demonstrates the borate anomaly. The conversion of some boron atoms from B_3 to B_4 with the addition of PbO makes the bond character three-dimensional from the

previously layered borate glass structure and hence makes the glass structure tighter, which is responsible for the initial increase in T_g . Upon further addition of modifier, the conversion does not proceed and O/B ratio drops. The additional oxygens added from the modifier create non-bridging oxygens and weaken the structure, thereby reducing the T_g .

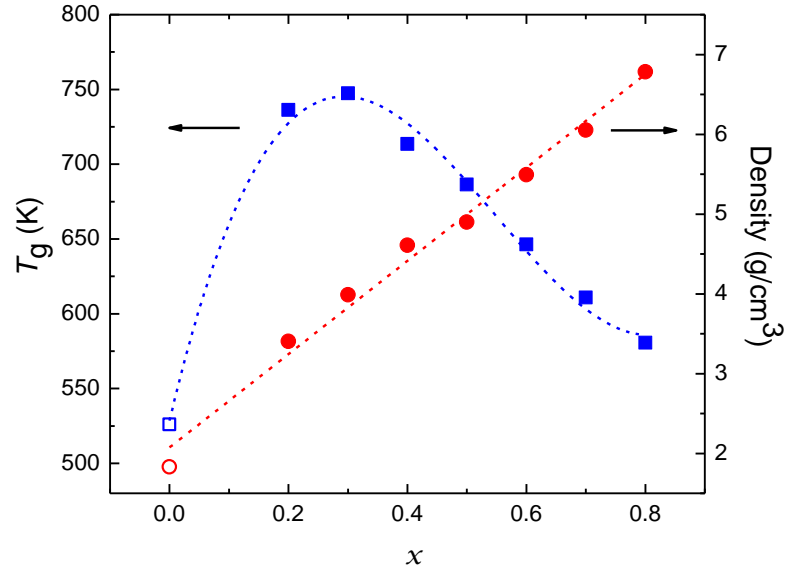


Fig. 3.1. The density and glass transition temperature (T_g) in lead-borate glasses of various composition x . Dashed lines are guides to the eye. Values for pure B_2O_3 (shown in open symbols) are from Ref. [107].

Fig. 3.2 shows the longitudinal (V_l) and transverse (V_t) sound velocities in the lead-borate glasses. These are used to estimate the Debye velocity,

$$V_D = \left(\frac{(1/V_l^3) + (2/V_t^3)}{3} \right)^{-1/3} \quad (3.60)$$

It can be seen that the sound velocities also exhibit a maxima at $x = 0.3$. This reflects the initial increase in network connectivity and later disruption of covalent bonds with increase of PbO. The composition dependence of the elastic moduli can be estimated from the sound velocities of these glasses using the following expressions:

$$L = \rho V_l^2 \quad (3.61)$$

$$G = \rho V_t^2 \quad (3.62)$$

$$K = L - \frac{4}{3}G \quad (3.63)$$

$$E = G \frac{(3L - 4G)}{L - G} \quad (3.64)$$

where L , G , K and E are the longitudinal, shear, bulk and Young's modulus, respectively. These values are shown as an inset in Fig. 3.2. It can be seen that the elastic properties exhibit a broad maxima $\sim x = 0.4$. The elastic moduli represent the ability of the structure to transmit elastic energy. Structural imperfections like disintegrated networking reduce the elastic constants. The increase in elastic moduli represents the enhancement in structural integration with increasing PbO, while its decrease indicates breakage of the borate glass network structure and rise in the number of non-bridging oxygens by formation of polyanions, which act as centres for energy dissipation of the elastic wave propagation.

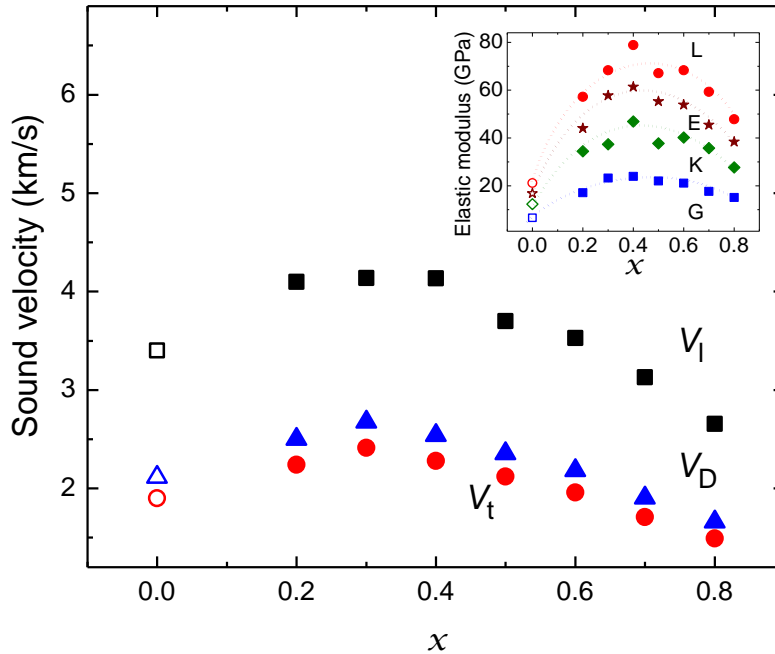


Fig. 3.2. The longitudinal (squares), transverse (circles) and Debye (triangles) velocities of the lead-borate glasses. Values for pure B_2O_3 (shown in open symbols) are from Ref. [107]. Inset shows the variation of the longitudinal (L), shear (G), bulk (K) and Young's (E) modulus. Dashed curves are guides to the eye.

The variation of properties based on cross-linking in the network of lead-borate glasses should be reflected from the composition dependence of the average coordination number $\langle r \rangle$. The Phillips-Thorpe topological constraint theory [24] predicts that a glass network is optimal (glass forming ability is maximized) if the number of mechanical constraints are just balanced by the number of atomic degrees of freedom. It establishes that a covalent network of discrete bonds undergoes a transition from floppy to stressed-rigid configuration near a rigidity percolation threshold, which occurs when the average number of covalent bonds per atom reaches $\langle r \rangle = 2.4$. The network is flexible or floppy for $\langle r \rangle < 2.4$ and over-constrained with $\langle r \rangle > 2.4$, while it is isostatic and stable at $\langle r \rangle = 2.4$. This deviation from the threshold has been associated with increase in fragility of many glassy systems [102]. Although, the theory was originally established for purely covalent systems, it has demonstrated similar results for oxide systems with some fraction of ionic bonding [102]. As PbO has been found to act as a glass modifier at low x and former at high x , we have calculated $\langle r \rangle$ considering the Pb–O bond as either purely ionic where only B–O bonds are considered for the calculation of $\langle r \rangle$, or as purely covalent where both Pb–O and B–O bonds are taken for the calculation. We have calculated the individual coordination numbers of the structural units (BO_4^- , BO_3 , BO_2O^- , BOO_2^{2-} , BO_3^{3-}) according to Hayashi *et al.* [109]. The average coordination number $\langle r \rangle = \sum c \langle n \rangle$, where $\langle n \rangle$ is the coordination number of a structural unit and c is its fraction at that composition. The fraction of a structural unit at a particular x has been estimated from the Gupta model [88] of structural units in borate glasses. Fig. 3.3 shows the composition dependence of the average coordination number calculated for (a) purely ionic and (b) purely covalent bonds. Pure B_2O_3 glass has $\langle r \rangle = 2.4$ which is the most stable glass topologically. For (a), the $\langle r \rangle$ value increases, maximizes at $x = 0.3$ and then decreases rapidly. It shows glasses with $x > 0.4$ are floppy. The same trend is followed in (b), except that the floppy regime starts with $x > 0.6$. The $\langle r \rangle$ values of the lead-borates

will be somewhere between these two extreme cases. It can be seen that for pure covalent bonding, the values for higher x are more close to the rigidity threshold and hence are expected to be stronger glasses compared to those with only ionic bonding. In either case, $\langle r \rangle$ is maximized at $x = 0.3$. This confirms the results obtained from T_g and the elastic properties. However, it has to be realized that this considers the borate network structure only and at higher x , PbO itself forms PbO_4 tetrahedra which may further increase the cross-linking in the glass.

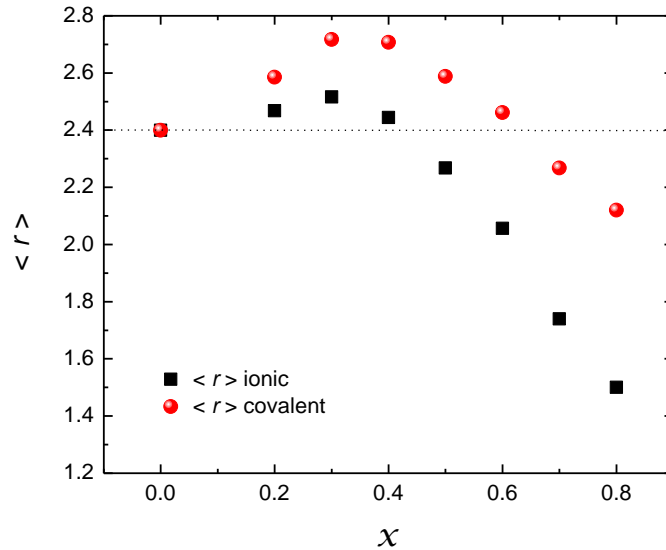


Fig. 3.3. Average coordination number calculated by considering (a) purely ionic bonds (black squares) and (b) purely covalent bonds (red circles).

3.3.2 Composition dependence of high-frequency Raman modes

In order to understand the changes in structural coordination along with bond behaviour in the glasses, Raman spectroscopy was carried out for the high-frequency modes. Fig. 3.4 exhibits the high-frequency Raman spectra of the lead-borate glasses for various x . The spectrum of pure B_2O_3 glass [110] exhibits a sharp intense peak at 806 cm^{-1} . It corresponds to the symmetric breathing mode of the six-membered boroxol rings. It shifts to lower frequencies (780 cm^{-1}) for $x = 0.2$, as seen in Fig. 3.4, lowers in intensity and gradually vanishes at $x = 0.4$. A nearby peak appears at 752 cm^{-1} for $x = 0.2$, rises in

intensity at the expense of the boroxol peak, then softens and finally disappears at $x = 0.5$. The decrease in intensity of this peak is simultaneously occupied by the growth of a peak at 695 cm^{-1} , which continues to pick up intensity with increasing x . A small hump appears at 600 cm^{-1} at $x = 0.5$ and rises in intensity as x increases. Another adjacent band appears $\sim 560 \text{ cm}^{-1}$ at $x = 0.6$ and grows in intensity with x . The band at 890 cm^{-1} is very weak for low x and grows intense with increasing PbO. The band at 1060 cm^{-1} grows in intensity up to $x = 0.4$ and then disappears with the appearance of a new band at 990 cm^{-1} from $x = 0.5$, which rapidly shifts to lower frequencies with increasing x . A broad band is present $\sim 1350 \text{ cm}^{-1}$ for all the spectra which shifts to lower frequencies with increasing x . A shoulder is present on its low-frequency side and a high-frequency shoulder appears at $x = 0.7$.

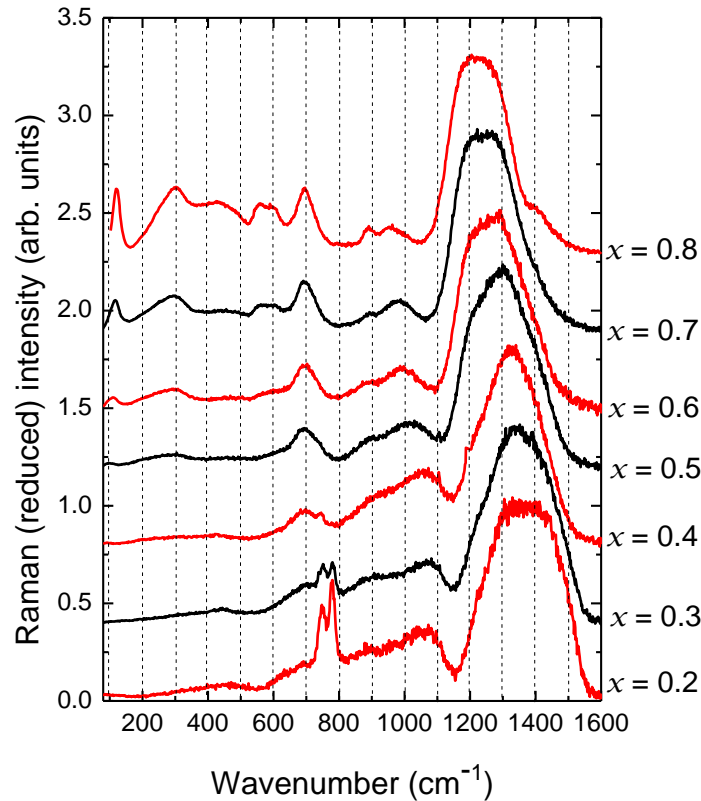


Fig. 3.4. High-frequency Raman spectra of lead-borate glasses corrected for the Bose factor.

A peak appears at 110 cm^{-1} for $x = 0.5$ and rises in frequency and intensity with increasing x . This peak has been assigned to the symmetric Pb–O stretch in the PbO_4 tetragonal pyramid [111]. Two more peaks appear at 300 and 450 cm^{-1} at $x = 0.5$ and increase in intensity with x and are assigned to vibrations of crystalline PbO [112]. The appearance of these bands for $x \geq 0.5$ confirms the role of PbO as a glass former for higher concentrations.

Table 3.1. Mode wavenumber and assignment of the high-frequency Raman bands in lead-borate glasses.

Wavenumber (cm^{-1})	Band assignment
110, 300, 450	Pb–O vibrations in PbO_4 tetragonal pyramid
560	Vibrations of loose BO_4^- tetrahedra
600	In-plane bending mode of orthoborate units (BO_3^{2-})
695	Ring-breathing vibration of ring-type metaborates
752	Symmetric breathing vibrations of six-membered rings containing BO_3 triangles and BO_4^- tetrahedra
780	Symmetric breathing mode of boroxol rings
890	Due to pentaborate groups; vibrations of diborate groups; symmetric stretching of B–O–B bridges in pyroborate ($\text{B}_2\text{O}_5^{4-}$) groups
990	Symmetric stretching vibration of planar orthoborate units
1060	Vibrations of diborate groups
1220	Symmetric stretching vibration of terminal B–O \cdot bonds in pyroborate units
1350	Stretching vibration of the terminal B–O \cdot bonds in metaborate triangular units
1500	Out-of-plane bending mode of orthoborate units

Since Raman spectra of crystalline PbO does not have bands $> 500\text{ cm}^{-1}$, all the other bands have been assigned to the borate network structural units [59]. Assignment of the Raman mode wavenumber is given in table 3.1. The peak at 752 cm^{-1} is assigned in literature [110,113] to the symmetric breathing vibrations of six-membered rings with

one (triborate, tetraborate or pentaborate) or two (diborate, ditriborate or dipentaborate) BO_4^- tetrahedra. Crystalline α - $K_2O \cdot 5B_2O_3$ contains only pentaborate groups and produces Raman bands at 765 and 885 cm^{-1} . Raman frequency for tetraborate and triborate groups is ~ 770 cm^{-1} . This is indicative of the presence of pentaborate units [59] in the present lead-borate glasses owing to the simultaneous occurrence of the band at 890 cm^{-1} . The increase in intensity of the 752 cm^{-1} peak with concurrent decrease of the 780 cm^{-1} peak demonstrates the conversion of B_4 at the expense of B_3 . The peak at 695 cm^{-1} is attributed to ring-type metaborate units [114]. Its increase with the simultaneous decrease of the 752 cm^{-1} peak indicates the disruption of pentaborate groups with increasing x . However, the 890 cm^{-1} band increases in intensity implying that some other units also have a Raman band in that region. The bands at 890 and 1060 cm^{-1} have been assigned to diborate groups in lead-borate glasses [59]. This implies the growth of diborate units as the concentration of PbO increases. Hence, above $x = 0.3$, diborate units are the predominant superstructural units containing four-coordinated boron atoms. The 1060 cm^{-1} band disappears around $x = 0.5$ and the 695 cm^{-1} peak grows more intense. This shows that diborate units are destroyed along with formation of metaborate rings or loose diborate groups at higher PbO concentration. The band at 890 cm^{-1} represents pentaborate units at low x and diborate units at $x > 0.3$. However, diborate groups disappear at $x = 0.5$ and yet the 890 cm^{-1} band continues to increase. For $x > 0.5$, the 890 cm^{-1} band is assigned [113] to the symmetric stretching of B–O–B bridges in pyroborate ($B_2O_5^{4-}$) groups, indicating back-conversion of B_4 to B_3 . The band at 990 cm^{-1} is assigned to the symmetric stretching vibration of planar orthoborate units (BO_3^{3-}). The two low-intense bands at 600 and 560 cm^{-1} are assigned to the in-plane bending mode of orthoborate units and loose BO_4^- tetrahedra, respectively [91]. The intense high-frequency envelope at 1350 cm^{-1} downshifts in frequency to 1225 cm^{-1} for $x = 0.8$. This band has been assigned to the stretching vibration of the terminal B–O $^-$ bonds in metaborate triangular units

[114]. The low-frequency shoulder is assigned to the symmetric stretching vibration of terminal B–O⁻ bonds in pyroborate units [113] while the high-frequency shoulder represents out-of-plane bending mode of orthoborate units [91].

Therefore, the evolution of the Raman spectra with increasing PbO indicates the depolymerization of the borate network through the formation of borate structural anions which are detached from the covalent network. PbO acts as a glass former from $x = 0.5$. Boroxol groups exist up to $x = 0.4$, while BO_4^- tetrahedra appear in ring structures from $x = 0.2$ with the formation of pentaborate units and disappear at $x = 0.5$. The disruption of pentaborate units result in the formation of ring-type metaborates. Diborate units are the major B_4 containing groups from $x = 0.3$ to 0.5. Above $x = 0.5$, pyroborates, orthoborates and loose BO_4^- tetrahedra form the major components of the borate structural units in the lead-borate glasses.

3.3.3 Composition dependence of low-frequency Raman spectrum

The low-frequency ($10\text{-}200\text{ cm}^{-1}$) vibrational spectra of glasses exhibit a universal characteristic feature called as the Boson peak. This peak arises due to an excess of low-energy vibrational states, not accounted for in the continuum elastic prediction of the Debye model and appears as an asymmetric broad band in the low-frequency Raman [43,115] or neutron [45,116] scattering. Fig. 3.5(a) shows the Boson peak in lead-borate glasses for various x . Even though, the intensity of the Boson peak is considered as a measure of disorder of the glassy network, it is actually quite difficult to compare absolute intensities of different Raman spectra, especially, when glasses of variable composition are involved. In order to normalize the effect of focussing and optical alignment on the Raman intensities, careful experiments were carried out as described in section 3.2. After obtaining the Raman spectra, a background corresponding to the value of Raman intensity at the highest investigated frequency (325 cm^{-1}) was subtracted from

each spectrum. It was then found that the high-frequency tail of the Boson peak gets to the same value in all samples as depicted in Fig. 3.5(a). From this, it was found reasonable to compare the Boson peak intensity of the different samples, discussed later in this work, as it is also expected that addition of more amount of highly polarizable Pb^{2+} cations will affect the Raman intensity. The Boson peak has been fit with a log-normal function [106] as shown in Fig. 3.5(b), to obtain the peak frequency and intensity:

$$I_{BP}(\omega) = B \exp \left\{ -\frac{[\log(\omega/\omega_{BP})]^2}{2W^2} \right\} \quad (3.65)$$

where ω_{BP} is the Boson peak frequency, W is related to the width of the Boson peak and $B = \frac{I_0^{BP}}{\sqrt{2\pi W^2}}$ and I_0^{BP} is the amplitude factor. The Boson peak shifts in position and grows in intensity as PbO is increased. A second peak develops in the high-frequency wing of the Boson peak for glasses with $x > 0.4$. This peak at 130 cm^{-1} for the glass with 80 mol% PbO is assigned to the symmetric Pb–O stretch in PbO [111]. The Raman spectrum of β -PbO also has a strong peak in this frequency [117], which indicates that Pb atoms in these glasses are arranged in the same structural arrangement as in the crystalline oxide. This peak was also observed in the high-frequency Raman spectra in Fig. 3.4. ^{207}Pb NMR [92] affirms the presence of such pyramids in lead-borate glasses with higher x . This peak increases in frequency and intensity with increasing x , indicating stiffening of Pb–O stretching vibrations due to increased covalency and increase in the number of such PbO_4 pyramidal units which enhance the role of PbO as a glass former.

The Boson peak positions extracted from the fits are shown in Fig. 3.6. It can be observed that the Boson peak also exhibits a behaviour similar to the borate anomaly, apart from an anomalous dip at $x = 0.3$. This is in contrast to the composition dependence of other structural features where a maxima was observed at $x = 0.3$. The composition

dependence of the Boson peak frequency in alkali-borate glasses were found to increase with x and so did their transverse sound velocities [113]. The shift of Boson peak in lead-borate glasses is therefore, different from other modified borates. Owing to the transverse character and acoustical energy range of the Boson peak, it can be thought to originate merely from the variation of the elastic constants and density. If it is so, it should vary like the Debye frequency,

$$\omega_D = V_D (6\pi^2 \rho)^{1/3} \quad (3.66)$$

where ρ is the density. Inset to Fig. 3.6 shows a comparison of ω_{BP} and ω_D where the frequencies have been normalized to 1 for $x = 0$. It can be seen that the relative shift of the Boson peak is very much different from that of the Debye frequency. ω_D shows a maximum at $x = 0.3$ and varies according to the short-range structural change induced by PbO in the vitreous structure as mentioned earlier. But the evolution of the Boson peak does not follow this pattern and therefore must originate from orderings beyond the atomic distances.

Several models have been proposed to interpret the excess vibrational contribution leading to the appearance of the Boson peak. The explanations in these models can be roughly grouped into three classes: (a) soft potential or defect models, (b) models with spatially fluctuating elastic constants that strongly scatter sound waves, and (c) models associated with nanometric heterogeneities. In the present study, we have tried to understand our experimental results based on the concepts of these different models. Table 3.2 summarizes the inferences drawn using these models, discussed below in the context of lead-borate glasses. However, as discussed in Chapter 1, it is extremely difficult to ascertain experimental results to a particular model and establish its applicability. In this thesis, we have not carried out analysis of the Boson peak to establish any of these models.

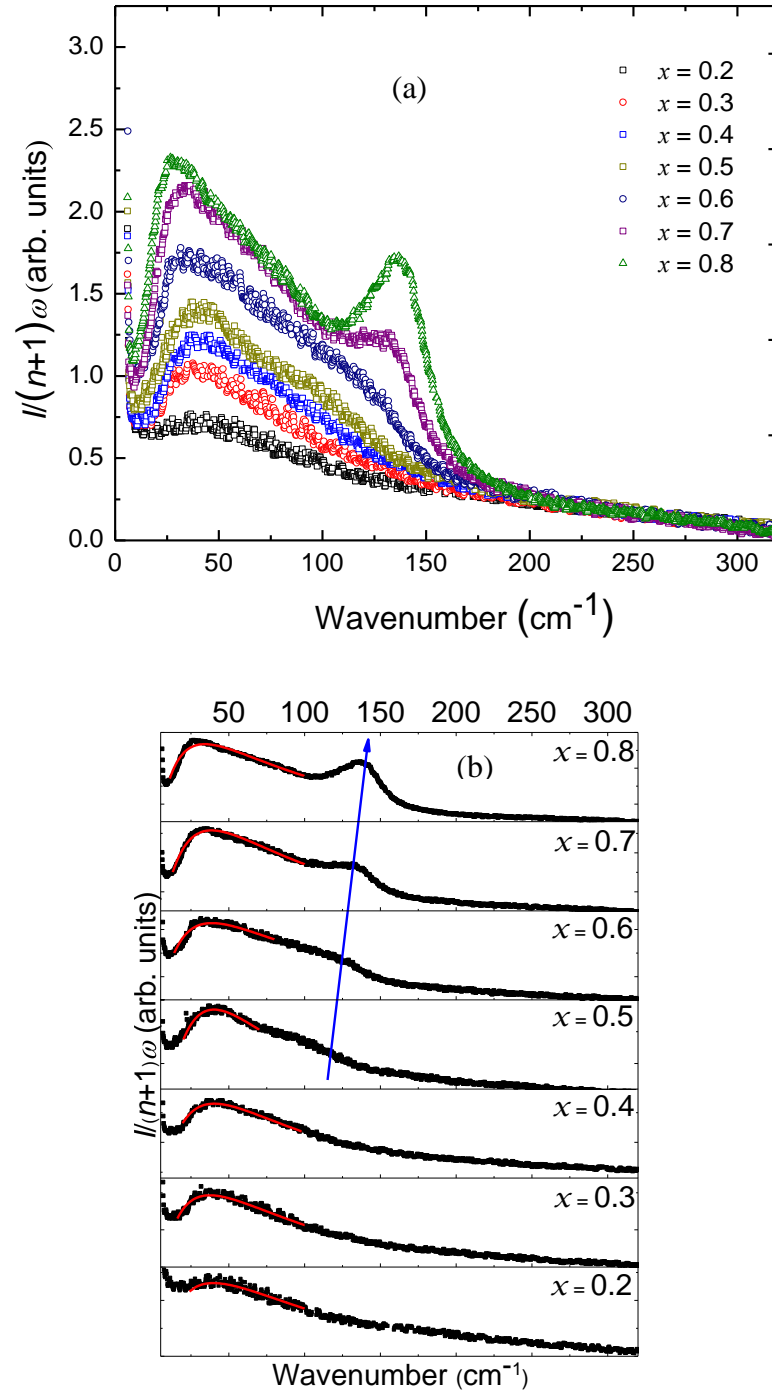


Fig. 3.5. Low-frequency Raman (reduced) spectra for the lead-borate glasses (a) depicting the background-corrected Boson peak with the high-frequency tail reaching the same value in all samples, which aids for a reasonable comparison of intensities from (b) the log-normal fits shown by the red curves. The blue arrow is a guide to the eye for the growing peak assigned to lead oxide polyhedra.

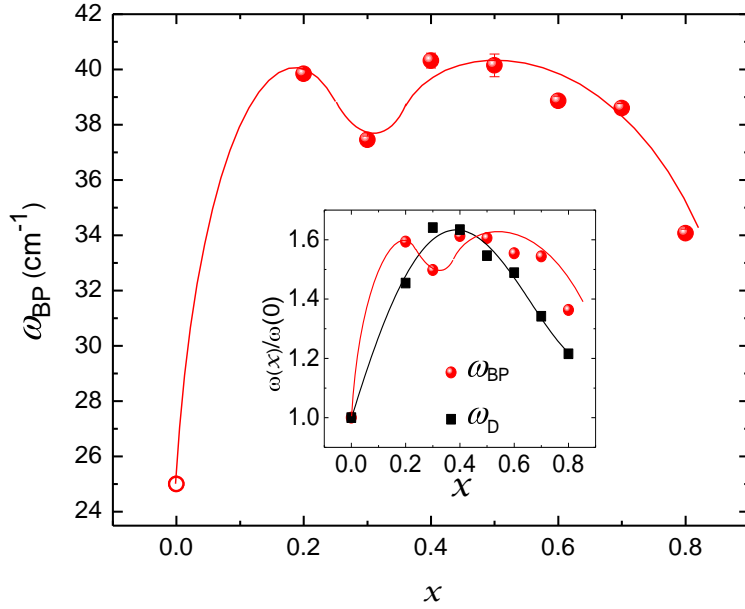


Fig. 3.6. Boson peak frequency of lead-borate glasses. Value for pure B_2O_3 are from Ref. [107]. Inset shows the Boson peak frequency and the Debye frequency normalized to 1 for $x = 0$.

Defect models [118] demonstrate that defects with very small elastic constants, near which anharmonic interactions are important (soft potentials), can generate quasi-local states, which if hybridized with acoustic excitations, results in a Boson peak [49,119]. Detailed information about the short- and intermediate-range structure of glasses is frequently obtained by comparing vibrational spectra of glasses and crystals precipitating from these glasses. The increased electrostatic interactions of the rattling guest cations hosted in the low atomic density regions of alkali-borate glasses were assumed to be responsible for shifting of the position of the Boson peak [44,120]. Intense bands in the far-infrared spectra were observed in lead-phosphate glasses which were assigned to the vibrations of the localized metal cations [121]. Also, the low-frequency vibrational modes of the corresponding crystalline samples correlate well with the range of localization of the Boson peak of the lead-containing glasses [121,122]. Pb^{2+} is a heavy cation and the rising polarization power of Pb^{2+} with increasing content of PbO enhances the rattling motion in the lead-borate glasses and causes the Boson peak to shift

to higher frequencies. Decrease in intensity of the Boson peak is a natural consequence of the mode shifting to higher frequencies [44]. Upon further increasing PbO, the Pb–O bond length decreases as the bonds acquire increasing covalent character ($x \geq 0.5$). At these compositions, Pb is no longer weakly coupled in the network. Therefore, the electrostatic interactions decrease with simultaneous reduction in the rattling and shifting of the Boson peak to lower frequencies and concurrent increase of intensity.

In the models [51,123] with spatially fluctuating elastic constants, the Boson peak marks the low-frequency bound of a band of randomly hybridizing delocalized states [118]. Localized states were only found [118] near the Debye frequency, i.e., in the high-frequency regime of the vibrational spectrum. Schirmacher *et. al.* [124] solved a fluctuating force-constant scalar-vibration model using a Gaussian distribution of nearest-neighbour force constants, with a lower cutoff, which was allowed to extend into the negative force constants regime. The disorder in this model was found to give rise to a Boson peak. They showed that shifting the cutoff of the truncated Gaussian distribution down (increasing the disorder), leads to a downshift of the maximum of the Boson peak with a concurrent increase in intensity, and further showed that shifting the cutoff below a critical (negative) value led to an instability and concluded [125] that the Boson peak is a precursor of an elastic instability [126]. This implies that the degree of disorder decreases and then increases with increasing x for the lead-borate glasses, as depicted by the position of the Boson peak in Fig. 3.6.

From the point of view of the defect (local oscillators) models, the vibrations giving rise to the Boson peak arise as a result of quasilocal excitations supposed to be connected with some correlation length of the vitreous structure. These models associate the Boson peak with the characteristic frequency of vibration of nanometer-sized clusters [127]. Models associated with nanometric heterogeneities attribute the Boson peak to

phonon localization by glass disorder through the mechanism of strong scattering of phonons by density fluctuations [128,129]. All of these models associate the Boson peak with a dynamic correlation length L , which represents a range over which the system is homogeneous for phonons and for the light that they scatter,

$$L = V_t/2\pi c\omega_{BP} \quad (3.67)$$

corresponds to dynamic correlations or density fluctuations in the intermediate-range and hence is an estimation of the intermediate-range length-scale in these glasses. Here, V_t is the transverse sound velocity and c is the velocity of light in vacuum. On the other hand, assuming spatially fluctuating shear modulus in the model of fluctuating elastic constants, it emerges that the transverse vibrational degrees of freedom, affected by the structural disorder are responsible for the Boson peak, which occurs at the frequency at which the mean free path of the transverse waves becomes equal to their wavelength (Ioffe-Regel limit [36]). Schirmacher [130] made a comparison of the fluctuating elasticity model with the local oscillator model and showed that the quasi-local disorder-induced oscillators described in the soft-potential model if coarse-grained in a mesoscopic volume, will lead to spatially fluctuating elastic constants, and thus, a combination of both models provide a fair description of the VDOS of network glasses. Fig. 3.7 shows the composition dependence of L in lead-borate glasses. The correlation L decreases with increasing PbO, except for an increase at $x = 0.3$. However, since the density also increases with x , the decrease in L does not necessarily mean the decrease in intermediate-range order. To understand the true behaviour of these correlations, we compare L with the average inter-particle length,

$$a = \left[\frac{M(x)}{\rho(x)} \right]^{1/3} \quad (3.68)$$

where $M(x) = xM(\text{PbO}) + (1-x)M(\text{B}_2\text{O}_3)$ is the molar mass of the respective glass composition. The variation of a with x is shown in inset 'a' in Fig. 3.7. Even though, it

exhibits a non-monotonic decreasing trend, the ratio L/a as shown in inset ‘b’ in Fig. 3.7 depicts an exactly similar trend to the variation of L . This demonstrates an absolute decrease in the correlations with increasing x , apart from the anomalous rise at $x = 0.3$.

Table 3.2. Summary of the various models for the Boson peak.

Model	Basis of the model	Inference on lead-borate glasses
1. Defect models <ul style="list-style-type: none"> • Soft potentials • Rattling ions 	<ul style="list-style-type: none"> • Anharmonic soft potentials generate quasi-local states, which hybridize with acoustic modes to give rise to a Boson peak • Increased electrostatic interactions of the rattling cations shift the Boson peak spectrum 	<ul style="list-style-type: none"> • Characteristic frequency of vibration of nanometer-sized clusters define a dynamic correlation length which exhibits a monotonic decrease with a peak at $x = 0.3$ • Initial increase of PbO increases the rattling motion of Pb^{2+} and shifts the Boson peak to higher frequencies, while further increase of PbO increases the covalency in the network and the peak shifts to lower frequencies
2. Models with spatially fluctuating elastic constants	Boson peak marks the low-frequency bound of a band of randomly hybridizing delocalized states	The degree of disorder decreases and then increases with increasing x for the lead-borate glasses
3. Models associated with nanometric heterogeneities	Nanometric inhomogeneities cause mean free path of the transverse phonons to become equal to their wavelength (Ioffe-Regel limit)	Phonon localization by nanometric density fluctuations result in the dynamic correlations given by L

In order to understand the anomalous behaviour of the Boson peak at $x = 0.3$, the other unique feature of borate glasses, i.e. the presence of superstructural units at low values of x has to be invoked. The idea of a random network structure of borates comprising superstructural units was initiated by Krogh-Moe [131] and further supported by Bray [132]. The largely open structure of a network with more of superstructural units

compared to the basic BO_3 and BO_4 structural units results in a low-density structure. There is evidence of the presence of superstructural units in the borate melts which inhibits crystallization and promotes glass forming ability of borate systems [88]. These units are made of well-defined arrangements of the basic borate structural units with no internal degrees of freedom. A systematic formation and then destruction of superstructural units (pentaborate, tetraborate, diborate, pyroborate and orthoborate groups) with increasing Li_2O , which comprise the main components of the borate network was found in $Li_2O-B_2O_3$ glasses [133].

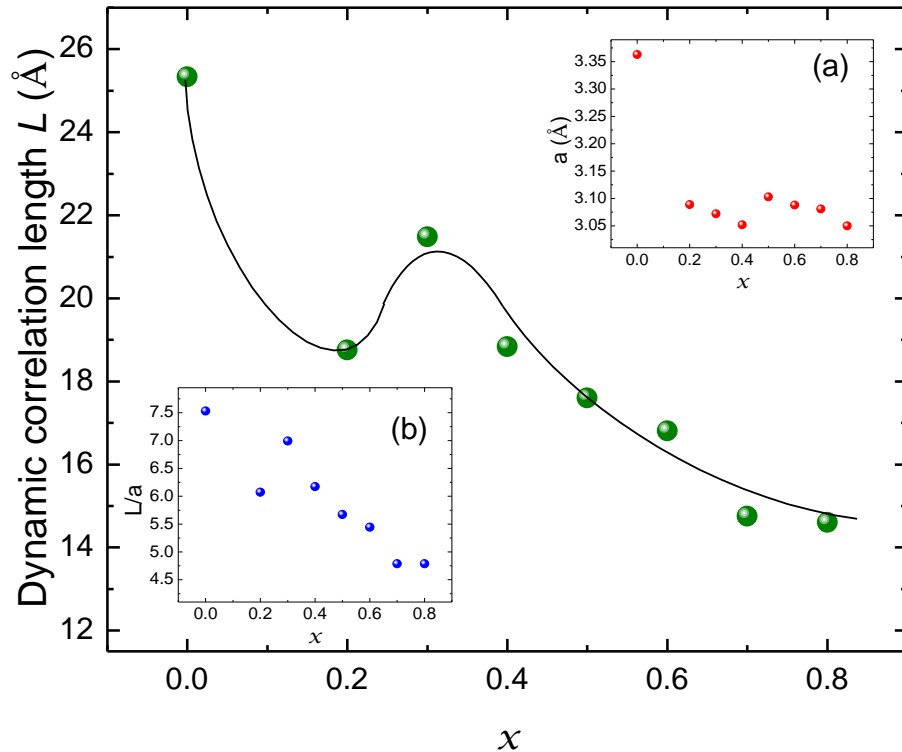


Fig. 3.7. Dynamic correlation lengths in lead-borate glasses. Insets show the variation of (a) the average inter-particle distance, a and (b) the ratio of the dynamic correlation length L to a with increasing x .

The origin of the Boson peak in B_2O_3 glass has been attributed to the vibrational motion of boroxol rings from inelastic neutron scattering [116] and hyper-Raman scattering studies [134]. The boroxol units are thus considered to give rise to the intermediate-range order in B_2O_3 glass. The introduction of PbO , which acts as a glass

modifier at low concentrations, increases coordination number of some borons and results in formation of superstructural units with four-fold coordinated borons. NMR investigations on modified borate glasses depict that fraction of boroxol and loose BO_3 units decrease, while tetraborate, diborate and loose BO_4^- units increase at their expense with increasing x . Raman analysis of the high-frequency vibrational modes also present a similar picture (Fig. 3.4). This coexistence of different types of structural units reduces the length-scale of the intermediate order and hence the dip in L at $x = 0.2$. Moreover, the fraction of pentaborate and tetraborate units, which are much bigger units in comparison to other borate superstructural units maximizes [135] at $x = 0.3$, and then decreases (also confirmed from Raman analysis). This makes the correlation length to increase at $x = 0.3$. Similar viewpoint was demonstrated by Uchino *et al.* [136] using molecular orbital calculations depicting the Boson peak in B_2O_3 as arising from standing waves formed from the localized vibrations over a pair of boroxol rings. The normal mode analysis exhibited out-of-plane bending motions of the whole skeleton of the cluster, whose wavelength became shorter with increasing frequency of the modes. The mean-free path of the low-frequency mode was found to be limited to the intermediate-range order by virtue of the phase cancellation process induced by the disorder [136]. Thus, the increase of correlation length at $x = 0.3$ in the lead-borate glasses derives from the growing length-scales of the superstructural units predominant at that composition. Furthermore, as pointed out earlier, the effective radius and charge of the network-modifying cation, and the degree of ionicity in its bonding is an important stereochemical consideration in the glass network. Krogh-Moe [88,137] observed that the structures of crystalline $SrO \cdot 2B_2O_3$ and $PbO \cdot 2B_2O_3$ ($x = 0.33$ for glass) consist of a network of corner-sharing BO_4^- units where one of the oxygen atoms in the asymmetric unit is 3-coordinated by boron (OB_3^+) unit. This structure demonstrates a precarious balance of boron coordination number between 3 and 4, along with low activation energy for activating states with 4-

coordinated boron and 3-coordinated oxygen. The dynamic correlation length of lead-borate glass at $x = 0.3$ could be high owing to such a bond-switching mechanism in the glassy state. Beyond $x = 0.3$, non-bridging oxygens are formed in the structure which reduces L . However, the diborate fraction continues to increase till [138] $x = 0.5$ and PbO acts as a glass former [92] for $x > 0.5$. There is a competition between these opposing factors and hence decrease in L slows down and saturates $\sim x = 0.7$.

3.3.4 Composition dependence of FSDP

Intermediate-range order in glasses is also captured by another almost universal feature in glasses, the FSDP. This feature of the diffraction data which appear for network-forming glasses and liquids, is supposed to be related to the presence of a non-random structural ordering beyond the short-range order. Since, by definition, every diffraction pattern must have a first peak, the term FSDP is reserved for those pre-peaks to the main diffraction pattern that behave in an anomalous way compared with other diffraction peaks, as a function of temperature, pressure or composition; such FSDPs are characteristic of cross-linked network-forming glasses [139]. Fig. 3.8 shows the scaled intensity of the x-ray diffraction patterns of the lead-borate glasses. These results are in good agreement with those of Takaishi *et al.* [92]. The first feature in the structure factor of pure B_2O_3 [140] is a peak at $Q_1 = 1.61 \text{ \AA}^{-1}$. On the addition of just 20 mol% PbO to the B_2O_3 network, a new peak arises at $Q_0 = 1.19 \text{ \AA}^{-1}$, implying ordering on a larger length scale. This peak shifts to higher Q values and lowers in intensity with increasing x . It is not discernible above $x = 0.6$. However, the FSDP observed in B_2O_3 at 1.61 \AA^{-1} is replaced by a second peak at larger Q ($Q_1 \sim 1.95 \text{ \AA}^{-1}$) in the lead-borate glasses. The intensity of this peak increases with x but it exhibits almost no change in position. Therefore, two clear peaks, Q_0 and Q_1 are observed in all the low-lead glass compositions, one below and one above the position of the FSDP in pure B_2O_3 glass.

Their position and intensity appear to be strongly dependent on the concentration of the modifier oxide.

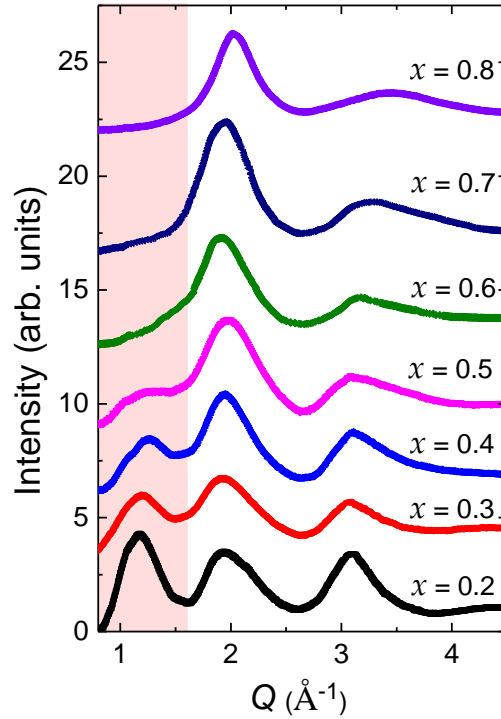


Fig. 3.8. X-ray diffraction of the lead-borate glasses depicting the first sharp diffraction peak (FSDP) in glasses with low x in the shaded region.

From a combination of neutron and x-ray diffraction, Price *et al.* [141] could correlate the contributions from different atom pair-correlations to the first two peaks in the structure factor of rubidium-germanate glasses. These glasses have shown the evidence of a similar pre-peak in the static structure factor after the addition of rubidium oxide. Furthermore, a modifier atom with positive scattering length will reduce the contrast between the structural units and the filled void and therefore will reduce the FSDP intensity, while a modifier atom with negative scattering length will have the opposite effect and increase the intensity of the FSDP [142]. On similar lines, we ascribe Q_1 to the cation-cation correlations arising from structural voids resulting from the arrangements of BO_3 or B_3O_6 units present in the boron matrix. On the other hand, we

ascribe Q_0 to the correlations arising from rings of wider size originating from the structural modifications of the network by the lead cations.

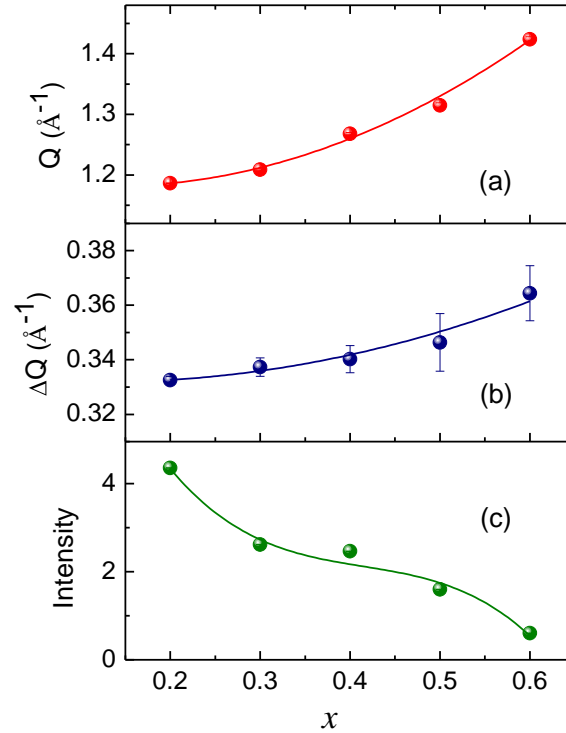


Fig. 3.9. FSDP (a) position, (b) width and (c) intensity for various x .

Fig. 3.9 shows the position, width and intensity extracted from fitting the pre-peak Q_0 . As can be observed, the position and width increase with increasing x . The increase in width signifies the decrease in correlations while its position reflects some repetitive characteristic distance between structural units. The decrease in its intensity as shown in Fig. 3.9(c) indicates that the structural units leading to the intermediate-range ordering are poorly defined. Elliot [33] ascribed the FSDP to a chemical-order pre-peak arising from the clustering of interstitial voids around cation-centred clusters, where the FSDP position is given by,

$$Q = 2\pi/D \quad (3.69)$$

where D is termed as the static correlation length [143]. The FSDP in B_2O_3 glass thus corresponds to a correlation length $\sim 3.90 \text{ \AA}$, while the peak Q_1 corresponds to a length scale $\sim 3.14 \text{ \AA}$. This is slightly smaller than the characteristic length for the intermediate-range order in B_2O_3 glass. Also Q_0 shows a decrease in correlation length from 5.30 \AA at $x = 0.2$ to 4.41 \AA at $x = 0.6$, as depicted in Fig. 3.10. This pre-peak is assigned as the FSDP in the modified-borate glasses as its behaviour can be explained in terms of a chemical ordering of Pb and B with a period given by D . The FSDP in pure B_2O_3 glass arises from the succession of network cages, while in the lead-borate glasses, Pb^{2+} cations enter the larger cages and displace the oxygen atoms on their boundaries. This peak is, therefore, associated with strong oxygen correlations and with a chemical order arising from the alternate arrangement of B and Pb. As more and more Pb replace B, decaging of the Pb^{2+} cations occur and the topological ordering of oxygen atoms around Pb^{2+} is hindered; also the chemical ordering of the two cations is broken. This decreases the length scales of Q_0 and reduces the number of such voids, thereby reducing its intensity with increasing x . Moreover, as the increase in molar concentration of PbO simultaneously increases the coordination number of boron from 3 to 4 and decreases the coordination number of lead cation [92] from 6 to 3, the length-scales of the correlations [143] arising from the structural voids decreases and the FSDP position shifts to larger Q . PbO acts as a network former possessing PbO_4 pyramidal units for $x > 0.5$. The cation-cation correlations in these structures add to the intensity of Q_1 without shifting its position.

Fig. 3.10 depicts a comparison of the dynamic and static correlation lengths obtained from Boson peak and FSDP, respectively. It can be observed that the values of D are small compared to L . Inset to Fig. 3.10 shows that these correlation lengths are not related linearly and hence refer to different spatial regions in the structure. Unlike L , D does not exhibit an abrupt rise at $x = 0.3$. The dynamic correlation length (L) signifies an

intermediate-range order arising from the superstructural units. Since D decreases with increasing x , it implies that the distance between the cation-centred voids reduces. This in turn shows that the characteristic length of the structural units also decreases with a concurrent increase in their number density. This is also affirmed by the increase in Boson peak intensity (Fig. 3.14 inset (b)) with increasing x , which shows that the number of such units giving rise to L increases. Fig. 3.12 depicts a schematic of the two different correlation lengths present in the lead-borate glass network and their variation in the low-lead glasses.

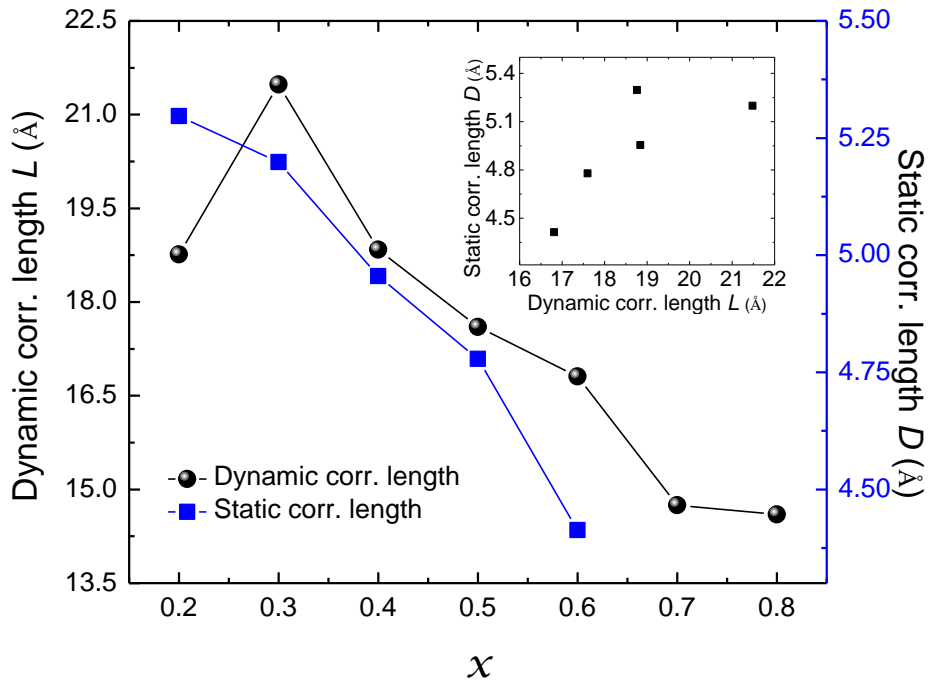


Fig. 3.10. Dynamic and static correlation lengths. Inset shows that these correlation lengths are not related linearly.

3.3.5 Composition dependence of fragility

The fragility m of glass forming liquids is obtained from the slope of $\log \eta$ vs. T_g/T plots as,

$$m = \left[\frac{\partial \log \eta}{\partial (T_g/T)} \right]_{T=T_g} = \frac{E}{RT_g} \quad (3.70)$$

where η is the viscosity, E is the activation energy of viscous flow at T_g and R is the gas constant. This is also known as the kinetic fragility. For most inorganic liquids, the activation energy for glass transition, E_a , is indistinguishable [144] from the activation energy E of viscous flow at T_g . Therefore, determining the values of E_a is often undertaken to understand the strong-fragile characteristics of the glass forming liquids. E_a can be determined from the specific heat measurements across T_g or from the dependence of T_g on the heating rate β of the glass [104]. According to the structural relaxation model of the glass transition [144],

$$\log \beta = - \frac{E_a}{RT_g(\beta)} + \text{const.} \quad (3.71)$$

where $T_g(\beta)$ is the glass transition temperature measured at heating rate β . The slopes of the plots of $\log \beta$ vs. $1/T_g(\beta)$ gives the activation energy values as E_a/R . Inset to Fig. 3.11 shows these plots for the lead-borate glasses. The fragility is then estimated as,

$$m = \frac{E_a}{RT_g^m} \quad (3.72)$$

where T_g^m is the mean T_g measured for various heating rates β . The m values for the lead-borates are presented in Fig. 3.11. Value for $x = 0$ is taken from Novikov *et al.* [145]. The fragility dependence on PbO also behaves similar to the Boson peak, as it increases and then decreases with a similar anomalous dip $\sim x = 0.3$. This shows that the fragility first increases with addition of PbO. Fragile liquids comprise of structures that fluctuate over a variety of orientations and coordination states. The lead-borate glass at $x = 0.2$ exhibits coexistence of different superstructural units emerging from the conversion of some B_3 to B_4 units and the introduction of Pb^{2+} changes the intermediate-range order by forming constrained sites [136] that are unstable and promote structural reorganization that leads

to increased fragility. Hence, the presence of different groups like boroxols, triborates, pentaborates aids to fragility in this glass. Fragility decreases thereafter for $x = 0.3$ which shows that the corresponding liquid gains characteristics of a strong glass former. This is due to the increase in the fraction of pentaborate and tetraborate groups at this composition, which show simultaneous increase in L . It is important to note that since this behaviour of L is different from that observed in alkali-borate glasses [107], Pb^{2+} cations are responsible for this anomaly. Alkali oxides form borate glasses even at very low concentration of modifier. Superstructural units begin to form with the slightest increase of x , and the size of these units gradually decreases with increasing x , thereby decreasing L effectively [138]. The situation is different with PbO as a modifier as small concentrations of x do not yield stable glass. Glass formation begin at $x = 0.2$ with coexistence of triborates and pentaborates as B_4 -containing units, which reduces L initially. With further increase of PbO , bigger units of penta- and tetraborates comprise the majority of B_4 units which increase L and make a stronger glass. Upon addition of more PbO , m increases again at $x = 0.4$. At this composition of glass, the fragility is maximum. Similar observation was noted in $\text{SnO-B}_2\text{O}_3$ glasses [109] where the glass fragility increased to maximum at $x = 0.4$, decreased with further addition of x , and increased again at $x = 0.8$. For the lead-borate glasses with $x = 0.4$, the non-bridging oxygens start forming in the glass and pentaborate groups diminish. Hence, the intermediate order reduces with concurrent increase in weaker ionic bonds. It is also well-known that ionic liquids are more fragile compared to covalently-bonded structures [104]. Beyond $x = 0.4$, the fragility monotonically decreases with increasing x . This is because even if the dynamic correlation length L decreases slowly owing to the decrease in superstructural units and destruction of the borate network structure, yet PbO starts behaving like a glass former with reduction in Pb-O distances, increased covalency and

cross-linking for $x \geq 0.5$. This induces strong character in the flow units which makes the glass formers stronger for $x > 0.4$.

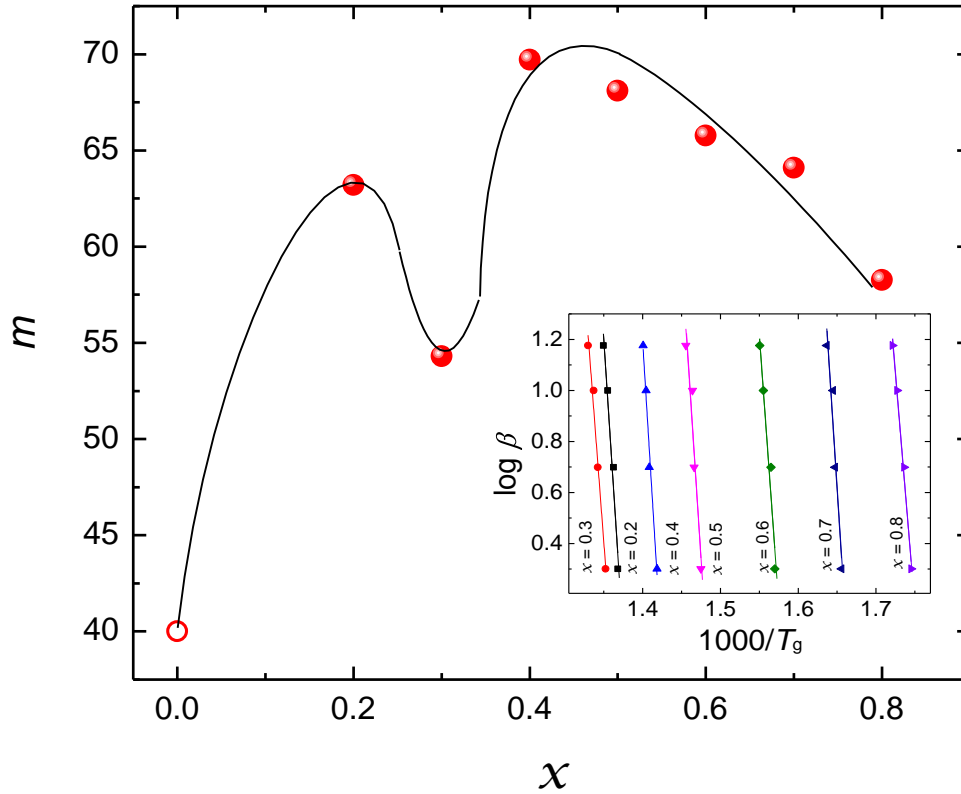


Fig. 3.11. Fragility (m) of lead-borate glasses. Value at $x = 0$ is taken from Ref. [145]. Inset shows the $\log \beta$ vs. $1000/T_g$ plots for the calculation of the activation energy E_a/R . Lines are linear fits to the data for various x .

Fig. 3.12 presents a schematic of the lead-borate glass network for low x compositions ($x = 0.0, 0.2, 0.3$) depicting the dynamic correlations L in pink shaded regions showing the correlations from the superstructural units, and static correlations D in blue encircled regions showing the correlations among the cation-centered voids. The top panel of the plot in the figure shows the dynamic properties (ω_{BP} and m) scaled at their respective highest values while the bottom panel exhibits similar scaling for the short-range structural properties ($\langle r \rangle$, T_g and V_l). As observed from the gray shaded region in the plot, the anomalous dip in dynamic properties occurs at the composition ($x =$

0.3), where the structural properties exhibit a maxima. This clearly shows that these dynamic properties owe their origin at the correlations among the superstructures in the lead-borate glasses.

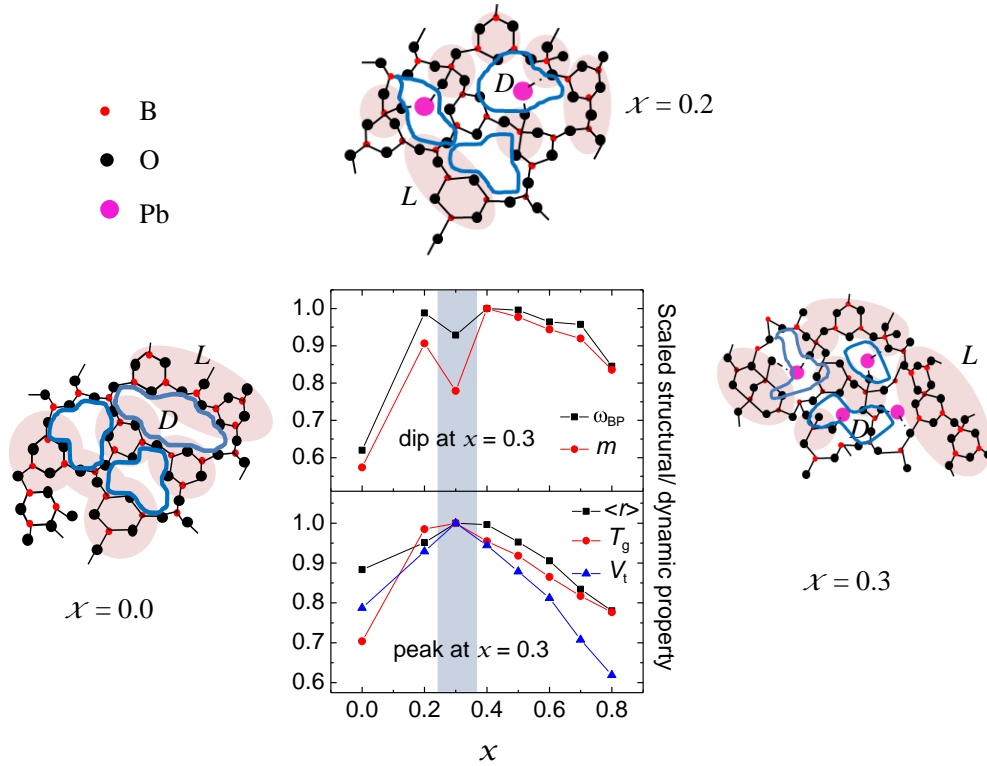


Fig. 3.12. Schematic representation of the lead-borate glass network for low x compositions ($x = 0.0, 0.2, 0.3$) depicting the dynamic correlations L in pink shaded regions and static correlations D in blue encircled regions. The top panel of the plot shows the dynamic properties (ω_{BP} and m) scaled at their respective highest values while the bottom panel shows similar scaling for the short-range structural properties ($\langle r \rangle$, T_g and V_t). The gray shaded region in the plot indicates the anomalous dip in dynamic properties at the composition ($x = 0.3$) where the structural properties exhibit a maxima.

With the increase of temperature in a glass, the atomic packing fraction decreases owing to thermal expansion, which results in a decrease of atomic connectivity. This results in softening of the glass causing a decrease of the shear modulus with temperature. Krausser *et al.* [146] have demonstrated that the rate of this process is controlled by the steepness of the repulsive short-range interatomic interaction potential.

This mechanism propagates to the viscosity, controls its temperature dependence, and in metallic glasses, leads to fragile behaviour when interatomic repulsion is steep and to strong behaviour when the repulsion is softer [146]. In the modified borate network glasses, the lead-cations are surrounded by a number of neighbouring oxygen atoms, forming a disordered cage, whose stability is governed by the repulsive interaction between the particles. With increasing temperature, atoms move farther apart and the stabilizing energy decreases. For glass compositions with steeper interatomic repulsion, this process of destabilization is more abrupt [146], leading to faster variation of the shear modulus and viscosity with temperature above T_g , and hence results in a more fragile glass. It is seen from Fig. 3.11 that m increases with x and then decreases, with a clear dip at $x = 0.3$. Incorporation of atoms with d -shell orbitals have been found to effectively soften the interatomic repulsion, while s -shell electrons are associated with steeper repulsion [146]. This can also be a reason for the decrease of fragility with increasing Pb content for glasses with $x > 0.4$, while an increased fragility for $x = 0.2$. The Pb cross-linking increases in these high-lead glasses and it can be thought as if smaller B atoms added to a network of larger Pb atoms, thereby rendering a softer average pseudopotential. The sudden decrease of fragility for the glass with $x = 0.3$ may owe to its high value of $\langle r \rangle$ and larger superstructures.

The jump in specific heat capacity across T_g also indicates the strong-fragile character of glass formers. This is known as the thermodynamic fragility, to distinguish it from the kinetic fragility determined by Eq. 3.11. For kinetically strong liquids such as, SiO_2 and GeO_2 , the viscous flow occurs by a defect mechanism involving oxide jumping, in contrast to a cooperative rearrangement mechanism found in fragile liquids, because of the rigid covalent bonding that opposes changes in the short- and intermediate-range ordering with changing temperatures [147]. The heat capacity jump at T_g reflects the additional energy required to activate the degrees of freedom necessary for each new

configuration. The strong bonding in the network glasses minimizes the configurational degeneracy which results in a small jump in heat capacity for strong liquids whereas, fragile liquids contain non-directional bonding that allows many new particle arrangements resulting in a large jump in heat capacity.

Inset to Fig. 3.13 shows the heat capacity jump in the lead-borate glasses for various x . The value of C_p at T_g , C_{pg} , is the heat capacity of the glassy state while C_{pl} is the heat capacity of the liquid state. The difference $\Delta C_p = C_{pl} - C_{pg}$ gives the change in heat capacity from the transition from glass to supercooled liquid [148]. The quantity $\Delta C_p/C_{pg}$ is used to classify strong-fragile behaviour [4]. $\Delta C_p/C_{pg}$ is smaller for stronger liquids. This ratio is a relative measure of fragility. Fig. 3.13 depicts the $\Delta C_p/C_{pg}$ values for the lead-borate glasses at different x . It can be seen that the ratio increases to $x = 0.4$ and then decreases indicating that the glass at $x = 0.4$ is the most fragile. A clear dip at $x = 0.3$ is not observed even though the initial rise and then decrease of fragility for $x > 0.4$ is clearly seen. Glasses with composition $x > 0.4$ become more strong with increasing PbO incorporation. It needs to be mentioned here that kinetic and thermodynamic fragilities do not exhibit a positive correlation in all glass-formers [149], and specifically for polymeric glass-formers, they exhibit negative correlation [150]. Similarly, P_2O_5 is an example [147] of a strong inorganic glass-former which also shows large heat capacity jump at T_g . We observe a similar response for the lead-borate glass with $x = 0.3$, which is kinetically strong but exhibits intermediate behaviour for the thermodynamic fragility. The connection between the thermodynamic and kinetic data which can solve this discrepancy in correlation is still not clear yet. The observation simply implies that the configurational degeneracy present in the liquid with $x = 0.3$ above T_g which is responsible for a larger $\Delta C_p/C_{pg}$ is somehow not available for the structural relaxation [147].

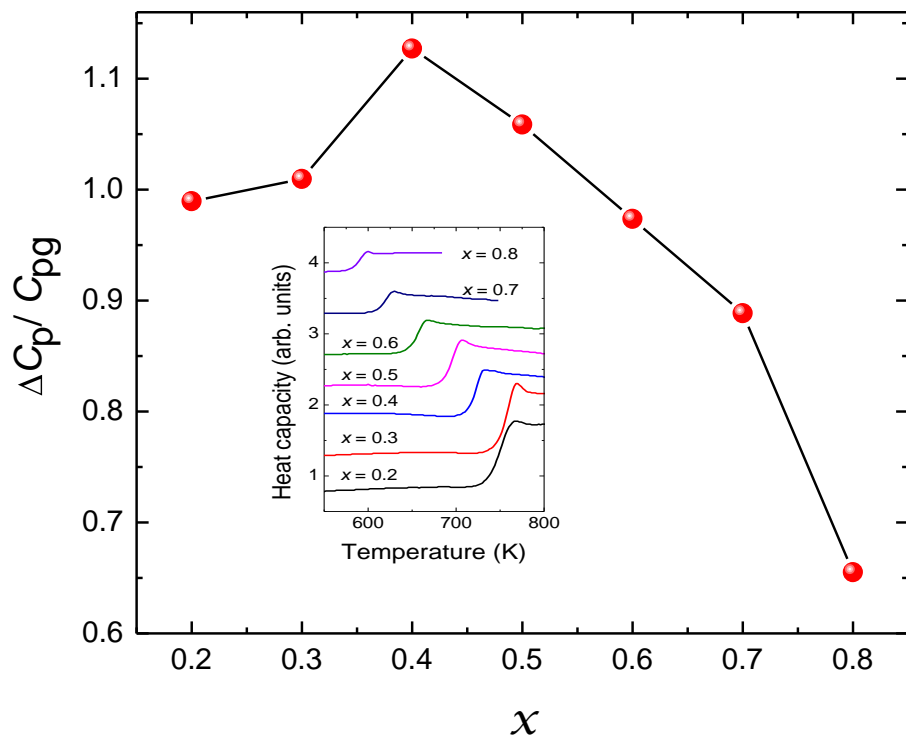


Fig. 3.13. The dependence of $\Delta C_p / C_{pg}$ for various x . Inset shows the rise in heat capacity across the glass transition.

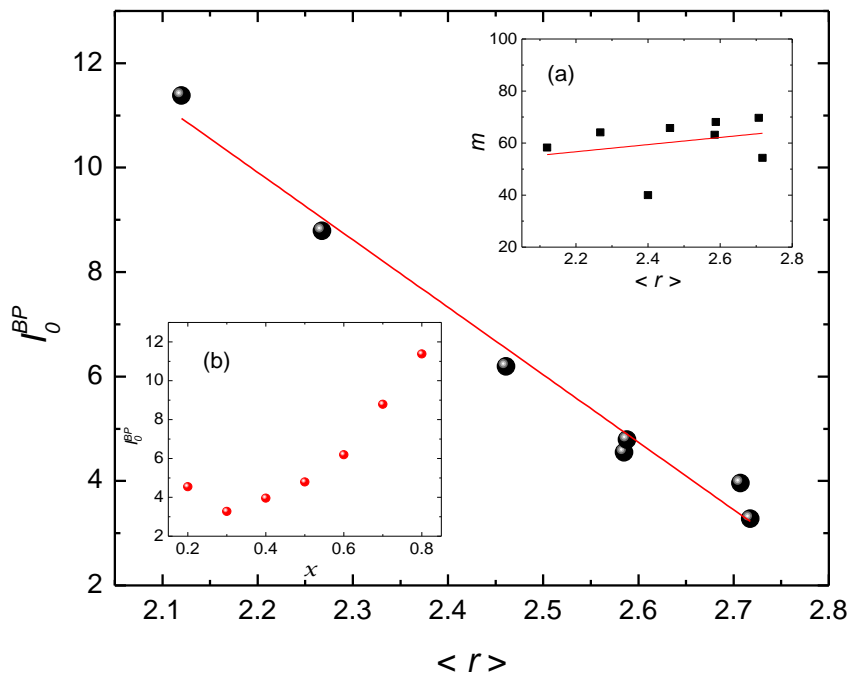


Fig. 3.14. Correlation of I_0^{BP} and average coordination number. Insets show (a) correlation of fragility and average coordination number and (b) dependence of I_0^{BP} on x .

Fig. 3.14 (a) shows a linear correlation exists in these glasses between the average coordination number $\langle r \rangle$ and m . Inset (b) shows the dependence of I_0^{BP} on x . The Boson peak amplitude exhibits a dip at $x = 0.3$ and then increases for increasing x . Fig. 3.14 shows the correlation of I_0^{BP} and average coordination number. It shows that the intensity decreases linearly with increasing $\langle r \rangle$. The decrease of the intensity with $\langle r \rangle$ implies that the number of such units decrease with increase of coordination. This is understandable since the increase of cross-linking in the network structure will reduce the number of units responsible for the intermediate order.

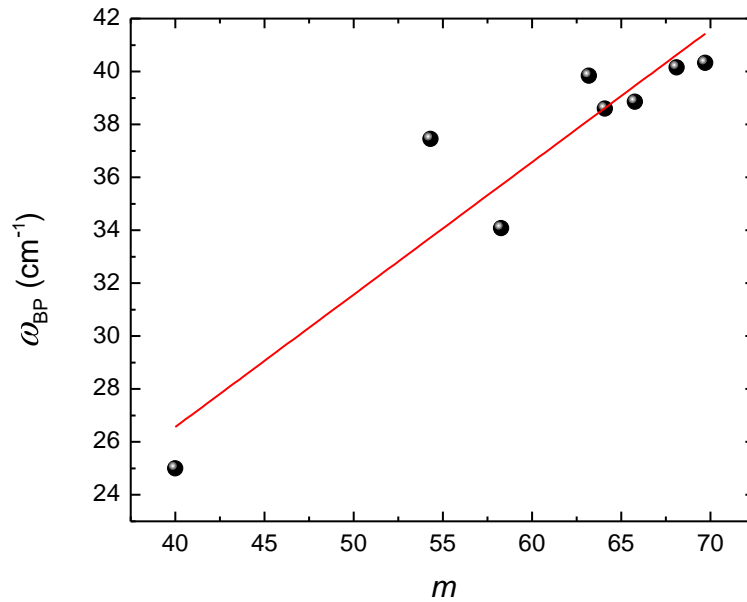


Fig. 3.15. Correlation between Boson peak frequency and fragility.

Fig. 3.15 depicts a linear correlation between the Boson peak frequency and fragility. This proves that both these features of the glass are correlated and are manifestations of the presence of intermediate-range ordering in the glass. Their behaviour is completely different from the elastic properties and glass transition temperature which are governed by the short-range structure as depicted in Fig. 3.12. The anomalous behaviour at $x = 0.3$ is exhibited by both these properties which confirm their

common origin in the intermediate-range length scale. The difference in behaviour with alkali-borate glasses is because of the divalent Pb^{2+} cations which aid in formation of larger superstructures and increase the intermediate-range order at $x = 0.3$.

3.3.6 Composition dependence of longitudinal acoustic mode

Fig. 3.16 (a) shows the composition dependence of the room temperature Brillouin spectra of the lead-borate glasses. The spectra shows Brillouin doublet of a longitudinal acoustic (LA) mode. Fig. 3.16 (b) depicts the longitudinal acoustic (LA) mode frequency (ν_B) of lead borate glasses for increasing x . The initial increase in glass network rigidity is manifested in the increase in LA mode frequency which owes its origin to a modification in the amount of cross-linking borate units, as indicated earlier in the increase in sound velocities and T_g .

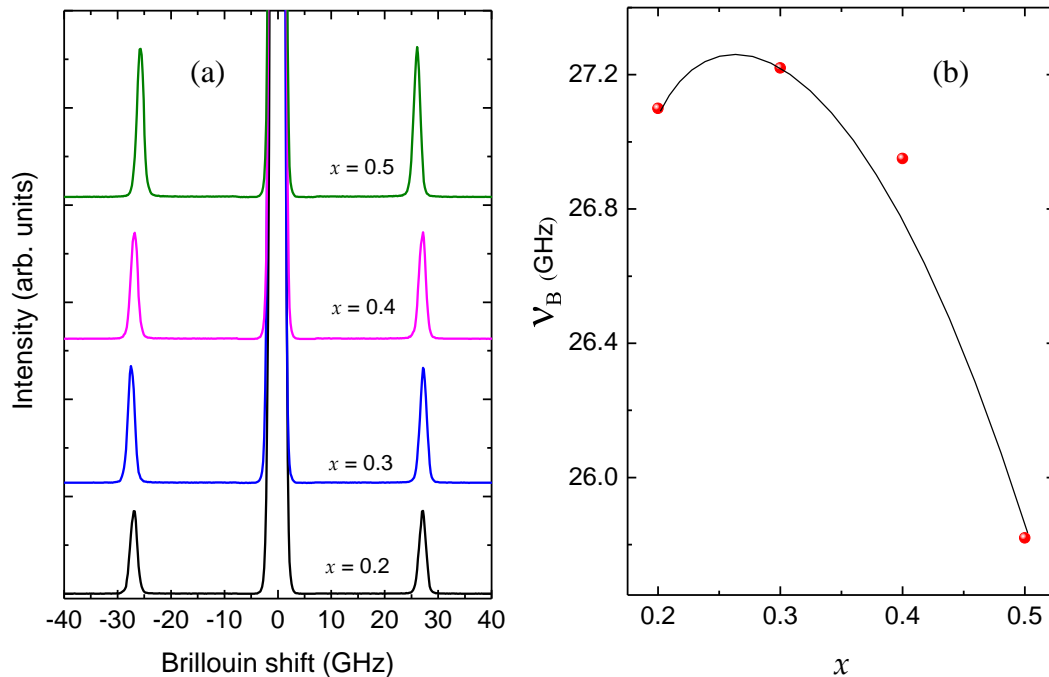


Fig. 3.16. (a) Brillouin spectra of $x\text{PbO}:(1-x)\text{B}_2\text{O}_3$ ($x = 0.2, 0.3, 0.4, 0.5$) glasses at ambient. (b) The longitudinal acoustic (LA) mode frequency (ν_B) of lead-borate glasses for increasing x .

3.3.7 Temperature dependence of elastic properties

The Brillouin doublet for $x = 0.3$ of $x\text{PbO}:(1-x)\text{B}_2\text{O}_3$ glass at selected temperatures is shown in Fig. 3.17. It reveals that the LA mode exhibits softening with increasing temperature. Fig. 3.18 shows the temperature dependence of the LA mode frequency for the various lead-borate glasses. As can be seen for each sample, initially, the mode frequency shows a slightly decreasing trend due to usual increase of anharmonic effects with temperature and a consequent reduction in the elastic modulus. Anharmonic effects also arise when phonon propagation is hindered by the presence of structural imperfections or broken and disordered networking, characteristic of glasses. However, as observed here, the decrease becomes slightly non-linear and the frequency shows a slight increase at higher temperatures close to T_g . Above a certain temperature, the LA mode frequency drops steeply and this point of inflection is identified as the glass transition. This is attributed to structural disintegration and loss of network connectivity once the system reaches the supercooled liquid state. A monotonic steep slope of mode frequency after glass transition suggests disruption of the network structure and structural relaxations taking place in the supercooled liquid state.

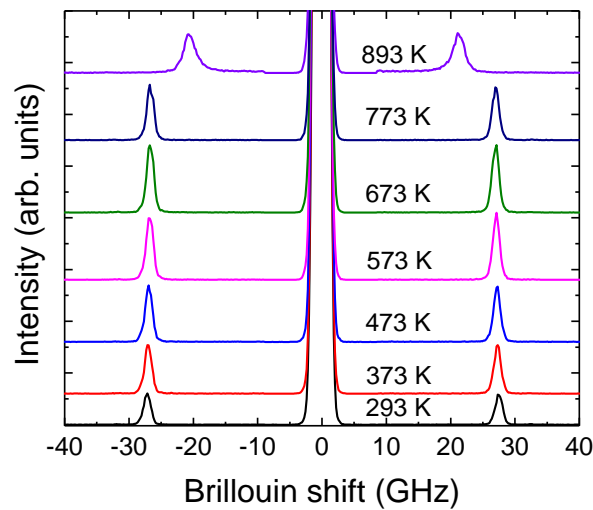


Fig. 3.17. Temperature dependence of Brillouin spectra of $x\text{PbO}:(1-x)\text{B}_2\text{O}_3$ glass for $x = 0.3$ at several temperatures depicting the longitudinal acoustic (LA) mode.

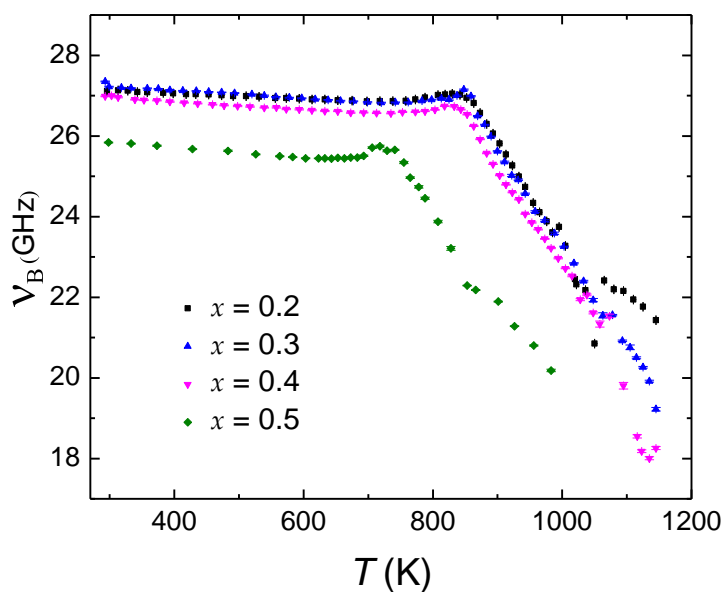


Fig. 3.18. Temperature dependence of the Brillouin shift (v_B) of the LA mode of $x\text{PbO}:(1-x)\text{B}_2\text{O}_3$ ($x = 0.2, 0.3, 0.4, 0.5$) glasses.

3.3.8 Scaling of elastic properties

In order to understand the temperature dependence of the elastic properties in the glassy and supercooled liquid states, the LA mode frequencies for each glass composition, were scaled by their values at the glass transition and plotted on a temperature axis scaled by T_g . The scaled temperature dependence of the mode frequencies is shown in Fig. 3.19, where all curves collapse to lie on a single universal curve up to T_g and exhibit only marginal deviation in the supercooled liquid state. This implies that the variation of the glass structure with temperature and hence its elastic properties are similar up to T_g even with different PbO content.

Scaled temperature dependence of longitudinal sound velocities have also been examined in alkali-borate glasses [151], where it was shown that glasses with different alkali ion size but same composition exhibited scaling of sound velocities up to T_g .

however, scaled composition variation of potassium-borate glasses did not fall into the same master curve. However, the scaling in the present work indeed shows that the temperature evolution of the elastic behaviour in lead-borate glasses is independent of the amount of doping within the glassy regime. This universal behaviour implies that doping with PbO modifies the network structure and hence its elastic constant and T_g in a systematic manner. Since the scaled longitudinal modulus does not change much within the glassy state, it implies that the structure retains its inherent rigidity in each composition of modifier. Once whatever initial modification is done to the structure by PbO is normalized by the scaling, no further composition-dependent modification is brought about by temperature up to the transition, as seen in the master curve. The curves, however, separate from each other after T_g , since the differently modified structures now behave differently with temperature.

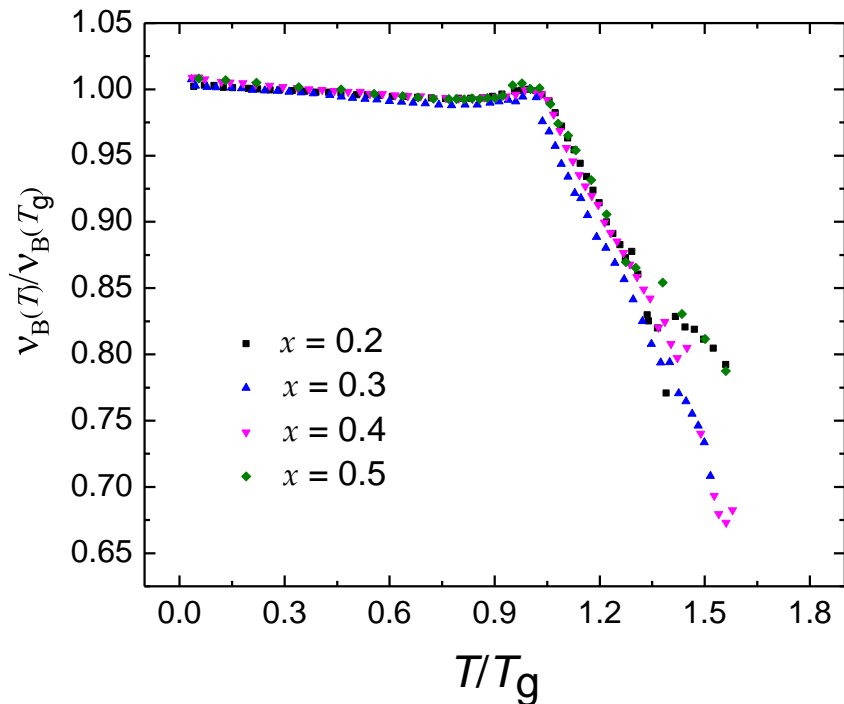


Fig. 3.19. Scaled temperature dependence of the LA mode frequency of $x\text{PbO}:(1-x)\text{B}_2\text{O}_3$ ($x = 0.2, 0.3, 0.4, 0.5$) glasses. $\nu_B(T)$ is scaled with respect to ν_B at T_g and T is scaled with respect to T_g .

3. 4. Conclusions

The present work was intended to study the structural and dynamical properties in lead-borate [$x\text{PbO}:(1-x)\text{B}_2\text{O}_3$] glasses upon increasing the concentration of PbO. The T_g and elastic moduli were found to exhibit a broad maxima around $x = 0.3$. Similar behaviour was also seen with the average coordination number $\langle r \rangle$. High-frequency Raman spectroscopy demonstrated the gradual conversion of three-coordinate (B_3) to four-coordinate (B_4) boron species in the glass structure as PbO was increasingly incorporated. The various superstructural units formation and thereafter destruction with increasing PbO was observed. PbO was found to act as a glass former for $x > 0.5$. The Boson peak and fragility were found to behave similar to the above structural properties except an anomalous dip at $x = 0.3$. The corresponding dynamic correlation length was found to decrease except a peak at $x = 0.3$ with increasing x . The static correlation lengths estimated from the FSDP, did not follow a linear trend with the dynamic correlation lengths, indicating a different spatial origin. From the analysis of the Boson peak and FSDP, it was suggested that while the Boson peak arises from intermediate-range ordering within the network units, the FSDP arises due to ordering of voids between such units. The anomalous behaviour of the Boson peak and fragility were found to be connected to their common origin in the intermediate-range ordered structures. The Boson peak intensity showed a linear decrease with increasing $\langle r \rangle$, while the Boson peak position and fragility were found to vary linearly. The anomalous variation in the intermediate-range length scale reflects the critical role of Pb^{2+} in tuning the intermediate-range structure of the vitreous network. The dynamic processes occurring over the glass transition in different compositions of lead-borate glasses were probed in detail by Brillouin scattering spectroscopy. All the samples were found to show a marked drop in the LA mode frequency above T_g . The scaled LA mode frequency within the glassy regime were found to fall on a single master curve for all the samples, which

shows that the variation of the glass structure with temperature varies linearly even with different PbO content. This shows that the temperature dependence of the elastic behaviour within the glassy state is independent of the amount of modifier.

4

COMPOSITION AND TEMPERATURE-INDUCED STRUCTURAL CHANGES IN LEAD-TELLURITE GLASSES AND MELTS AT DIFFERENT LENGTH-SCALES

4. 1. Introduction

Tellurite (TeO_2) glasses have been the subject of intense scientific investigations owing to their promising optical properties of high non-linear behaviour, low phonon energies and wide infrared transmission range [152,153]. Furthermore, transparent tellurite glass ceramics containing ferroelectric crystalline phases have been shown to exhibit strong second harmonic generation [154], indicating the high potential of these glasses as new optical functional materials. Attempts to understand the origin of these non-linear optical properties have resulted in a lot of studies on the local structure and thermal behavior of these glasses [65,155].

TeO_2 is a conditional glass former and requires addition of other metal oxides to form stable glasses [60]. Presence of a lone pair of electrons in Te, which aids the formation of an asymmetric coordination environment, enables tellurites to adopt a variety of structures. The structure of tellurite glasses is generally suggested as a network of TeO_4 , TeO_{3+1} and TeO_3 polyhedra sharing corners. Numerous reports describe the structure of tellurite glasses as being similar to the crystalline phase of paratellurite (α - TeO_2), which is a three-dimensional network of TeO_4 trigonal bipyramids (tbp) [63]. Each TeO_4 unit has two types of Te–O bonds: two shorter equatorial Te– O_{eq} bonds and two longer axial Te– O_{ax} bonds oriented at larger angle in a plane perpendicular to the $\text{O}_{\text{eq}}\text{–Te–O}_{\text{eq}}$ plane, with the lone electron pair at the tellurium atom located in the equatorial plane [64]. The $\text{TeO}_4\text{–tbp}$ units connect with each other forming $\text{Te}_{\text{eq}}\text{O}_{\text{ax}}\text{–Te}$ linkages.

Using Raman spectroscopic investigations [63], it has been shown that the introduction of a network modifier elongates one of the Te–O_{ax} bonds and results in the gradual formation of the deformed TeO₃₊₁ units and subsequently with the addition of more metal-oxide, the weakly bonded oxygen in TeO₃₊₁ gets disconnected to form TeO₃ trigonal pyramids (tp) with terminal Te=O bond. Therefore, due to its unique low-symmetry structural configurations, i.e., TeO₄ trigonal bipyramids and TeO₃ trigonal pyramids, TeO₂ is different from conventional glass formers like silicates which have symmetrical SiO₄ tetrahedra as the main structural units.

The relationship between the tellurite glass structure and metal ion concentration has been studied for various alkali and transition metal oxides [156]. Metastable phases formed during the crystallization of TeO₂-rich glasses have exhibited efficient second harmonic generation [157]. Unusual crystallization behaviour was observed for Li₂O-TeO₂ glasses, where it was observed that crystallization occurs easily on heating the glasses but hardly occurs when the corresponding liquids are cooled [156]. Furthermore, tellurite glasses with relatively weak cations were found to have a strong tendency to an immiscibility behaviour resulting in amorphous phase separation and distinct crystallization processes [158]. Similarly, a strong structural correlation between ZnO:TeO₂ glasses and Zn₂Te₃O₈ crystalline phase was observed [66] where the glass structure became increasingly Zn₂Te₃O₈-like with increasing ZnO. Such interesting thermal behaviour stimulates further investigations to gain insight into the structural organization and crystallization mechanism of tellurite glasses.

For enhancing the optical behaviour of tellurite glasses and their possible use as base materials for photonic devices, other heavy metal oxides such as PbO and ZnO have been incorporated [159,160]. PbO is an interesting component in glasses due to its dual role [161] of a network modifier at low concentrations when Pb–O bond is ionic, while it

aids in glass network formation as a function of its increasing concentration, owing to the formation of PbO_4 structural units, when Pb–O bond is covalent. It also contributes to the further increase in refractive index of modified tellurite glasses [162] owing to its high polarizability. Due to their very high chloride solubility, lead-tellurite glasses are, furthermore, being investigated [163] for immobilizing used chloride electrolytes produced in molten salt electrochemical reprocessing of spent nuclear fuel.

In order to enlarge the applications of lead-tellurite glasses, it is important to investigate the glass transition (T_g) and the effect of temperature on the structural evolution of the system at different length scales. It is also important to estimate the kinetic parameters which provide useful information on the devitrification processes. Thermo-analytical techniques such as, differential scanning calorimetry (DSC), are very powerful tools for the kinetic analysis of nucleation and crystal growth mechanism in amorphous solids [164]. These experiments are usually carried out in isothermal or non-isothermal (linear heating) conditions. The experimental data obtained can be analyzed based on isokinetic (crystallization mechanism and kinetic parameters are assumed to be the same throughout the temperature/time range) or isoconversional methods (kinetic parameters are considered to be dependent on the extent of conversion/crystallization at different temperature and time without assuming any particular form of the reaction model).

In the present work, we report the results of Brillouin and Raman spectroscopic measurements in $x\text{PbO}:(1-x)\text{TeO}_2$ ($x = 0.1-0.3$) glasses. Both the acoustic and high-frequency vibrational spectra are studied as a function of temperature from ambient up to 725 K in each composition of glass. The room temperature longitudinal sound velocities calculated from the acoustic mode frequencies obtained from Brillouin measurements were compared with those obtained from ultrasonic pulse-echo technique. The reduced

Raman spectra have been discussed in the context of anomalies across the glass transition and structural relaxations within the glassy phase. The changes induced by the metal-oxide modifier and the evolution of the structure as a function of temperature has been discussed to elucidate the differences between the structures of glassy and supercooled lead-tellurites. We further describe the structural evolution during temperature induced crystallization processes in 0.3PbO:0.7TeO₂ glass using DSC and XRD. We investigate the kinetics of glass transition and crystallization, and employ isokinetic method to determine the kinetic parameters during the primary crystallization of the lead-tellurite glass. We further discuss the influence of the addition of PbO on the phase transformation behaviour both during heating the glass and cooling the melt.

4.2. Experimental

The binary glasses $x\text{PbO}:(1-x)\text{TeO}_2$ ($x = 0.1-0.3$) were synthesized from the commercially available pure oxides. Details of the synthesis procedure are described in Chapter 2. The glass pellets were polished using standard procedure. The non-crystalline nature of the samples was tested by XRD, carried out in a STOE diffractometer, using Cu $K\alpha$ radiation of wavelength 1.54060 Å. XRD was also carried out to identify the devitrified phases in the annealed and melt-cooled samples of 0.3PbO:0.7TeO₂ glass. The longitudinal sound velocity measurements were performed at room temperature using the ultrasonic pulse-echo technique from a 15 MHz delay line contact transducer (Accu-Tron). The refractive indices at 532 nm were obtained using a rotating polarizer-type ellipsometer (M/s. SOPRA, France). The glass transition temperature T_g for all the lead-tellurite glass samples were determined by a heat flux differential scanning calorimeter (DSC) at a heating rate of 10 K/min. The primary crystallization kinetics of lead-tellurite glass (0.3PbO:0.7TeO₂) was also investigated using a continuous heating regime with heating rates of 2, 4, 6 and 10 K/min.

Brillouin scattering experiments were performed in a 180° back-scattering geometry with a Sandercock (3+3)-pass tandem Fabry-Perot interferometer using the 532 nm line from a DPSS (Innolight, Germany) laser. The spectra were recorded between 300 and 725 K using a commercially available heating stage with a stability of ± 0.1 K. The sample temperature was measured using a thermocouple placed adjacent to the sample inside the heating stage, while measurements were performed in increasing temperature cycle. The Brillouin spectra were analyzed for mode frequencies and line-widths through curve fitting.

The high-frequency Raman spectra were excited using the 514.5 nm line of an Ar⁺ laser and recorded in the back-scattering geometry using a high-throughput micro-Raman spectrometer (Renishaw model Invia). The lead-tellurite glass samples were placed inside a Linkam THMS600 temperature-controlled heating/ cooling stage for carrying out the temperature-dependent Raman studies from 300 and 725 K. For the glass, 0.3PbO:0.7TeO₂, temperature-dependent Raman spectroscopy was carried out from 300 to 823 K to study its structure during devitrification.

The Raman spectra were corrected for the thermal population factor and the reduced spectra were fitted numerically to obtain the band frequencies, line-widths (Γ) and intensities. In the absence of clear spectral evidence for the multiplicity of the expected normal modes, a multi-component fitting procedure using Gaussian line shapes was adopted, in order to follow quantitatively the temperature-induced changes in the structure across the glass transition. An appropriate number of Gaussian lines were selected after careful consideration for a good agreement between the data and the total fitted spectrum as sum of Gaussians. Although one could attempt curve-fitting less number of Raman bands in a restricted wavenumber range of the spectra, we included more number of bands to represent the full spectrum. It was felt that a restricted fitting

would be unreliable due to intensities from the wings of neighbouring bands. For obtaining the best-fit we used the strategy of using minimum number of bands that give a faithful representation of the complete spectrum at ambient.

4.3. Results and discussion

4.3.1. X-ray diffraction

Fig. 4.1 shows the XRD patterns of the lead-tellurite glasses at different compositions. The result shows that the samples are x-ray amorphous. Unlike in the lead-borate glasses, we do not observe any FSDP in the diffraction data of lead-tellurite glasses. This implies that ordering of voids around modifier cation (Pb^{2+}) centres is absent in these glasses.

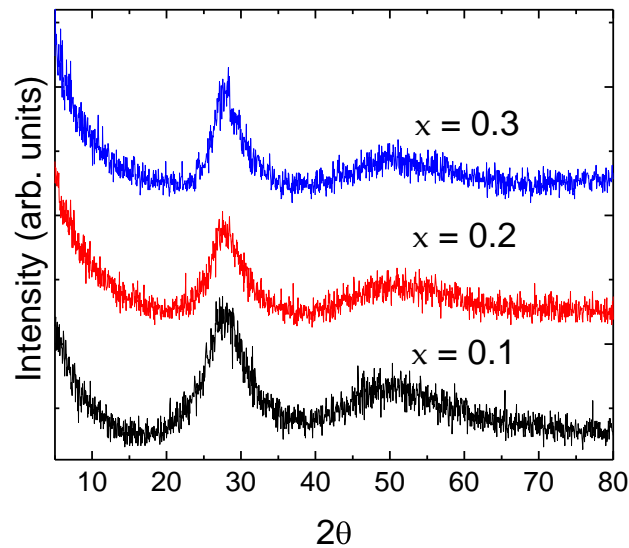


Fig. 4.1. X-ray diffraction of $x\text{PbO}:(1-x)\text{TeO}_2$ ($x = 0.1-0.3$) glasses.

4.3.2. Brillouin scattering

Brillouin light scattering monitors dynamical changes in structure, associated with density fluctuations. This technique reveals the complex elastic modulus of structures on a scale of several hundred interatomic distances. The real and imaginary components of

the complex modulus, respectively, represent the ability of the structure to transmit elastic energy and the viscous dissipation owing to the structural disintegrality.

Fig. 4.2 shows the composition dependence of the room temperature Brillouin spectra of the $x\text{PbO}:(1-x)\text{TeO}_2$ glasses. The spectra show the doublet of Brillouin peaks of a longitudinal acoustic (LA) mode arising from the energy exchange of light upon interaction with propagating hyper-sound. The LA mode shifts to lower frequencies with increasing PbO content. The Brillouin doublet for $x = 0.2$ at selected temperatures, as shown in the inset to Fig. 4.2, reveals that the LA mode frequency decreases with increasing temperature. The changes in the acoustic mode frequency reflect the changes in the elastic properties of the glass taking place upon increasing PbO content and also as a function of temperature.

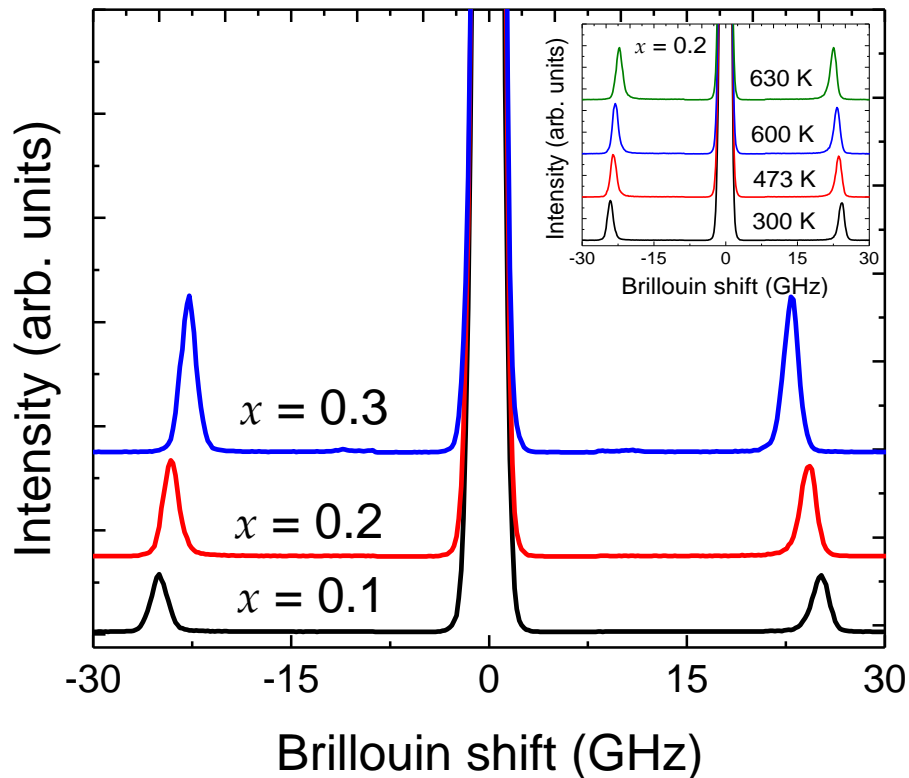


Fig. 4.2. Brillouin spectra of $x\text{PbO}:(1-x)\text{TeO}_2$ ($x = 0.1-0.3$) glasses at ambient. The inset represents the spectra for $x = 0.2$ at various temperatures.

Fig. 4.3 shows the temperature dependence of the LA mode frequency and its line width for different glass compositions. All the samples show a similar dependence of the mode frequencies and the respective line widths. Initially, the mode frequencies show a slightly decreasing trend due to usual increase of anharmonic effects with temperature and a consequent reduction in the elastic modulus. Anharmonic effects also arise when phonon propagation is hindered by the presence of structural imperfections or broken and disordered networking, characteristic of glasses. However, as observed here, the decrease becomes slightly non-linear and the frequency shows a slight increase at higher temperatures. Above a certain temperature, the LA mode frequency drops steeply and this point of inflection is identified as the glass transition. This is attributed to structural disintegration and loss of network connectivity once the system reaches the supercooled liquid state. Such behaviour of the acoustic modes is common in other borate [151], germanate [165] and float [166] glasses. A monotonic steep slope of mode frequency after glass transition suggests disruption of the network structure and structural relaxations taking place in the supercooled liquid state. The non-linearity observed in mode frequencies below T_g has been attributed to residual stresses in as-quenched glasses [167].

Table 4.1. T_g values, slope of mode frequency above T_g , density, refractive index, ultrasonic sound velocities and those estimated from Brillouin measurements, and longitudinal elastic modulus at ambient for lead-tellurite glasses.

x	T_g (K) (DSC)	(dv_B/dT) above T_g	Density ρ (g/cc)	Refractive index	Sound velocity (m/s) (Brillouin)	Sound velocity (m/s) (Ultrasonic)	Longitudinal elastic modulus (GPa) (Brillouin)
0.1	633	0.028	5.12	1.9563	3411	3370	59.57
0.2	603	0.025	5.89	2.0779	3099	3011	56.57
0.3	543	0.020	6.19	2.0831	2911	2675	52.45

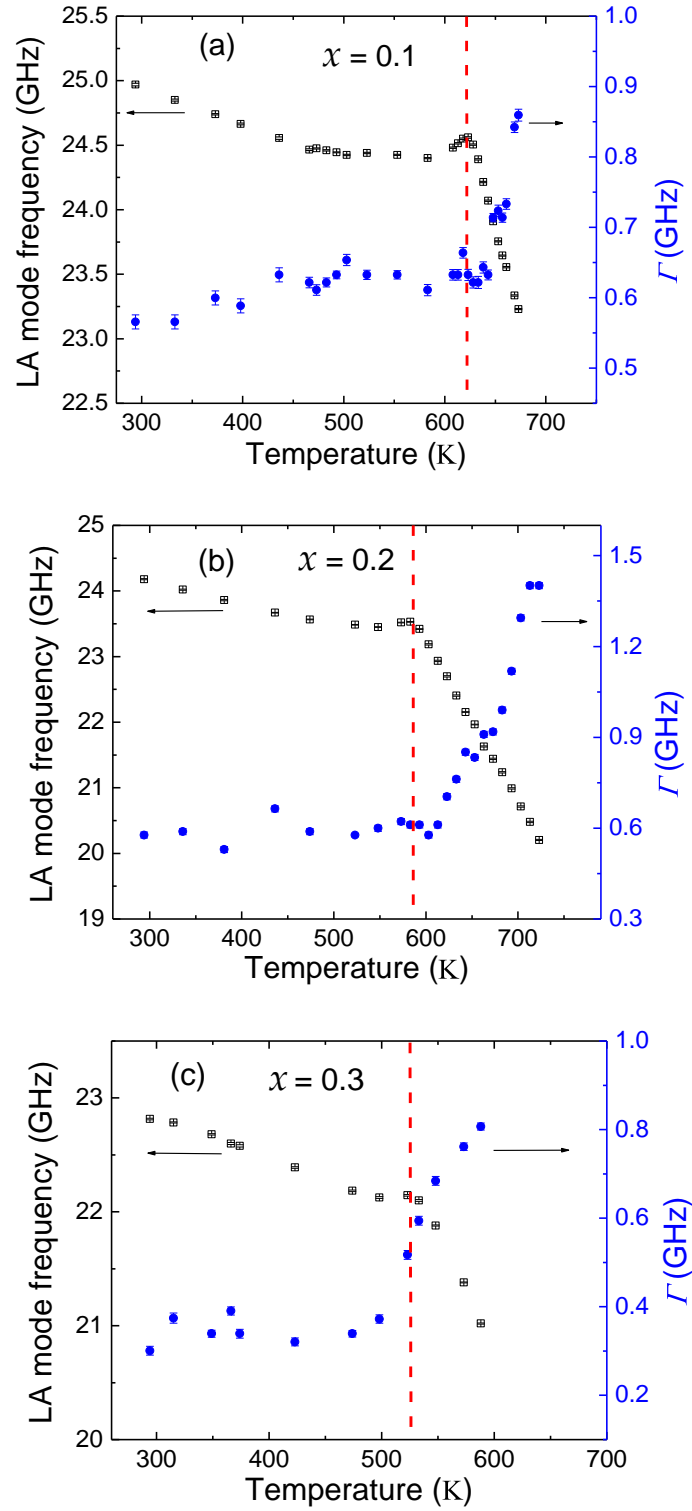


Fig. 4.3. Temperature dependence of the Brillouin shift and line width of the LA mode for $x =$ (a) 0.1, (b) 0.2 and (c) 0.3. The dashed vertical line marks the glass transition in the respective glass composition.

Table 4.1 lists the T_g values obtained from the DSC thermograms for the $x\text{PbO}:(1-x)\text{TeO}_2$ ($x = 0.1-0.3$) glasses. The transition from glass to supercooled liquid state corresponds to an endothermic process detected as a dip in the heat flow profile. The T_g values obtained from DSC are 633, 603 and 543 K, respectively, for the glass compositions $x = 0.1, 0.2$ and 0.3 , while those obtained from the Brillouin data are 623, 593 and 533 K, respectively, as seen in Fig. 4.3. However, a meaningful comparison of T_g values obtained from different techniques would require identical heat treatment of the samples and faster Brillouin data acquisition to match with that of DSC (DSC was done at 10 K/min heating rate). The DSC thermogram of the glass with $x = 0.3$ reveals a crystallization peak with an onset at 623 K. This is discussed later in Section 4.3.5. Such a crystallization exotherm is not observed in the other two compositions. Thus the addition of more PbO into the glass structure makes it devitrify easily.

As depicted in Fig. 4.2, the acoustic mode frequency decreases with increase of PbO content. In addition, the glass transition temperature decreases with increased PbO content as shown in Fig. 4.3. T_g reflects the strength or structural rigidity of a glass. A doped cation may add strength to the glass structure by becoming a part of the network or may enter into the structure as a modifier, bonding ionically to the bridging oxygens and breaking the back bone of the network. Here, PbO acts as a network modifier which weakens the Te-O_{ax} bond and eventually breaks these bonds, thereby modifying the atomic bonding in the glass structure and introducing different bonding characteristics in the primarily extended covalently bonded random network structure. The increase in the PbO content, thus, increases the number of non-bridging oxygen atoms thereby decreasing the network rigidity and hence lowering the glass transition.

The slope of mode frequency above T_g is found to decrease with increasing PbO content as listed in table 4.1. This is in contrast to that observed in phosphate [167] and

borate [151] glasses where the absolute values of the slopes increase with modifier content. The marked drop in mode frequencies above T_g is a result of localized structural reorganizations. The decreased rate of change of acoustic mode frequency above T_g observed in the tellurite glasses with increasing content of metal-oxide modifier suggests a slower rate of structural and configurational rearrangements in these glasses with higher PbO. This implies that the fragility in these glasses decreases with increasing PbO. This further reveals that even though the glass with low modifier content is more rigid below the glass transition, its rigidity decreases faster compared to that of the glasses with higher PbO content, once it has surpassed the transition. This suggests that the introduction of more PbO into the structure, which was responsible for reducing the glass rigidity below T_g does not influence to modify the network connectivity above the transition. As the glass with higher PbO composition already has low degree of networking and structural integrity, the effect of temperature is less pronounced. Furthermore, glasses rich in modifier tend to be more dense-packed as the modifier ions get accommodated in the open structure of the network. This could be one of the reasons for their slower rearrangements after the transition despite having a comparatively less rigid structure below T_g . Higher content of modifier leads to increased number of ionic bonds and easier nucleation aided by disintegrated structures. A direct correlation between the Poisson's ratio and glass densification has been observed by Rouxel *et al.* [168] where the maximum post-decompression density change under high hydrostatic pressure has been related to the resistance in contraction in the transverse direction. It was observed that higher value of this ratio leads to lesser density change. In analogy, in the present system of tellurite glasses, with adjunction of more PbO into the structure the atomic packing increases and the atomic cross-linking degree decreases. Probably because of a relatively high atomic packing density, the present glasses with higher x exhibit decreased rate of fall of rigidity.

The Brillouin mode frequencies are a direct measure of the sound velocities, which are governed by the elastic properties in the material. Table 4.1 presents the values of the densities and the refractive indices along with the longitudinal sound velocities for the tellurite glasses at room temperature, respectively, obtained from Brillouin and ultrasonic velocity measurements. It can be observed that the sound velocities obtained using ultrasonic method are of lower values compared to those determined using Brillouin light scattering. This is so because the ultrasound wavelengths are orders of magnitude larger, and hence, the ultrasonic method probes larger length scales and corresponds to MHz frequencies, while Brillouin scattering probes smaller length scales corresponding to GHz frequencies. Furthermore, the glass transition, being a relaxation phenomena, depends on the probing frequency and hence is dependent on the experimental techniques used. Therefore, the elastic anomaly observed from the LA mode frequency and width at the liquid-glass transition temperature using Brillouin spectroscopy, as depicted in Fig. 4.3 may also be observed using the ultrasonic method, while T_g may be lower than that observed using Brillouin scattering. The refractive indices are found to increase monotonically with increase of metal oxide concentration. Similar observations have been reported in many other lead-tellurite glasses [60]. Larger refractive indices have been known to arise due to the large polarizability of the doping cations [169]. The room temperature refractive indices (n) of each glass composition have been used to calculate the sound velocities (V) from the Brillouin shift (ν_B) using the following equation;

$$V = (\lambda \times \nu_B) / 2n \quad (4.73)$$

where, λ is the incident laser wavelength (532 nm). The hypersonic velocity obtained from Brillouin scattering experiments are as usual higher than those obtained using ultrasonic pulse echo technique (as observed from table 4.1). The refractive index and acoustic velocities of glasses are sensitive to structural modification with composition

and type of cation. $\text{TeO}_2\text{-XO}$ ($X = \text{Ba}, \text{Ti}$) glasses have shown different evolution based on the type of doped cation [170]. BaO-rich glasses exhibit a decrease of refractive index and sound velocity with composition while TiO_2 -rich glasses show a corresponding increase. PbO-doped glasses in the present study show an increase in refractive index owing to large polarizability, while a decrease in sound velocity with increased composition. This behaviour is similar to BaO which acts as network modifier whereas, TiO_2 acts as network former, bonding more covalently with the tellurite network and hence an increase in the observed acoustic velocity, in the TiO_2 -based glasses.

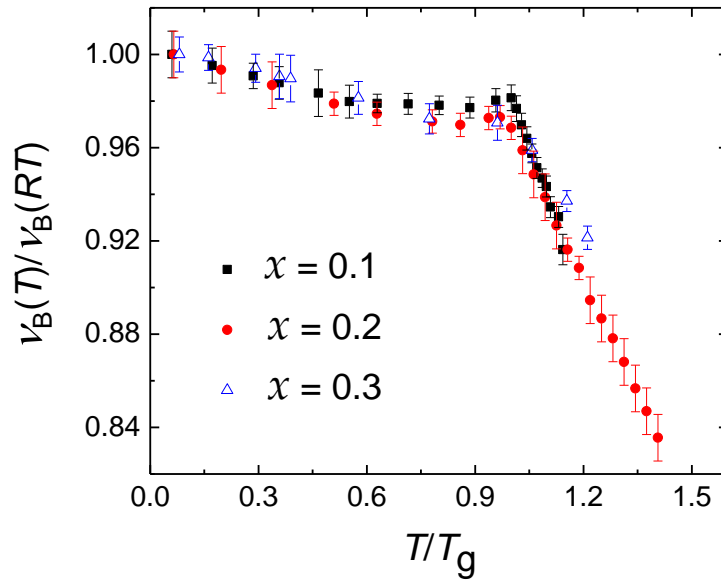


Fig. 4.4. Scaled temperature dependence of the LA mode frequency of $x\text{PbO}:(1-x)\text{TeO}_2$ ($x = 0.1\text{-}0.3$) glasses. $v_B(T)$ is scaled with respect to v_B at ambient and T is scaled with respect to T_g .

The decrease in the longitudinal elastic moduli with addition of modifier to the structure is responsible for reducing the sound velocity with increasing PbO concentration. The longitudinal acoustic velocity found above, can be used to calculate the longitudinal elastic constant;

$$C = \rho V^2. \quad (4.74)$$

The dependence of C with increasing PbO molar concentration, as depicted in table 1, clearly shows that the glass rigidity at ambient is lowered with the addition of more PbO.

As shown in Fig. 4.3, the line-widths (Γ) of the LA mode remain almost constant, till the glass transition and then show a sudden rise above T_g for all the glasses. Generally, line-widths of vibrational modes go up with increasing temperature due to increase of the scattering processes which indicate a reduction in the vibrational life times. The remarkable rise of Γ above T_g for all the compositions indicates the damping of the longitudinal acoustic wave caused by the breakage of the glass network structure and rise in the number of non-bridging oxygens, which act as centres for energy dissipation of the elastic wave propagation. This viscous dissipation relates to the aperiodic movements and irreversible structural reorientations in the system. In the tellurite glass system, this drastic increase of Γ is also associated with the changes in the structure of the polyhedral units [171]. A vanishing line-width observed not too far below T_g implies high degree of transmission of elastic wave and very less energy loss experienced by the propagating hyper-sound. This gives the insight that the structural elements remain intact and are well connected even up to some 10 K below T_g . The kinetically arrested frozen-in liquid gains enough energy for rapid structural relaxations and faster reorientations just across the transition.

In order to understand the temperature dependence of the elastic properties in the glassy and supercooled liquid states, the LA mode frequencies for each glass composition, were scaled by their ambient values and plotted on a temperature axis scaled by T_g . The scaled temperature dependence of the mode frequencies is shown in Fig. 4.4, where all curves collapse to lie on a single universal curve up to T_g and exhibit only marginal deviation in the supercooled liquid state. This implies that the variation of the glass structure with temperature and hence its elastic properties are similar up to T_g

even with different PbO content. Scaled temperature dependence of longitudinal sound velocities have been examined in alkali-borate glasses [151] for different compositions, where sound velocities were scaled with respect to their values at T_g . However, this type of scaling did not show a universal behaviour for lead-tellurite compositions below T_g . On the other hand, the alternate scaling done in the present work indeed shows that the temperature evolution of the elastic behaviour is independent of the amount of doping within the glassy regime. This universal behaviour implies that doping with PbO modifies the network structure and hence its elastic constant and T_g in a systematic manner. Since the scaled longitudinal modulus does not change much within the glassy state, it implies that the structure changes its rigidity in a linear way for each composition of modifier. The three curves separate from each other after T_g , since the differently modified structures now behave differently with temperature. The system in the supercooled liquid state becomes highly compressible and the compressibility increases at a faster rate for the glass with lower content of PbO. As explained earlier, this could be due to the dense packed structure in the high modifier content glass which causes a hindrance to the rate of compressibility.

4.3.3. High-frequency Raman scattering

Fig. 4.5 (a) shows the ambient condition Raman spectra of the $x\text{PbO}:(1-x)\text{TeO}_2$ glasses. The spectra comprises of two broad features. The former region at $300\text{-}550\text{ cm}^{-1}$ consists of two bands: one at about 350 and the other near 475 cm^{-1} . The band at 350 cm^{-1} is found to become more intense, while the one at 475 cm^{-1} is found to lower its peak position with increase of PbO molar concentration. Similarly, the high-frequency feature at $600\text{-}900\text{ cm}^{-1}$ (at about 680 and 760 cm^{-1}) also show a decrease in mode-wavenumber with increasing modifier content. In addition, the band at 760 cm^{-1} shows a marked increase in intensity with addition of metal-oxide modifier.

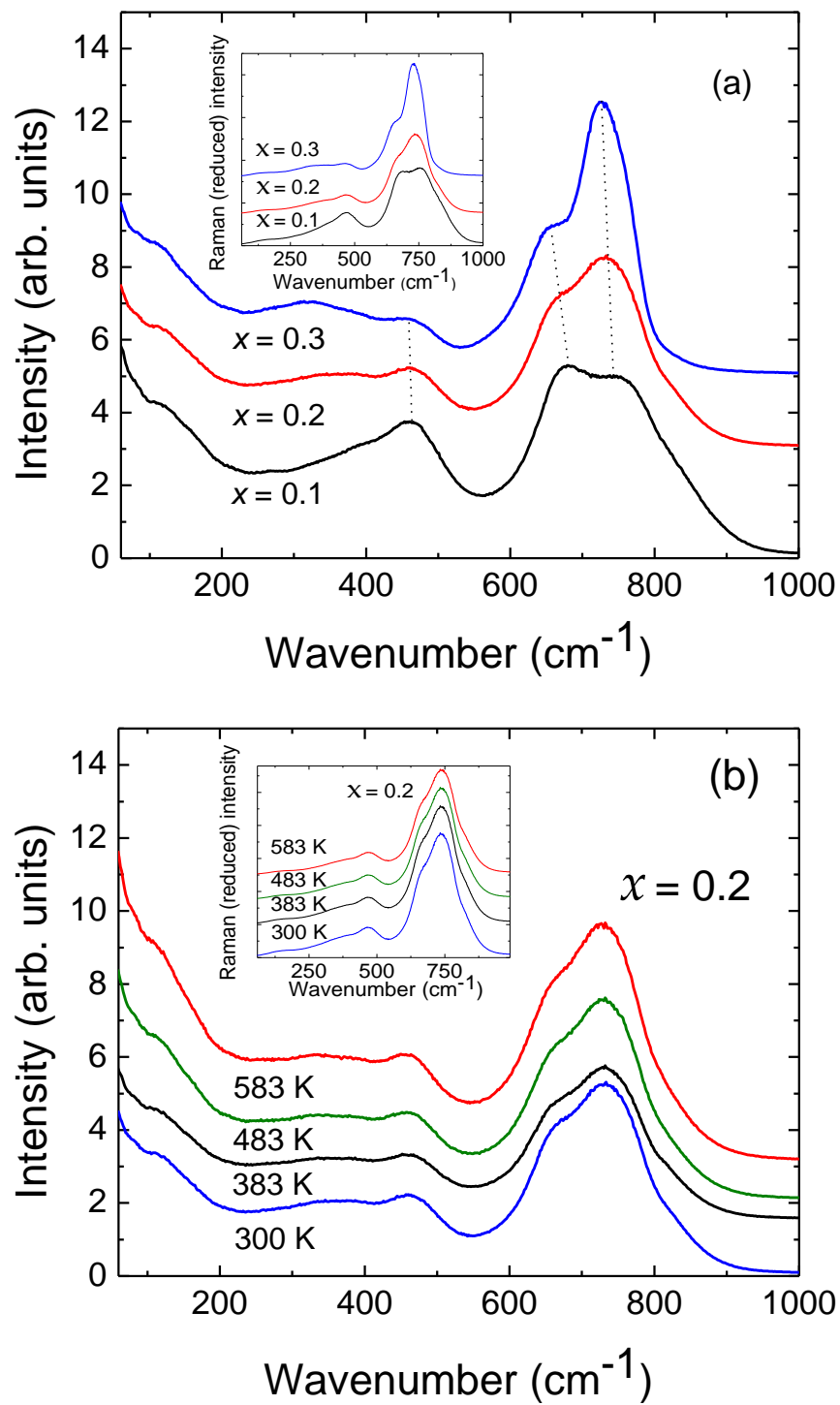


Fig. 4.5. Raman spectra of $x\text{PbO}:(1-x)\text{TeO}_2$ glasses for (a) $x = 0.1-0.3$ at ambient and (b) $x = 0.2$ at selected elevated temperatures. The insets show the corresponding reduced Raman spectra obtained after correcting for the thermal population factor.

Raman spectra at elevated temperatures are shown in Fig. 4.5 (b) for $x = 0.2$. In order to eliminate the trivial temperature effects for an unambiguous quantitative analysis of the spectra, the raw spectra have been corrected using Eq. 2.20, $I^{\text{red}}(\omega) = \omega I^{\text{expt}}(\omega) / [1 + n(\omega, T)]$, for the thermal population factor. The reduced Raman spectra at ambient conditions for the three different compositions and for various temperatures of the glass with $x = 0.2$, are respectively shown in the insets in Figs. 4.5 (a) and 4.5 (b). The temperature-corrected reduced spectra, thus obtained, are essential for identifying and ascertaining the effects of structural changes arising at elevated temperatures.

The reduced Raman spectra were fitted using Gaussian line profiles. A total of eight Gaussians along with a linear background were found to be adequate to fit the spectra. The fitting is shown in Fig. 4.6 for the glass with $x = 0.1$ at 323 K where the fitting procedure helped in the identification of four bands centered at $\sim 160, 280, 392$ and 476 cm^{-1} in the region below 550 cm^{-1} and another four at $\sim 605, 674, 751$ and 830 cm^{-1} in the region of $550\text{-}1000 \text{ cm}^{-1}$.

Table 4.2. Observed Raman mode frequencies in lead-tellurite glasses and their assignments.

Mode wavenumber (cm^{-1})	Assignment
160	Optic mode of the parent TeO_2 crystalline structure
280	Optic mode of the parent TeO_2 crystalline structure
392	Bending mode of Te-O-Te or O-Te-O linkages/ optic mode of lead-tellurite compounds
476	Bending mode of Te-O-Te or O-Te-O linkages
605	Stretching mode of TeO_4 tbp units
674	Stretching mode of TeO_4 tbp units
751	Stretching mode of TeO_3 tp units
830	Stretching mode of TeO_3 tp units

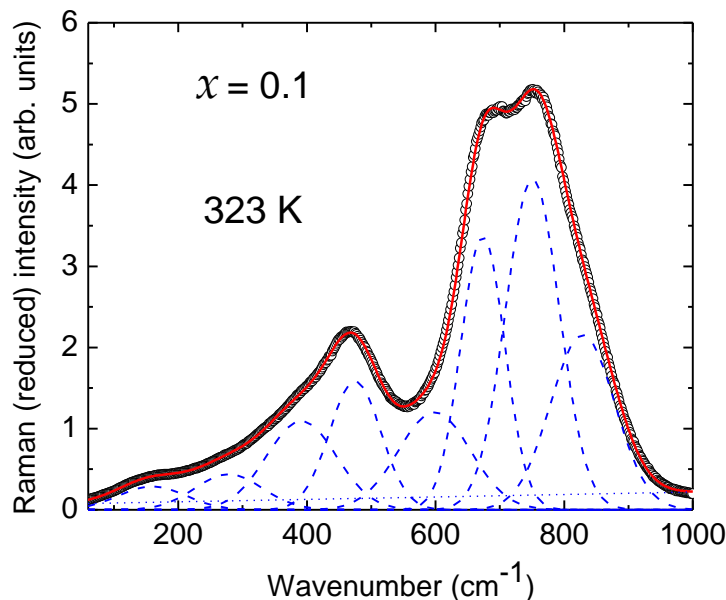


Fig. 4.6. The reduced Raman spectrum for the lead-tellurite glass with $x = 0.1$ at 323 K, along with the Gaussian fits and a linear background. The dashed curves represent the fitted Gaussians. The total fitted spectrum is shown as a continuous curve.

In Fig. 4.6, the band at $\sim 751 \text{ cm}^{-1}$ and its corresponding high-frequency shoulder at $\sim 830 \text{ cm}^{-1}$ are attributed to the stretching modes of $\text{TeO}_3\text{-tp}$ units containing terminal Te–O bonds such as $\text{Te}=\text{O}$ and $\text{Te}-\text{O}^-$ with non-bridging oxygen atoms [64]. The doublet occurring at 674 and 605 cm^{-1} has been assigned to the stretching modes of the backbone of the TeO_2 glassy network comprising the $\text{TeO}_4\text{-tbp}$ units with bridging oxygens [64]. These two bands belong to two different oxygen atoms (those at the equatorial plane and the others at the axial plane). The bands occurring at ~ 476 and 392 cm^{-1} are attributed to the bending modes of Te–O–Te or O–Te–O linkages. The band at 476 cm^{-1} is found to reduce in intensity and downshift in frequency with increase of molar concentration of PbO as seen in Fig. 4.5 (a). Similar behaviour has been observed in other tellurite glasses as a function of doping [60]. High-temperature Raman spectra in $20\text{Li}_2\text{O}:80\text{TeO}_2$ revealed that the $\text{TeO}_4\text{-tbp}$ units present at ambient were converted into $\text{TeO}_3\text{-tp}$ units with non-bridging oxygens as the temperature was increased to above the melting

temperature, while the major structural units in conventional glass-formers such as alkali silicates were not likely to change with increasing temperature indicating large fragility in this tellurite glassy system [155]. In addition, x-ray absorption studies also clearly illustrate a continuous change of the oxygen polyhedron around Te from tbp to tp as the modifier content x increases [65,161]. Thus the observed composition-induced spectral variations are in agreement with those reported earlier [60,64], which demonstrate the gradual increase of TeO₃-tp at the expense of TeO₄-tbp with the increasing presence of PbO modifier. The downshift of mode frequency implies the decrease of the force constants of the relevant bonds and hence the reduction in the rigidity of the glassy network with the incorporation of more PbO. This is consistent with that obtained from the Brillouin data. The decrease of intensity reflects the reduction in the number of units with bridging oxygen bonds. We also observe an increase in intensity of the 392 cm⁻¹ band with PbO doping as indicated in Fig. 4.5 (a). This band differs in position and relative intensity for different metal-oxide dopants [60]. Therefore, an alternate assignment of this band may be the optic modes of lead-tellurite compounds formed when these glasses crystallize. The increase in its intensity implies the structural modification in the tellurite glasses with increased PbO doping. The two bands in the low-frequency region at ~ 160 and 280 cm⁻¹ are assigned to the optic modes of the parent TeO₂ crystalline structure. The assignments of the Raman bands are given in table 4.2.

The standard errors of the parameters of the weak and broad Raman bands in the low-frequency side of Fig. 4.6 were found to be large, not showing any systematic temperature-dependence, and hence were not considered for any further analysis. Only the parameters of the most prominent modes at ~ 674 and 751 cm⁻¹ have been followed as a function of temperature for their mode-wavenumber, line-width and relative intensity to quantitatively analyze their behaviour in the glassy and supercooled liquid state, and discussed further. The parameters are also shown (Figs. 4.7 – 4.9) with their standard

errors. One can see that the discontinuous changes in the trends of these parameters are unambiguous.

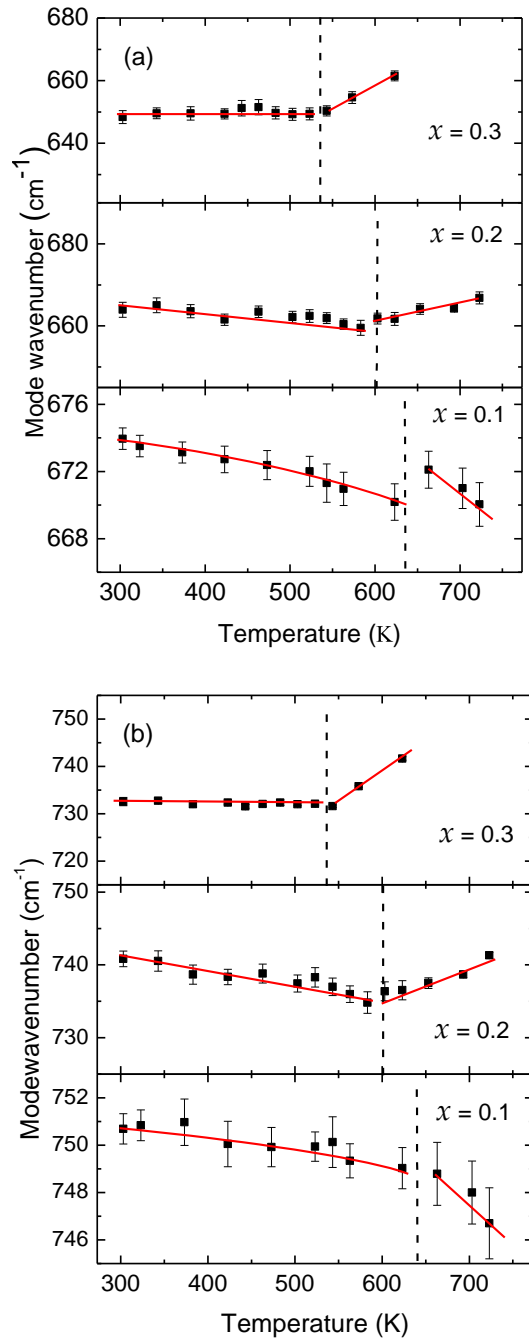


Fig. 4.7. Temperature dependence of the mode frequencies of the (a) 674 cm^{-1} mode and (b) 751 cm^{-1} mode for the glasses with $x = 0.1, 0.2$ and 0.3 . The lines through the data are guides to the eye. The dashed vertical lines mark the glass transition in the respective glass composition.

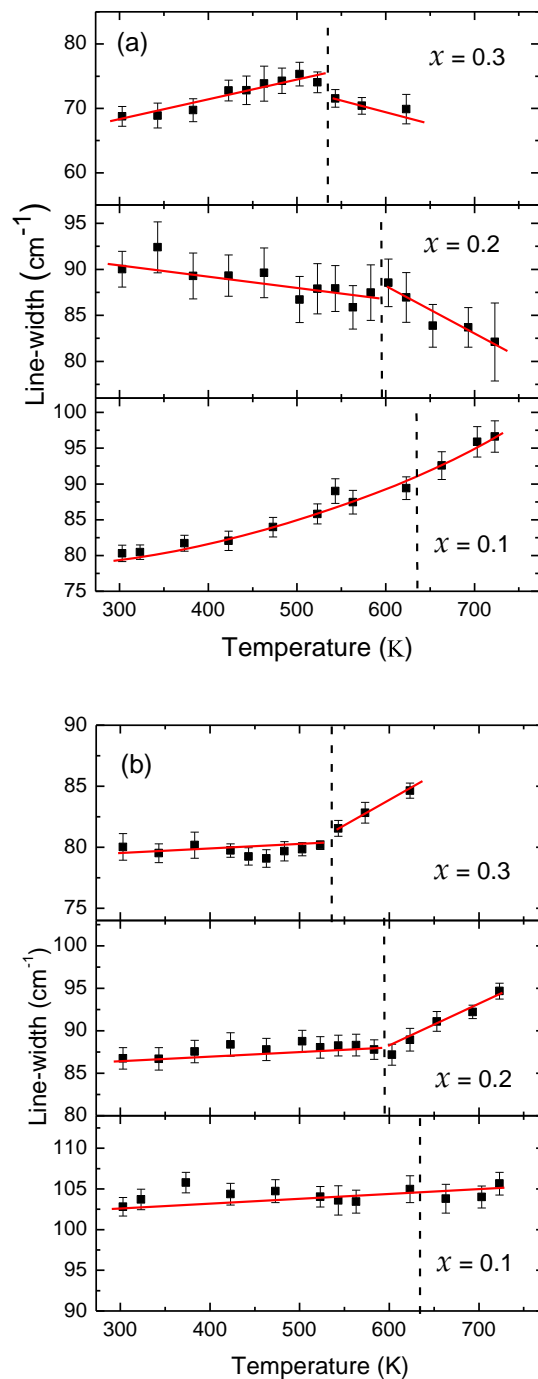


Fig. 4.8. Temperature dependence of the line-widths of the (a) 674 cm^{-1} mode and (b) 751 cm^{-1} mode for the glasses with $x = 0.1, 0.2$ and 0.3 . The lines through the data are guides to the eye. The dashed vertical lines mark the glass transition in the respective glass composition.

Fig. 4.7 (a) shows the temperature dependence of the 674 cm^{-1} mode. This stretching mode of TeO_4 -tbp units is found to behave differently for the different glasses.

This mode shows regular anharmonic behaviour with a distinct discontinuity across the transition for $x = 0.1$. On the other hand, for $x = 0.2$, it does not show any appreciable change upto T_g , while it hardens in frequency in the supercooled state. This anomalous stiffening of the force constants suggests structural relaxations taking place above T_g . The glass with $x = 0.3$ shows hardening even in the glassy state and a change of slope near T_g , where the hardening increases in the supercooled state. This anomalous mode hardening with higher PbO content implies changes in the average molecular configuration of the TeO_4 -bipyramids. This suggests that the addition of PbO not only breaks the bridging oxygens creating more of TeO_3 -tp units, it also has an effect on the existing TeO_4 -tbp units in a way as to reduce the bond lengths in these structures. A similar behaviour is also shown by the 751 cm^{-1} mode (Fig. 4.7 (b)). For the glass with $x = 0.1$, the mode frequency of this mode shows normal anharmonic behaviour in both the glassy, as well as, supercooled state, with a clear change of slope at the transition. The slope increases beyond T_g . This mode associated with the stretching vibrations of TeO_3 -tp units shows marginal anharmonicity up to T_g for $x = 0.2$ and then hardens beyond it. On the other hand, this mode in the $x = 0.3$ glass shows almost no change in frequency up to T_g and then increases in frequency. This observation strengthens the above argument that the addition of PbO stiffens the stretching force constants in the backbone network structure including the terminals made of TeO_3 -tp units. Interestingly, Silva *et al.* reported a drastic change in the local order around Pb with a strong shortening of the Pb–O distances with $x = 0.5$ and a simultaneous reduction of the mean coordination number of the oxygen polyhedra [161]. The breaking of Pb–O–Te linkages could result in such reorganizations.

Fig. 4.8 shows the temperature dependence of the line-widths (Γ) of the 674 and 751 cm^{-1} modes. Large Γ of Raman modes essentially represents inhomogeneous broadening. The Γ of 674 cm^{-1} mode shows different behaviours for the different glasses. For $x = 0.1$, the stretching mode of TeO_4 -tbp units show the normal behaviour of increase

of Γ . The inherent cause of temperature-induced broadening of the mode is the increase of scattering processes at higher temperatures which reduces the vibrational lifetimes. No clear difference is observed here between the glassy and supercooled liquid state. On the other hand, for the glass with $x = 0.2$, Γ decreases in the glassy state and above T_g , it reduces more rapidly. This anomalous sharpening of the mode with temperature indicates that the addition of PbO into the structure narrows down the distribution of bond lengths and bond angles in the parent glass network structure. For the glass with $x = 0.3$, Γ of this mode first increases in the glassy state but decreases beyond the transition. Here also a sharp change in the behaviour of the mode is observed at T_g . The increase of Γ below T_g and its decrease above the transition suggests initial increase in the bond-length spread in the glassy state and subsequent narrowing down of bond length distribution. Fig. 4.8 (b) shows the line-width dependence for the 751 cm^{-1} mode on temperature. This mode shows a linear rise in Γ without any anomaly near T_g for the glass with $x = 0.1$. For the other glass with $x = 0.2$, Γ increases linearly in the glassy state, and a change in slope occurs across T_g . In the glass with $x = 0.3$, Γ remains almost constant in the glassy state but it increases beyond T_g . Comparing these modes for the three glasses, it emerges that the effect of increasing PbO in the structure tends to bring down the bond-length distribution of the TeO_4 -tbp units with rising temperature, while not affecting the distribution of the TeO_3 units much. X-ray absorption studies [161] indicate a mixture of two TeO_n entities (and the intermediate polyhedra TeO_{3+1}) for the glass with $x = 0.3$ and hence a mixture environment of coordination sub-shells. Glass with $x = 0.1$ was shown to have TeO_4 -tbp polyhedra in two different inter-atomic distances in Te–O pairs, while $x = 0.5$ exhibited a single-distance shell as in the case of TeO_3 -tp structure. Furthermore, Pb–Te contribution like in PbTe_3O_7 crystalline compound was found and attributed to a medium-range order in which Pb atoms also participate in an important role in glass network formation. The role of PbO as a network former might induce structural

rearrangements in the $\text{TeO}_4\text{-tp}$ units that favor to narrow the bond length distribution with temperature.

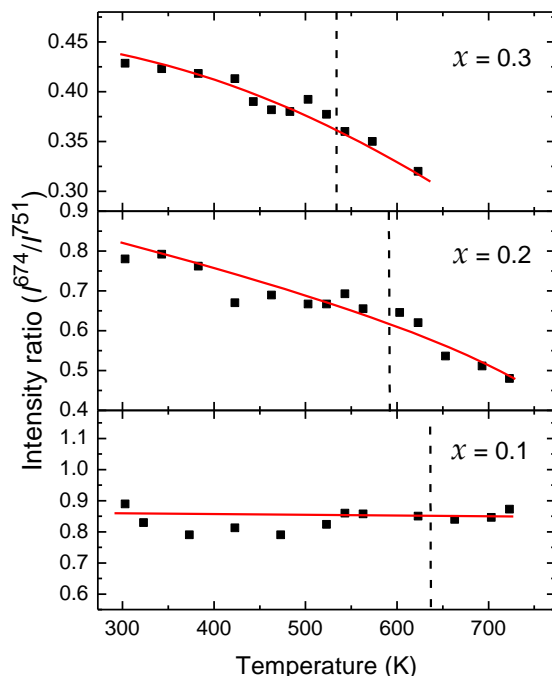


Fig. 4.9. Temperature dependence of the intensity ratio of the 674 cm^{-1} mode with respect to the 751 cm^{-1} mode (I^{674}/I^{751}) for the glasses with $x = 0.1, 0.2$ and 0.3 . The lines through the data are guides to the eye. The dashed vertical lines mark the glass transition in the respective glass composition.

Fig. 4.9 depicts the temperature dependence of the intensity ratios of the 674 cm^{-1} mode with respect to the 751 cm^{-1} mode (I^{674}/I^{751}) for the three tellurite glasses with different molar concentrations of PbO. For the glass with composition $x = 0.1$, the intensity ratio remains almost constant throughout the temperature region. However, for the glass with $x = 0.2$ and 0.3 , the intensity ratios decrease rapidly with increasing temperature, thereby suggesting that the $\text{TeO}_3\text{-tp}$ units increase at the expense of $\text{TeO}_4\text{-tp}$ units with increasing temperature for a given composition. In addition, same behaviour was also found with increasing modifier content. The effect becomes more prominent with temperature for the glass with higher content of modifier. Similar inferences were drawn from $20\text{Li}_2\text{O}:80\text{TeO}_2$ glass upon heating, i.e., the rise in the

relative intensity of the TeO_3 stretching mode at the expense of TeO_4 units [155]. Quantitative interpretation of Raman intensities in terms of change of population of species is motivated by the reported x-ray studies on conversion from TeO_4 to TeO_3 with composition change at ambient. Although a change of polarizability tensor can also induce a change in intensity, the ratio of polarizabilities of different species is not expected to be strongly dependent on temperature.

The present results thus suggest that incorporation of more PbO into the tellurite structure reduces the network rigidity as evident from the decrease of longitudinal elastic constant. PbO affects the bonding characteristics of the structure by forming more of non-bridging oxygens and hence more of TeO_3 -tp units as shown in the composition dependent Raman spectra at ambient. As seen in Fig. 4.9, temperature also plays a similar role in modifying the structure by gradually transforming the TeO_4 units into TeO_3 units. However, as shown in table 1, the slope of the LA mode frequency decreases beyond T_g with the addition of more PbO, implying increase of rigidity and slowing down of structural relaxations after the transition with increase of modifier. Furthermore, we observe from the Raman mode analysis in Fig. 4.7 that the TeO_4 and TeO_3 stretching vibrations show hardening with gradual increase of modifier, both in the glassy and supercooled state. The hardening increases more prominently beyond the transition with increase of PbO. This implies that the bonds become stiffer both as a function of temperature and addition of PbO.

Table 4.3. Effect of PbO network modifier on micro- and macroscopic length-scales

<u>Technique</u>	<u>Raman spectroscopy</u>	<u>Brillouin spectroscopy</u>
length-scale	microscopic	macroscopic
observation	mode hardening for higher x	decrease of elastic constant for higher x
inference	molecular bond-stiffening	loss of network rigidity

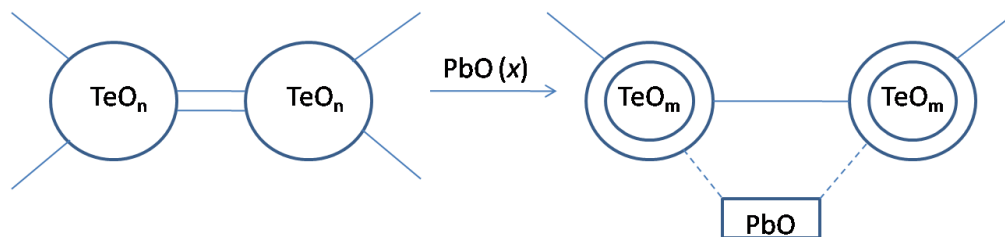


Fig. 4.10. Schematic diagram of the lead-tellurite network glass showing building blocks such as TeO_n and PbO units. Addition of PbO to the glass breaks the inter-molecular network bonds between the units and weakens the network. Consequent conversion of some of the TeO_4 -tbp units into TeO_3 -tp units ($\langle m \rangle < \langle n \rangle$) makes the intra-molecular Te-O stretching vibration force constant stiffer.

The observations made using the two techniques and the inferences drawn are summarized in table 4.3. The stiffening of the force constants of molecular units at a microscopic length scale and decrease of elastic constant, attributed to loss of network rigidity on a macroscopic length scale appear to be opposite. In order to have an insight of the microscopic origin for an apparently opposite behaviour at the two length scales, we consider a simplified microscopic model of the structure of the glass using the TeO_n molecular building blocks connected with network bonds (Fig. 4.10). Incorporation of PbO in the glass breaks/ weakens the inter-molecular network bonds and consequently converts some of the TeO_n units to TeO_m , where $\langle m \rangle < \langle n \rangle$. For example, conversion of TeO_4 -tbp to TeO_3 -tp is known in tellurite glasses upon alkali-doping. Concurrent creation of TeO_m molecular units makes the intra-molecular Te-O stretching vibration force constant stiffer, i.e., intra-molecular bonds are strengthened at the cost of inter-molecular bonds due to addition of PbO , thus explaining the apparently opposite behaviours found from Raman and Brillouin spectroscopy. The macroscopic decrease of the elastic modulus basically arises due to weak links between TeO_m units, while hardening of microscopic vibrational modes arises due to internal modes of stiffer TeO_m units. Increase of temperature also has effect similar to that of PbO doping as evident from the temperature dependence of intensity ratio (Fig. 4.9). Slower rate of decrease of elastic

constant above T_g for glass with higher x (table 4.1), which infers lowering of glass fragility with addition of PbO, is due to greater hindrance to structural reorientations by PbO as it causes the structural units of the glass network to stiffen.

4.3.4. Thermal analysis: Glass transition and the Kauzmann temperature

As discussed earlier, the lead-tellurite glass with $x = 0.3$ exhibits crystallization peak in DSC. Fig. 4.11 shows the non-isothermal DSC thermograms of the lead-tellurite glass (0.3PbO:0.7TeO₂) at four linear heating rates. A glass transition hump followed by two crystallization exotherms can be seen. The glass transition temperature (T_g) and the peak crystallization temperatures (T_{cry1} and T_{cry2}) for the first and second crystallization events are identified from the thermograms. The glass transition results in a sudden increase in specific heat due to increased relaxations on reaching the supercooled liquid state. T_g reflects the strength or structural rigidity of a glass. It was observed from the analysis of Fig. 4.11 that the T_g values shift to higher temperatures with increasing heating rates (β). This is due to the increase in structural relaxations and decrease in relaxation time with increasing β [172]. Fig. 4.12 shows the variation of T_g with the logarithm of heating rate. The data has been fitted to a linear relation according to Lasocka [173],

$$T_g = A_g + B_g \log \beta \quad (4.75)$$

where A_g and B_g are empirical constants with values 542.5 K and 11.3, respectively, for the 0.3PbO:0.7TeO₂ glass. Extrapolation of this line to $\beta = 1$ K/min, i.e., $T_{g1} = A_g$, predicts the lower limit of T_g within the laboratory time scales. Transformation to a glass takes place over a range of temperature and T_{g1} is considered to be the low-temperature edge of the transformation region. The slope B_g of the plot indicates the heating rate-dependence of the changes among various configurational states across the glass to supercooled liquid transition. A higher glass-quenching rate would manifest a more

pronounced dependence of T_g on β , which implies a steeper slope B_g in the above equation. This means, the higher the value of the constant B_g , the farther is the glassy state away from equilibrium. The B_g value of 11.3 for the lead-tellurite glass, is within the range generally found true for many glass [174] systems.

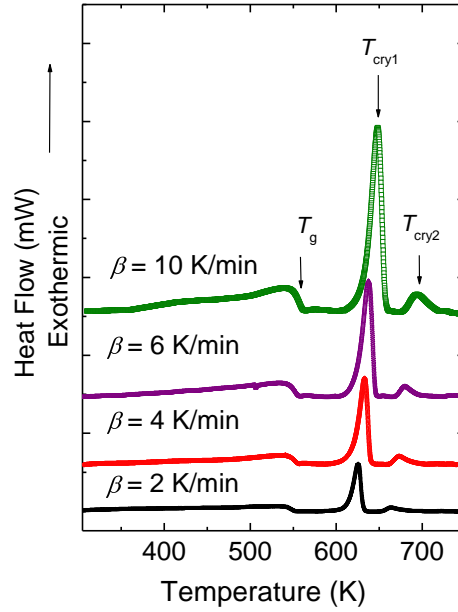


Fig. 4.11. DSC thermograms of 0.3PbO:0.7TeO₂ glass at different heating rates. The glass transition temperature (T_g) and the peak crystallization temperatures (T_{cry}) are indicated in the figure (subscripts 1 and 2 refer to first and second crystallization peaks).

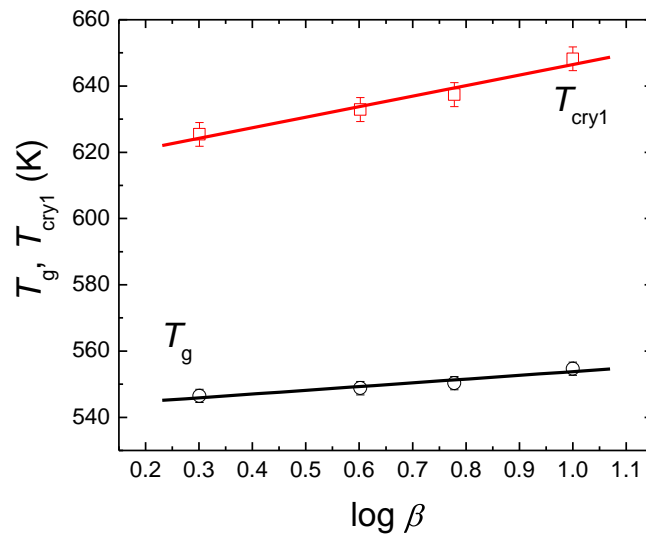


Fig. 4.12. Dependence of T_g and T_{cry1} on ($\log \beta$).

Furthermore, Lasocka's relation for the glass transition has also been found to be valid for the heating rate dependence of the crystallization temperature [174,175],

$$T_{\text{cry}} = A_c + B_c \log \beta \quad (4.76)$$

as shown in Fig. 4.12 for the first crystallization exotherm. Variation of T_{cry} with $\log \beta$ is steeper than that of T_g since crystallization, being a kinetic process, is controlled by atomic diffusion, whereas glass transition encounters configurational changes due to structural relaxations. A_c is the lower limit for the crystallization temperature within laboratory time scales ($\beta = 1$ K/min), and signifies the temperature at which atoms gain mobilities on heating. A_c and B_c values for the present glass are 614.7 K and 31.7, respectively. Combining Eqs. 4.3 and 4.4, a linear correlation between T_g and T_{cry} is obtained as,

$$T_g = \left(\frac{A_g B_c - B_g A_c}{B_c} \right) + \left(\frac{B_g}{B_c} \right) T_{\text{cry}}, \quad (4.77)$$

which for the present glass is,

$$T_g = 323.4 + 0.36 T_{\text{cry}}. \quad (4.78)$$

This relation shows that glass transition and crystallization are dependent on each other and T_g increases linearly with T_{cry} . The above relation can be used to determine the Kauzmann temperature T_K , which is defined as the temperature at which the entropy of the supercooled liquid becomes equal to that of the equilibrium crystal [11]. This is the temperature below which a liquid cannot be supercooled even at the slowest cooling rate. Assuming a heating rate β_K such that, $T_g = T_{\text{cry}} = T_K$, and using Eq. 4.5, we obtain $T_K = 502.5$ K, and the corresponding $\beta_K = 3.2 \times 10^{-4}$ K/min. Due to such a small heating rate, it is extremely difficult to attain this ideal glass transition in practice. On the contrary, very small quenching rate will be sufficient to realize the glassy state in this system. T_K and β_K are also the respective temperature and heating rate that corresponds to the intersection of the extrapolation of the two curves of Fig. 4.12. Using the allowed deviations from the extrapolated lines, the range of the intersection point, which also correspond to the error

in estimating the values, was obtained as $T_K = 502.5 \pm 3.7$ K and $\beta_K = 3.2 \times 10^{-4}$ ($\pm 3.3 \times 10^{-4}$) K/min. Since these curves will meet at very low β , the glass to supercooled liquid transition is always observable on heating, under conventional heating rates. This shows that the lead-tellurite supercooled liquid has high thermal stability and good glass-forming ability.

4.3.5. Crystallization kinetics: Non-isothermal studies

Equal masses (± 0.01 mg) of the sample were used for different heating rates to eliminate mass-dependent effects on the peak shifts. Fig. 4.13 shows the DSC exotherms of the two-stage crystallization of 0.3PbO:0.7TeO₂ glass at various heating rates after baseline correction. It is observed that the crystallization peak temperature rises with increasing heating rate, along with elevation in the peak height, indicating increasing crystallization enthalpy. The Kissinger peak shift method is used to evaluate the activation energy for crystallization (E_c), only from the knowledge of the crystallization peak temperature and the heating rate, using the Kissinger equation [176],

$$\ln\left(\frac{T_{cry}^2}{\beta}\right) = \ln\left(\frac{E_c}{RK_0}\right) + \frac{E_c}{RT_{cry}} \quad (4.79)$$

where K_0 is the frequency factor. The plots of $\ln(T_{cry}^2/\beta)$ versus $1/T_{cry}$ result in straight lines as shown in Figs. 4.14 (a) and (b) for the first and second crystallization peaks, respectively. The slope depicts E_c while the intercept yields K_0 . For the first crystallization, we obtained activation energy E_{c1} as 223.7 kJ/mol and K_0 as $7.37 \times 10^{17} \text{ s}^{-1}$, and similarly for the second crystallization, E_{c2} as 238.7 kJ/mol and K_0 value as $8.77 \times 10^{17} \text{ s}^{-1}$. While E_c denotes the required threshold energy to overcome the barrier and begin the crystallization process, the value of K_0 indicates the number of such attempts made by the atomic entities per second to participate in the crystallization process and hence it is called as the frequency factor.

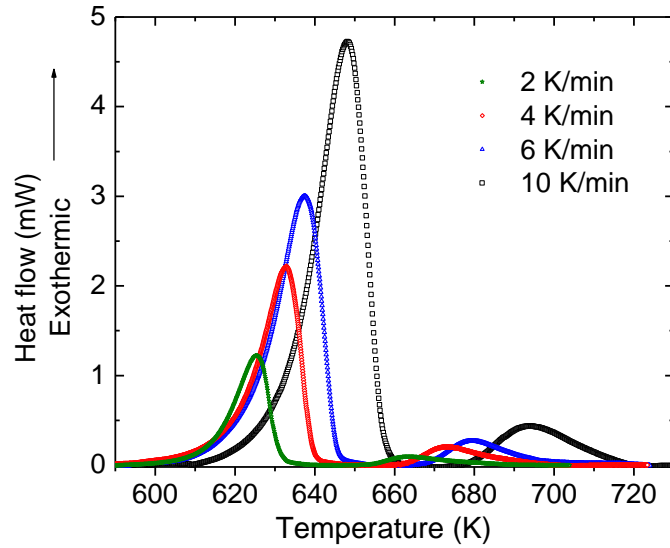


Fig. 4.13. Baseline-corrected exothermal curves of the two-stage crystallization of 0.3PbO:0.7TeO₂ glass at various heating rates.

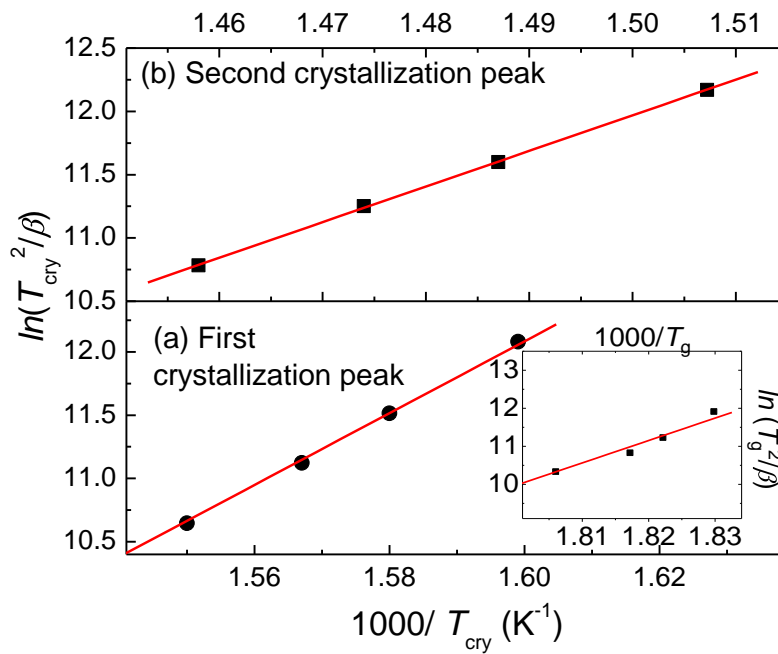


Fig. 4.14. Kissinger plots of $\ln(T_{\text{cry}}^2/\beta)$ versus $1000/T_{\text{cry}}$ for the (a) first and (b) second crystallization peaks. Inset: Plot of $\ln(T_g^2/\beta)$ versus $1000/T_g$ to evaluate the glass transition activation energy.

Since the glass transition temperature exhibits a similar dependence on β as the crystallization temperature, the above Kissinger equation, originally derived for the

crystallization process, can be applied to determine the activation energy, E_g , for the glass transition [177,178],

$$\ln\left(\frac{T_g^2}{\beta}\right) = \frac{E_g}{RT_g} + \text{const.} \quad (4.80)$$

The inset to Fig. 4.14 (a) shows the linear plot to the above equation and from the slope E_g is found to be 489.8 kJ/mol. It can be observed that E_g is much higher compared to E_{c1} and E_{c2} , even though the glass transition occurs at temperatures lower than the crystallization events. E_g signifies the energy required for structural relaxation and rearrangement of molecular units around T_g . It is mainly governed by viscosity and cooperative behaviour of the molecular units comprising the tellurite glass network. The high value of E_g implies that high activation energy is required for the internal configurational relaxation of this covalently bonded network glass, while processes governing crystallization is mainly through diffusion of the molecules requiring lower energies.

4.3.5.1. Isokinetic method: JMA Analysis

The Kissinger method uses only the peak crystallization temperature for the estimation of E , which may provide only approximate results. Most of the isokinetic methods are based on the JMA rate equation (Eq. 1.11). The non-isothermal DSC experiments impose the condition that the temperature T of the transforming sample changes at a constant rate with respect to time, i.e., $T = T_0 + \beta t$, where T_0 is the crystallization onset temperature. The changes observed in the thermal behaviour forms the basis of determination of the crystallization kinetic parameters of the sample. In this work, we have focused on detailed analysis of only the first crystallization peak.

The rate of reaction for the crystallization process is based on the basic kinetic equation,

$$\frac{d\alpha}{dt} = K(T)f(\alpha) \quad (4.81)$$

where, $K(T)$ is the rate constant described by Eq. 1.10 and $f(\alpha)$ is the reaction model which gives Eq. 1.11 under the JMA formalism. The conversion dependence is described by a function $f(\alpha)$ which depends on the physical mechanism assumed in the mathematical formalisms. The outcome of the kinetic analysis is the kinetic triplet: K_0 , E and $f(\alpha)$, which provides a physical interpretation to the obtained experimental data.

Using Eqs. 1.9 and 1.10 to the non-isothermal condition, the time-dependent JMA equation can be modified to a temperature-dependent form for the transformed volume fraction (α) as,

$$\alpha = 1 - \exp \left[-\frac{K_0}{\beta} \int_{T_0}^T \exp \left(-\frac{E}{RT} \right) dT \right]^b \quad (4.82)$$

In the absence of an exact solution to the above integral, various approximations [179,180] have been made to evaluate this integral and extract out information on the parameters E , b and K_0 . Utilizing the approximation [179],

$$\int_{T_0}^T \exp \left(-\frac{E}{RT'} \right) dT' \cong T \exp \left(-\frac{E}{RT} \right) \sum_{m=1}^{\infty} \left(\frac{RT}{E} \right)^m (-1)^{m-1} m! \quad (4.83)$$

and considering only $m = 1$ term, we obtain,

$$\int_{T_0}^T \exp \left(-\frac{E}{RT'} \right) dT' \cong \frac{RT^2}{E} \exp \left(-\frac{E}{RT} \right) \quad (4.84)$$

Using Eq. 4.12 in Eq. 4.10, we obtain,

$$\alpha = 1 - \exp \left[-\left\{ \frac{K_0 RT^2}{\beta E} \exp \left(-\frac{E}{RT} \right) \right\}^b \right] \quad (4.85)$$

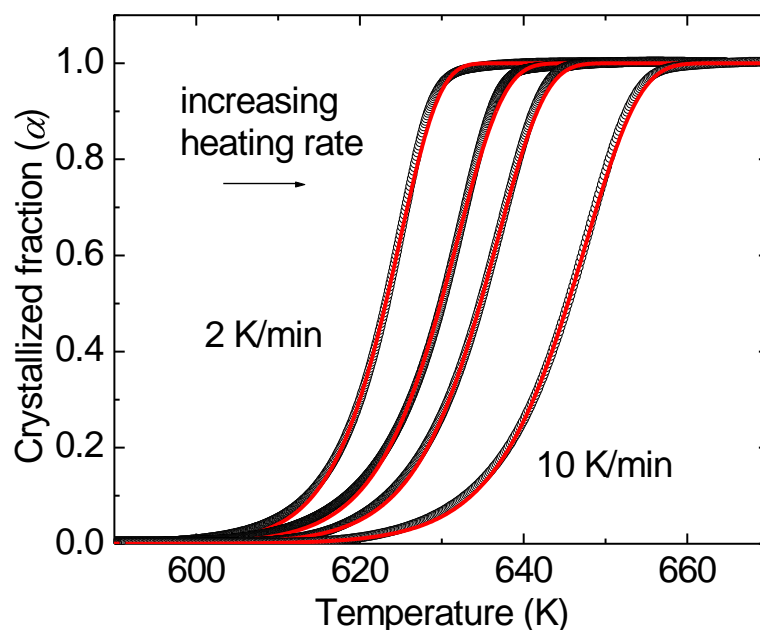


Fig. 4.15. Fractional crystallization (α) as a function of temperature for the first peak obtained from the DSC thermograms at various heating rates. The solid red lines show the curve fitting according to Eq. 4.13 using the method of least squares.

The crystallized volume fraction (α) is the integral curve of the area under the first exothermic crystallization peak obtained experimentally in Fig. 4.13. The resulting normalized data appear as typical sigmoid curves as presented in Fig. 4.15 for the different heating rates. The low temperature stage of the curve signifies nucleation, the intermediate stage depicts growth of nuclei and the final stage represents coalescing crystallites indicating completion of crystallization [181]. The experimentally obtained α for different heating rates were fitted to Eq. 4.13 using the iterative least-square fitting method as depicted in Fig. 4.15. The initial estimates of E and K_0 are taken from the Kissinger analysis (Eq. 4.7). The values of the parameters E , b and K_0 obtained from the fitting are presented in table 4.4.

It can be observed that the JMA analysis gives activation energy of ~ 220 kJ/ mol for the first crystallization, which is consistent with that derived from Kissinger analysis.

It can also be noted from the table that the Avrami exponent (b) is nearly close to 3. Generally, the exponent is a multiple of 0.5 for diffusion-controlled growth and a multiple of 1 for a reaction with constant rate of movement of the interface (linear growth) [182]. It is therefore evident that the crystallization in 0.3PbO:0.7TeO₂ glass is an interface-controlled growth transformation [183] within the limitations of the JMA formalism since $3 \leq b \leq 4$. In general, when nuclei are formed during a previous heat treatment before thermal analysis, then $b = a$. When nuclei are formed during the heating run for kinetic analysis, $b = a+1$. Usually, b strongly depends on β , but for cases of pure site saturation, b does not vary significantly and is nearly constant, as observed in the present case. The entire nucleation process, therefore, takes place during the early stages of transformation in the event of site saturation and becomes negligible later, and hence the crystallization is an isokinetic process [180].

Table 4.4. Values of the activation energy (E), Avrami (growth) exponent (b) and the frequency factor (K_0) obtained by fitting the experimental fractional crystallization data for the first exothermic peak at different heating rates using Eq. 4.13.

Heating rate (K/ min)	JMA model		
	E (kJ/ mol)	b	K_0 (10^{17} s ⁻¹)
2	219.62	2.94	3.09
4	223.27	2.52	7.69
6	223.14	2.50	7.99
10	220.69	2.35	3.96

4.3.6. Structural studies: Phase formation during heating and cooling crystallization

TeO₂ in the crystalline phase at ambient conditions occurs in several polymorph forms [184]. The lone electron pair in Te complicates the short-range atomic arrangement

in TeO_2 , making the first coordination sphere around Te highly asymmetric and variable [185]. To identify the phases those crystallize during the thermal analysis procedures, x-ray diffraction was carried out for the glass annealed for 30 min at the first and second crystallization peak temperatures at a heating rate of 10 K/min. Fig. 4.16 shows the XRD patterns of the heat treated samples under different conditions. The pattern for the sample annealed at 648 K (first crystallization peak temperature) matches well with PbTeO_3 crystallized in the orthorhombic structure [186]. There are small peaks corresponding to the $\alpha\text{-TeO}_2$ structure also, indicating coexistence of phases in the amorphous matrix. The sample annealed at the second crystallization temperature (693 K) depicts intense and clear peaks of the PbTeO_3 structure, along with those of $\alpha\text{-TeO}_2$. This indicates that both the crystalline peaks observed in the thermal analysis are associated with the formation of identical phases. It can be due to a metastable nanocrystalline phase formation first, followed by the transformation into crystalline PbTeO_3 and $\alpha\text{-TeO}_2$.

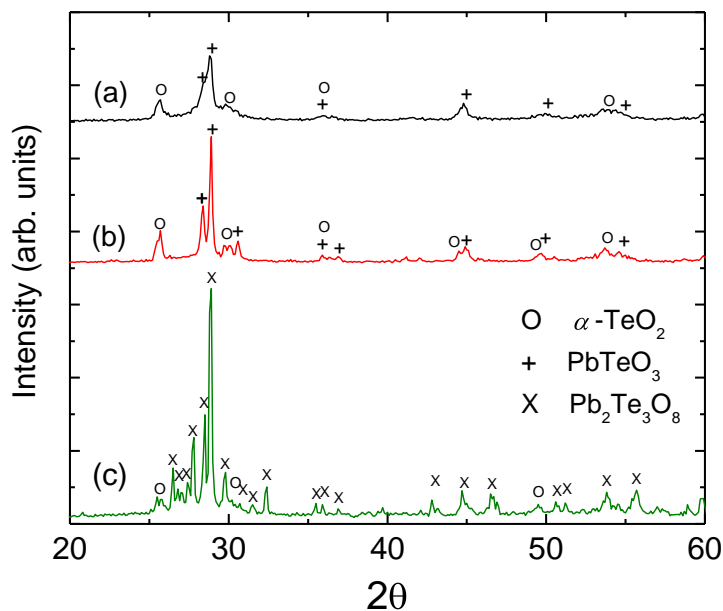


Fig. 4.16. X-ray diffraction patterns for the glass samples annealed at (a) 648 K and (b) 693 K while heating, and (c) the melt-cooled sample at ambient. The symbols at the top of the peaks indicate the respective phases they correspond to.

The crystallization behaviour was also identified while investigating high temperature Raman spectra of the glass sample when the bands became sharp, implying the onset of crystallization at ~ 623 K, as observed in Fig. 4.17. As the viscosity of the glass rapidly decreases above T_g , and the glass network ruptures with added modifier, the required mobility for crystallization is achieved. The analysis of the spectra shows presence of modes corresponding to α -TeO₂ (640 cm⁻¹) and PbTeO₃ (750 and 100 cm⁻¹) in the devitrified sample [187]. These modes persist through both the crystallization temperatures and until the sample melts at 823 K (see inset to Fig. 4.17), whereupon the spectra resembles that of the parent glass. The phase information obtained from the Raman spectra corroborates with that analyzed from XRD. However, the metastable phase is not well understood at this stage. The Raman spectra observed during cooling from 823 K exhibited different modes, unlike heating cycle, as shown in the inset to Fig. 4.17, indicating crystallization into other phases. The modes at 763, 740 and 698 cm⁻¹, which appeared in place of the mode at 750 cm⁻¹ depicts the characteristic vibrations of the [Te₃O₈]⁻⁴ anions in the Pb₂Te₃O₈ structure [188]. In the Pb₂Te₃O₈ compound the [TeO₄] and [TeO₃] structural units are interconnected by two Te–O–Te bridges into a linear tri-nuclear [Te₃O₈]⁻⁴ anion [189]. X-ray diffractogram of the melt-cooled sample further confirms the formation of orthorhombic Pb₂Te₃O₈ structure alongwith α -TeO₂ as shown in Fig. 4.16.

Tellurite glasses manifest a great diversity in the structure of the constituent complex anions depending on the proportion of the modifier content, unlike the atomic arrangement in the classic oxide glasses like alkali-silicates, which bear direct resemblance to their equilibrium crystalline lattices. The melt state of modified tellurite glasses comprise of charged entities (modifier cations such as Pb⁺² and ortho anions of TeO₃⁻²) and neutral polar molecules (TeO₂). The formation of a lead-tellurite glass of the present composition can be described by a reaction

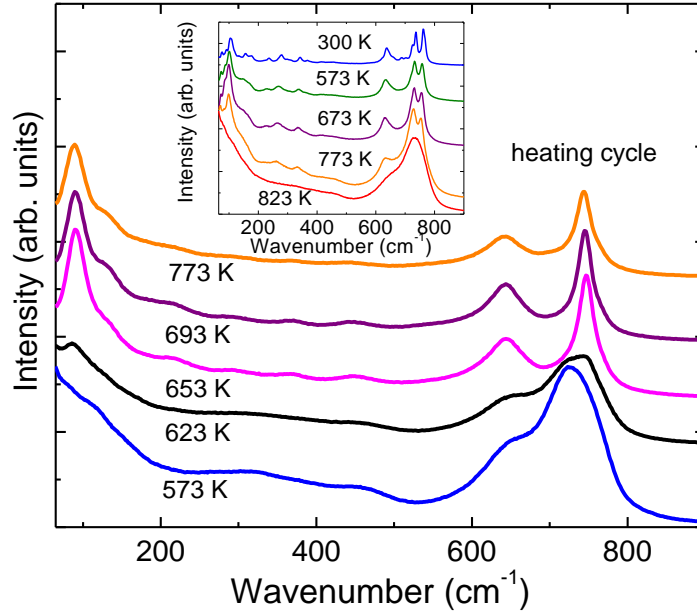
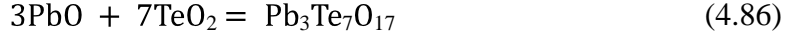
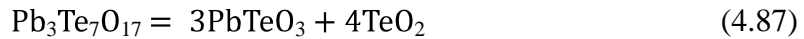


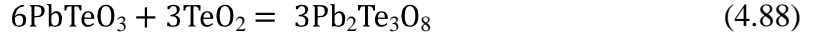
Fig. 4.17. Raman spectra of 0.3PbO:0.7TeO₂ glass at various temperatures while heating. Inset shows the spectra at various temperatures while cooling the sample.

In order to minimize electrostatic energy of the melt, the positive Pb⁺² ions would approach the negatively charged ortho-groups TeO₃⁻², thus expelling TeO₂ molecules which hinder this process. The consequence of such electrostatic repulsions results in phase separation [158] of PbTeO₃ and TeO₂ phases. This hypothesis suggested for tellurite melts suggests inherent immiscibility in these glasses. The amorphous phase separation in the resulting glasses manifest themselves during the thermally activated crystallization process and hence the formation of PbTeO₃ and TeO₂ phases identified from XRD and Raman spectra during heating cycle is understood as



As the supercooled liquid is phase separated, grain growth is characterized by local atomic rearrangements, without involving composition change, and transport of materials across crystal-liquid interface. Thus, most of the available free energy is

dissipated in the process of transferring atoms across the interface, and consequently the growth is interface-controlled. Once the devitrification takes place, further heating would allow the melt to undergo new reaction and hence phase separate as,



Such a phase separation is indeed observed in the cooling cycle of Raman spectra and the x-ray diffraction pattern of the melt-cooled crystallized sample. This exhibits the complexity of the crystallization behavior in tellurite glasses with modification by metal oxides owing to the distinct structural entities in the tellurite melts.

4.4. Conclusions

The dramatic dynamic processes occurring over the glass transition in lead-tellurite $x\text{PbO}:(1-x)\text{TeO}_2$ ($x = 0.1-0.3$) glasses have been probed in detail both with the help of acoustic vibrations, as well as, the high-frequency Raman bands associated with the local atomic vibrations. All the samples are found to show a marked drop in the LA mode frequency above T_g . Introduction of PbO in the glass is found to lower the glass rigidity, which is attributed to the formation of non-bridging oxygens in the structure. This results in lowering the elastic modulus with increasing x and a consequent decrease in the longitudinal sound velocity. The evolution of the LA mode frequency with temperature follows a similar trend for all glasses up to T_g and the scaled mode frequencies are shown to fall on a universal curve. A slower decrease of rigidity in the supercooled liquid state with temperature was observed at higher PbO content. From the analysis of the reduced Raman spectra of these glasses, several modes were found to exhibit anomalous behaviour in the glassy and supercooled liquid state and also across the transition. Instead of the expected anharmonic behaviour, the stretching vibrations of the TeO_4 -tbp units and TeO_3 -tp units are found to show anomalous hardening suggesting stiffening of the force constants with temperature. The rate of hardening increases above

T_g . The effect is more pronounced with increasing PbO content. In addition, the TeO_4 -tbp bond length distribution also narrows down with increasing x , as evident from the sharpening of its Raman band. A redistribution of vibrational density of states between TeO_3 -tp and TeO_4 -tbp units at elevated temperature is also evident from the intensity ratios of their Raman bands. The apparently opposite behaviour of decrease of elastic constants on a macroscopic scale and the stiffening of force constants of molecular units on a microscopic scale is explained with the help of a microscopic model, which connects the processes occurring at the two length scales.

Tellurites manifest distinct crystallization behaviour owing to highly asymmetric structural units. Non-isothermal DSC and Raman spectroscopy in conjunction with XRD, have been used to examine the kinetics of crystallization and structural evolution of the 0.3PbO:0.7TeO₂ eutectic glass composition during heating of the glass and cooling the liquid. The glass was found to devitrify in a two-stage crystallization process. A linear correlation was found to exist for the glass transition and crystallization temperatures obtained at various heating rates. The activation energies for the various processes were estimated and the lead-tellurite glass was found to undergo bulk nucleation with two-dimensional growth using the JMA model. Structural studies showed coexistence of phases of PbTeO_3 and $\alpha\text{-TeO}_2$ during the two-stage crystallization processes, while anomalous crystallization into $\text{Pb}_2\text{Te}_3\text{O}_8$ phase was observed when the devitrified melt was cooled. Immiscibility inherent to the tellurite glass system owing to the presence of unique structural units was found to result in the anomalous crystallization from the melts.

5

TEMPERATURE-INDUCED STRUCTURAL CHANGES IN IRON-PHOSPHATE GLASS AT SHORT-RANGE LENGTH-SCALE

5. 1. Introduction

Iron-phosphate glasses are being extensively investigated for their possible applications as host materials for encapsulation and vitrification of environmentally hazardous nuclear wastes [190-194]. Borosilicate glasses, being used industrially at present, suffer the disadvantage of phase segregation while loading certain phosphates, sulphates, oxides and heavy metals that form the major components in nuclear wastes [195]. Phosphate glasses were being considered as an alternative, owing to their low processing temperature and better solubility of wastes. Despite of these properties, the easily hydrolyzable $-P-O-P-$ bridging links render poor chemical durability to these glasses [196]. Binary iron phosphate glasses have been reported to overcome this shortcoming of phosphate glasses by replacing majority of the weak electropositive phosphorus atom with the strongly electropositive iron atom to form hydration resistant $-Fe-O-P-$ linkages, thereby providing these glasses with excellent chemical durability [197].

In recent years, a large number of studies have been carried out on iron phosphate glasses for their structure and the dependence of their properties on their compositions and synthesis conditions. Most of these are on the structural changes induced by the waste elements upon immobilization in the host matrix [191,194,197-201]. Glasses loaded with cesium showed an increase in glass transition temperature and then decrease with increasing mol% of Cs_2O [75] while those loaded with cerium showed a linear rise

[202]. The molecular level structures of iron-phosphate glasses depend on the fraction of ferrous (Fe^{2+}) ions, the Fe/P ratio and the overall O/P ratio [192,203]. Raman spectra of iron-rich glasses ($\text{Fe/P} > 1$) show tendency towards crystalline phase compared to conventional iron-phosphate glasses with $\text{Fe/P} < 1$ [190]. Glasses with O/P $\sim 4, 3.5$ and 3 are respectively classified as orthophosphates, pyrophosphates and metaphosphates with corresponding PO_4 tetrahedral units with zero, one and two bridging oxygens (labeled as Q^0, Q^1 and Q^2 tetrahedra), respectively, as dominating structures.

It has been reported [197] that iron-phosphate glasses with an approximate composition $40\text{Fe}_2\text{O}_3\text{-}60\text{P}_2\text{O}_5$ (mol%) leads to a ferric pyrophosphate structure which possess the best chemical durability. Here, some of the Fe^{3+} ions reduce to Fe^{2+} ions to yield a structure based on Fe^{3+} and Fe^{2+} ions in distorted octahedral sites acting as network formers and network modifiers, respectively [193,204]. Raman spectra of these glasses reveal peaks of Q^1 tetrahedra accompanied by shoulders of Q^2 and Q^0 tetrahedra [202], while the pyrophosphate composition should possess mostly Q^1 tetrahedra. It was suggested [205,206] based on a disproportionation reaction in the melt that equilibrium exists between the pyrophosphate anions and those of the meta- and orthophosphates: $2\text{Q}^1 \leftrightarrow \text{Q}^2 + \text{Q}^0$. Fang *et al.* [204] have shown that the Raman and infrared (IR) spectra of these glasses do not show any significant change with the melting temperature suggesting no change of structure. Although, much work has been done [198,202-204,207,208] to study the iron redox equilibrium, and the structure and properties of these glasses using a variety of techniques such as DTA, Mossbauer, IR and Raman spectroscopy, there is none on the temperature dependence of the vibrational properties. When immobilized with nuclear wastes, the structure of these glasses should sustain temperature effects arising from decay heat produced by the radioactive nuclei. Therefore, temperature dependent studies of these glasses are important to elucidate the effects of temperature on their structure.

The dynamics and glass transition of network glasses can be studied from vibrational processes occurring due to short-range ordering in these glasses. The nature of glass transition is still a subject of debate as to whether kinetic or thermodynamic processes drive the transition. While transport properties such as diffusion and viscosity change by orders of magnitude, thermodynamic quantities such as volume and entropy vary continuously at the transition. Local atomic vibrations giving rise to high-frequency Raman modes generally follow the usual thermal softening behaviour. This indicates that even though the viscosity changes drastically, the local atomic structure remains unaffected at the transition. However, certain relaxation times, attributed to cooperative dynamics, extracted from the analysis of the Raman line-shape have been shown to exhibit discontinuity across the glass transition [209]. There are also reports on changes in the temperature dependence of the high-frequency Raman modes for polymeric [210] and chalcogenide [211] glasses at the glass transition temperature, T_g . In addition, temperature dependence of band intensities of certain polyhedral units has been used for ascertaining their stability in different ranges of temperatures [212]. The glassy, supercooled liquid and melt states have been identified from the behaviour of mode-wavenumbers and line-widths [213]. Furthermore, Stavrou *et al.* have shown that the low-frequency vibrations characteristic of all glasses (the Boson peak) show strong temperature dependence near T_g [214]. In the present work, detailed high-frequency Raman spectroscopic studies were carried out on iron-phosphate glass (40Fe₂O₃-60P₂O₅ (mol%); O/P = 3.5; Fe/P = 0.67) in the temperature range 81-873 K with the aim of understanding the behaviour of the vibrational modes with increasing temperature and across its T_g . The spectra were analyzed using curve fitting, after correcting for the thermal population factor. The temperature dependences of mode-wavenumbers and line-widths were examined for possible signatures across the glass transition. The results are discussed in the context of structural relaxations.

5.2. Experimental

Synthesis of iron-phosphate glass, used in the present study, from rapid solidification of melt from 1423 K has been described in Chapter 2. For the 40:60 glass, the T_g was found to be 782 K [215], consistent with that reported by other researchers [190]. The glass pellets were polished using standard procedure. A high-throughput micro-Raman spectrometer (Renishaw model Invia) was used to record the Raman spectra in the backscattering geometry using the 514 nm excitation from an Ar ion laser and a charge coupled device (CCD) was used for detecting the scattered light in the wavenumber range 50-1600 cm^{-1} . A 20 \times microscope objective lens was used to focus the laser beam onto the sample, which was placed inside a Linkam THMS600 temperature-controlled heating/ cooling stage for carrying out temperature dependent Raman studies ranging from 81-873 K. The spectra were corrected for the thermal population factor and the reduced spectra were fitted to Gaussian line shapes by using PEAKFIT software (Jandel Scientific) to determine the wavenumber and line-width of the vibrational modes. The temperature dependences of the mode wavenumbers and their line-widths were analyzed to understand their overall behaviour and that across T_g .

5.3. Results and discussion

Fig. 5.1 shows the Raman spectra of iron-phosphate glass at selected temperatures. The spectra consist of broad features of vibrational modes typical of all glassy structures. As the Raman intensities are governed by the changes in the bond polarizabilities, the Raman spectra of glasses turn out to be broad due to the spread in the bond polarizabilities. The most intense peak in the spectra is observed near 1090 cm^{-1} which represents the characteristic asymmetric stretching vibration of Q^1 tetrahedra of $[\text{P}_2\text{O}_7]^{4-}$ units of pyrophosphate glasses. This broad peak is accompanied by a shoulder

each on the right and left side. A large number of overlapping, low intensity modes are observed on the lower wavenumber side to this most intense peak.

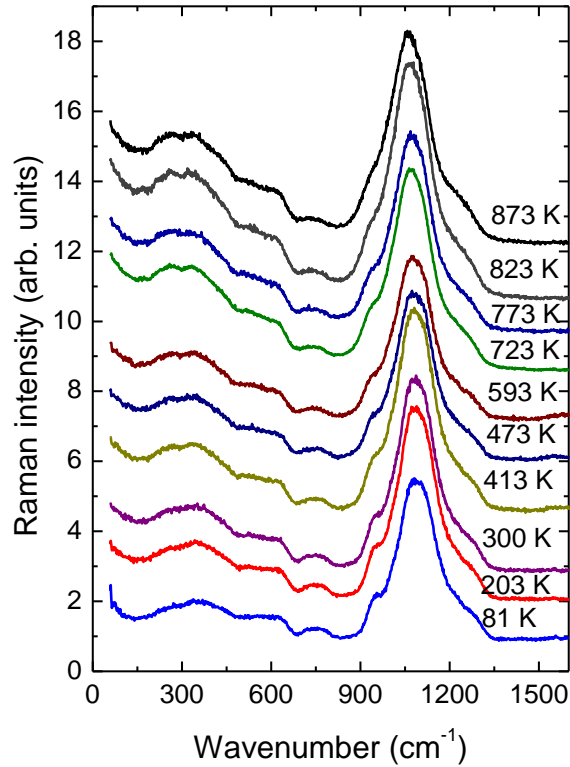


Fig.5.1. Raman spectra of iron-phosphate glass at various temperatures.

A breakdown of the $q = 0$ Raman selection rule of crystalline solids (where q is the phonon wave vector) in disordered materials allows all vibrational modes to participate in the scattering process. Raman spectrum of glasses and amorphous solids is thus closely related to the vibrational density of states. The lower wavenumber modes, as seen in Fig. 5.1, appear to become more intense with increasing temperature. This is a consequence of the temperature dependence of the thermal population of vibrational energy levels, governed by the Bose-Einstein statistics. Therefore, it was required to extract the vibrational density of states (VDOS) weighted by the photon-phonon Raman coupling coefficient (which is proportional to the scattering cross section of a vibrational mode at wavenumber ω), from the experimentally measured Raman scattered intensity $I^{\text{expt}}(\omega)$. The measured spectra were corrected for thermal population factor using Eq.

2.20, $I^{\text{red}}(\omega) = \omega I^{\text{exp}}(\omega) / [1 + n(\omega, T)]$, where, $n(\omega, T) = [\exp(\hbar\omega/kT) - 1]^{-1}$ is the Bose-Einstein occupation number with \hbar and k being the Planck and Boltzmann constant, respectively. Fig. 5.2 shows the corrected spectra at 81, 300 and 873 K. An examination of these reduced spectra reveals that the trivial thermal population effects in the low wavenumber part of Fig. 5.1 have been eliminated. The low wavenumber region of the 300 K spectrum is also shown in Fig. 5.2 after an ordinate expansion for unambiguous identification of modes.

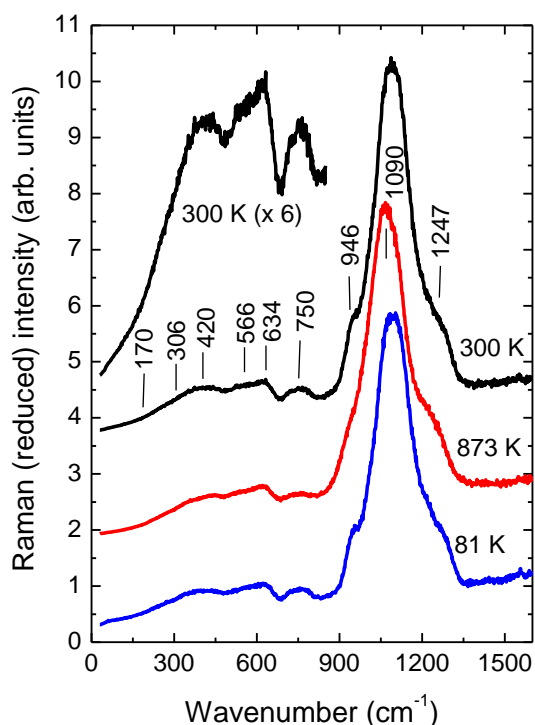


Fig.5.2. The reduced Raman spectra obtained after correction for the thermal population factor. The low wavenumber part of the 300 K spectrum is also shown after an ordinate expansion by a factor of 6.

These spectra extend over a large range of wavenumbers from 50-1600 cm^{-1} revealing broad spectral features. As mentioned earlier, the intensities of modes below 850 cm^{-1} are much lower than that of the 1090 cm^{-1} mode. In order to obtain reliable fitted parameters of the modes in each of the spectral regions, multi-Gaussian fitting

(with a suitable linear background) was carried out for the full spectra in two separate ranges; one below 850 cm^{-1} and the other above 850 cm^{-1} .

The spectral line shape can be Gaussian, Lorentzian or a Voigt function depending on the nature of the vibrational dephasing process [209]. Often Gaussian line shapes have been used for describing static or frozen environment resulting in an inhomogeneous broadening. Six peaks were used for fitting the spectra in the low-wavenumber region and three peaks were used for the high wavenumber region. Fig. 5.3 shows the reduced spectra at 300 and 773 K, corresponding to room temperature and T_g , respectively, fitted to a total of nine Gaussians.

The fitting procedure helped in identification of the modes occurring at 170, 306, 420, 566, 634 and 750 cm^{-1} in the low wavenumber region and 946, 1090 and 1247 cm^{-1} in the high wavenumber region corresponding to the spectrum at 300 K (table 5.1). The most intense mode at 1090 cm^{-1} is attributed to the asymmetric stretching of Q^1 tetrahedra of $[P_2O_7]^{4-}$ units [204] implying large number of pyrophosphate groups in the network of these glasses. The shoulders at 946 and 1247 cm^{-1} are assigned to asymmetric stretching of Q^0 tetrahedra of $[PO_4]^{3-}$ units and Q^2 tetrahedra of $[PO_3]^-$ units [204] and these indicate the presence of small number of ortho- and metaphosphate groups. The peak at 750 cm^{-1} is due to symmetric stretching [204] mode of P–O–P bridging bonds in the Q^1 structures. Characteristic vibrations for a phosphate network structure are represented by the modes at 420, 566 and 634 cm^{-1} arising due to bending of the PO_4 networks [190,202]. The mode at 306 cm^{-1} is assigned to the bending vibrations of Q^0 units [190,202] with iron as modifier forming Fe–O polyhedral and the 170 cm^{-1} mode is due to network vibrations. It may be pointed that the 170 and 306 cm^{-1} mode were included in the fitting on the basis of their clear presence in the unreduced spectra (Fig. 5.1). In the reduced spectra these do not manifest themselves as clear peaks or a shoulder.

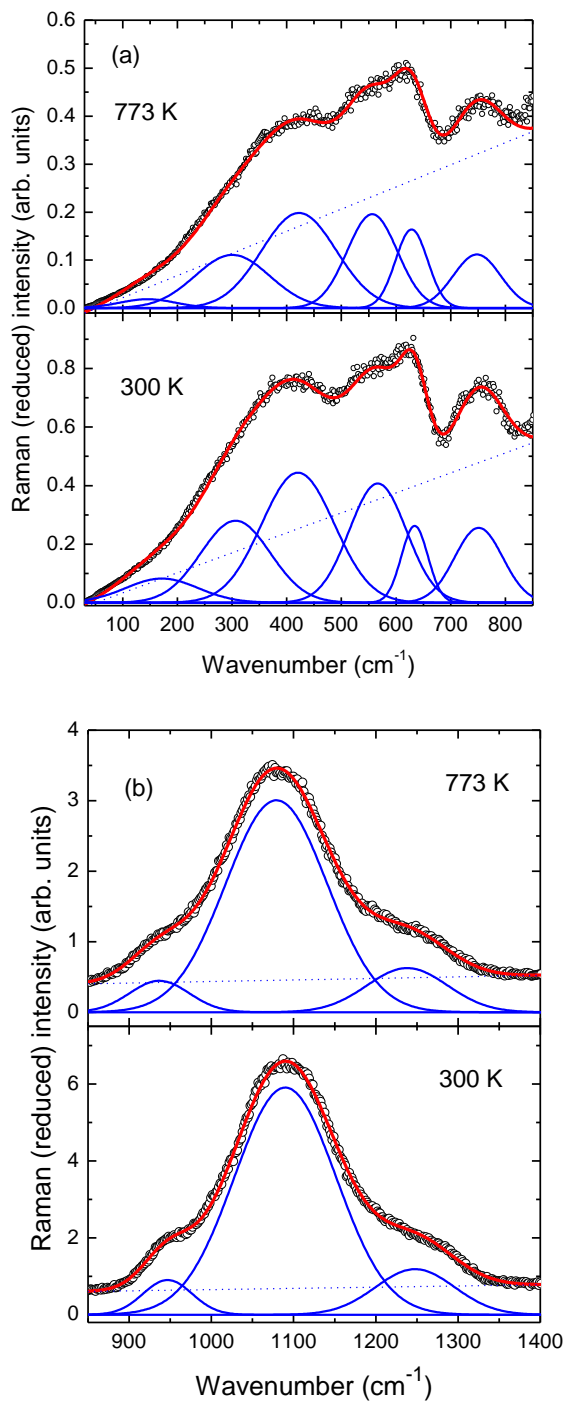


Fig.5.3. The reduced spectra at 300 and 773 K for (a) the low wavenumber region (below 850 cm⁻¹) and (b) the high wavenumber region (above 850 cm⁻¹), along with the Gaussian fits and a linear background. The continuous curves represent the fitted Gaussians. The total fitted spectra are also shown as continuous curves.

Table 5.1. Observed Raman bands of 40Fe₂O₃:60P₂O₅ glass at ambient temperature and their assignments.

Mode wavenumber (cm ⁻¹)	Assignment
1247	Asymmetric stretching of Q ² tetrahedra of [PO ₃] ⁻ units
1090	Asymmetric stretching of Q ¹ tetrahedra of [P ₂ O ₇] ⁴⁻ units
946	Asymmetric stretching of Q ⁰ tetrahedra of [PO ₄] ³⁻ units
750	Symmetric stretching of P–O–P bridging bonds in Q ¹ tetrahedra
634	Bending of PO ₄ network
566	Bending of PO ₄ network
420	Bending vibrations of PO ₄ network
306	Librational motion of Q ⁰ units formed with iron as modifier
170	Network vibration mode

The mode wavenumbers obtained from fitting are plotted as a function of temperature, in Fig. 5.4. As seen in Fig. 5.4 (a), the modes at 170, 306 and 420 cm⁻¹ arising as a result of network vibrations, librations of Fe–O polyhedral and phosphate network units, respectively, show a slight increase of mode wavenumbers with temperature. Generally, mode wavenumbers are found to decrease at elevated temperatures. This arises due to vibrations of atoms in anharmonic potentials. Anharmonicity causes the material to expand (macroscopically) upon heating. On a microscopic scale, this implies elongation of bond-distances. An increase in the bond length reduces the corresponding force-constant, thereby lowering the mode wavenumber. However, the behaviour observed here is opposite of the expected anharmonic behavior. This suggests stiffening of the force constants associated with these vibrational modes with increasing temperature. A stiffening of force constant could occur due to shortening of bond length in the corresponding polyhedral unit. Thus, this anomalous behavior of mode wavenumbers suggests structural relaxations in the glass. Such relaxations could involve changes in the average molecular configuration in a manner that even though the bond lengths decrease, the individual polyhedron units

comprising the network structure of these glasses, have their angles opened-up, making the overall network to expand with temperature.

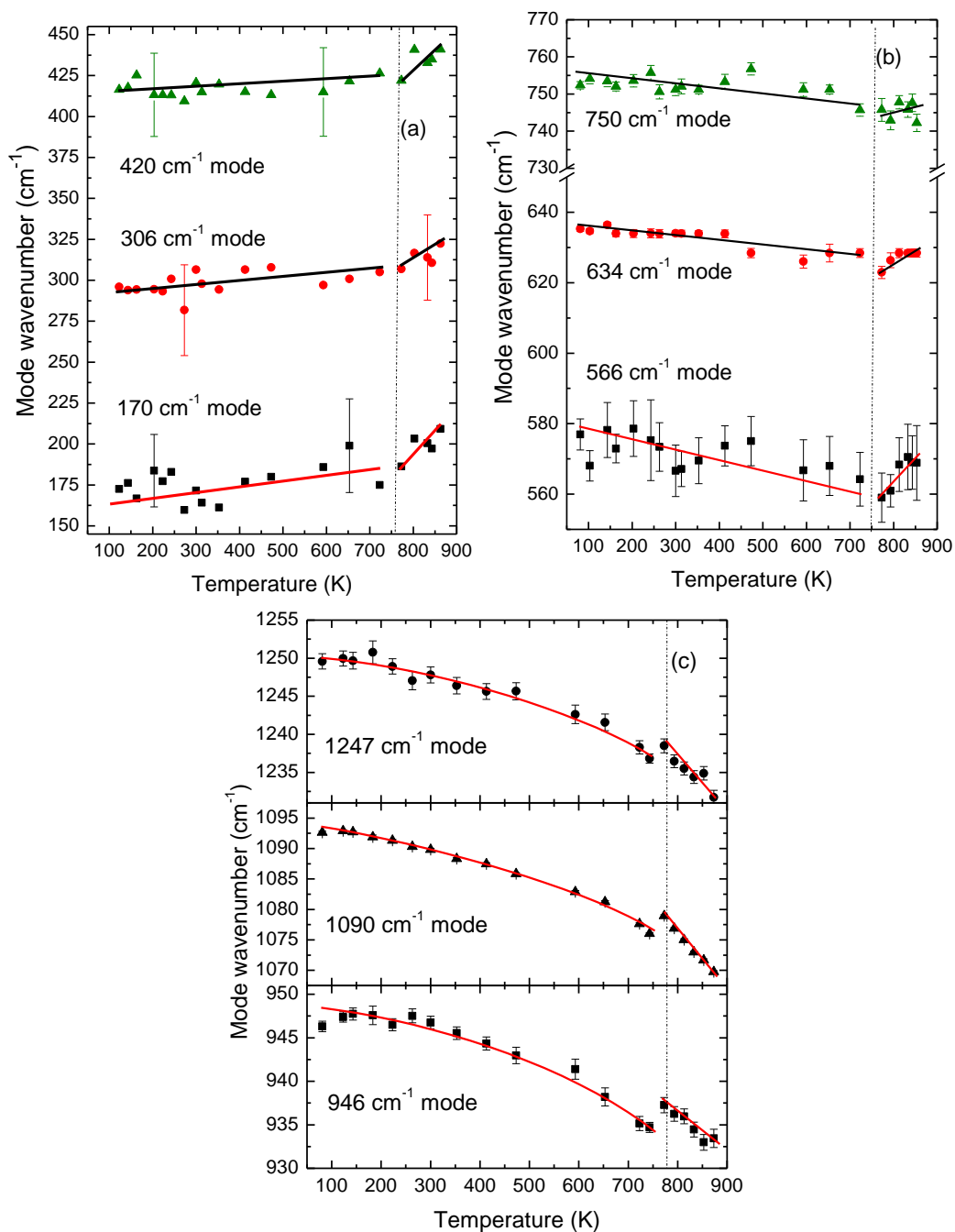


Fig.5.4. Temperature dependence of mode wavenumbers for all the eight modes. The lines through the data are guides to the eye.

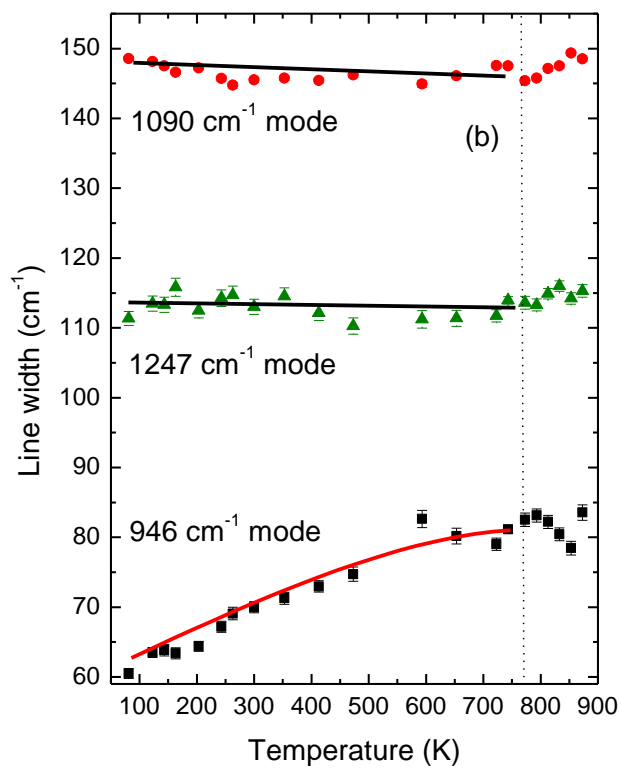
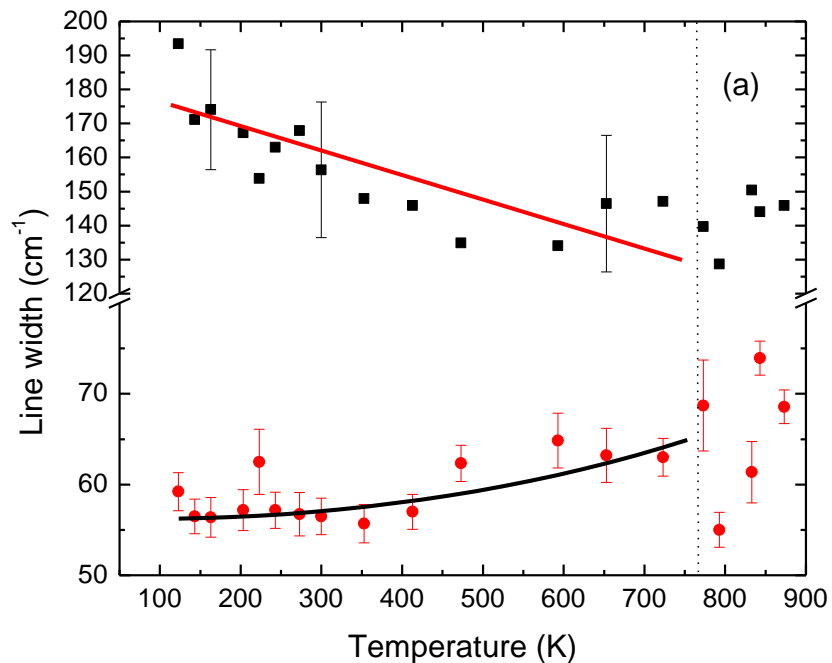


Fig.5.5. Temperature dependence of the line widths of (a) the 170 and 634 cm⁻¹ modes and of (b) the 946, 1090 and 1247 cm⁻¹ modes. The lines through the data are guides to the eye. The dashed vertical line marks the glass transition.

Apart from these modes, all other higher wavenumber modes show a softening behavior with increasing temperature thus exhibiting regular anharmonicity as depicted in Fig. 5.4 (b, c), until close to T_g . The 1090 cm^{-1} mode decreases by 20 cm^{-1} when heated to its T_g . As can be seen in Fig. 5.4, all the modes show anomalies near T_g . This suggests the existence of structural relaxations in the network structure of the glass as it is heated across its glass transition. Though an as-prepared glass is in a thermodynamically metastable state, it lowers its free energy continuously by a series of structural and configurational rearrangements to attain equilibrium configuration, giving rise to the phenomenon of structural relaxations. These relaxations are manifested as changes in the physical properties of the glass. The modes at 946 , 1090 and 1247 cm^{-1} show discontinuities in their behaviour near T_g as shown in Fig. 5.4 (c) and continue to soften after T_g is crossed. The rate of decrease of mode wavenumbers is also found to increase after T_g as their slopes become steeper. This suggests that anharmonicity of these vibrational modes increases compared to that in the glassy state, suggesting structural relaxations occurring at T_g . It may be pointed out that the anomalies such as discontinuous change in the mode wavenumbers or a change of slope have been reported in polymeric glass [210] and chalcogenide glasses [211] earlier; however, the observed changes were rather small, $\sim 1\text{ cm}^{-1}$. On the other hand, in As_2O_3 and $2\text{BiCl}_3:\text{KCl}$ systems [209] and in the present phosphate glass, much larger discontinuities in the mode wavenumbers are found across T_g for several modes. Generally, the time-scale for the structural relaxations decreases rapidly with increasing temperature. However, above T_g , the structure rearranges promptly in response to temperature and attains the properties of the equilibrium liquid.

The 170 , 306 and 420 cm^{-1} modes also show discontinuities in their hardening behaviour, and the mode hardening increases further above T_g . A higher rate of change of mode wavenumber above T_g is similar to the trend shown by the high frequency modes at

946, 1090 and 1247 cm^{-1} . This suggests that the nature of the inter-atomic potentials corresponding to these modes of vibrations remain similar after the transition. The modes at 566, 634 and 750 cm^{-1} also exhibit discontinuous changes. However, these modes show a clear change of slope above T_g with an increase of mode wavenumbers thereafter with increasing temperature. This indicates that the force constants for the atoms executing these vibrations increase, thereby altering the inter-atomic potentials in the liquid state.

The variation of line-width, Γ , with temperature for a few selected modes is shown in Fig. 5.5. One can see that line widths of the modes at 170 and 634 cm^{-1} have large scatter between successive temperatures, although the standard error of the fitted parameters of individual spectra is not so large. The scatter in the data thus essentially represents the random errors. Often in multi-peak fitting procedures the parameters of adjacent modes may exhibit strong correlations and lead to systematic errors. The parameter correlation matrix of the fitted parameters was examined to identify the parameters that exhibit strong correlations. This is important especially for weak modes. The line widths of adjacent modes were found to be oppositely correlated. The modes at 634 and 946 cm^{-1} show an increase of Γ with temperature up to T_g while those at 170, 1090 and 1247 cm^{-1} became narrower at high temperatures. A broadening is generally observed because of increase of scattering processes at higher temperatures which reduces the phonon lifetimes. This causes an inherent increase of the line widths. However, the sharpening of 170, 1090 and 1247 cm^{-1} modes at higher temperatures suggest an anomalous behaviour. The variation of Γ with temperature does not show any marked change in behaviour across T_g , unlike prominent differences observed in mode wavenumbers versus temperature. The supercooled region probed in the present study is rather small (only 100 K above T_g) and owing to large standard errors in the fitted data, a clear difference in the glassy and supercooled regions was not found from the line width

data. It is important to point out that this system undergoes crystallization at ~ 973 K and finally melts at 1373 K. However, the present measurements are done only upto 873 K. A clear difference between glassy and supercooled liquid state could not be found in Figs. 5.5 probably due to large error in fitted parameters.

5.4. Conclusions

To summarize, Raman spectra of iron phosphate glass were recorded over a wide range of temperature and spanning through its T_g . The spectra were corrected for thermal population effects and the reduced spectra were fitted to Gaussians. The analysis of the mode wavenumbers and line widths show anomalies from regular behavior for several modes. In contrast to the behaviours reported in polymeric and chalcogenide glasses, several vibrational modes in iron phosphate glass are found to exhibit dramatic changes near the glass transition and are attributed to structural relaxations. The occurrence of mode hardening and narrowing provides evidence of structural relaxation in the glass involving contraction and rotation of polyhedral units.

6.1 Summary

The properties of a glass are controlled by the microscopic structure, which in turn depends on the composition of the glass, and hence, investigating the inter-relationship between composition and network structure constitutes an important study. Such study enables one to prepare glass compositions with desired properties [216]. This thesis discussed the results of Raman and Brillouin spectroscopic investigations to understand the interplay of dynamics and structure in strong network glasses as a function of composition and temperature. A combined use of these two techniques have allowed us to capture vibrations that span different frequency regimes and monitor structural changes at short-, intermediate-range and bulk scale in the glasses across and around T_g . This thesis, therefore, explores the implications of glass modification on the network structure by varying the concentration of modifier and focuses on its consequences on glass structure and properties. Three systems of network glasses have been chosen: borate, tellurite and phosphate glasses. Oxides of divalent cations have been used as modifiers. The corresponding unmodified glass systems have coordination number of three, mixture of three and four, and four, respectively for the borate, tellurite and phosphate glasses. The basis for the choice of these systems is the unique response of these glasses to structural modification [62,87,159,195,204]. The basic concepts relevant to the phenomenology of glasses and the variety of universal phenomena linked to glass and the supercooled liquid states along with the relevant background literature were presented in **Chapter 1**.

In **Chapter 2**, the details of glass synthesis procedures and experimental techniques used for investigation of their structure and dynamics were discussed. Lead-borate glasses [$x\text{PbO}:(1-x)\text{B}_2\text{O}_3$ ($x = 0.2, 0.3, 0.4, 0.5, 0.6, 0.7, 0.8$)] and iron-phosphate glass [$40\text{Fe}_2\text{O}_3:60\text{P}_2\text{O}_5$] were prepared [70,73] by melt-quenching, while lead-tellurite glasses [$x\text{PbO}:(1-x)\text{TeO}_2$ ($x = 0.1, 0.2, 0.3$)] were prepared [71] by splat-quenching techniques. Details about the theories and instrumentation of the inelastic light scattering using Raman and Brillouin spectroscopy were discussed. The relevant theories of these techniques applicable for the study of glasses were also described. Characterization techniques such as XRD and DSC are also described in detail.

We now summarize the major scientific findings and conclusions that emerge from this thesis.

In **Chapter 3** of the thesis, we have studied lead-borate glasses with respect to their structure and dynamics at different length-scales. The initial three-coordinated (BO_3) network structure in borate glasses favour up-conversion of some fraction of units to four-coordinated (BO_4^-) borons with modifier addition up to a certain concentration [88]. This results in their non-monotonic variation of properties which is termed as the borate anomaly [56]. Borate and modified-borate glasses exhibit substantial intermediate-range order ($\sim 20 \text{ \AA}$) arising from superstructural units [86]. Network modifiers play an important role in defining the length-scale of the intermediate-range order [88]. PbO forms borate glasses over a large range of modifier concentration [87]. We have studied the changes in dynamic and structural behaviour in lead-borate [$x\text{PbO}:(1-x)\text{B}_2\text{O}_3$] glasses in a wide variation of x (0.2-0.8). We have carried out a detailed study of the short-range borate structure using density, T_g , sound velocity, elastic constants and Raman spectroscopic measurements. Low-frequency Raman spectroscopy and x-ray diffraction were used to study the composition-dependence of the Boson peak and the first sharp

diffraction peak (FSDP). Fragility was determined from rate-dependent DSC. Properties such as, T_g and elastic moduli exhibit a broad maxima around $x = 0.3$, in congruence with the average coordination number $\langle r \rangle$ of boron atoms, and attributed to the gradual conversion of BO_3 to BO_4 units, using Raman spectroscopy [70]. However, dynamic properties like the BP and fragility behave similar to the above structural properties except for an anomalous dip at $x = 0.3$. PbO was found to act as a glass former for higher concentrations. Static correlation lengths estimated from the FSDP did not follow a linear trend with dynamic correlation lengths (extracted from Boson peak), indicating a different spatial origin. However, the Boson peak position and fragility were found to vary linearly [70]. This correlation was found to emerge from the evolution of network packing and connectivity with the addition of modifier. An anomalous variation in dynamical properties reflects the critical role of Pb^{2+} in tuning the intermediate-range structure of the vitreous network. Moreover, using high-temperature Brillouin scattering on lead-borate glasses from 300-1150 K, a drastic decrease of network rigidity above T_g was observed, which was attributed to network disruption and structural relaxation in the supercooled liquid [217].

Chapter 4 of the thesis deals with the composition and temperature-induced changes in the structure of lead-tellurite glasses at different length-scales. Tellurium oxide glasses are being increasingly studied for their remarkable non-linear optical properties [62]. For enhancing their optical behaviour, other heavy metal-oxides such as PbO and ZnO have been incorporated [159]. The introduction of a network modifier elongates one of the Te-O bonds in TeO_4 and results in a gradual formation of TeO_3 units with addition of more metal oxide [63]. The elastic properties of glassy materials exhibit significant changes across T_g , even though the local atomic structure do not exhibit dramatic changes. To study the structural evolution of the system at different length-scales and across T_g , $x\text{PbO}:(1-x)\text{TeO}_2$ ($x = 0.1-0.3$) glasses were investigated using high-

temperature Brillouin and Raman spectroscopy in the temperature range 300-723 K. For all the samples investigated [71], the temperature-dependence of longitudinal acoustic (LA) mode was found to exhibit a scaling below T_g and a rapid softening above T_g . From an analysis of Raman spectra, several modes were found to exhibit hardening suggesting stiffening of the force constants with temperature, the effect being more pronounced in glasses with higher x . The stiffening of force constants of molecular units with temperature at a microscopic length-scale and decrease of elastic constant attributed to loss of network rigidity on a macroscopic length-scale appear to be inconsistent with each other. These different behaviours at two length-scales are understood on the basis of a microscopic model involving TeO_n and PbO units in the structure, which connects the two processes [71]. Moreover, metastable phases formed during crystallization of TeO_2 -rich glasses have been found to exhibit efficient second-harmonic generation [157]. Unusual crystallization behaviour has been observed for $\text{Li}_2\text{O}:\text{TeO}_2$ glasses, where crystallization occurred easily on heating the glass but hardly occurred when the corresponding liquid was cooled [156]. In this context, we have studied the structural evolution during temperature-induced crystallization processes in $0.3\text{PbO}:0.7\text{TeO}_2$ glass using DSC, Raman spectroscopy and x-ray diffraction. The kinetics of crystallization is investigated using isokinetic method to determine the kinetic parameters during crystallization of the glass. Crystallization was found to agree well with the Johnson-Mehl-Avrami model, suggesting the microstructural evolution as two-dimensional growth [72]. The structural evolution of the devitrified phases depicted coexistence of phases (PbTeO_3 and $\alpha\text{-TeO}_2$). Anomalous crystallization into $\text{Pb}_2\text{Te}_3\text{O}_8$ phase was observed when the devitrified melt was cooled, which is explained using amorphous phase separation inherent to tellurites [72].

In **Chapter 5**, we have studied the temperature dependence of the Raman modes in iron-phosphate glass across T_g . Iron-phosphate glasses have been extensively

investigated for their possible applications in vitrification of environmentally hazardous nuclear wastes [195]. This glass is a network of PO₄ tetrahedral units, where iron enters the network as Fe²⁺ or Fe³⁺ cations [198]. Glasses with oxygen-to-phosphorous (O/P) ratio ~ 4, 3.5 and 3 are respectively classified as ortho-, pyro- and meta-phosphates having corresponding PO₄ units with 0, 1 and 2 bridging oxygens (Q⁰, Q¹ and Q² tetrahedra) as the dominating structures [192]. We have studied a 40Fe₂O₃:60P₂O₅ glass with a ferric-pyrophosphate structure, which has been shown to possess the best chemical durability, using detailed Raman spectroscopic studies in the temperature range 81-873 K. The temperature-dependences of mode wave-numbers of nearly all the modes were found to exhibit anomalies near T_g . Below T_g , the asymmetric stretching of Q⁰, Q¹ and Q² tetrahedra exhibit conventional anharmonic behaviour, whereas the network vibration, iron-polyhedral and PO₄ network bending modes show hardening [73]. The asymmetric vibrations of Q¹ and Q² along with the network vibration mode became anomalously narrower at high temperatures. Thus, the occurrence of mode hardening/ softening provide evidence of structural relaxations in the iron-phosphate glass [73].

6.2 Conclusions

The novel aspects presented in this thesis are as follows:

1. Properties driven by short-range structural changes in lead-borate [$x\text{PbO}:(1-x)\text{B}_2\text{O}_3$] glasses exhibit a broad maxima around $x = 0.3$, in congruence with the average coordination number $\langle r \rangle$, owing to the gradual conversion of three-coordinate (B_3) to four-coordinate (B_4) boron species in the glass structure with increasing concentration of PbO up to a certain x , as evidenced by Raman scattering. Whereas, dynamic properties such as the Boson peak and fragility in $x\text{PbO}:(1-x)\text{B}_2\text{O}_3$ glasses behave similar to short-range structural properties except an anomalous dip at $x = 0.3$. These two properties exhibit linear correlation [70].

2. Analysis of the Boson peak and FSDP revealed that while the Boson peak arises from intermediate-range ordering within the network units, the FSDP arises due to ordering of voids between such units. The anomalous behaviour of the Boson peak and fragility are found to be connected to their common origin in the intermediate-range ordered structures. The anomalous variation in the intermediate-range length scale reflects the critical role of Pb^{2+} in tuning the intermediate-range structure of the vitreous network [70].
3. A drastic decrease of network rigidity above T_g was observed from high-temperature Brillouin scattering in the lead-borate glasses, which was attributed to network disruption and structural relaxation in the supercooled liquid [217].
4. The longitudinal acoustic mode frequency in lead-tellurite glasses shows a scaling behaviour in the glassy state. PbO was found to affect the tellurite network by stiffening the molecular units at a microscopic scale, while reducing the network rigidity on a macroscopic length-scale, upon increasing the temperature [71].
5. Microstructural evolution during devitrification in $0.3\text{PbO}:0.7\text{TeO}_2$ glass confirms a two-dimensional growth mechanism. This glass is found to crystallize into PbTeO_3 phase while heating, while anomalous crystallization into $\text{Pb}_2\text{Te}_3\text{O}_8$ phase was observed when the devitrified melt was cooled. This interesting observation was explained using amorphous phase separation inherent to the tellurite glass system owing to the presence of unique asymmetric structural units in the melts [72].
6. Raman mode frequencies and line-widths of iron-phosphate glass were found to exhibit anomalous behaviour and discontinuous changes were observed across T_g . These anomalies are attributed to structural relaxations in the glass [73].

6.3 Future scope

- ❖ The Boson peak appears over an excess of Debye density of states and can be observed in low-temperature specific heat measurements and inelastic neutron scattering measurements apart from Raman scattering. A study of Boson peak for lead-borate glasses from specific heat and neutron scattering will improve our understanding of the nature and origin of these excess states in borate glasses.
- ❖ A q -dependent inelastic neutron scattering (using synchrotron source) study of the Boson peak in lead-borate glasses will enrich our understanding of its origin based on the recent theoretical models.
- ❖ A high-pressure study of the Boson peak and FSDP in lead-borate glasses will manifest the changes in the medium-range corresponding to the superstructural units and cation-centered void-ordering, respectively.
- ❖ A Raman study of the Boson peak in lead-tellurites at high temperature will be useful to see the effect of PbO in the medium-range order. A molecular dynamics simulation study can be employed to get insight on the type of unit structures in tellurites that give rise to the medium-range correlations.
- ❖ Boson peak and fragility studies in iron-phosphate glasses for different compositions of Fe_2O_3 will throw light on the effect of the modifier cation on the intermediate-range length-scales and temperature response of relaxations in the phosphate melts.

References

- [1] A.K. Varshneya, Academic Press, Inc. (1994).
- [2] P.G. Debenedetti, F.H. Stillinger, *Nature* 410 (2001) 259.
- [3] B. Karmakar, K.R. and, A.L. Stepanov, William Andrew (Elsevier) (2016).
- [4] C.A. Angell, *Science* 267 (1995) 1924.
- [5] M. Matthieu, *Reports on Progress in Physics* 79 (2016) 066504.
- [6] J.E. Shelby, *The Royal Society of Chemistry* 2nd Ed. (2005).
- [7] P. Boolchand, World Scientific Publishing Co. Pte. Ltd. *Series on Directions in Condensed Matter Physics*, Vol 17 (2000).
- [8] H.E.S. F. Mallamace, IOS Press *Proceedings of the International School of Physics <Enrico Fermi>* (1997).
- [9] M.D. Ediger, C.A. Angell, S.R. Nagel, *The Journal of Physical Chemistry* 100 (1996) 13200.
- [10] R. Zallen, WILEY-VCH Verlag GmbH & Co. KGaA, Weinheim (2004).
- [11] W. Kauzmann, *Chemical Reviews* 43 (1948) 219.
- [12] K. Tanaka, K. Shimakawa, Springer (2011).
- [13] G.N. Greaves, S. Sen, *Advances in Physics* 56 (2007) 1.
- [14] L. Berthier, G. Biroli, *Reviews of Modern Physics* 83 (2011) 587.
- [15] M. Paluch, C.M. Roland, S. Pawlus, J. Ziolo, K.L. Ngai, *Physical Review Letters* 91 (2003) 115701.
- [16] B. Ruta, Ph. D. Thesis at European Synchrotron Radiation Facility - Grenoble, France (2010).
- [17] G.P. Johari, M. Goldstein, *The Journal of Chemical Physics* 55 (1971) 4245.
- [18] G.P. Johari, M. Goldstein, *The Journal of Chemical Physics* 53 (1970) 2372.
- [19] S.M. Kosslyn, *Science* 267 (1995) 1615.
- [20] C.A. Angell, *Journal of Non-Crystalline Solids* 73 (1985) 1.
- [21] J. Jackle, *Reports on Progress in Physics* 49 (1986) 171.
- [22] W.H. Zachariasen, *J. Amer. Chem. Soc.* 54 (1932) 3841.
- [23] J.C. Phillips, *Journal of Non-Crystalline Solids* 34 (1979) 153.
- [24] J.C. Phillips, M.F. Thorpe, *Solid State Communications* 53 (1985) 699.

- [25] J.C. Mauro, American Ceramic Society Bulletin 90 (2011) 31.
- [26] W. A. Johnson, R.F. Mehl, Trans. Am. Inst. Min. (Metall.) Eng. 135 (1939) 416.
- [27] M. Avrami, The Journal of Chemical Physics 7 (1939) 1103.
- [28] M. Avrami, The Journal of Chemical Physics 8 (1940) 212.
- [29] M. Avrami, The Journal of Chemical Physics 9 (1941) 177.
- [30] H. Yinnon, D.R. Uhlmann, Journal of Non-Crystalline Solids 54 (1983) 253.
- [31] M.J. Starink, Journal of Materials Science 36 (2001) 4433.
- [32] D.W. Henderson, Journal of Non-Crystalline Solids 30 (1979) 301.
- [33] S.R. Elliott, Nature 354 (1991) 445.
- [34] L.E. Busse, Physical Review B 29 (1984) 3639.
- [35] H. Tsutsu, K. Tamura, H. Endo, Solid State Communications 52 (1984) 877.
- [36] S.R. Elliott, Longman, London 2nd Edn. (1990).
- [37] D.L. Price, S.C. Moss, R. Reijers, M.L. Saboungi, S. Susman, Journal of Physics C: Solid State Physics 21 (1988) L1069.
- [38] S.R. Elliott, Physical Review Letters 67 (1991) 711.
- [39] C. Kittel, John Wiley & Sons, Inc. 8th Ed. (2005) 567.
- [40] W.A. Phillips, Topics in Current Physics: Springer (1981).
- [41] R.C. Zeller, R.O. Pohl, Physical Review B 4 (1971) 2029.
- [42] S.N. Yannopoulos, K.S. Andrikopoulos, G. Ruocco, Journal of Non-Crystalline Solids 352 (2006) 4541.
- [43] A.P. Sokolov, E. Rössler, A. Kisliuk, D. Quitmann, Physical Review Letters 71 (1993) 2062.
- [44] G. D'Angelo, G. Carini, C. Crupi, M. Koza, G. Tripodo, C. Vasi, Physical Review B 79 (2009) 014206.
- [45] U. Buchenau, N. Nücker, A.J. Dianoux, Physical Review Letters 53 (1984) 2316.
- [46] D. Engberg, A. Wischnewski, U. Buchenau, L. Börjesson, A.J. Dianoux, A.P. Sokolov, L.M. Torell, Physical Review B 58 (1998) 9087.
- [47] A.I. Chumakov, G. Monaco, A. Monaco, W.A. Crichton, A. Bosak, R. Rüffer, A. Meyer, F. Kargl, L. Comez, D. Fioretto, H. Giefers, S. Roitsch, G. Wortmann, M.H. Manghnani, A. Hushur, Q. Williams, J. Balogh, K. Parliński, P. Jochym, P. Piekarczyk, Physical Review Letters 106 (2011) 225501.

- [48] E. Duval, A. Boukenter, T. Achibat, *Journal of Physics: Condensed Matter* 2 (1990) 10227.
- [49] V.L. Gurevich, D.A. Parshin, H.R. Schober, *Physical Review B* 67 (2003) 094203.
- [50] D.A. Parshin, H.R. Schober, V.L. Gurevich, *Physical Review B* 76 (2007) 064206.
- [51] W. Schirmacher, G. Ruocco, T. Scopigno, *Physical Review Letters* 98 (2007) 025501.
- [52] S.N. Taraskin, Y.L. Loh, G. Natarajan, S.R. Elliott, *Physical Review Letters* 86 (2001) 1255.
- [53] T.S. Grigera, V. Martin-Mayor, G. Parisi, P. Verrocchio, *Nature* 422 (2003) 289.
- [54] F. Léonforte, A. Tanguy, J.P. Wittmer, J.L. Barrat, *Physical Review Letters* 97 (2006) 055501.
- [55] K.J. Rao, Elsevier Science & Technology Books (2002).
- [56] A.C. Wright, G. Dalba, F. Rocca, N.M. Vedishcheva, *Physics and Chemistry of Glasses - European Journal of Glass Science and Technology Part B* 51 (2010) 233.
- [57] A.C. Wright, *Int. J. Appl. Glass Sci.* 6 (2015) 45.
- [58] A.C. Wright, *Phys. Chem. Glasses: Eur. J. Glass Sci. Technol. B* 51 (2010) 1.
- [59] B.N. Meera, A.K. Sood, N. Chandrabhas, J. Ramakrishna, *Journal of Non-Crystalline Solids* 126 (1990) 224.
- [60] C. Duverger, M. Bouazaoui, S. Turrell, *Journal of Non-Crystalline Solids* 220 (1997) 169.
- [61] E. Yousef, M. Hotzel, C. Rüssel, *Journal of Non-Crystalline Solids* 342 (2004) 82.
- [62] Y. Yoshinori, T. Katsuhisa, S. Jinhai, H. Kazuyuki, *Journal of Physics: Condensed Matter* 14 (2002) 13493.
- [63] T. Sekiya, N. Mochida, A. Ohtsuka, M. Tonokawa, *Journal of Non-Crystalline Solids* 144 (1992) 128.
- [64] A.G. Kalampounias, S. Boghosian, *Vibrational Spectroscopy* 59 (2012) 18.

- [65] H. Yamamoto, H. Nasu, J. Matsuoka, K. Kamiya, *Journal of Non-Crystalline Solids* 170 (1994) 87.
- [66] H. Bürger, K. Kneipp, H. Hobert, W. Vogel, V. Kozhukharov, S. Neov, *Journal of Non-Crystalline Solids* 151 (1992) 134.
- [67] S. Manning, H. Ebendorff-Heidepriem, T.M. Monro, *Opt. Mater. Express* 2 (2012) 140.
- [68] L.B. Fletcher, J.J. Witcher, N. Troy, S.T. Reis, R.K. Brow, R.M. Vazquez, R. Osellame, D.M. Krol, *Opt. Mater. Express* 1 (2011) 845.
- [69] A.K. Yadav, P. Singh, *RSC Advances* 5 (2015) 67583.
- [70] Soumee Chakraborty, V. Sivasubramanian, L. Herojit Singh, R. Venkata Krishnan, A.K. Sinha, *J. Alloys and Comp.* Under Review.
- [71] S. Chakraborty, A.K. Arora, V. Sivasubramanian, P.S.R. Krishna, R.V. Krishnan, *Journal of Physics: Condensed Matter* 24 (2012) 505401.
- [72] S. Chakraborty, R.V. Krishnan, V. Sivasubramanian, S. Kalavathi, *Materials Research Express* 1 (2014) 045203.
- [73] S. Chakraborty, A.K. Arora, *Vibrational Spectroscopy* 61 (2012) 99.
- [74] K.J. Rao, Elsevier Science Ltd. (2002).
- [75] K. Joseph, K. V. G. Kutty, P. Chandramohan, P.R.V. Rao, *J. Nucl. Mater.* 384 (2009) 262.
- [76] J.E. Shelby, The Royal Society of Chemistry (2005).
- [77] M. Cardona, Springer-Verlag Second Edition (1983).
- [78] J. R. Ferraro, K. Nakamoto, C.W. Brown, Elsevier Science Ltd. (2003).
- [79] C. V. Raman, K.S. Krishnan, *Nature* 121 (1928) 501.
- [80] W. Hayes, R. Loudon, Dover Publications, Inc. (1978).
- [81] R. Shuker, R.W. Gammon, *Physical Review Letters* 25 (1970) 222.
- [82] J.F. Nye, Oxford University Press (1985).
- [83] J.R. Sandercock, JRS Scientific Instruments.
- [84] F. Balestra, ISTE Ltd and John Wiley & Sons, Inc. First Edition (2014) 156.
- [85] B.E. Warren, *Chemical Reviews* 26 (1940) 237.
- [86] A.C. Wright, *International Journal of Applied Glass Science* 6 (2015) 45.

- [87] A.C. Wright, N.M.V. and, B.A. Shakhmatkin, MRS Online Proceedings Library Archive 455 (1996) 381.
- [88] A.C. Wright, Physics and Chemistry of Glasses - European Journal of Glass Science and Technology Part B 51 (2010) 1.
- [89] H. Ushida, Y. Iwadate, T. Hattori, S. Nishiyama, K. Fukushima, Y. Ikeda, M. Yamaguchi, M. Misawa, T. Fukunaga, T. Nakazawa, S. Jitsukawa, Journal of Alloys and Compounds 377 (2004) 167.
- [90] Y. Iwadate, T. Hattori, S. Nishiyama, K. Fukushima, N. Igawa, K. Noda, Journal of Materials Science Letters 15 (1996) 776.
- [91] E.I. Kamitsos, G.D. Chryssikos, Journal of Molecular Structure 247 (1991) 1.
- [92] T. Takaishi, J. Jin, T. Uchino, T. Yoko, Journal of the American Ceramic Society 83 (2000) 2543.
- [93] R.E. Youngman, S.T. Haubrich, J.W. Zwanziger, M.T. Janicke, B.F. Chmelka, Science 269 (1995) 1416.
- [94] S.R. Elliott, Journal of Physics: Condensed Matter 4 (1992) 7661.
- [95] K. Witke, M. Willfahrt, T. Hübert, P. Reich, Journal of Molecular Structure 349 (1995) 373.
- [96] A.P. Sokolov, A. Kisliuk, M. Soltwisch, D. Quitmann, Physical Review Letters 69 (1992) 1540.
- [97] L. Börjesson, A.K. Hassan, J. Swenson, L.M. Torell, A. Fontana, Physical Review Letters 70 (1993) 1275.
- [98] N.V. Surovtsev, J. Wiedersich, A.E. Batalov, V.N. Novikov, M.A. Ramos, E. Rössler, The Journal of Chemical Physics 113 (2000) 5891.
- [99] M. Massot, S. Souto, M. Balkanski, Journal of Non-Crystalline Solids 182 (1995) 49.
- [100] N.A. Mauro, M. Blodgett, M.L. Johnson, A.J. Vogt, K.F. Kelton, Nature Communications 5 (2014) 4616.
- [101] Y. Matsuda, Y. Fukawa, M. Kawashima, S. Mamiya, M. Kodama, S. Kojima, Physics and Chemistry of Glasses - European Journal of Glass Science and Technology Part B 50 (2009) 367.

- [102] S.-K. Lee, M. Tatsumisago, T. Minami, *Journal of the Ceramic Society of Japan* 103 (1995) 398.
- [103] A. Hayashi, M. Nakai, M. Tatsumisago, T. Minami, Y. Himei, Y. Miura, M. Katada, *Journal of Non-Crystalline Solids* 306 (2002) 227.
- [104] E. Stavrou, S. Kriptou, C. Raptis, S. Turrell, K. Syassen, *physica status solidi (c)* 8 (2011) 3039.
- [105] Y. Cheng, H. Xiao, W. Guo, W. Guo, *Ceramics International* 33 (2007) 1341.
- [106] V.K. Malinovsky, V.N. Novikov, A.P. Sokolov, *Physics Letters A* 153 (1991) 63.
- [107] S. Kojima, V.N. Novikov, M. Kodama, *The Journal of Chemical Physics* 113 (2000) 6344.
- [108] J.E. Shelby, *Journal of the American Ceramic Society* 66 (1983) 225.
- [109] A. Hayashi, M. Nakai, M. Tatsumisago, T. Minami, *Comptes Rendus Chimie* 5 (2002) 751.
- [110] W.L. Konijnendijk, J.M. Stevels, *Journal of Non-Crystalline Solids* 18 (1975) 307.
- [111] Z. Pan, S.H. Morgan, B.H. Long, *Journal of Non-Crystalline Solids* 185 (1995) 127.
- [112] W.L. Konijnendijk, H. Verweij, *Journal of the American Ceramic Society* 59 (1976) 459.
- [113] B.P. Dwivedi, B.N. Khanna, *Journal of Physics and Chemistry of Solids* 56 (1995) 39.
- [114] A.A. Osipov, L.M. Osipova, *Journal of Physics and Chemistry of Solids* 74 (2013) 971.
- [115] V.K. Malinovsky, A.P. Sokolov, *Solid State Communications* 57 (1986) 757.
- [116] D. Engberg, A. Wischnewski, U. Buchenau, L. Börjesson, A.J. Dianoux, A.P. Sokolov, L.M. Torell, *Physical Review B* 59 (1999) 4053.
- [117] A.M. Zahra, C.Y. Zahra, B. Piriou, *Journal of Non-Crystalline Solids* 155 (1993) 45.
- [118] W. Schirmacher, B. Schmid, C. Tomaras, G. Viliani, G. Baldi, G. Ruocco, T. Scopigno, *physica status solidi (c)* 5 (2008) 862.

- [119] U. Buchenau, Y.M. Galperin, V.L. Gurevich, H.R. Schober, *Physical Review B* 43 (1991) 5039.
- [120] G. D'Angelo, C. Crupi, G. Carini, C. Vasi, *Physical Review B* 84 (2011) 172201.
- [121] G. Le Saoût, P. Simon, F. Fayon, A. Blin, Y. Vaills, *Journal of Raman Spectroscopy* 33 (2002) 740.
- [122] V.N. Sigaev, I. Gregora, P. Pernice, B. Champagnon, E.N. Smelyanskaya, A. Aronne, P.D. Sarkisov, *Journal of Non-Crystalline Solids* 279 (2001) 136.
- [123] W. Schirmacher, M. Wagener, *Philosophical Magazine Part B* 65 (1992) 607.
- [124] W. Schirmacher, M. Wagener, *Solid State Communications* 86 (1993) 597.
- [125] W. Schirmacher, G. Diezemann, C. Ganter, *Physical Review Letters* 81 (1998) 136.
- [126] W. Schirmacher, G. Diezemann, C. Ganter, *Physica B: Condensed Matter* 263–264 (1999) 160.
- [127] T. Pang, *Physical Review B* 45 (1992) 2490.
- [128] S.R. Elliott, *EPL (Europhysics Letters)* 19 (1992) 201.
- [129] M.I. Klinger, *Physics Letters A* 170 (1992) 222.
- [130] W. Schirmacher, *Journal of Non-Crystalline Solids* 357 (2011) 518.
- [131] J. Krogh-Moe, *Phys. Chem. Glasses* 1 (1960) 26.
- [132] P.J. Bray, *Journal of Non-Crystalline Solids* 75 (1985) 29.
- [133] J. Krogh-Moe, *Phys. Chem. Glasses* 3 (1962) 1.
- [134] G. Simon, B. Hehlen, E. Courtens, E. Longueteau, R. Vacher, *Physical Review Letters* 96 (2006) 105502.
- [135] T. Yano, N. Kunimine, S. Shibata, M. Yamane, *Journal of Non-Crystalline Solids* 321 (2003) 137.
- [136] T. Uchino, T. Yoko, *The Journal of Chemical Physics* 105 (1996) 4140.
- [137] J. Krogh-Moe, *Acta Cem. Scand.* 18 (1964) 2055.
- [138] R.E. Youngman, J.W. Zwanziger, *The Journal of Physical Chemistry* 100 (1996) 16720.
- [139] S.R. Elliott, *Journal of Non-Crystalline Solids* 182 (1995) 40.

- [140] V.V. Brazhkin, Y. Katayama, K. Trachenko, O.B. Tsiok, A.G. Lyapin, E. Artacho, M. Dove, G. Ferlat, Y. Inamura, H. Saitoh, *Physical Review Letters* 101 (2008) 035702.
- [141] D.L. Price, A.J.G. Ellison, M.-L. Saboungi, R.Z. Hu, T. Egami, W.S. Howells, *Physical Review B* 55 (1997) 11249.
- [142] J. Swenson, L. Börjesson, W.S. Howells, *Physical Review B* 52 (1995) 9310.
- [143] C. Crupi, G. Carini, M. González, G. D'Angelo, *Physical Review B* 92 (2015) 134206.
- [144] C.T. Moynihan, *Journal of the American Ceramic Society* 76 (1993) 1081.
- [145] V.N. Novikov, Y. Ding, A.P. Sokolov, *Physical Review E* 71 (2005) 061501.
- [146] J. Krausser, K.H. Samwer, A. Zaccone, *Proceedings of the National Academy of Sciences* 112 (2015) 13762.
- [147] S.W. Martin, C.A. Angell, *The Journal of Physical Chemistry* 90 (1986) 6736.
- [148] D. Zhu, C.S. Ray, W. Zhou, D.E. Day, *Journal of Non-Crystalline Solids* 319 (2003) 247.
- [149] D. Huang, G.B. McKenna, *The Journal of Chemical Physics* 114 (2001) 5621.
- [150] K.L. Ngai, O. Yamamuro, *The Journal of Chemical Physics* 111 (1999) 10403.
- [151] M. Kawashima, Y. Matsuda, S. Kojima, *Journal of Molecular Structure* 993 (2011) 155.
- [152] A.P. Mirgorodsky, M. Soulis, P. Thomas, T. Merle-Méjean, M. Smirnov, *Physical Review B* 73 (2006) 134206.
- [153] J.S. Wang, E.M. Vogel, E. Snitzer, *Optical Materials* 3 (1994) 187.
- [154] K. Shioya, T. Komatsu, H.G. Kim, R. Sato, K. Matusita, *Journal of Non-Crystalline Solids* 189 (1995) 16.
- [155] M. Tatsumisago, S.-K. Lee, T. Minami, Y. Kowada, *Journal of Non-Crystalline Solids* 177 (1994) 154.
- [156] M. Tatsumisago, S.-i. Kato, T. Minami, Y. Kowada, *Journal of Non-Crystalline Solids* 192–193 (1995) 478.
- [157] G. Vrillet, C. Lasbruggas, P. Thomas, O. Masson, V. Couderc, A. Barthélémy, J.-C. Champarnaud-Mesjard, *Journal of Materials Science* 41 (2006) 305.

- [158] O. Noguera, T. Merle-Méjean, A.P. Mirgorodsky, P. Thomas, J.C. Champarnaud-Mesjard, *Journal of Physics and Chemistry of Solids* 65 (2004) 981.
- [159] K. Kumar, S.B. Rai, D.K. Rai, *Spectrochimica Acta Part A: Molecular and Biomolecular Spectroscopy* 66 (2007) 1052.
- [160] A. Narazaki, K. Tanaka, K. Hirao, N. Soga, *Journal of Applied Physics* 85 (1999) 2046.
- [161] M.A.P. Silva, Y. Messaddeq, S.J.L. Ribeiro, M. Poulain, F. Villain, V. Briois, *Journal of Physics and Chemistry of Solids* 62 (2001) 1055.
- [162] N. Hiroyuki, U. Tomoyoshi, K. Kanichi, K. Hirohisa, K. Ken'ichi, *Japanese Journal of Applied Physics* 31 (1992) 3899.
- [163] J.S. McCloy, B.J. Riley, A.S. Lipton, C.F. Windisch, N.M. Washton, M.J. Olszta, C.P. Rodriguez, *The Journal of Physical Chemistry C* 117 (2013) 3456.
- [164] K. Joseph, R. Venkata Krishnan, K.V. Govindan Kutty, P.R. Vasudeva Rao, *Thermochimica Acta* 494 (2009) 110.
- [165] K. Kaneda, K. Arae, M. Kodama, S. Kojima, *Journal of Non-Crystalline Solids* 358 (2012) 799.
- [166] C. Levelut, R. Le Parc, A. Faivre, B. Champagnon, *Journal of Non-Crystalline Solids* 352 (2006) 4495.
- [167] G. Le Saoût, Y. Vaills, Y. Luspain, *Solid State Communications* 123 (2002) 49.
- [168] T. Rouxel, H. Ji, T. Hammouda, A. Moréac, *Physical Review Letters* 100 (2008) 225501.
- [169] E.M. Vogel, S.G. Kosinski, D.M. Krol, J.L. Jackel, S.R. Friberg, M.K. Oliver, J.D. Powers, *Journal of Non-Crystalline Solids* 107 (1989) 244.
- [170] J.C. Sabadel, P. Armand, F. Terki, J. Pelous, D. Cachau-Herreillat, E. Philippot, *Journal of Physics and Chemistry of Solids* 61 (2000) 1745.
- [171] K. John, A.J. Jacqueline, N. Oleg, D.B. Jay, *Journal of Physics: Condensed Matter* 18 (2006) 903.
- [172] C.T. Moynihan, A.J. Easteal, J. Wilder, J. Tucker, *The Journal of Physical Chemistry* 78 (1974) 2673.
- [173] M. Lasocka, *Materials Science and Engineering* 23 (1976) 173.

- [174] T. Ichitsubo, E. Matsubara, H. Numakura, K. Tanaka, N. Nishiyama, R. Tarumi, *Physical Review B* 72 (2005) 052201.
- [175] B. Yao, H. Ma, H. Tan, Y. Zhang, Y. Li, *Journal of Physics: Condensed Matter* 15 (2003) 7617.
- [176] H.E. Kissinger, *Analytical Chemistry* 29 (1957) 1702.
- [177] R.T. Savalia, K.N. Lad, A. Pratap, G.K. Dey, S. Banerjee, *Journal of Thermal Analysis and Calorimetry* 78 (2004) 745.
- [178] E.R. Shaaban, Y.B. Saddeek, M. Abdel Rafea, *Philosophical Magazine* 89 (2009) 27.
- [179] N.S. Mohan, R. Chen, *Journal of Physics D: Applied Physics* 3 (1970) 243.
- [180] K.N. Lad, R.T. Savalia, A. Pratap, G.K. Dey, S. Banerjee, *Thermochimica Acta* 473 (2008) 74.
- [181] K.M. Benson, K. Hariharan, *Journal of Physics: Condensed Matter* 21 (2009) 115102.
- [182] M.J. Starink, A.M. Zahra, *Thermochimica Acta* 298 (1997) 179.
- [183] H. Hermann, N. Mattern, S. Roth, P. Uebele, *Physical Review B* 56 (1997) 13888.
- [184] A.P. Mirgorodsky, T. Merle-Méjean, J.C. Champarnaud, P. Thomas, B. Frit, *Journal of Physics and Chemistry of Solids* 61 (2000) 501.
- [185] O. Noguera, T. Merle-Méjean, A.P. Mirgorodsky, M.B. Smirnov, P. Thomas, J.C. Champarnaud-Mesjard, *Journal of Non-Crystalline Solids* 330 (2003) 50.
- [186] PbTeO₃ (Pb[TeO₃]_m) Crystal Structure: Datasheet from "PAULING FILE Multinaries Edition – 2012" in SpringerMaterials (http://materials.springer.com/isp/crystallographic/docs/sd_1901544). Springer-Verlag Berlin Heidelberg & Material Phases Data System (MPDS), Switzerland & National Institute for Materials Science (NIMS), Japan.
- [187] J. Machacek, P. Kostka, M. Liska, J. Zavadil, O. Gedeon, *Journal of Non-Crystalline Solids* 357 (2011) 2562.
- [188] H.-L. Jiang, J.-G. Mao, *Journal of Solid State Chemistry* 181 (2008) 345.
- [189] S. Rada, E. Culea, M. Rada, *Materials Chemistry and Physics* 128 (2011) 464.
- [190] L. Zhang, R.K. Brow, M.E. Schlesinger, L. Ghussn, E.D. Zanutto, *Journal of Non-Crystalline Solids* 356 (2010) 1252.

- [191] M. Karabulut, G.K. Marasinghe, C.S. Ray, G.D. Waddill, D.E. Day, Y.S. Badyal, M.-L. Saboungi, S. Shastri, D. Haeffner, *Journal of Applied Physics* 87 (2000) 2185.
- [192] R.K. Brow, *Journal of Non-Crystalline Solids* 263–264 (2000) 1.
- [193] G.K. Marasinghe, M. Karabulut, C.S. Ray, D.E. Day, M.G. Shumsky, W.B. Yelon, C.H. Booth, P.G. Allen, D.K. Shuh, *Journal of Non-Crystalline Solids* 222 (1997) 144.
- [194] B.C. Sales, M.M. Abraham, J.B. Bates, L.A. Boatner, *Journal of Non-Crystalline Solids* 71 (1985) 103.
- [195] D.E. Day, Z. Wu, C.S. Ray, P. Hrma, *Journal of Non-Crystalline Solids* 241 (1998) 1.
- [196] G.N. Greaves, S.J. Gurman, L.F. Gladden, C.A. Spence, P. Cox, B.C. Sales, L.A. Boatner, R.N. Jenkins, *Philosophical Magazine Part B* 58 (1988) 271.
- [197] X. Yu, D.E. Day, G.J. Long, R.K. Brow, *Journal of Non-Crystalline Solids* 215 (1997) 21.
- [198] G.K. Marasinghe, M. Karabulut, C.S. Ray, D.E. Day, D.K. Shuh, P.G. Allen, M.L. Saboungi, M. Grimsditch, D. Haeffner, *Journal of Non-Crystalline Solids* 263–264 (2000) 146.
- [199] M.G. Mesko, D.E. Day, *Journal of Nuclear Materials* 273 (1999) 27.
- [200] B.C. Sales, R.S. Ramsey, J.B. Bates, L.A. Boatner, *Journal of Non-Crystalline Solids* 87 (1986) 137.
- [201] S.T. Reis, D.L.A. Faria, J.R. Martinelli, W.M. Pontuschka, D.E. Day, C.S.M. Partiti, *Journal of Non-Crystalline Solids* 304 (2002) 188.
- [202] Y.M. Lai, X.F. Liang, S.Y. Yang, J.X. Wang, L.H. Cao, B. Dai, *Journal of Molecular Structure* 992 (2011) 84.
- [203] L. Zhang, R.K. Brow, *Journal of the American Ceramic Society* 94 (2011) 3123.
- [204] X. Fang, C.S. Ray, A. Moguš-Milanković, D.E. Day, *Journal of Non-Crystalline Solids* 283 (2001) 162.
- [205] A. Chahine, M. Et-tabirou, J.L. Pascal, *Materials Letters* 58 (2004) 2776.
- [206] R.K. Brow, D.R. Tallant, S.T. Myers, C.C. Phifer, *Journal of Non-Crystalline Solids* 191 (1995) 45.

- [207] C.S. Ray, X. Fang, M. Karabulut, G.K. Marasinghe, D.E. Day, *Journal of Non-Crystalline Solids* 249 (1999) 1.
- [208] B. Pivac, A. Mogaš-Milanković, D.E. Day, *Journal of Non-Crystalline Solids* 226 (1998) 41.
- [209] S.A. Kirillov, S.N. Yannopoulos, *The Journal of Chemical Physics* 117 (2002) 1220.
- [210] H. Liem, J. Cabanillas-Gonzalez, P. Etchegoin, D.D.C. Bradley, *Journal of Physics: Condensed Matter* 16 (2004) 721.
- [211] E.L. Gjersing, S. Sen, B.G. Aitken, *Journal of Non-Crystalline Solids* 355 (2009) 748.
- [212] S.N. Yannopoulos, A.G. Kalampounias, A. Chrissanthopoulos, G.N. Papatheodorou, *The Journal of Chemical Physics* 118 (2003) 3197.
- [213] A.G. Kalampounias, S.N. Yannopoulos, G.N. Papatheodorou, *The Journal of Chemical Physics* 124 (2006) 014504.
- [214] E. Stavrou, C. Tsiantos, R.D. Tsopouridou, S. Kripotou, A.G. Kontos, C. Raptis, B. Capoen, M. Bouazaoui, S. Turrell, S. Khatir, *Journal of Physics: Condensed Matter* 22 (2010) 195103.
- [215] K. Joseph, M. R. R, K. V. G. Kutty, P.R.V. Rao, *Proc. of the National Symposium on Science and Technology of Glass and Glass-Ceramics, Mumbai* (2008) p. 267.
- [216] M.M. Smedskjaer, J.C. Mauro, S. Sen, Y. Yue, *Chemistry of Materials* 22 (2010) 5358.
- [217] Soumee Chakraborty, V. Sivasubramanian, Under Preparation.